

**CFD simulation of Jet and Vortex Actuators (JaVA)
with and without cross flow boundary layer**

A thesis accepted by the Faculty of
Aerospace Engineering and Geodesy of the Universität Stuttgart
in partial fulfilment of the requirements for the degree of
Doctor of Engineering Sciences (Dr. –Ing.)

by

Muhammad Aqeel Rashad
born in Sheikhpura, Pakistan

Main-referee : apl. Prof. Dr.-Ing. Ulrich Rist
Co-referee : Prof. Dr. Hasan Gunes
Date of defence : Aug 26th, 2010

Institut für Aerodynamik und Gasdynamik
Universität Stuttgart

2010

ACKNOWLEDGMENT

First and foremost, I am grateful to The Almighty, without his help and mercy it was not possible for me to complete this work. I pray that He will make this work useful for many.

I would like to profoundly thank my advisor Professor Dr. Ulrich Rist. His unparalleled compassion, kindness and generosity allowed me to cruise through the demands of this research. One thing among many which I learned from him is how to stay positive in every problem you face. Thank you so much.

I would like to thank my advisor Professor Dr. Hasan Gunes for his interest in my work and also becoming co-examiner. His thorough review and comments helps to improve this manuscript.

I would also like to thank all the transition group members at the institute of Aerodynamic and Gas dynamic for their help and friendly atmosphere.

I would like to extend especial thanks to Higher Education Commission (HEC) of Pakistan and Airbus for financially supporting this research. Without their help it was not possible for me to take this initiative. Also I want to say thanks to DAAD (German Academic Exchange Service) whose cooperation with HEC accommodated a number of students in Germany. Thank you very much.

I also want to say thanks to German people and Germany. I have learned lot of things from your rich culture. This will help me throughout my life. Thanks for making this a wonderful stay with lot of beautiful memories.

I also want to say thanks to my late parents. I owe my success to them and am extremely grateful for the inspiration and encouragement I received from them thought my life.

Last but not least, my family deserves a special thanks and gratitude. The incredible sacrifice of time offered by my wife Farzana is invaluable. Without her support it was not possible for me to complete this research. My son Ahmad also deserves a special praise whose smiles and talks were a source of energy for me. My daughter Amna who come in this world during my stay in Germany really enlightened my life.

Thank you all so much for making my life and my stay joyful and beautiful.

Table of content

ACKNOWLEDGMENT	i
Table of content	iii
Abstract	vii
Zusammenfassung	ix
List of symbols	xi
1. Introduction	1
1.1 Background.....	1
1.2 Research overview.....	2
1.3 Introduction of JaVA	5
1.4 Motivation.....	7
1.5 Objectives	7
2. Basic theory	9
2.1 Numerical approach.....	9
2.1.1 Boundary conditions and grid distribution (original design).....	10
2.1.2 Boundary conditions and grid distribution (modified design).....	12
2.2 Theoretical background and conservation equations used in Fluent.....	13
2.2.1 The mass conservation equation.....	13
2.2.2 Momentum conservation equations.....	14
2.3 Overview of moving zone approaches	15
2.3.1 Dynamic mesh	15
2.3.2 Sliding mesh theory	17
3. Test case study	19
3.1 Cavity with open bottom	19
3.2 Cavity with closed bottom.....	29
3.3 Comparison.....	38
3.3.1 Comparison of open (case 1) and closed (case 2) cavity bottom	38
3.3.2 Comparison of closed cavity bottom (case 2) and Lachowicz et al. ..	40
3.4 Summary and conclusions	42
4. Comparative study of different actuator parameters	43

4.1	Geometric parameters study	44
4.1.1	Cavity depth study	44
4.1.2	Plate position study	49
4.1.3	Summary	53
4.2	Material properties study	54
4.2.1	Summary	57
4.3	Flow parameters study	57
4.3.1	Angled jet.....	57
4.3.2	Free jet	59
4.3.3	Wall jet.....	61
4.4	Summary and conclusions	64
5.	Modified design	67
5.1	Geometry and grid distribution.....	67
5.2	Cases studied.....	68
5.2.1	Case-3.1 Vortex flow	69
5.2.2	Case 3.2 Angled (free) jet	82
5.2.3	Case 3.3 Vertical jet.....	83
5.2.4	Case 3.4 Unsteady vortex flow	84
5.3	Comparison of all cases	87
5.4	Summary	95
6.	JaVA in cross flow	97
6.1	Geometry and grid distribution.....	97
6.2	Cases studied.....	98
6.3	Case-4.1 original design (2D).....	99
6.3.1	Configuration-1	99
6.3.2	Configuration-2.....	105
6.3.3	Direct comparison of the 2D cases	110
6.4	Modified design (2D).....	112
6.5	Modified design (3D).....	116
6.5.1	Without cross flow	116
6.5.2	Configuration-1 (with cross flow)	123
6.5.3	Configuration 2 (with cross flow).....	128

6.5.4	Comparison of all cases	136
6.6	Summary and conclusions	138
7.	Summary and conclusions	139
	References.....	145
	Appendix.....	149
	Curriculum Vitae.....	153

Abstract

In the present study an active flow control actuator is studied numerically. This type of actuator was first studied experimentally by Lachowicz et al. and called “Jet and Vortex Actuator” (JaVA). This kind of active flow control actuator produces different flow fields depending upon the frequency and the scaled amplitude of the imposed oscillation. Thus, it can be used to produce different net reactions, like vertical jets, wall jets, or a vortex flow. The actuator under consideration consists of a cavity and a rigid plate which serves as the actuation surface. The actuator plate acts like a piston pumping air out of the cavity on the down stroke and sucking air into the cavity on the upstroke. Different cases are selected for validation of the simulations. Our simulations yield the *unsteady* flow field, whereas only time-averaged data are available from literature. Thus, our simulations provide extra details of the flows through the gaps intended for a better understanding of the actuator flow. Qualitative and quantitative comparisons of the time-averaged data with the experiments are very encouraging. Especially, the different flow regimes appear for the same parameters as in the experiments. Different parameters like cavity depth and plate position relative to the cavity upper wall and compressibility effects are also studied.

In the present work we also presented a modified design in order to improve and understand flow mechanisms. In this new design the horizontal plate is stationary and a vertical plate inside the cavity moves left and right to push fluid through the narrow and wide gap alternatively. Interestingly, in this new design like in the original, once again we get different flow modes like vertical jet, angled jet, vortex and wall jet but from the narrow gap. Different parameters like cavity depth and gap widths and plate position relative to the cavity upper wall are also studied. Relations between different nondimensional parameters like Reynolds number, Stokes number, Strouhal number and scaled amplitude and their effect upon the flow field are also presented in detail.

In the present work 3D results are also presented for the modified design. It was found that strong 3D end effects are present. The flow field is completely different for 2D and 3D simulations. For the same set of parameters in 2D we get a very nice vortex as where in 3D we get a vertical jet.

We also presented results with a cross-flow boundary layer for 2D cases of original and modified design with different orientations of gaps with respect to the

cross-flow. It was found that configuration-2 in the original design in which the narrow gap comes first to the cross flow and the wide gap later, is more effective with respect to increasing the flow momentum close to the wall and in controlling the boundary layer. For the 3D modified design with the cross flow boundary layer two different gap orientations with respect to the oncoming flow are used. In the first configuration the gaps are oriented across the flow with the wide gap coming first and the narrow later. In the second configuration the gaps are oriented along the boundary layer. In the 3D case this second configuration turns out to be the most effective with respect to increasing the flow momentum close to the wall, such that this kind of actuator can be used for boundary layer (separation) control.

For the present investigations the commercial CFD-software FLUENT is used for flow calculation and visualization. The accompanying grid-generation software GAMBIT is used for geometry specification and grid generation.

Zusammenfassung

In der vorliegenden Studie wird ein Aktuator für die aktive Strömungskontrolle numerisch untersucht. Erste experimentelle Untersuchungen zu dem betrachteten „Jet and Vortex Actuator“ (JaVA) wurden von Lachowicz et. al. durchgeführt. Abhängig von der gewählten Frequenz und normierten Amplitude der erzwungenen Oszillation lassen sich unterschiedliche Strömungsbilder erzeugen. So ist es beispielsweise möglich, vertikale oder wandanliegende Strahlen sowie Wirbelströmungen zu erzeugen. Der Aufbau des Aktuators besteht aus einem Hohlraum und einer ebenen Platte, welche als Aktuatoroberfläche dient. Die Funktionsweise ähnelt der eines Kolbens. Bewegt sich die Platte nach unten, so wird Luft aus dem Hohlraum herausgeblasen, bewegt sie sich nach oben, so wird Luft angesaugt. Für die Validierung der Simulationen werden verschiedene Testfälle betrachtet. In der vorliegenden Arbeit werden *instationäre* Strömungsfelder berechnet, während der Literatur bisher nur zeitlich gemittelte Daten zu entnehmen sind. Daher ermöglichen unsere Simulationen einen detaillierteren Einblick in die Strömungsbedingungen durch die Spalten und damit in die Funktionsweise des gesamten Aktuators. Sowohl qualitative als auch quantitative Vergleiche mit den zeitlich gemittelten Daten aus dem Experiment stimmen sehr zuversichtlich. Im Besonderen werden gute Übereinstimmungen der verschiedenen Strömungsbilder in Abhängigkeit der gewählten Parameter fest gestellt. Zusätzlich werden weitere Parameter, wie die Tiefe des Hohlraumes und die Relativposition der Platte zur Hohlraumoberfläche, untersucht.

In der vorliegenden Arbeit wird zusätzlich ein modifiziertes Design zur Verbesserung des Strömungsfeldes und unseres Verständnisses von ihm präsentiert. Das neue Design besteht aus einer festen, horizontalen Platte und einer nach links und rechts verschiebbaren vertikalen Platte darunter, welche das Fluid alternativ durch eine schmale oder breite Spalte drückt. Interessanter Weise stellen sich für dieses veränderte Design wieder verschiedene Strömungsbilder wie vertikaler oder angewinkelter Freistrahler, Wirbel oder wandnaher Strahl ein, jedoch diesmal vom schmalen Schlitz aus. Verschiedene Parameter wie Hohlraumtiefe, Schlitzbreite und Plattenposition werden auch für diesen Fall untersucht. Die Zusammenhänge zwischen den unterschiedlichen dimensionslosen Parametern wie Reynolds-, Stokes-

oder Strouhalzahl sowie der normierten Amplitude und ihr Einfluss auf das Strömungsfeld werden detailliert dargestellt.

Zudem werden für das modifizierte Design auch 3D Ergebnisse gezeigt. Es wurden starke 3D-Einflüsse auf das Strömungsfeld festgestellt. Das gesamte Strömungsbild unterscheidet sich von den simulierten 2D-Fällen. So stellt sich beispielsweise für gegebene Parameter im 2D-Fall eine Wirbelströmung ein während im 3D-Fall ein vertikaler Freistrah beobachtet wird.

Ausserdem zeigen wir 2D-Ergebnisse mit einer Grenzschicht mit Querströmung für das ursprüngliche und das modifizierte Design für verschiedene Relativpositionen der Schlitze zur Querströmung. Es zeigt sich, dass bei Konfiguration 2, bei der der schmale Schlitz in Strömungsrichtung zuerst kommt, effizienter im Hinblick auf die Erhöhung des Strömungsimpulses nahe der Wand und damit auch im Hinblick auf die Grenzschichtkontrolle ist. Für den modifizierten 3D-Fall mit Grenzschicht mit Querströmung werden zwei unterschiedliche Schlitzorientierungen relativ zur Anströmung verwendet. Bei der ersten Konfiguration sind die Schlitze quer zu Anströmung ausgerichtet, wobei der breite Schlitz zuerst kommt und der schmale dahinter. Bei der zweiten Konfiguration sind die Schlitze parallel zur Grenzschicht angeordnet. Im 3D-Fall erweist sich die zweite Konfiguration als effektiver beim Impulstransport zur Wand hin und damit auch für die Grenzschicht- (Ablöse-) Kontrolle.

Die vorliegende Arbeit wurde mit dem kommerziellen CFD-Softwarepaket FLUENT für die Strömungssimulation und Visualisierung durchgeführt. Das dazugehörige Gittergenerierungsprogramm GAMBIT wurde für die Geometrieerstellung und Gittererstellung verwendet.

List of symbols

Symbols

X	x-axis
Y	y-axis
Z	z-axis
x	length in X-direction
y	length in Y-direction
z	length in Z-direction
f	frequency
a	Amplitude (mean to peak plate distance)
S_a	scaled amplitude ($2\pi a/b$) or ($2\pi a/h$)
Str	Strouhal number ($\text{Str} = f W_n / U_{\max}$)
T	oscillation Period ($1/f$)
W_n	Narrow gap width
W_w	Wide gap width
b	Plate width
h	cavity depth (plate height in new design)
g_n	Ratio of narrow gap width to plate width (W_n/b)
g_w	Ratio of wide gap width to plate width (W_w/b)
Re	Reynolds number
Re_{plate}	Plate Reynolds number ($U_p b/\nu$)
Re_{gap}	Gap Reynolds number ($U_{\max \text{ gap}} W_n/\nu$)
D	$W_n + W_w + b$
1-D	One diameter
2-D	Two diameter
2D	Two dimensional
3D	Three dimensional
ω	Circular frequency ($2\pi f$)
U, u	velocity
U_n	Velocity in narrow gap
ρ	density
t	time
∇	$\partial/\partial x + \partial/\partial y + \partial/\partial z$

δ	Boundary layer thickness
π	Circular constant (3.14159)
μ	Dynamic viscosity
ν	Kinematics viscosity
θ	phase
$^{\circ}$	degree
α_1	Layer split factor
α_2	Layer collapse factor
P	Pressure
B	Body force
g	Gravitational force
Φ	General scalar
S_{Φ}	source term of Φ
Γ	diffusion coefficient
\vec{u}_g	grid velocity of the moving mesh
n	Quantity at current time
$n+1$	Quantity at next time level
V	Volume
A	Area
Δ	Step size
r	Grid cell height
w.r.t	With respect to
$>$	Greater than
$<$	Less than
Up	Plate velocity
V_{gap}	Gap velocity
h	Cavity height
hp	Plate thickness
%	percent

Abbreviations

DNS	Direct numerical simulation
JaVA	Jet and vortex actuator
VGJ	Vortex generator jet
MEMS	Micro-Electro-Mechanical Systems
6DOF	Six degree of freedom
ZNMF	zero-net-mass-flux
UDF	User defined function
vel.	velocity
min	Minimum
max	Maximum

1. Introduction

1.1 Background

Actuator flow control can be of two kinds passive and active: Flow control for improving aircraft aerodynamic performance has been predominantly passive. Passive control is characterized by fixed devices that are configured to improve the system performance over a given flight regime. An example of a passive separation control device is the fixed vortex generator used on high-lift systems. At landing/takeoff conditions, the vortex generator transports high-momentum fluid from the outer boundary layer towards the wing surface, energizing the boundary layer and delaying separation. Though these fixed devices are simple, rugged, and relatively low in cost to manufacture, there are two significant disadvantages:

- i) Passive devices cannot be optimized for multiple flight conditions (e.g. for landing/takeoff flight and maneuvering flight); and
- ii) Most passive devices add parasitic drag when they are not in use e.g. in steady cruise condition.

Active flow control actuators minimize both these disadvantages. These actuators can be used in multiple flight condition in contrast to passive flow control devices. Furthermore, an active flow control actuator produces negligible drag when the system is not actuated. Future aircraft will need active flow control devices to meet increasing demands on efficiency and lower emissions (noise and fuel burnt). According devices typically use suction and blowing in a more or less cyclic manner. These devices may be installed within the external surfaces of the airframe for separation control, noise reduction and control of laminar-turbulent transition or inside the engines and other tubing to increase their efficiency or to make them quieter. A great variety of possible actuator designs are proposed and studied by many researchers. And there is a lot of activity but not free of problems. Foreseeable open problems are the durability and resistance of these actuators with respect to dirt and use, maximizing their efficiency and keeping their weight and manufacturing costs reasonably low. There is a clear need to study and understand the influence of the different geometrical parameters on the flow induced by an actuator and also to accurately predict its behavior (to eliminate “trial-and-error” designs). Therefore in

the present study we select an actuator which was presented by Lachowicz et al. [18] as a reference to contribute to this research. The reason to select this actuator is its surprising ability to produce different flow regimes only by changing the actuation parameters, i.e. frequency and amplitude but no need to change geometrical parameters. We will also present a variation of this actuator and characterize it in detail. We will also see its behavior in the cross-flow on a computer perhaps for the first time.

1.2 Research overview

Jet actuation is of prime importance in the aerospace industry and over the years many researchers have investigated them both experimentally and numerically using computers. This section presents an overview of the relevant research found in the open literature. The main objective of this is to highlight and extract the principal features of the actuator and associated fluid dynamics, and to identify unresolved issues. Active flow control is achieved by momentum addition techniques including streamwise vortex generation via discrete blowing or injection through dynamically activated and driven devices, and direct tangential injection of high velocity fluid. Of particular interest is the use of discrete jet injection for streamwise vortex generation.

This concept arose in the 1950s. The vortex generator jet method was first examined almost 50 years ago by Wallis [33] and Wallis and Stuart [34], primarily for the purpose of delaying shock-induced separation of turbulent boundary layers and is the subject of research for Zhand and Sheng 1987, Reynolds et al. 1988, Johnston and Nishi [13], Compton and Johnston [2], McManus et al. [15]; Seifert et al. 1996; Gad-el-Hak [5] and Bushnell [6]; Wiltse and Glezer [36]; Jacobson and Reynolds [12]. What is of particular interest is the ability to apply vortex generators as required.

Johnston and Nishi [13] employ a spanwise array of small, skewed, pitched jets from the holes in the surface. They showed that the jets can produce longitudinal vortices strong enough to reduce or eliminate a large stalled region of a turbulent separated flow. Compton and Johnston [2], Hasegawa and Matsuuchi [9] showed that the generation of stream wise mixing vortices with vortex-generator jets (VGJ) that are pitched at an acute angle relative to the main flow surface and skewed with respect to the local main flow direction is useful for separation control. The maximum vorticity strongly depends on the blowing ratio. Compton and Johnston [2] also measured the longitudinal velocity and maximum vorticity distributions with variation

of the velocity ratio and skew angle in the range between 0 and 180 degrees to investigate the flow and heat transfer characteristics. The maximum vorticity was strongly dependent on the jet velocity and skew angle, and an optimal skew angle was obtained between 45 and 90 degrees.

McManus et al. [15] conducted a series of experiments in the laboratory in which pulsed jets were employed to improve the leading-edge flap effectiveness on a high-performance fighter. Their separation-control technique exploits the remarkable vorticity-generation capabilities of impulsively started jets to enhance boundary-layer-momentum transport and thus suppress stall for both compressible and incompressible flows. In addition to the customary streamwise vortices, large-scale turbulent vortex rings are also generated in the flow as a result of pulsing the jets. The net effect is to achieve fairly good stall suppression with substantially lower jet mass-flow rate.

In recent years, the application of vortex-generator jets to control the dynamic stall produced by changing the angle of attack of the airfoil has been reported. However, the control system does not have the ability to adaptively suppress the flow separation caused by changing flow conditions. Applications of vortex generator jets (VGJ) to time-varying flow fields have not yet been reported. Unlike conventional vortex generators, the drag penalty of the VGJ is negligible when the jets are turned off. The jet and vortex actuator (JaVA) of the current study also provides negligible drag when the system is not actuated, yet requires no external plumbing (unlike the VGJ) since it is a zero-net-mass flux system. This allows for reduced vehicle mass, decreased aircraft signature, and design simplicity. The JaVA operates over a range of amplitudes and frequencies, potentially allowing control over different flight regimes.

Numerous devices for actuating a variety of flow fields have been advanced during the last decade. This has mostly been motivated by the quest to achieve efficient reactive flow control of turbulent flows. Most of the focus has been on surface mounted actuators. An example of a surface mounted zero-net-mass flux actuator is the synthetic jet developed by Wiltse and Glezer [36]. They opened an interesting path when they used piezoelectric-driven cantilevers as flow-control actuators to beneficially affect free shear layers. The basic actuator consists of a diaphragm that is oscillated in response to cyclic pressure fluctuations generated within an enclosed cavity. At relatively high frequencies, these actuators operate similar to acoustic streaming devices studied by Ingard and Labote [10]. Following

the idea of Wiltse and Glezer [37], Jacobson and Reynolds [11] designed an actuator that has the piezoelectric cantilever beam mounted flush with a boundary surface. The cantilever beam was placed asymmetrically within a cavity to form wide and narrow gaps see Figure 1.1. The cantilever was oriented in the stream wise direction, fixed to the wall at its upstream end, and could flex out into the flow and down into the cavity in the wall. The actuator was tested in water of a free stream velocity of 0.25 m/s and a tip-amplitude and frequency of 0.13 mm and 330 Hz, respectively. When the cantilever flexes into the cavity, it forces fluid out of the cavity into the external flow, and when the cantilever flexes out of the cavity, fluid is drawn into the cavity from the external flow see *Figure 1.1*. A periodically emerging jet, from the narrow slot, generated longitudinal vortical disturbances when interacting with external flow. In their application, disturbances produced by the actuator were designed to cancel vortical disturbances generated by a cylinder placed upstream of the actuator. (In the uncontrolled boundary layer, the cylinder-induced vertical disturbances ultimately led to laminar-turbulent transition.) The actuator system delayed transition by about 40 displacement thicknesses. Neither Wiltse and Glezer [37] nor Jacobson and Reynolds [11] used MEMS technology to fabricate their actuators. However the main conclusion drawn Jacobson and Reynolds [11] and [12] was that future actuators must be MEMS-based in order to match the relevant scales of turbulent flows.

Koumoutsakos [17] conducted a parametric numerical study of an actuator with no external flow. Instead of simulating the motion of a cantilevered beam, piston-type motion was simulated in order to determine the fundamental physical mechanisms responsible for disturbance generation from the actuator. For a given slot width, Koumoutsakos [17] showed that at relatively high frequencies, a periodic jet developed from the narrow slot, while at relatively low frequencies, the periodic jet developed from the wide slot. This suggested that the actuator slot flow is Stokes number dependent. However, Saddoughi et al. [31] conducted a series of experiments using a cantilevered-beam type actuator with the same Stokes number as Jacobson and Reynolds [11]. It was found that the flow patterns in the two experiments were qualitatively different.

Thus, similar to the study of Koumoutsakos [17], a more basic actuator motion, the piston-type motion, is used in this study to better understand the actuator flow physics. However, the stand-alone jet and vortex actuator (JaVA) operates at relatively low frequencies and is capable of producing multiple flow fields. For

example, in addition to producing jet-like flow fields, the stand-alone JaVA can generate a mono-directional vortex flow field.

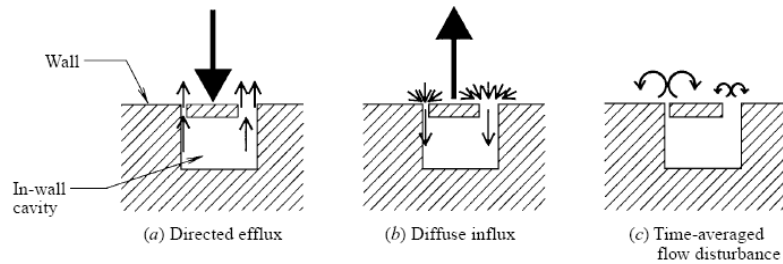


Figure 1.1 Flow distribution as a cantilever section of the wall moves into and out of a wall cavity. Jacobson and Reynolds [11]

1.3 Introduction of JaVA

The active flow control actuator which is used as a reference for our study here stems from Lachowicz et al. [18], where it is called a "Jet and Vortex Actuator" (JaVA), due to its unique capabilities of using multiple flow types, depending on the actuation parameters (frequency and amplitude). The current JaVA system evolved from an earlier flow actuator developed by Jacobson and Reynolds [11] see *Figure 1.1*. In an effort to contribute to this, Lachowicz et al. [18] have built a somewhat generic setup Jet and Vortex actuator (JaVA) that allows to change and to assess the influence of different parameters independently. The original actuator, see *Figure 1.2*, (JaVA) consists of a cavity and a rigid plate which serves as the actuation surface. The plate is placed at the top of the cavity such that it forms a narrow and a wide gap when viewed from the top. The plate is oscillated in the vertical direction such that the plate motion is uniform along its length and width. The actuator plate acts like a piston pumping air out of the cavity on the down stroke and sucking air into the cavity on the upstroke. The flow field was computed and visualized by varying the size of the actuator, width of narrow and wide gap and also by varying the amplitude and frequency of oscillation. According to Lachowicz et al. [18] depending on four non-dimensional parameters (Reynolds number, amplitude ratio, and narrow and wide gap widths), a free jet through the wide gap, a vortex through the wide gap, a vectored free jet through the wide gap, or a horizontal wall jet through the narrow gap are generated by the actuator. A free jet is produced at relatively low amplitude and high frequency from the narrow gap while at relatively high amplitude and low frequency a free jet is produced from the wide gap. As the amplitude increases a wall jet is created. The wall jet is primarily horizontal near the narrow gap and is characterized

by steady horizontal flow pumping from the wide gap end to the narrow gap end. In non-dimensional space (scaled amplitude S_a vs. Reynolds number Re) a typical arrangement of flow regimes is shown in *Figure 1.3*. Such actuators may be used to energize the boundary layer by accelerating the fluid tangentially near the wall surface. The vortex regime may be used to promote mixing and suppress boundary layer separation.

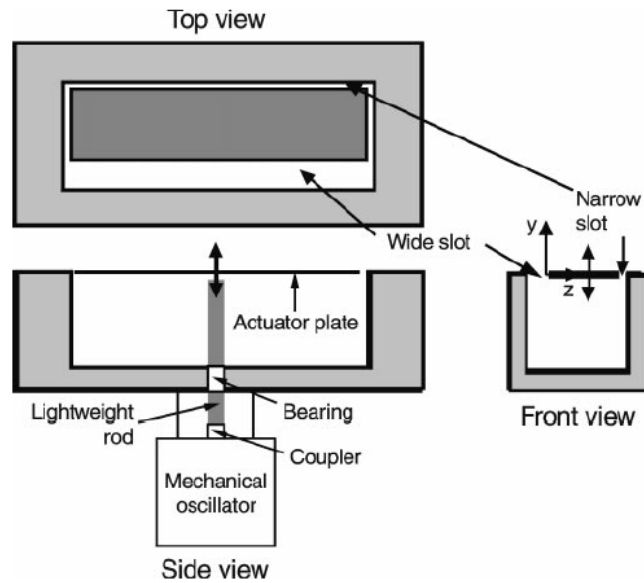
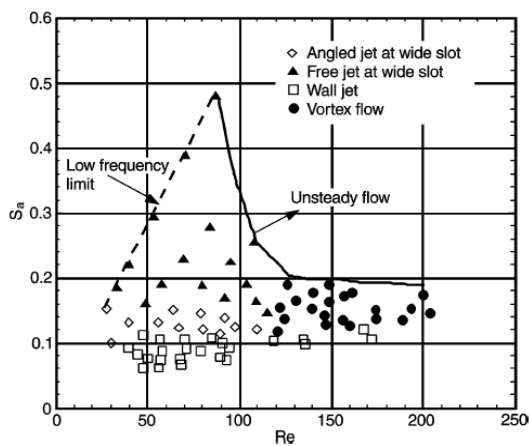
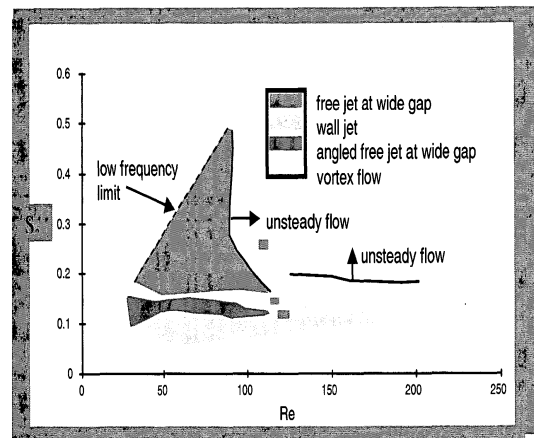


Figure 1.2 Basic set-up of the JaVA, from Lachowicz et al. [18]



(a) Lachowicz et al. [18]



(b) Lachowicz et al. [18]

Figure 1.3 JaVA's produced flow fields

1.4 Motivation

Apart from few attempts to model this flow on the computer (Koumoutsakos [17] Joslin et al. [14], Kandil et al. 2000 [25]) no thorough investigation of this extremely versatile actuator device or variants thereof are known to us. Another surprising fact is that the actuator has mostly been investigated in still air, i.e. its reactions on a boundary layer type flow are not really well known. Only the vortex-type mode of operation appears with some preliminary (but encouraging) results towards the end of the publication by Lachowicz et al. [18]. This apparent void has led us to propose the current investigations.

In the present work we will perform detailed studies of the above actuator geometry and variants thereof with the aim to fully understand the influence of all parameters and to make predictions and optimizations. The investigated cases will therefore not be restricted to the design given, this will merely consist a starting point. We will also investigate thoroughly a variation of this design. Another extra with respect to previous research will be the coupling of the actuator vortex mode of operation (in different geometrical configurations) with an external boundary layer flow towards the end of the present research.

For the actuator simulation, however, a new challenge appears: complex geometry with moving boundaries. Therefore, the first step consists of selecting the most appropriate simulation strategy, its implementation and its verification and validation for the current problems. For the present investigations the commercial CFD-software FLUENT is used for flow calculation and visualization. Structured dynamical grids with sliding interfaces between different blocks were used. The accompanying grid-generation software GAMBIT is used for geometry specification and grid generation. The same software has been successfully chosen by Tang and Zhong [32] for their simulations of another kind of zero-net-mass-flux actuator.

1.5 Objectives

The main objective of this thesis is to investigate a new actuator for active control of boundary layers and flow separation, which is characterized by a high flexibility of operation. The project is expected to achieve control of drag in boundary layers and to re-energize laminar and turbulent boundary layers to resist to separation. For improving aircraft aerodynamic performance existing flow control has been mostly

passive. Passive control means that fixed devices are used to control the flow. Fixed vortex generators might be an example for passive flow control. These devices are simple and low cost in manufacture, but they have two significant disadvantages: first passive flow control devices cannot be optimized for multiple flight conditions (landing, take-off, maneuver) and second they add extra drag in steady cruise conditions in which they are no longer needed. Active control can defeat these disadvantages and optimize overall performance of the flight. The jet and vortex actuator (JaVA) adds only negligible drag when the system is not actuated and it does not need any external fluid because it is a zero-net-mass flux system. The JaVA enables to achieve different flow regimes since it can operate over a range of amplitudes and frequencies. The main goal of the project is to develop and test a JaVA as an efficient active flow control device. As no 3D results are available and we don't know the presence of the 3D effects therefore it is also the aim of the project to perform 3D simulation to find the 3D end effects if present. It is also part of this project to see if there is any variation of this design in order to improve it. With the full understanding and interaction with boundary layers, a successful application of a JaVA system may lead to efficient flight control systems, thus maneuverability, stability and longer aircraft range can be possible at a reduced cost.

2. Basic theory

This chapter will describe the basic setup of the actuator and numerical approach used in our research. In this chapter we will also discuss the theoretical background of the basic physical model of FLUENT for fluid flow including sliding and dynamic meshes which we used for our research.

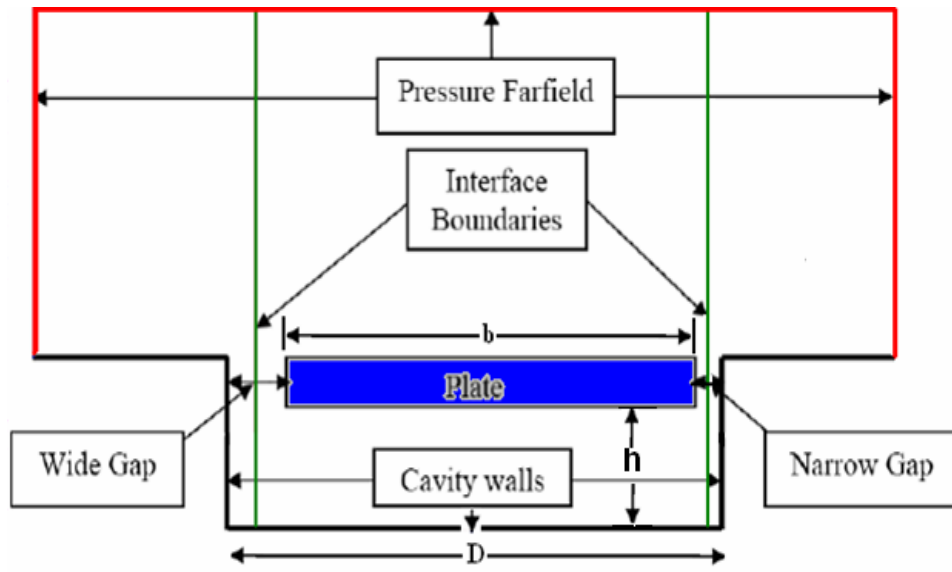
2.1 Numerical approach

The first step in any CFD simulation is to select an appropriate code according to the problem for the calculation of the flow field. For the present actuator-geometry simulations, use of general purpose CFD software seemed to be the most appropriate, because of the need for simulating rather complex geometries with moving boundaries at different flow speeds. Previous experience and according advice given by the CFD-consultants of the high-performance computer center at Universität Stuttgart led us to the decision to use Fluent from Fluent Inc. The accompanying grid-generation software GAMBIT is used for geometry specification and grid generation, see *Figure 2.1*. The same software has been successfully chosen by Tang and Zhong [32] for their simulations of another kind of zero-net-mass-flux (ZNMF) actuator. This software appears to be well-suited and established in the car industry for simulations of reciprocating engines, because of its versatility to deal with dynamic meshes. Different grid motion techniques are available in Fluent, a dynamic unstructured version that automatically follows the moving parts of the problem by removing grid points and generating new ones and also grid smoothing based on user-defined parameters and constraints. This, however, turned out to be overly time consuming, because of the need to remesh at every time step. A second technique uses structured deformable dynamical grids with or without the option of sliding interfaces between different blocks where necessary. Therefore, we selected the latter one as it seemed to be more appropriate and robust and there is no grid degeneration near the area of interest. For the specification of problem-specific boundary conditions Fluent uses the concept of “*user-defined functions(UDF)*”, i.e. the user has to specify a boundary conditions in a C-like syntax as a function that is bound to be executable upon execution. This is very flexible and general. However it turned out that it is not sufficient to simply specify wall motions (with the idea that this will automatically drive the flow via appropriate boundary conditions). Unexpectedly, it

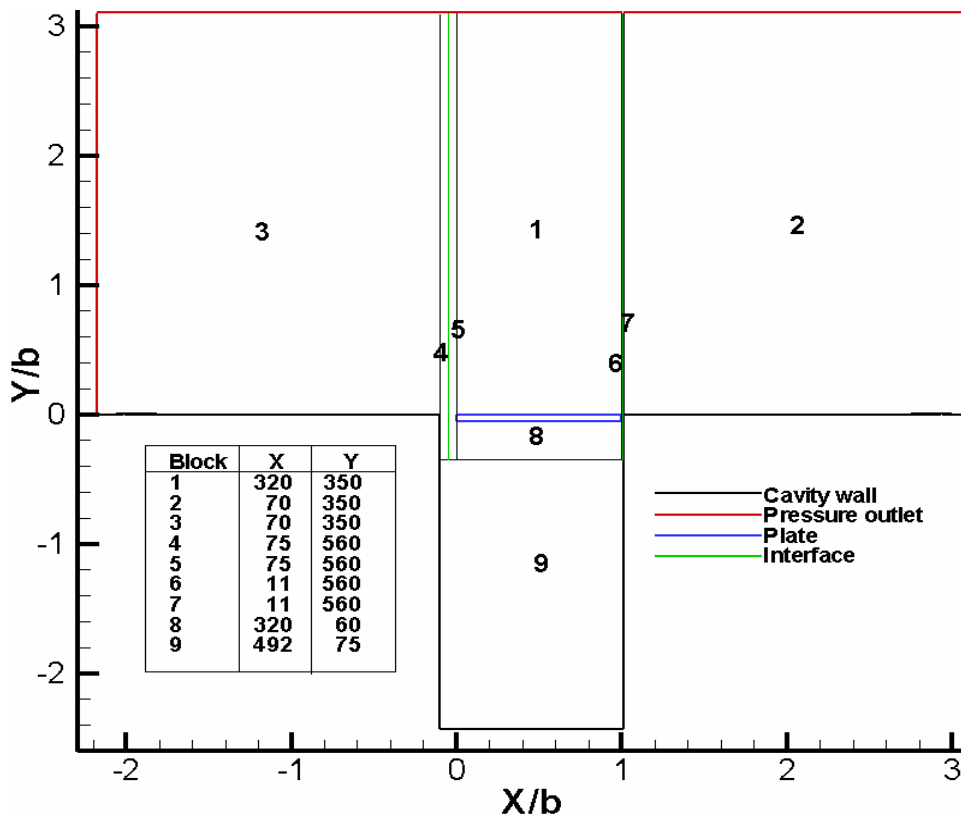
was necessary to specify extra boundary conditions for the fluid on the moving boundaries (as Fluent does not apply perpendicular component of velocity to the moving wall). This adds extra flexibility, like consideration of permeable walls, for instance, but careful checks are necessary in order to verify the use of appropriate boundary conditions for a given problem. In our simulation we performed incompressible simulations by using a dynamic mesh along with sliding boundaries. We also performed compressible simulations for some cases in order to see the compressibility effects. Both 2D and 3D simulations were carried out.

2.1.1 Boundary conditions and grid distribution (original design)

Since only two-dimensional measurements are available and the flow field in the middle of the actuator is considered to be two-dimensional (if placed in still air, i.e. without a freestream flow in the plane-normal direction), we begin with two-dimensional simulations. In our first case we reproduced the results of Lachowicz et al. [18]. *Figure 2.1* shows the setup and the integration domain used, together with its discretization into nine grid blocks. The number of grid cells in x and y direction of each block is given in the table in the insert and the boundary conditions are indicated using colors. Red for the “free-stream” boundaries where constant pressure is applied, it is therefore denoted as “pressure outlet”, black for the “no-slip boundary condition” of the rigid cavity walls, denoted “cavity”, and blue for the oscillating plate. Blocks numbers 1, 5, 6 and 8 are attached to the plate, i.e. they move up and down together with it while the block numbers 2, 3, 4, 7 and 9 remain stationary throughout the simulation. The connections between rigid parts and the moving part of the domain are performed by so-called “sliding interfaces” (green lines) between blocks number 4 and 5 at the left side of the actuator plate and between blocks number 6 and 7 at the right side. When the plate moves up and down, the grid slides at these interface boundaries. When the plate moves upward grid cells are eliminated at the top of block number 1 while at the same time grid cells are generated at the bottom of the block number 8 and vice a versa, depending upon the remeshing parameters specified. Therefore, these boundaries are kept away from the area of interest. Block number 9 in this setup is optional which means depending upon the required cavity depth; its vertical height can be varied or is even completely removed for some cases. Similarly, when we want to put the plate mean position inside the cavity we include an extra small block of grid above the plate as required.



(a) Arrangement of boundary conditions



(b) Grid Distributions

Figure 2.1 Boundary conditions and grid distribution (original design)

The motion of the plate is prescribed in a User-Defined Function (UDF) see [appendix](#) by the following set of equations

$$\begin{aligned}x(t) &= a \sin(\omega t) \\x'(t) = v(t) &= a \omega \cos(\omega t) \\T &= 1/f\end{aligned}$$

Where

$\omega = 2 \pi f$ Circular frequency

$T = 1/f$ Oscillation period

f Frequency

a Actuator amplitude (mean position to peak displacement)

In addition to these, the following geometry-related parameters play a role:

b Actuator plate width

W_w Wide gap width

W_n Narrow gap width

g_w Ratio of wide gap width w_w to actuator width b

g_n Ratio of narrow gap width w_n to actuator width b

S_a Scaled amplitude of the plate = $2\pi a/b$

2.1.2 Boundary conditions and grid distribution (modified design)

In our quest to improve this design and to develop a better understanding of this type of actuator we also investigated a variation of the JaVA. For the modified design two plates are used. A horizontal but stationary one which closes the cavity at its top (flush with the surrounding wall) and which just leaves the wide and the narrow gaps open, as before. And a second one which is placed vertically inside the closed cavity and oscillating towards the left and right which works like an oscillating piston, thus pumping and sucking fluid periodically out and in through the gaps. Here, the motion in each gap is always in anti-phase to that in the other gap. The horizontal plate has the same dimensions as in the original design while the vertical actuator plate has a smaller length but we vary it for different cases. The wide and narrow gap widths are also kept the same as before but variable for different cases. The geometry and grid distribution are shown in *Figure 2.2*. Since the cavity is now split into two parts with opposite flow rates (opposite signs but same magnitude) the flow through the narrow gap will become the more energetic one, and we can expect the narrow gap to take over a more decisive role compared to the original design. This actuator design has

the advantage over the original one that it is more robust with respect to wear or contamination with dirt because it has no moving parts at the surface. Furthermore in this case an interface boundary is not required as well. Due to these we require less grid cells to get a converged solution at each time step and therefore this is more robust with respect to time.

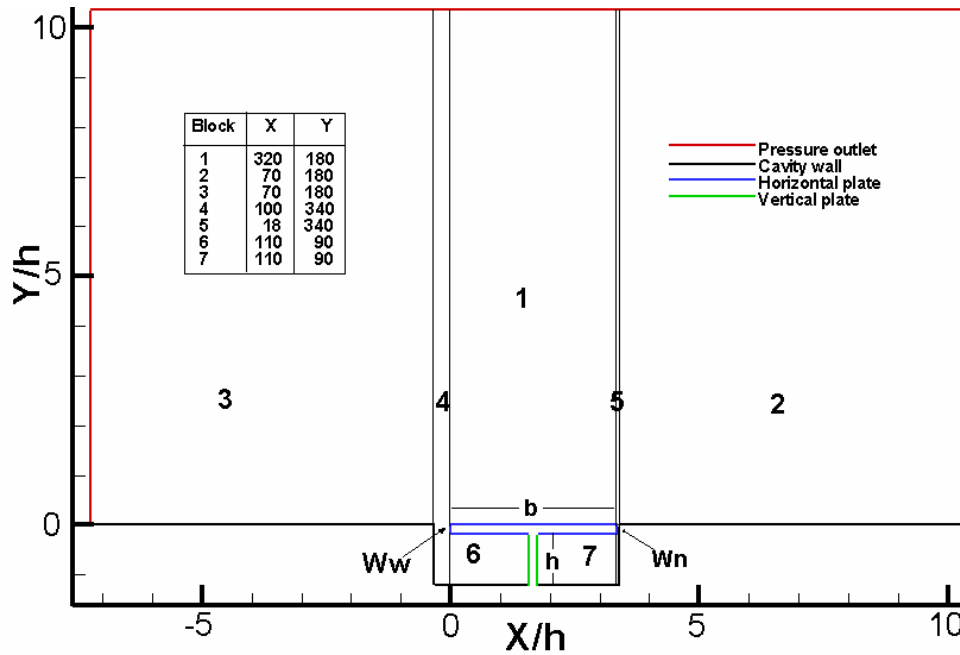


Figure 2.2 Boundary conditions and grid distribution (modified design)

2.2 Theoretical background and conservation equations used in Fluent

FLUENT provides comprehensive modeling capabilities for a wide range of incompressible and compressible, laminar and turbulent fluid flow problems. Steady-state or transient analyses can be performed. For all basic flows, FLUENT solves conservation equations for mass and momentum. In this section, the conservation equations for laminar flow are presented.

2.2.1 The mass conservation equation

The equation for conservation of mass, or continuity equation, can be written as follows:

$$\frac{\partial \rho}{\partial t} + \frac{\partial}{\partial x}(\rho u) + \frac{\partial}{\partial y}(\rho v) + \frac{\partial}{\partial z}(\rho w) = 0$$

It is the general form of the three-dimensional unsteady mass conservation equation and is valid for both incompressible as well as compressible flows. Here “ ρ ” is the

fluid density, “t” is time and “u, v, w” is the fluid velocity. In vector form this equation can be written as:

$$\frac{\partial \rho}{\partial t} + \nabla \cdot (\rho \vec{v}) = 0$$

For incompressible flows “ρ” is constant and the mass continuity equation simplifies (steady or unsteady) to

$$\frac{\partial u}{\partial x} + \frac{\partial v}{\partial y} + \frac{\partial w}{\partial z} = 0, \quad \text{or in vector form} \quad \nabla \cdot \vec{v} = 0$$

2.2.2 Momentum conservation equations

Conservation of momentum for an incompressible flow of a Newtonian fluid in the vector form is given below. It's well worth observing the meaning of each term

$$\rho \left[\overbrace{\frac{\partial \vec{v}}{\partial t}}^{\text{inertia (per volume)}} + \underbrace{\vec{v} \cdot \nabla \vec{v}}_{\text{convective acceleration}} \right] = \underbrace{-\nabla p}_{\text{pressure gradient}} + \underbrace{\mu \nabla^2 \vec{v}}_{\text{viscosity}} + \underbrace{\underline{B}}_{\text{body force}}$$

Here “B” represents body forces (forces per unit volume), such as gravity or centrifugal forces, “ $\mu \nabla^2 v$ ” is the shear stress term when the fluid is assumed incompressible and Newtonian and “ μ ” is the dynamic viscosity.

NOTE: The incompressible flow assumption typically holds well even when dealing with a "compressible" fluid such as air at room temperature at low Mach numbers (like in our case).

In Cartesian coordinates the momentum equation can be written as

$$\rho \left(\frac{\partial u}{\partial t} + u \frac{\partial u}{\partial x} + v \frac{\partial u}{\partial y} + w \frac{\partial u}{\partial z} \right) = -\frac{\partial P}{\partial x} + \mu \left(\frac{\partial^2 u}{\partial x^2} + \frac{\partial^2 u}{\partial y^2} + \frac{\partial^2 u}{\partial z^2} \right) + \rho g_x$$

$$\rho \left(\frac{\partial v}{\partial t} + u \frac{\partial v}{\partial x} + v \frac{\partial v}{\partial y} + w \frac{\partial v}{\partial z} \right) = -\frac{\partial P}{\partial y} + \mu \left(\frac{\partial^2 v}{\partial x^2} + \frac{\partial^2 v}{\partial y^2} + \frac{\partial^2 v}{\partial z^2} \right) + \rho g_y$$

$$\rho \left(\frac{\partial w}{\partial t} + u \frac{\partial w}{\partial x} + v \frac{\partial w}{\partial y} + w \frac{\partial w}{\partial z} \right) = -\frac{\partial P}{\partial z} + \mu \left(\frac{\partial^2 w}{\partial x^2} + \frac{\partial^2 w}{\partial y^2} + \frac{\partial^2 w}{\partial z^2} \right) + \rho g_z$$

Here “∂P” is the static pressure; “g_i” is the gravitational force.

These are the Navier-Stokes equations for an incompressible, constant viscosity fluid. Together with the continuity equation they describe the motion of an incompressible, viscous fluid. Note that the four equations have only four unknowns (u , v , w , and ∂P) if density and viscosity are known.

2.3 Overview of moving zone approaches

The moving grid capability in FLUENT provides a powerful set of features for solving problems in which the domain or parts of the domain are in motion.

2.3.1 Dynamic mesh

The dynamic mesh model in FLUENT can be used to model flows where the shape of the domain is changing with time due to the motion on the domain boundaries. The motion can be a prescribed motion (e.g., you can specify the linear and angular velocities about the center of gravity of a solid body with time) or an unprescribed motion where the subsequent motion is determined based on the solution at the current time (e.g., the linear and angular velocities are calculated from the force balance on a solid body, which is what the six degree of freedom (6DOF) solver does. The use of the dynamic mesh model needs to be provided by a starting volume mesh and the description of the motion of any moving zones in the model. FLUENT allows describing the motion using either boundary profiles, user-defined functions (UDFs), or the Six-Degree-of-Freedom solver (6DOF). If the model contains moving and non-moving regions, we need to identify these regions by grouping them into their respective cell zones in the starting volume mesh that is generated. We can use the conformal, nonconformal or sliding interface capability in FLUENT to connect the various zones in the final model.

a. Dynamic mesh conservation equations

Fluent uses a conservation equation for updating the mesh. We here reproduce these equations from the Fluent manual [4]. The integral form of the conservation equation for a general scalar “ Φ ” on an arbitrary control volume “ V ” whose boundary is moving can be written as

$$\frac{d}{dt} \int_V \rho \Phi dV + \int_{\partial V} \rho \Phi (\vec{u} - \vec{u}_g) \cdot d\vec{A} = \int_{\partial V} \Gamma \nabla \Phi \cdot d\vec{A} + \int_V S_\Phi dV$$

where ρ is the fluid density,

\vec{u} is the flow velocity vector,

\vec{u}_g is the grid velocity of the moving mesh,

Γ is the diffusion coefficient,

and S_Φ is the source term of Φ .

Here ∂V represents the boundary of the control volume V .

The time-derivative term in this equation can be written, using a first-order backward difference formula, as

$$\frac{d}{dt} \int_V \rho \Phi dV = \frac{(\rho \Phi dV)^{n+1} - (\rho \Phi dV)^n}{\Delta t},$$

where “ n ” and “ $n+1$ ” denote the respective quantity at the current and next time level. The $(n+1)$ the time-level volume V^{n+1} is computed from

$$V^{n+1} = V^n + \frac{dV}{dt} \Delta t,$$

where dV/dt is the volume time derivative of the control volume. In order to satisfy the grid conservation law, the volume time derivative of the control volume is computed from

$$\frac{dV}{dt} = \int_{\partial V} \vec{u}_g \cdot d\vec{A} = \sum_j^{n_f} \vec{u}_{g,j} \cdot \vec{A}_j,$$

where n_f is the number of faces on the control volume and \vec{A}_j is the j face area vector.

The dot product $\vec{u}_{g,j} \cdot \vec{A}_j$ on each control volume face is calculated from

$$\vec{u}_{g,j} \cdot \vec{A}_j = \frac{\delta V_j}{\Delta t}$$

where δV_j is the volume swept out by the control volume face j over the time step Δt .

b. Dynamic mesh update methods

Three groups of mesh motion methods are available in FLUENT to update the mesh in the deforming regions subject to the motion defined at the boundaries:

- smoothing methods
- dynamic layering
- local remeshing methods

As we use dynamic layering we only explain this method in detail.

Dynamic layering method

In prismatic (hexahedral and/or wedge) mesh zones, we can use dynamic layering to add or remove layers of cells adjacent to a moving boundary, based on the height “ r ” of the layer adjacent to the moving surface. The dynamic mesh model in FLUENT allows to specify an ideal layer height on each moving boundary. The layer of cells adjacent to the moving boundary is split or merged with the layer of cells next to it, based on the height of the cells in the layer. If the cells in the layer are expanding, the cell heights are allowed to increase until

$$r_{\min} > (1 + \alpha_1)r_{\text{ideal}},$$

where “ r_{\min} ” is the minimum cell height of the cell layer, “ r_{ideal} ” is the ideal cell height, and “ α_1 ” is the layer split factor. When this condition is satisfied, the cells are split based on the specified layering option (constant height or constant ratio).

If the cells in the layer are being compressed, they can be compressed until

$$r_{\min} > \alpha_2 r_{\text{ideal}}$$

where “ α_2 ” is the layer collapse factor. When this condition is satisfied, the compressed layer of cells is merged into the layer of cells above the compressed layer.

2.3.2 Sliding mesh theory

When a time-accurate solution rather than a time-averaged solution is desired, one must use the sliding mesh model in Fluent to compute the unsteady flow field. This is the model of choice if the grid interaction is strong and a more accurate simulation of the system is desired. Note, however, that because the sliding mesh model requires an unsteady numerical solution, it is computationally more demanding.

In the sliding mesh technique two or more blocks of grid are used. Each block is bound by at least one interface boundary where it meets the opposing interface boundary. The interface boundaries of adjacent blocks are associated with one

another to form a grid interface. The two blocks move relative to each other along the grid interface in discrete steps. In doing so, the grid nodes do not need to be aligned on the grid interface and within each block any type of grid (structured or unstructured) can be used. This situation requires a means of computing the flux across the two interface zones of each grid interface. To compute the interface flux, the intersection between the interface zones is determined at each new time step. The resulting intersection produces one interior zone and a pair of wall zones (which will be empty if the two interface zones intersect entirely). The resultant interior zone corresponds, where the two interface zones overlap. The number of faces in these intersection zones will vary as the interface zones move relative to one another. Principally, fluxes across the grid interface are computed using the nodes or faces resulting from the intersection of the two interface zones, rather than from the interface zone nodes or faces themselves.

Following are the grid requirements in Fluent to use sliding mesh.

- A different block of grid exists for each portion of the domain that is sliding with respect to each other.
- The grid interface must be situated such that there is no motion normal to it.
- The grid interface can be of any shape (including a non-planar surface, in 3D) provided that the two interface boundaries are based on the same geometry.
- If there are sharp features in the mesh (e.g., 90-degree angles), it is especially important that both sides of the interface closely follow that feature.
- If a single grid with multiple grid blocks is created, then it must be ensured that each block has a distinct boundary zone on the sliding boundary. The sliding boundary for two adjacent blocks will have the same position and shape, but one will correspond to one block and one to the other.

Note: It is also possible to create a separate grid file for each of the grid blocks.

3. Test case study

In this chapter we will discuss the procedure adopted for our solution. As a first step towards our solution we started with a design of Lachowicz et al. [18] but with very long cavity and with open bottom and compared our results with text book examples where possible in order to ensure that we can move further. In the second step we changed the boundary condition at the bottom of the cavity from outlet to wall (closed cavity) and performed simulations and in the last section of this chapter results of both cases will be compared.

Different cases studied in this chapter are given below

Case-1 Cavity with open bottom

Case-2 Cavity with closed bottom

3.1 Cavity with open bottom

In this case the oscillator (plate) of Lachowicz et al. [18] is placed at the entrance to a plane channel in such a way that at its mean position the upper surface is flush with the cavity top walls see *Figure 2.1*. The cavity depth is elongated to $20.725b$ and at the bottom of the cavity a pressure outlet boundary is used.

In this case following dimension and actuation parameters are used

3.1 Parameters for case-1

Parameter	b	Sa	f	h/b	hp/b	D/b	g_n	g_w
Dimension	9.65mm	0.1829	128Hz	20.725	0.0518	1.113	0.0145	0.09896

This leads to a peak velocity of the plate of $U_p = 2 \pi a f = 0.226$ m/s. This is used to normalize all velocities. As the oscillator moves up and down it accelerates the fluid in the channel and pushes it downward or sucks it upwards. To keep the actuator area near $y \approx 0$ free from possible in- and outflow effects at the bottom end of the channel the latter was made rather long ($20.725b$), see *Figure 3.1*. The simulation has been run over 19 oscillation cycles and results of the last cycle will be shown here. These will be labeled according to the ratio t/T , i.e. $t = 18.5 T$ is at 18.5 cycles after start-up when the plate passes its mean position in downward direction at maximum speed. Accordingly at $t = 19 T$ it moves upward, again at full speed.

Major fluid motions induced by the oscillating plate are confined to the area surrounding the plate. However, compared to the maximum velocity of the actuator a much larger velocity occurs in the wide gap, see the left color scale in *Figure 3.1a*

which is adjusted to the instantaneous velocity magnitude. More details of the flow field will be discussed further down. The downward motion of the oscillator induces a pressure rise at the upper end of the vertical channel. Since the lower end is kept at the atmospheric pressure level, a downward motion can be expected through the channel. However, the according pressure gradient is much weaker (because of the length of the channel) compared to the pressure gradient over the gaps where the free-stream pressure “almost collides” with the pressure rise inside the channel.

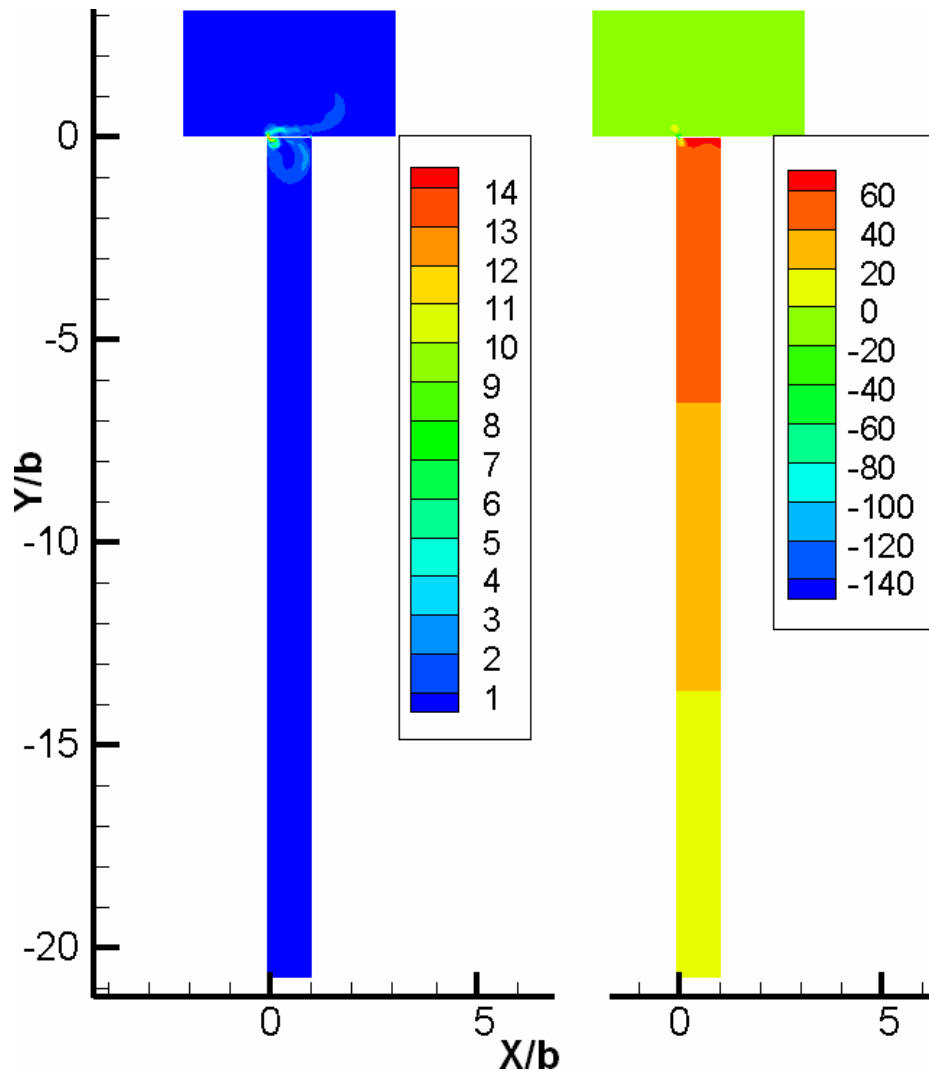


Figure 3.1 Instantaneous velocity magnitude and total pressure at $t = 18.5T$

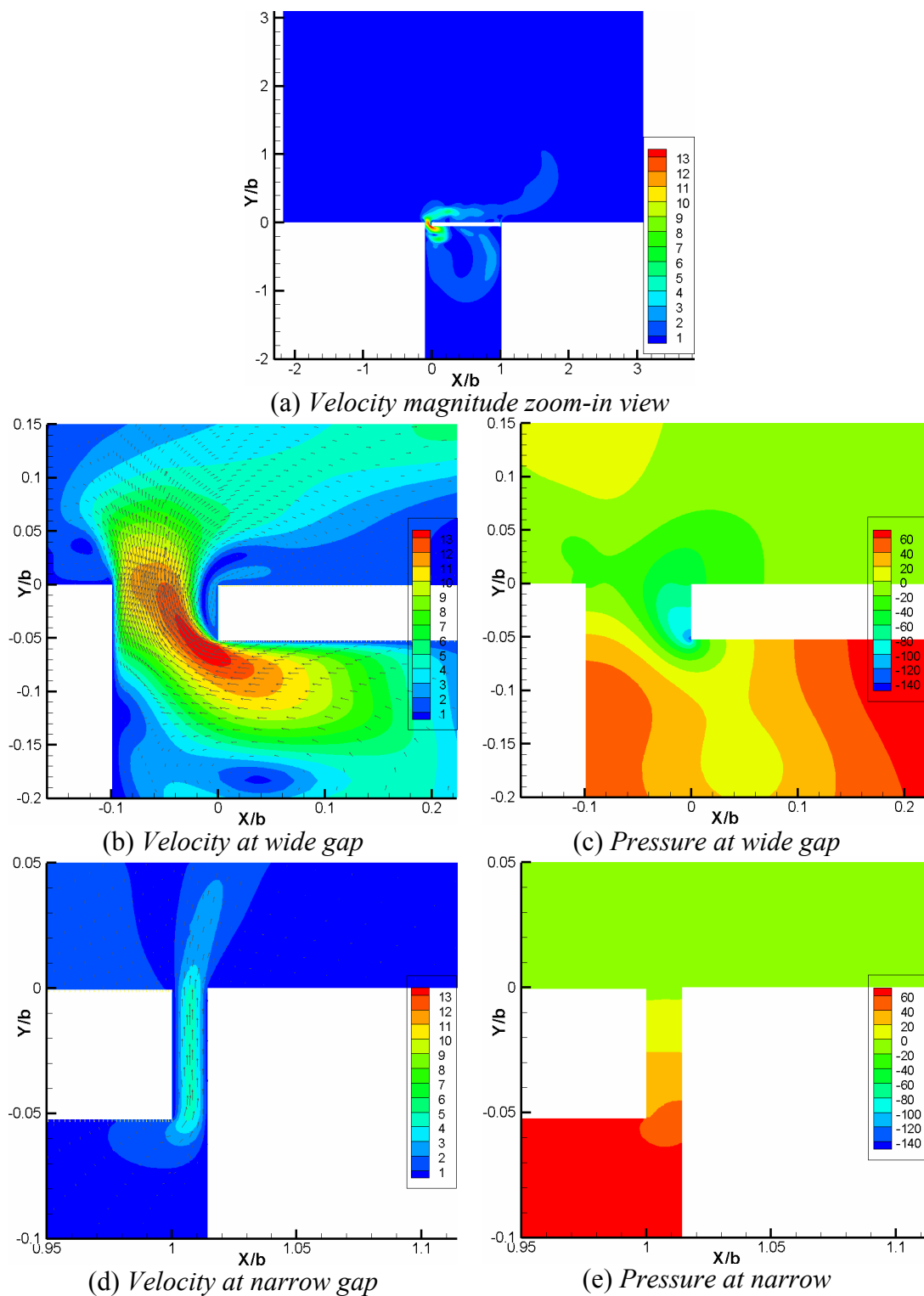
A zoom into the velocity magnitudes in the actuation area is shown in Figure 3.2a. It should be viewed together with the close-ups of the wide and narrow gaps in Figure 3.2 b and d. As anticipated from the global pressure field above, the fluid is expected to try to leave the channel through the sidewise gaps. Because of their different widths the fluid prefers the wide gap and there is only a relatively small jet at the narrow gap. The extremely high velocity at the wide gap is caused through

acceleration by the extremely large negative pressure gradient that occurs over the plate width. Part of the fluid that leaves the channel cavity turns right behind the actuator in order to fill the void that would occur behind the plate. The instantaneous velocity magnitude in *Figure 3.2a* exhibits a horizontal wall jet and a large but weak vortex above the wall that comes from the start-up of the simulation. Another vortex is generated under the plate. The fluid that is pushed downward by the plate turns upward again in the left part to fill the void generated by the upward jet. A strong counter-clock wise rotating secondary vortex occurs at the left wall below the exiting jet. It is clearly indicated by the low pressure region in *Figure 3.2c*.

The flow field in the wide gap is too complicated to be verified by theory. We therefore turn our attention towards the narrow gap which contains velocity profiles that look like a fully developed channel flow after a short entrance region (cf. *Figure 3.2d*). This is further illustrated in the extracted profiles in *Figure 3.3a* which exhibit “text-book quality” because they nicely show that the present flow can be considered as a superposition of plane Couette and plane Poiseuille (channel) flow, see e.g. White 1974 [3]. The first of these is driven by the moving wall and the second by a pressure gradient along the channel length, which can be seen in *Figure 3.2e*.

Since the pressure difference between the underside and the upper side of the plate is equal to the pressure at the plate's underside the pressure gradient across the plate can be easily estimated. It yields $\partial P / \partial y = (60 - 0) / 0.0000465 \text{ N/m}^3$. In plane Poiseuille flow this leads to a maximal velocity in the channel center that is $U_{\max} = W_n^2 \partial P / \partial y / (8\mu) = 1.05 \text{ m/s}$ for the present case. Half the plate speed must be subtracted from this to yield the center line velocity for mixed Couette-Poiseuille flow, i.e. $U_{\text{gap max}} = 1.05 \text{ m/s} - 0.113 \text{ m/s} = 0.94 \text{ m/s} = 4.159 U_p$. This is extremely close to the maximal velocities of $4.38 U_p$ observed in *Figure 3.3a*. Another observation is that the velocity profiles in the narrow gap for both up- and downward motion of the plate are perfectly symmetric with respect to the zero velocity. The pressure difference that occurs between upper and lower side of the oscillator must also be symmetric because of the harmonic oscillation of the latter. Thus the present numerical results appear to have a good quantitative accuracy. In *Figure 3.3b* velocity profiles at eight different time instances during the 19th period of oscillation are plotted. Another interesting observation is that the maximum negative velocity in the narrow gap is not in phase with the actuator motion. It occurs near $\theta = 315^\circ$, i.e. at $t = 18.875T$ instead of $t = 19T$ ($\theta = 360^\circ$), where the actuator maximum velocity

occurs. In the same vein the maximal positive velocity in the narrow gap is also out of phase with respect to the actuator plate, $\theta=135^\circ$ i.e. at $t = 18.375T$ instead of $t = 18.5T$ ($\theta=180^\circ$), where the actuator maximum velocity occurs. This means that the gap velocity reaches its maximum value after the plate is at its peak velocity in both-



suction and blowing phases. Even when the plate velocity is zero at $\theta=90^\circ$ and $\theta=270^\circ$ the velocities are not zero at $\theta=180^\circ$ and $\theta=360^\circ$ respectively. Furthermore the plate velocity at $\theta=45^\circ$ and $\theta=315^\circ$ (suction phase) is the same but in the gap at $\theta=45^\circ$ the velocity is minimum and almost zero while at $\theta=315^\circ$ it is maximum. Similarly, at $\theta=135^\circ$ and $\theta=225^\circ$ (blowing phase) the plate has the same velocity but in the gap at $\theta=225^\circ$ the gap velocity is almost zero and at $\theta=135^\circ$ the gap velocity is maximum. This is because there is a phase shift of about $\theta=45^\circ$.

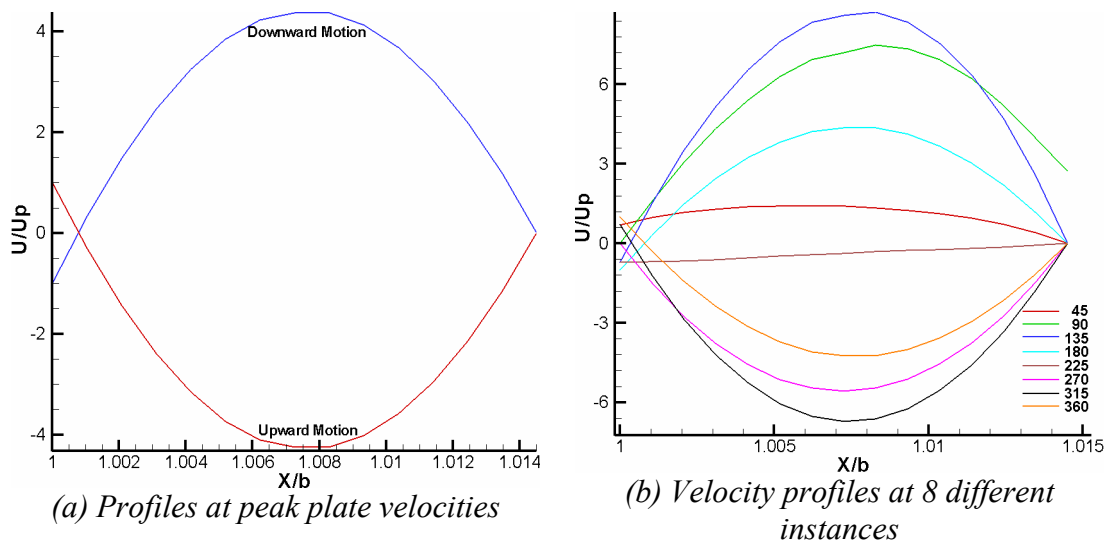


Figure 3.3 Velocity profiles in narrow gap

Before turning to the effects at the bottom of the channel, the flow field at the opposite motion of the actuator, i.e. at $t = 19 T$ will be shown for comparison to the above figures. Now the low pressure region occurs under the actuator and the fluid moves into the channel through the gaps.

The largest velocity magnitude occurs again in the wide gap see *Figure 3.5a* and *Figure 3.5b*. Fluid that enters the channel turns to the right in order to fill the area behind the plate. The wall jet points to the right, drives a clock-wise rotating large vortex in the (open) cavity. Above the oscillator the flow is drawn towards both gaps, such that the wall jet that occurred half a cycle ago above the oscillator persists, at least in the right half of the domain. A smaller counter-clockwise rotating vortex occurs behind the left edge of the oscillator plate, as depicted by the local pressure minimum in *Figure 3.5c*. In contrast to the wide gap where the flow fields at $t = 18.5T$ and $t = 19T$ are not just antisymmetric with respect to time, the flow field in the narrow gap exhibits such a symmetry, as already documented further above in *Figure 3.3a*. The same applies for the pressure fields in *Figure 3.2c* and *Figure 3.5e*.

The pressure difference from *Figure 3.5e* when the plate is moving upwards through its mean position, i.e. at $t = 19T$ yields $\partial P / \partial y = (0 - 3.87) / 0.0005 \text{ N/m}^3$. In plane Poiseuille flow this leads to a maximal velocity in the channel center that is $U_{\max} = W_n^2 \partial P / \partial y / (8\mu) = 0.95 \text{ m/s}$ for the present case. Half the plate speed must be subtracted from this to yield the center line velocity for mixed Couette-Poiseuille flow, i.e. $U_{\text{gap max}} = 1.06 \text{ m/s} - 0.113 \text{ m/s} = 0.95 \text{ m/s} = 4.19U_p$. Once again it is extremely close to the maximal velocities $-4.25U_p$ observed in *Figure 3.3a*.

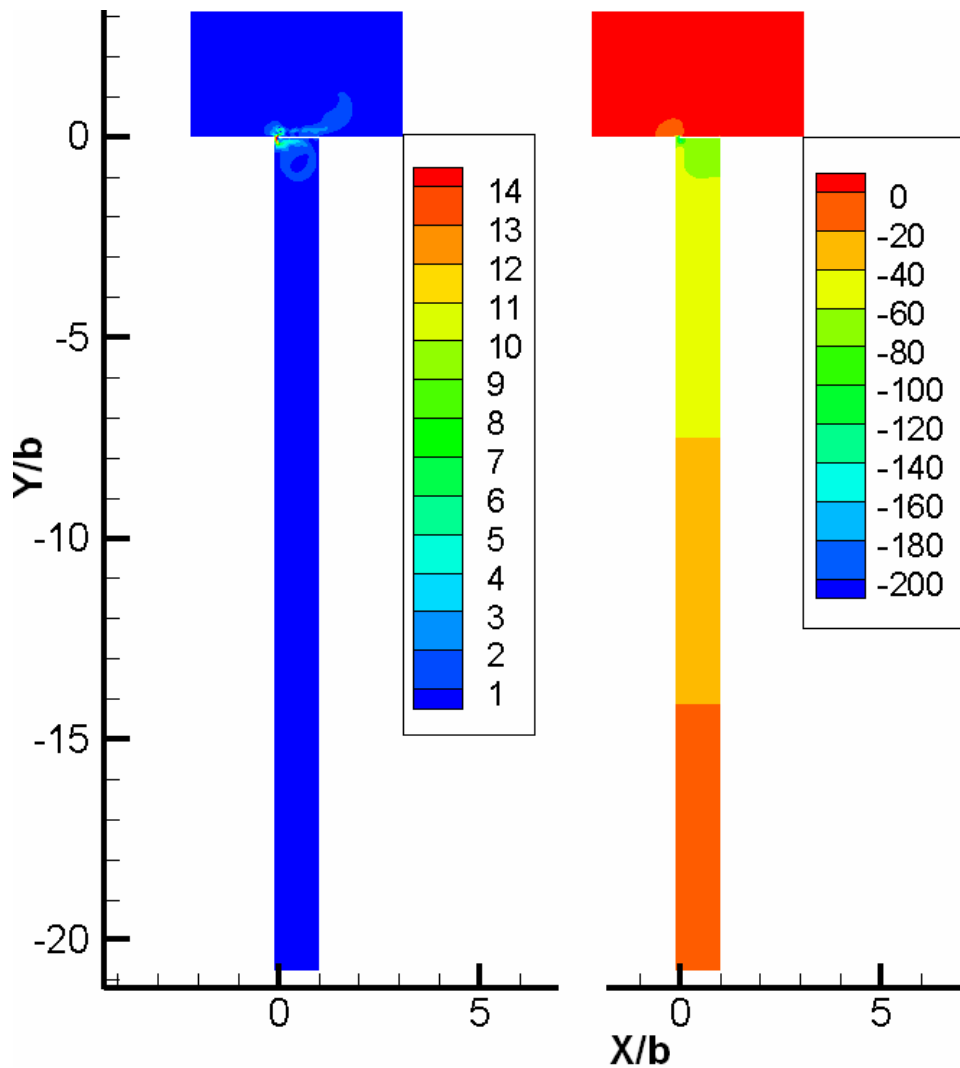
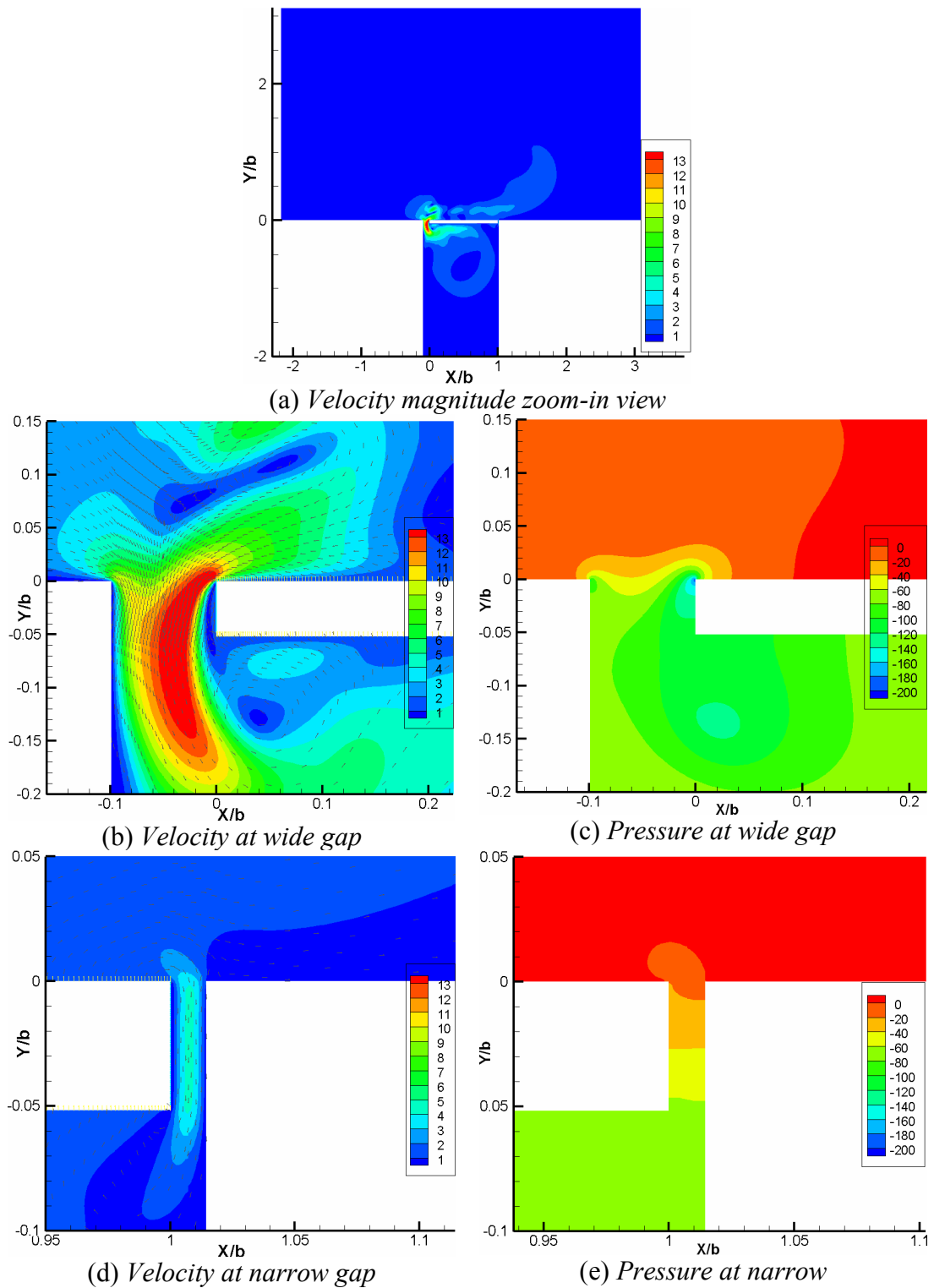


Figure 3.4 Instantaneous velocity magnitude and total pressure at $t = 19T$



Instantaneous velocity profiles in the middle of the wide gap are compared for both phases in Figure 3.6a. Since the channel formed by the wide gap has a larger width than length, the flow is not parallel to the side walls and the velocity profiles even show reverse flow. The latter is due to the oscillation. Instantaneously, the oscillator at the right and the fluid attached to it moves in opposite direction to the

bulk flow in the remaining part of the gap. Since the flow direction is somewhat oblique the two profiles in Figure 3.6 appear as if they were sheared in horizontal direction. The maximal inflow velocity magnitude at $t = 19T$ and the area under the profiles, i.e. the mass flow, are somewhat larger than the outflow velocity at $t = 18.5T$. There is no phase shift in the wide gap as can be seen in Figure 3.6b which shows the history of velocity at the center of the wide and narrow gap. Here we can clearly see a phase shift of 45° ($t = -0.125T$) in the narrow gap. It also shows a complete periodicity in the gaps.

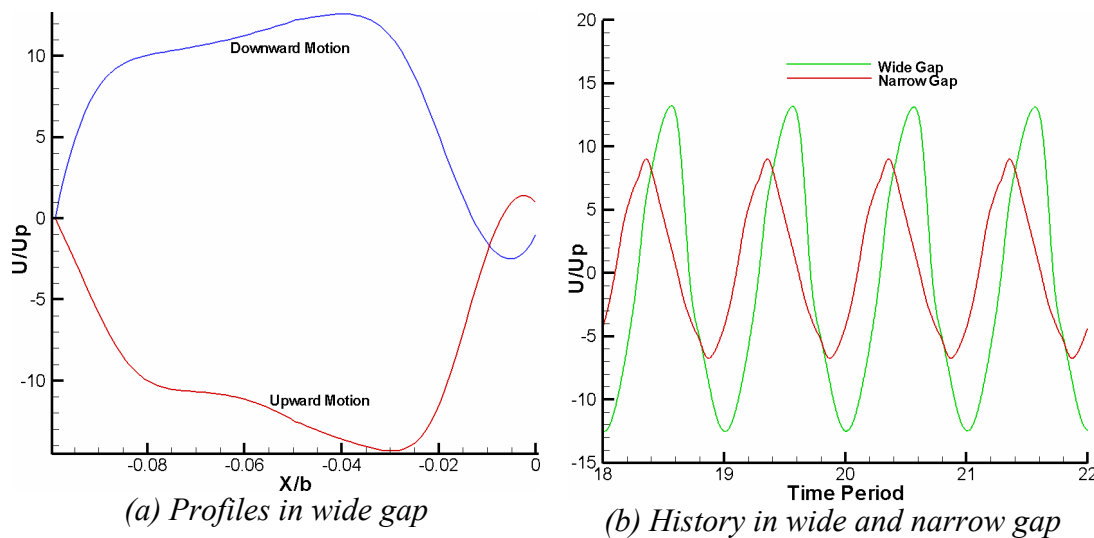


Figure 3.6 Profiles in wide gap at peak plate velocities

In Table 3.2 flow rates are compared through the gaps and bottom with the fluid that is pushed by the plate at eight different time instances. The flow rate through the bottom is subtracted from the flow rate by the plate. Comparing both net flows it can be observed that they are almost the same at every time instance which shows that mass is conserved. As already observed above there is a phase shift in the narrow gap and at the bottom of the cavity with respect to the plate as can once again be observed here. The maximum flow through the cavity bottom is at $\theta=45^\circ$ and $\theta=225^\circ$ in contrast to the plate at $\theta=360^\circ$ and $\theta=180^\circ$ respectively. Similarly the maximum flow through the narrow gap is at $\theta=135^\circ$ and $\theta=315^\circ$ in contrast to the plate at $\theta=360^\circ$ and $\theta=180^\circ$ respectively but there is no phase shift in the wide gap. Looking at the net flow, there is no phase shift which suggests that the wide gap flow is the strongest and drives the flow in- and out from the cavity. At $\theta=90^\circ$ and $\theta=270^\circ$ where the plate is at rest (which means zero flow rate), there is some flow through the gaps (especially in the narrow gap) because in the narrow gap there is a phase shift such that the flow still exists while in the wide gap, as the width of the gap is large

compared to the plate thickness the fluid follows the previous motion of the plate due to its inertia in spite the plate being at rest.

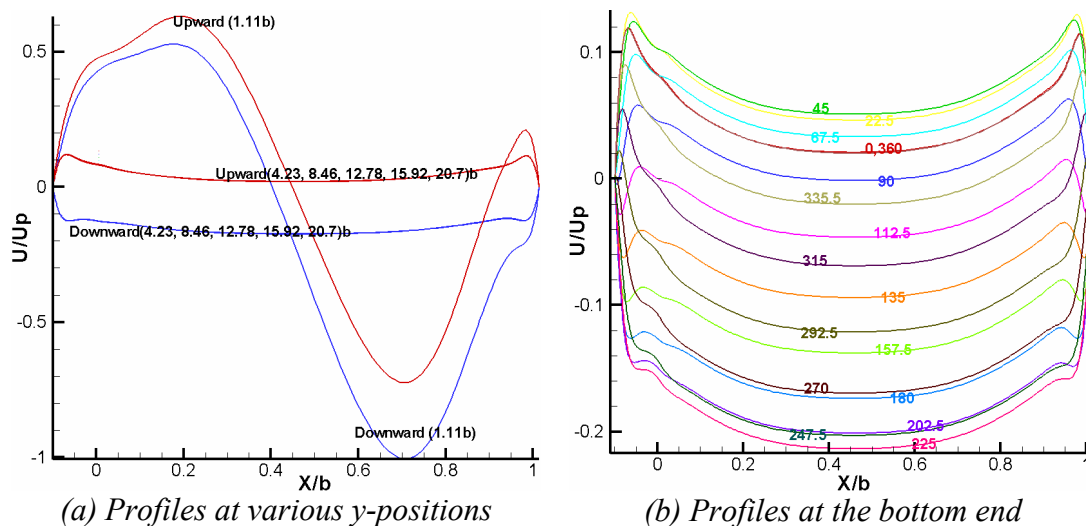
Table 3.2 Comparison of volume flow rate through gaps and cavity bottom

Phase (<i>o</i>)	Plate $Kg/s(10^{-3})$	Bottom $Kg/s(10^{-3})$	Net $Kg/s(10^{-3})$	Narrow Gap $Kg/s(10^{-3})$	Wide Gap $Kg/s(10^{-3})$	Net $Kg/s(10^{-3})$
45	1.522	0.1726	1.3494	0.0346	-1.4002	-1.3656
90	0	0.0407	-0.0407	-0.1325	0.1763	0.0438
135	-1.522	-0.1814	-1.3406	0.1827	1.1820	1.3647
180	-2.1809	-0.3685	-1.8124	0.0873	1.7250	1.8123
225	-1.522	-0.4548	-1.0672	-0.0122	1.0971	1.0849
270	0	-0.3400	0.34	-0.1192	-0.2250	-0.3442
315	1.522	-0.0979	1.6199	-0.1394	-1.5041	-1.6435
360	2.1809	0.112	2.0689	-0.0850	-1.9836	-2.0686

The vertical channel has been made extremely long in the present case in order to avoid possible finite-length effects. The above figures have shown that a large vortex develops under the plate in the upper 10-15b of the channel. This vortex is cut at $y = 1.11b$ below the plate in the velocity profiles of *Figure 3.7a*. The two according profiles taken at opposing phase of the oscillation cycle indicate that the vortex motion is even present in the mean and that it is not seriously affected by the instantaneous motion of the oscillator. The other five profiles for each time instant are taken further down the channel, as indicated in the plot. They are completely identical which means that the actual length of the channel has no influence as long as it extends beyond the area covered by the large vortex. The maximal velocity in the lower part of the channel amounts to 18% of the maximal actuator velocity. The flow is symmetric with respect to the horizontal center line of the channel and the profiles are identical to those of a wide channel that is subject to a periodical oscillation. Characteristic signs for this are the velocity overshoots close to the walls which can be related to Stokes' second problem. However, up- and down stroke profiles are not a mere mirror image of each other, because of the asymmetries at the upper channel entrance. The only reason for this is the time-dependent asymmetric flow through the wide gap already discussed above. A closer look at the velocity maxima in *Figure 3.6a*, for instance, reveals that the negative maximum is 16% larger than the positive one. This bias towards the downward direction persists until the bottom end of the channel, of course.

Seventeen instantaneous velocity profiles at the bottom end of the vertical channel in *Figure 3.7b* nicely depict the phase shifts of these profiles near the walls

due to the presence of Stokes' second problem. They also confirm that more fluid exits the channel at the bottom than enters. Our present device acts like a pump that sucks some material from the outside into the underlying structure. Closing the cavity under the vortex or applying a positive base pressure at the bottom clearly would avoid this. Another interesting observation is that the maximum negative velocity is not in phase with the actuator motion. It occurs near $\theta=225^\circ$ i.e. at $t = 18.625 T$ instead of $t = 18.5 T$ ($\theta=180^\circ$), where the actuator maximum velocity occurs. In the same vein the maximal positive velocity is also out of phase with the actuator plate, it occurs for the yellow curve at $\theta=45^\circ$. It is an interesting observation that an offset of about $\theta=45^\circ$ occurs which means that the response of the flow at the bottom is delayed by $\theta=45^\circ$. This is completely opposite to the narrow gap where the offset is $\theta=-45^\circ$.



(a) Profiles at various y -positions

(b) Profiles at the bottom end

Figure 3.7 Instantaneous velocity profiles at different positions inside the channel

However, since the main interest for the present investigations doesn't lie in the lower part of the channel, we return to the area of the oscillating plate and its influence on the outer flow field. This is illustrated best in terms of the time averaged velocity magnitude in *Figure 3.8*. Two vortices occur inside the cavity, a larger weaker one and a stronger but smaller one closer to the oscillator. The net effect on the external flow field consists of a horizontal wall jet that pushes fluid from the left to the right. The large vortex in the above right part is due to the start-up of the simulation. It should become weaker and disappear when the simulation is continued beyond the 19th oscillation cycle and when the time average is taken over more than just one single oscillation cycle.

A rather astonishing result is that the vertical oscillation of the actuator plate is translated into a horizontal fluid motion towards the right, which induces two horizontal wall jets, one above, the other one under the plate. Because of limited space in the horizontal direction the latter rolls up into a vortex.

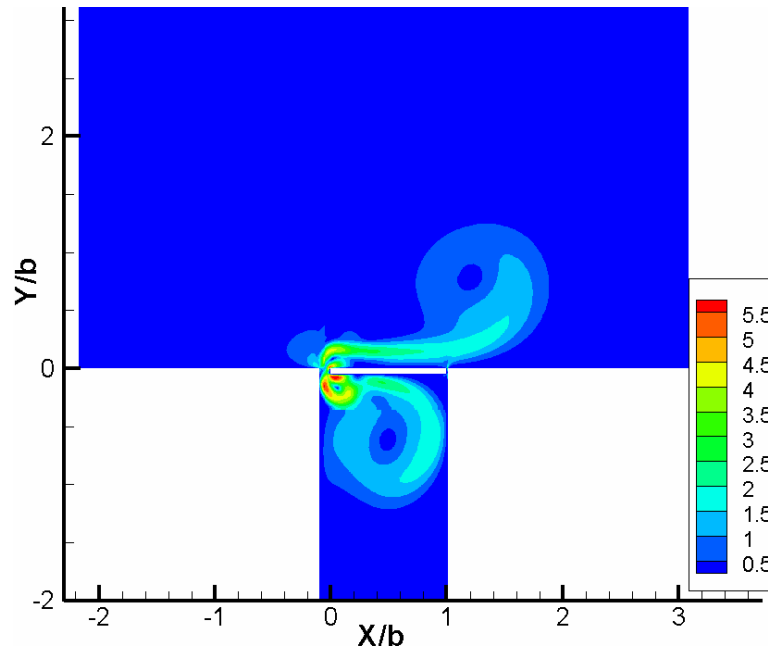
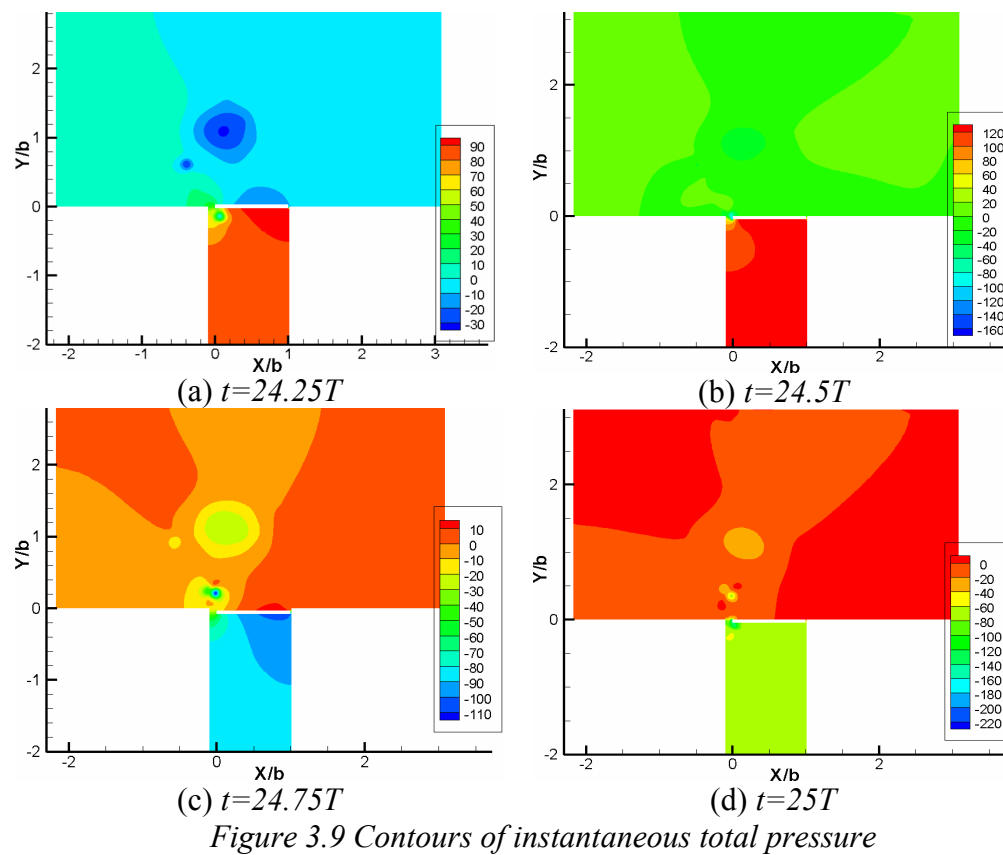


Figure 3.8 Time-averaged velocity magnitude (zoom in view)

3.2 Cavity with closed bottom

All the geometry and flow parameters are the same as in the previous case, the only difference from the previous section is that at the bottom of the cavity a wall boundary condition is used instead of pressure outlet. In this way it becomes representative of Lachowicz et al. [18] the only difference is that the cavity depth is very large. Nevertheless, we will compare these results with our previous case in order to see the effects of closing the cavity and we will also compare it with Lachowicz et al. [18] to see how close we are with their experiments. The simulation has been run over 24 oscillation cycles and results are averaged for last four cycles. Here only the results of the last cycle will be shown. Major fluid motions induced by the oscillating plate are confined to the area surrounding the plate, as expected. However, compared to the maximum velocity of the actuator a much larger velocity occurs in the wide gap in order to maintain continuity. As the oscillator moves up and down it accelerates the fluid in the gap and pushes it downward or sucks it upwards.

As in the previous case the main flow is through the wide gap. In this case a big vortex is produced above the plate, centered over the wide gap and a small vortex is produced inside the cavity also on the wide gap side. Both vortices show up as local pressure minima in the instantaneous total pressure contours in *Figure 3.9*, taken from the 24th oscillation period at different phases of the plate position. In subfigure (c) and (d) an instantaneous vortex pair emanating from the wide gap is also captured. This vortex pair later merges with the large vortex over the gap, as can be seen in subfigures (a) and (b). Product of plate velocity and fluid density are used to normalize pressures.



The zoom-in views into the narrow and wide gaps are shown in *Figure 3.10* and *Figure 3.11*, respectively. As already discussed in the previous section, the narrow gap behaves like an unsteady Couette-Poiseuille-type channel flow. The unsteady appearance and disappearance of the inner corner vortex at the left edge of the plate is nicely captured in *Figure 3.11*.

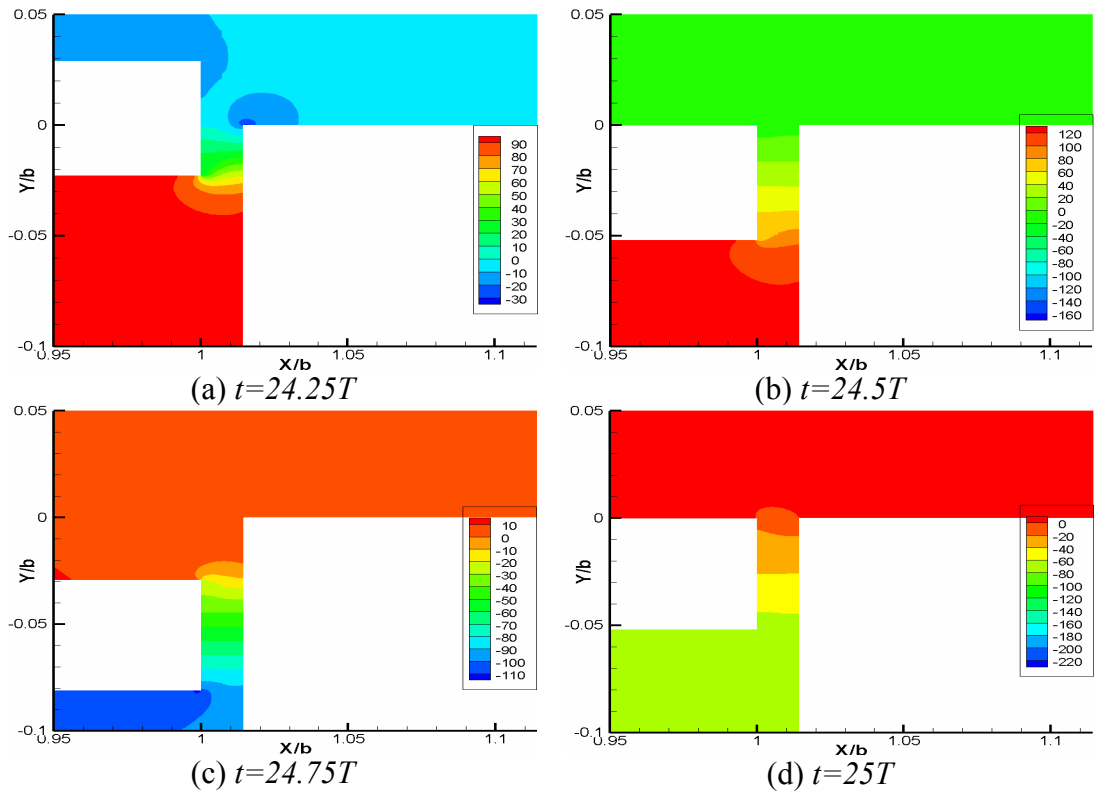


Figure 3.10 Instantaneous contours of pressure in the narrow gap

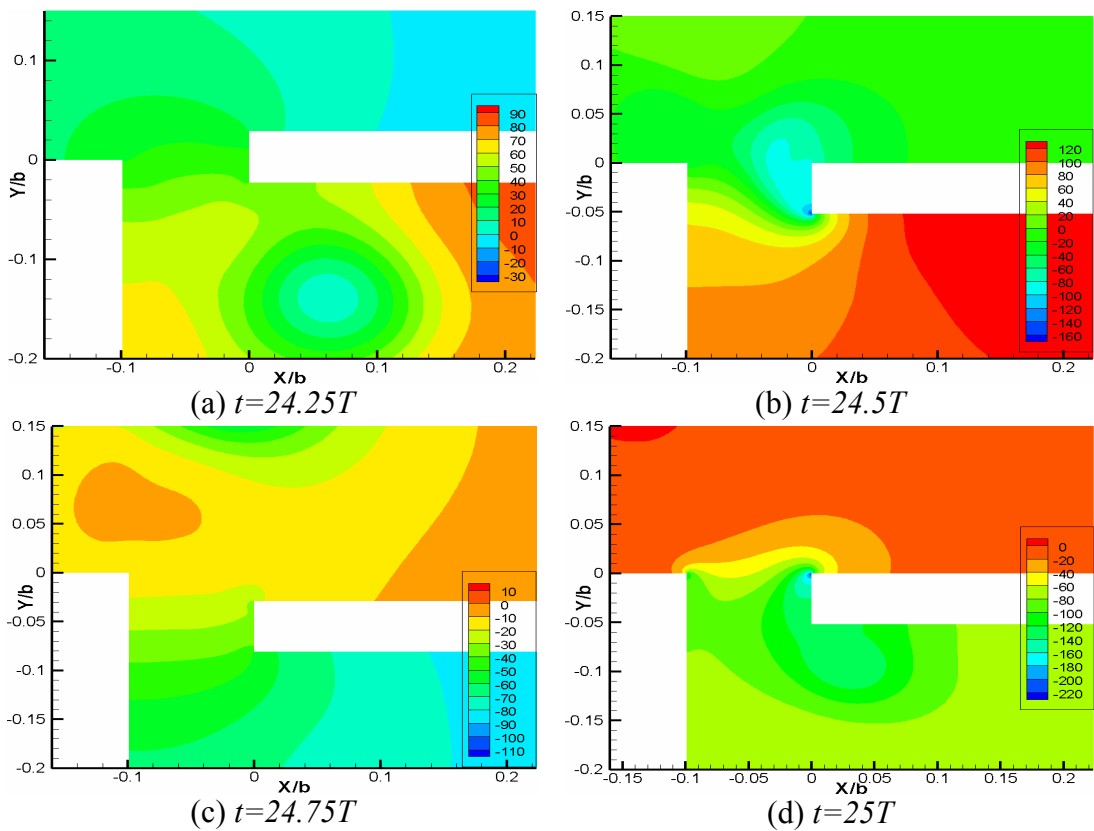


Figure 3.11 Instantaneous contours of pressure in the wide gap

Similarly *Figure 3.12* shows the contours of velocity magnitude in a zoom-in-view at four different time instances (two mean and two extreme plate positions). We can clearly see a very big vortex above the plate and a small vortex under the plate at the wide gap side. This vortex is present in all four time instances being strongest at $t=24.5T$ which corresponds to the blowing phase, i.e., the time instance of maximum plate velocity moving into the cavity. There is also a secondary big but very weak vortex inside the cavity. During each actuator cycle a pulse of high speed fluid ejects from the wide gap. These pulses combine to the main vortex and strengthen it. This can be seen in subfigures (b) and (c). Each of these velocity pulses is a sign of a counter-rotating vortex pair that gets ejected from the wide gap at each cycle. With increasing distance from the orifice these pulses merge with the average flow field thus strengthening the outside vortex. This can be seen in subfigures (a) and (b). The maximum velocity in the wide gap is more than $13U_p$ but in the vortex the maximum velocity is only $9U_p$.

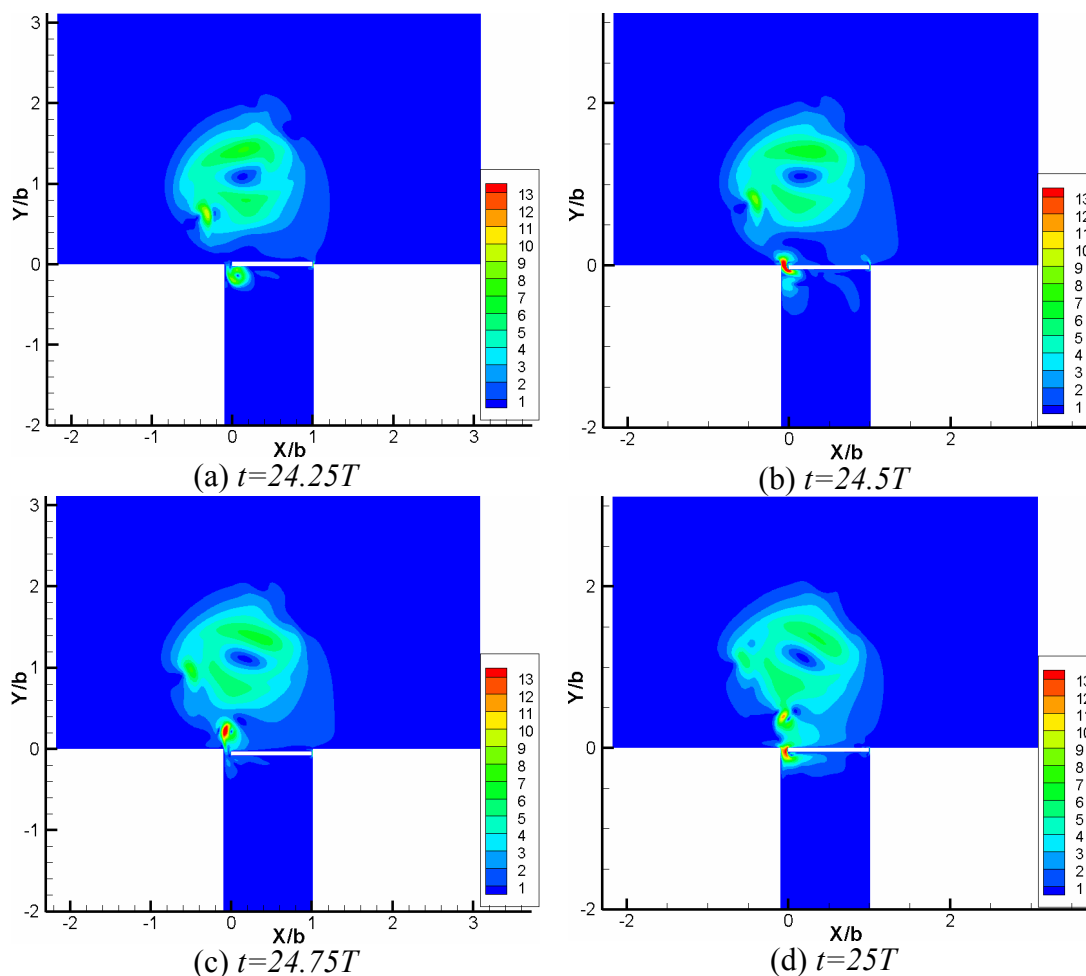


Figure 3.12 Instantaneous contours of velocity magnitude

Figure 3.13 shows the zoom-in-views of instantaneous velocity contours overlaid by velocity vectors in the narrow gap during four different time instances which are the same as in the previous figure. The maximum velocity in the narrow gap is around $10U_p$ in subfigure (a) (blowing) and minimum velocity is $5U_p$ in subfigure (d) (suction). These figures also show the plate position with respect to the cavity during different phases of plate oscillation.

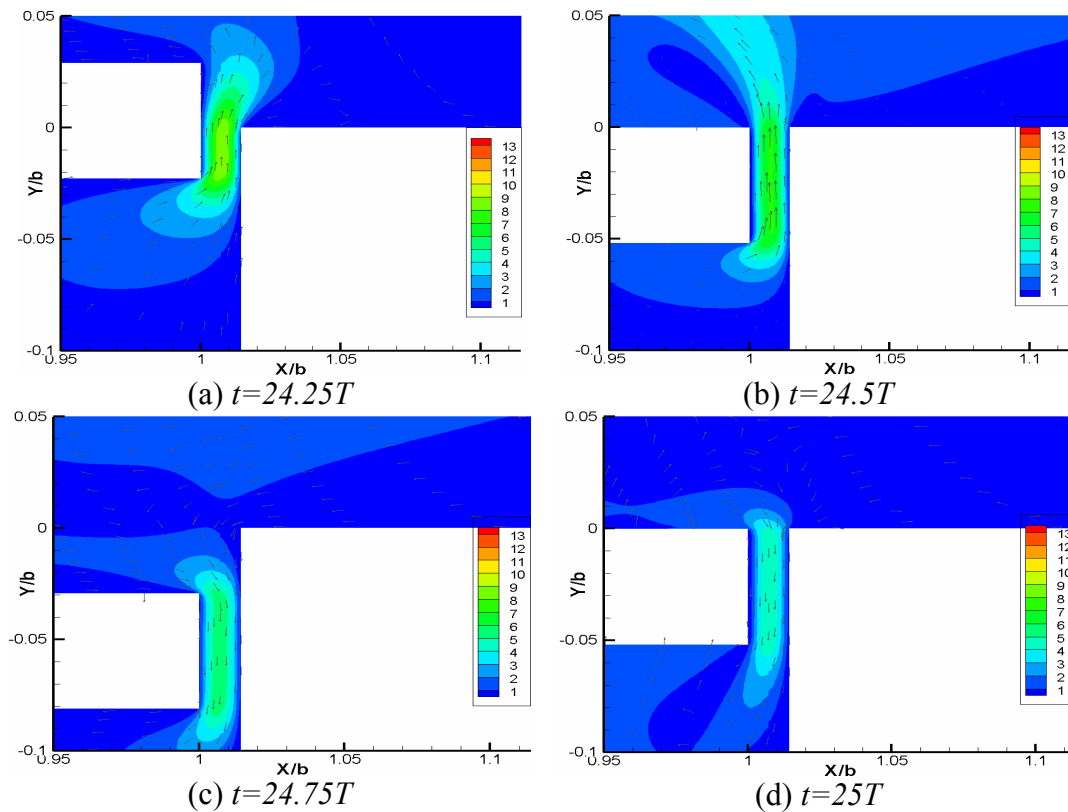


Figure 3.13 Instantaneous contours of velocity magnitude in narrow gap

Figure 3.14 shows the zoom-in-views of instantaneous velocity contours overlaid by velocity vectors in the wide gap during four time instances as in the previous figures. The maximum velocity in the wide gap is more than $13U_p$ in subfigure (b) and (d) for respective suction and blowing phases. We can observe from these figures that the velocity is not evenly distributed inside the gap and also blowing is stronger than suction. During the blowing phase high-speed fluid is closer to the cavity wall but during the suction phase high speed fluid is closer to the moving plate. Looking more closely at these figures we can see from the vectors' direction that near the plate the flow is opposite to the main flow which is more significant during blowing. In subfigures (a) and (c) where the plate is almost stationary this reverse flow is more significant as the plate is preparing to move in the opposite direction but the fluid is still moving in the previous direction. There is flow

separation and reversed flow. This can also be observed in *Figure 3.15a*, which shows the plots of instantaneous velocity in the wide gap for eight different phases of the flow. The reason for this complex flow behavior is that the wide gap width is very large compared to the plate thickness. As the flow in the wide gap is very complex and we cannot verify it from theory we now turn to the narrow gap. Another typical observation (for oscillating viscous flows) can be made in *Figure 3.15b* which shows the plots of velocity in the narrow gap for eight different phases of oscillation. From this figure it can be observed that the velocity profiles are no more symmetric as in the previous case when the cavity bottom was open. The maximal outflow velocity does not occur in phase with the plate oscillation. It occurs about 45° after the plate has reached its upper or lower turning point ($\theta = 90^\circ$ or $\theta = 270^\circ$). The green curve at $\theta = 90^\circ$ does not return to zero at the right end. This is simply because for the present set-up, the actuator plate has moved outside the cavity at this time instant and there is no longer a wall at $x > (0.00979b)$. There is no such phase shift in the wide gap as observed in *Figure 3.15a*.

Here, the flow is more like a mixed Couette-Poiseuille flow simply because the narrow gap width is very small compared to the plate thickness. The pressure difference between the underside and the upper side of the plate can be calculated from *Figure 3.10* and then used to calculate the maximum velocity in the narrow gap for the mixed Couette-Poiseuille flow. The pressure difference from *Figure 3.10d* when the plate is moving upward through its mean position, i.e. at $t = 24 T$ yields $\partial P / \partial y = (4.09 - (-0.306) / 0.0005) \text{ N/m}^3$. In plane Poiseuille flow this leads to a maximal velocity in the channel center that is $U_{\max} = W_n^2 \partial P / \partial y / (8\mu) = -1.203 \text{ m/s}$ for the present case. Half the plate speed must be subtracted from this to yield the center-line velocity for mixed Couette-Poiseuille flow, i.e. $U_{\text{gap max}} = -1.203 \text{ m/s} + 0.113 \text{ m/s} = -1.09 \text{ m/s} = -4.823U_p$. This is extremely close to the maximal velocities observed in *Figure 3.15b* which is $-4.646U_p$. A difference of only 3% exists between the two results. The pressure difference from *Figure 3.10b* when the plate is moving downwards through its mean position, i.e. at $t = 23.5 T$ yields $\partial P / \partial y = (-0.199 - 7.682) / 0.0005 \text{ N/m}^3$. In plane Poiseuille flow this leads to a maximal velocity in the channel center that is $U_{\max} = W_n^2 \partial P / \partial y / (8\mu) = 2.158 \text{ m/s}$ for the present case. Half the plate speed must be subtracted from this to yield the center line velocity for mixed Couette-Poiseuille flow, i.e. $U_{\text{gap max}} = 2.158 \text{ m/s} - 0.113 \text{ m/s} = 2.045 \text{ m/s} = 9.049U_p$. In this case the simulation yields a lower velocity which is $7.301U_p$. This

difference appears because the bottom of the cavity is closed due to which a higher pressure develops inside the cavity and due to that there is more flow through the wide gap as its width is higher.

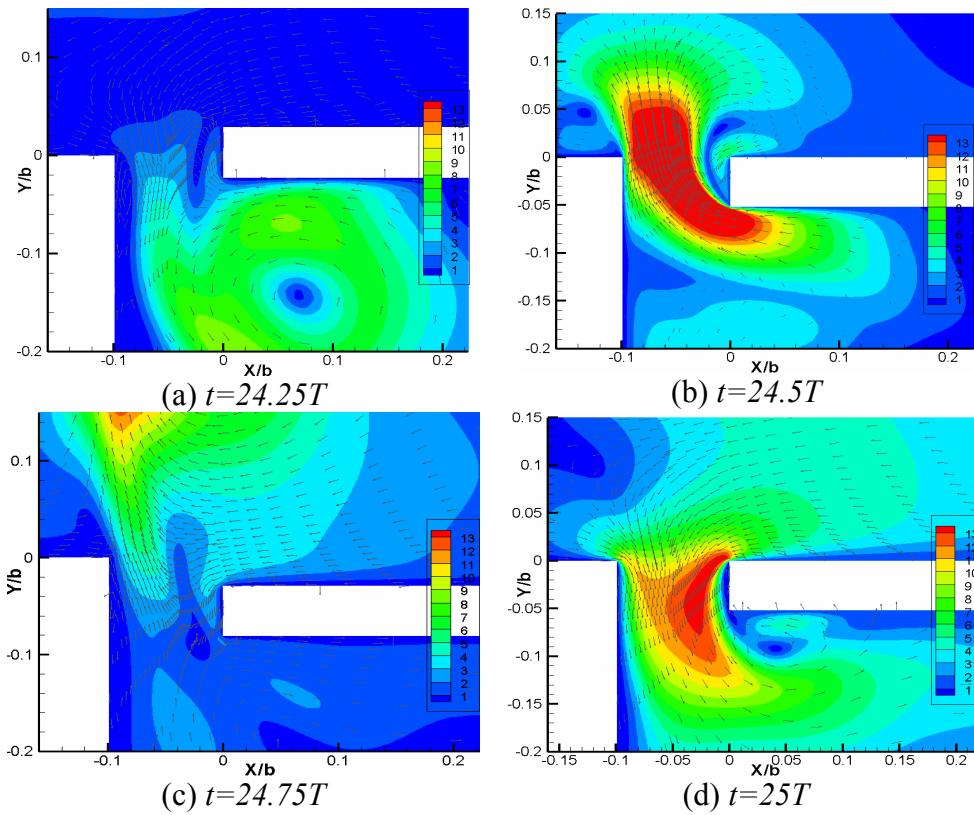


Figure 3.14 Instantaneous contours of velocity magnitude in wide gap

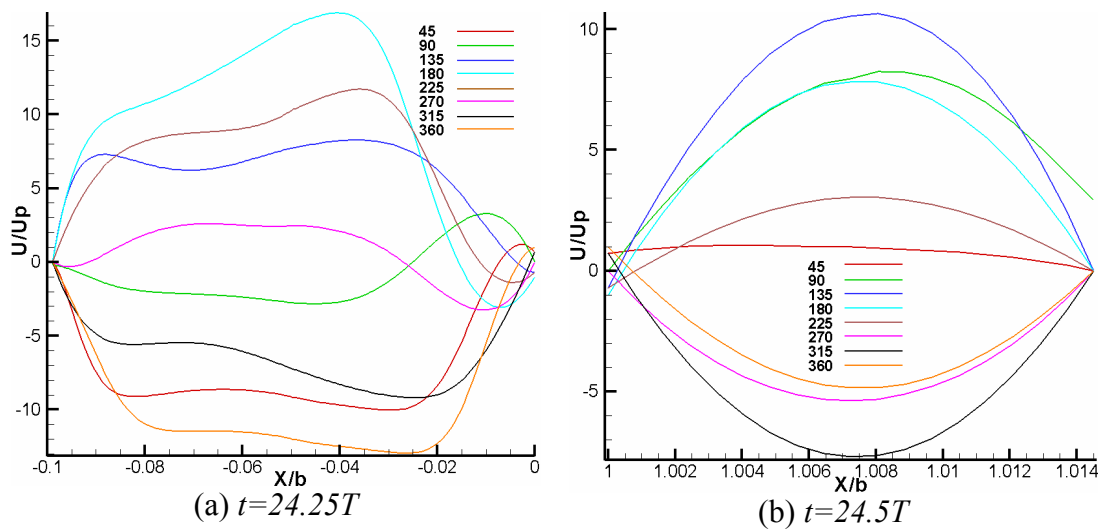


Figure 3.15 Plot of y -velocity in the wide and narrow gaps for various phases of oscillation in the 24th period

Figure 3.16 shows the evolution of velocity traces versus time steps at the centers of the narrow and wide gaps and at a point $0.1559b$ to the right of the wide gap and $0.312b$ above the plate for the last four complete periods for which time

averaged results have been computed. The data shows an excellent periodicity of the results. The peak velocities both in the wide and in the narrow gap are much higher than the maximum velocity of the actuator plate. Multiplying the maximal plate velocity with the ratio of gap widths to plate width ($b/(W_w + W_n)$) yields a peak velocity of $8.81U_p$ which comes very close to the narrow gap peak velocity of 8.6, apart from a small higher harmonic contribution (green curve) in *Figure 3.16*. Interestingly, the peak velocity in the wide gap turns out to be almost two times larger. Due to the closed cavity bottom all velocities have a positive mean and the positive peaks (blowing) are much stronger than the negative (suction) ones. In *Table 3.3* flow rates through the gaps are compared with the fluid that is pushed by the plate at eight different time instances. If we compare plate and net flow rates, it can be observed that both net flows are almost the same at every time instance which shows that mass is conserved. As already observed above, there is a phase shift in the narrow gap with respect to the plate which can be observed here once again. The maximum flow through the narrow gap is at $\theta=135^\circ$ and $\theta=315^\circ$ in contrast to the plate at $\theta=360^\circ$ and $\theta=180^\circ$, respectively, but there is no such phase shift in the wide gap. Looking at the net flow, there is no phase shift which suggests that the wide gap flow is the strongest and drives the flow outside the cavity. These are the same observations as in the previous case. At $\theta=90^\circ$ and $\theta=270^\circ$ where the plate is at rest (which means zero flow rate), there is some flow through the gaps (especially in the narrow gap) because of the phase shift such that a flow still exists, whereas in the wide gap the fluid follows the previous motion of the plate due to its inertia in spite of the plate being at rest.

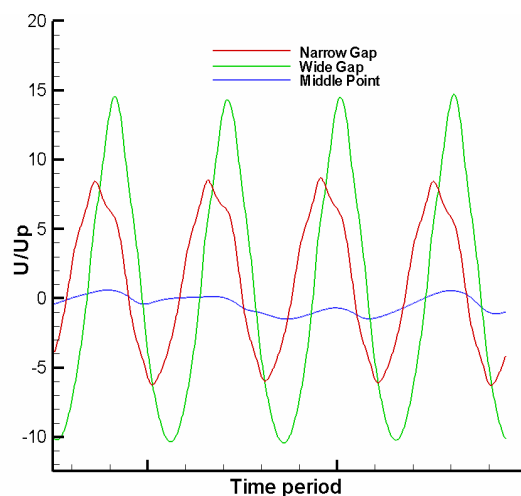


Figure 3.16 History of y-velocity at different points for the last 4 periods

Table 3.3 Volume flow rate through gaps at different phases

Phase (o)	Plate $m^3/s(10^{-3})$	Narrow Gap $m^3/s(10^{-3})$	Wide Gap $m^3/s(10^{-3})$	Net $m^3/s(10^{-3})$
45	1.522	0.030737967	-1.5853543	-1.5546164
90	0	0.19060096	-0.20768662	-0.0170856
135	-1.522	0.20606654	1.3229955	1.5290621
180	-2.1809	0.14603802	2.0377664	2.1838043
225	-1.522	0.03774833	1.5160651	1.5538135
270	0	-0.12050078	0.14019928	0.0196985
315	1.522	-0.15486934	-1.3728449	-1.527714
360	2.1809	-0.096081392	-2.084672	-2.180753

However, since the main interest of the present investigations lies in the area of the oscillating plate and its influence on the outer flow field we now turn to time-averaged results. These are shown in *Figure 3.17* a and b in terms of velocity magnitude and pressure. Data are averaged over the last four time periods. Two vortices occur inside the cavity, a larger weaker one and a stronger but smaller one closer to the oscillator. The net effect on the external flow field consists of a very big vortex. Lachowicz et al. [18] also observed a big vortex above the plate but in our case we get a vortex bigger as the one observed by Lachowicz et al.

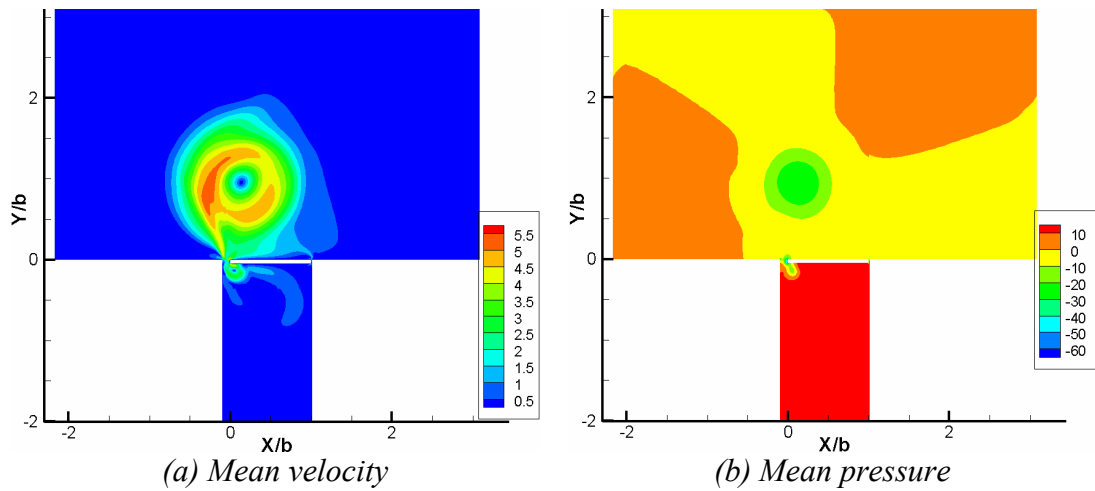


Figure 3.17 Contours of mean flow

3.3 Comparison

3.3.1 Comparison of open (case 1) and closed (case 2) cavity bottom

We will now show the influence of closing the cavity bottom and compare results. With open cavity bottom (*Figure 3.8*) we get a wall jet from the wide gap above the plate directed towards the narrow gap but with closed cavity we get a very big vortex from the wide gap which lies above the wide gap and half of the plate. *Figure 3.18* (a) and (b) show the comparison of instantaneous velocity profiles in the wide and narrow gaps, respectively. Closing the cavity bottom eliminates the leakage of fluid that has been shown in *Figure 3.7b* during the down-stroke of the plate such that more material must exit with a higher velocity through the gaps at the top of the cavity. This is nicely illustrated for the narrow gap in *Figure 3.18b* which exhibits a positive peak velocity increase by 64% when the plate moves into the cavity. This is in a striking contrast to the suction phase of the actuator where the negative velocity in the narrow gap increases by 8% only. The suction phase at the wide gap delivers a somewhat more even velocity profile and the maximum suction velocity is reduced by 5.8% compared to the open cavity, but the asymmetry of the flow (w.r.t. time) increases as well: the peak blowing velocity increases by 33% at the wide gap according to *Figure 3.18a*.

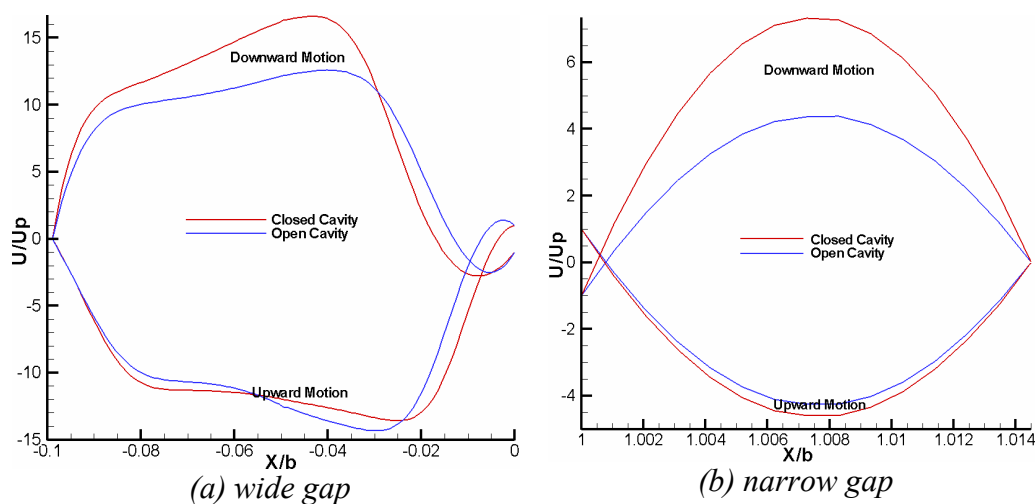


Figure 3.18 Comparison of gap profiles

Table 3.4 compares the maximum velocities from *Figure 3.18* with theory for plane Poiseuille-Couette flow for both the cases, for the suction phase at $\theta = 360^\circ$ and the blowing phase at $\theta = 180^\circ$. It is observed that the case with open cavity is in excellent agreement with the theory as well as the suction phase of the closed cavity

case but in the blowing phase there is a difference of 19%. The reason for this difference is due to the asymmetry of the flow field with respect to the actuator plate. Minor differences of the flow through the wide gap may also contribute to this difference. Note that for the calculation of analytical velocities we used the pressure difference of the simulation results.

Table 3.4 Comparison of instantaneous peak velocities in the narrow gap

Case	Phase	$\Delta p(\text{N/m}^3)$	Analytical max. vel.	Simulation max. vel.	% Difference
Open Cavity	180	7580	4.159	4.35	3
	360	7740	4.19	4.25	1
Closed Cavity	180	15762	7.301	9.049	19
	360	8792	-4.646	-4.823	3

An overview of the maximal vertical velocities in the center of the narrow and the wide gaps is given in *Table 3.5* together with the respective time phases ($\theta = 360^\circ t/T$) when these maxima occur. Here we observe that the velocity magnitudes of the maximal suction and blowing velocities in the narrow gap increase by closing the cavity at the bottom. The phase of the maximum velocity is also the same i.e., $\theta = 312^\circ$ and $\theta = 130^\circ$ for suction and blowing, respectively. The phase shift during suction is -48° and for blowing it is -50° . This large phase shift is due to the unsteady viscous nature of the narrow gap flow. The flow at the wide gap is completely different, as already shown by the previous velocity profiles across the gap further above. In case of the wide gap, closing the cavity bottom increases the blowing velocity but the suction velocity decreases. Here, also a slight phase shift exists which was not seen earlier by just observing the velocity profiles. For the open cavity the phase shift for blowing is higher: 23° , but for suction it is only 4° while for closed cavity case in both suction and blowing a phase shift of only 10° exists. These are interesting observations.

Table 3.5 Comparison of maximum vertical velocities

Open cavity	Phase (o)	Closed Cavity	Phase (o)
Narrow Gap			
9.01	130	10.044	130
-6.76	313	-7.35	312
Wide Gap			
13.19	203	17.0	190
-12.55	4	-12.2	10

Table 3.6 compares the flow rates through the gaps for open and closed cavity. As velocities in the gaps are higher for the closed cavity case therefore flow rates are also higher for this case. The difference of flow rates for the blowing phase is more significant than for the suction phase. In the narrow gap for the blowing phase there is a big difference of 40% but for the suction phase there is only a difference of 11%. In the wide gap the difference of flow rates through the gap is not as significant as in the narrow gap but the trend is the same i.e., blowing is more different (15%) than suction (4%).

Table 3.6 Comparison of flow rates through the gaps

Phase (o)	Open cavity $m^3/s(10^{-3})$	Closed Cavity $m^3/s(10^{-3})$	Difference %
Narrow gap			
180	0.0873	0.14603802	40
360	-0.0850	-0.096081392	11
Wide gap			
180	1.7250	2.0377664	15
360	-1.9836	-2.084672	4

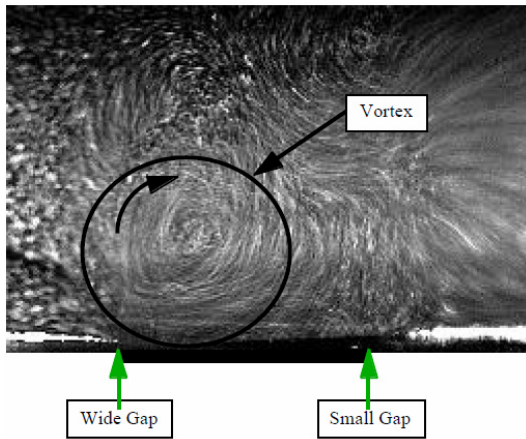
3.3.2 Comparison of closed cavity bottom (case 2) and Lachowicz et al.

Now we compare the results with the data available through Lachowicz et al. [18] and Joslin et al. [14]. Unfortunately these references do not contain abundant information. They are restricted to some long-time-exposure flow visualizations that show mean-flow stream lines, to scatter plots which document the observed flow structures with respect to the scaling parameters of the experiments and extremely few quantitative velocity profiles that are useful for a quantitative comparison.

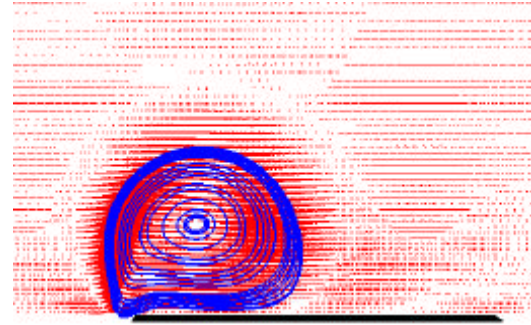
In Figure 3.19 (a), (b) and (c) contours of the mean velocity magnitude by Fluent are compared with Lachowicz et al. [18] and Joslin et al. [14]. We get a vortex from the wide gap which is in complete agreement with experimental results of Lachowicz et al. [18] who also get a vortex but in our case the size of the vortex is very big compared to the one by Lachowicz et al. [18]. The size of the vortex in the DNS results of Joslin et al. [14] is even smaller than Lachowicz et al. [18].

Figure 3.19d shows a comparison of mean velocity profiles through the center of the vortex for the closed cavity case with the experiments of Lachowicz et al. [18] and DNS results by Joslin et al. [14]. In our simulation we get a vortex that is almost 2.5times as large as the one that is observed in the experiment and in the DNS of Joslin et al. [14]. This was not a very good match but encouraging as for a first step

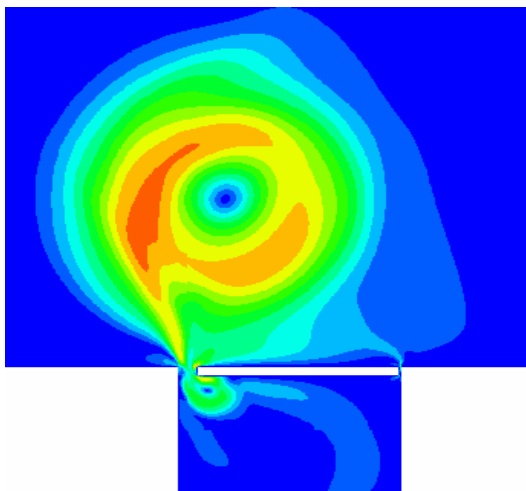
we were able to get a vortex with almost the same velocity peaks as in Lachowicz et al. [18]. Our hope at this point was that by changing the some actuator parameters (which were not specified by Lachowicz et al. [18]) we might get a better comparison.



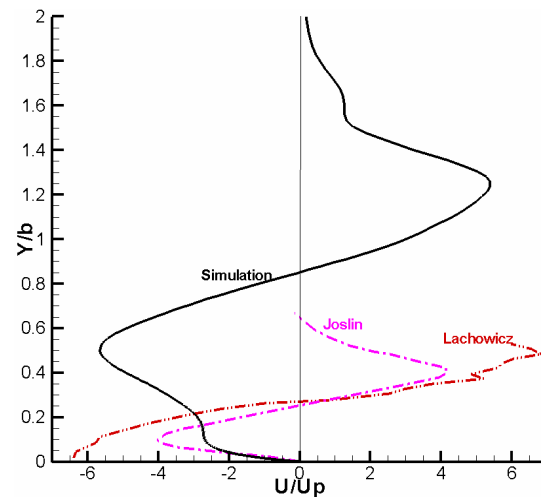
(a) Lachowicz et al. [18]



(b) Joslin et al. [14]



(c) Simulation



(d) velocity profiles through the vortex center

Figure 3.19 Comparison of velocity contours and profiles

3.4 Summary and conclusions

In the present chapter two different cases related to the actuator design proposed and investigated by Lachowicz et al. (1999-2001) have been studied using the commercial CFD software Fluent® available at the Universität Stuttgart. The aim of this was three-fold: learning to use the special features for dynamic meshes, moving boundaries and so-called "user-defined functions" (i), performing quantitative validations of the CFD results with respect to analytical solutions (ii), and understanding the contributions of the basic building blocks of the actuator (iii). Using this setup we were able to verify the computational results in a quantitative manner.

Simulations were performed by increasing the length of cavity to $20.725b$, first using the pressure outlet boundary at the bottom and then by closing the cavity. We also compared the results where possible with theory and also with Lachowicz et al. [18]. In case of open cavity we get a wall jet from the wide gap but with closed cavity we get a very big vortex like Lachowicz et al. [18]. The size of the vortex in our case is bigger than the experimental results but many parameters (like effects of cavity depth, plate position with respect to cavity wall) are missing in the literature and would be investigated in the next chapter. We hope to get good comparison. Some of the other interesting observations are, at the bottom of the cavity (first case) and in the narrow gap a phase shift of the velocity with respect to the plate velocity exists. Further velocities in the narrow and wide gap are higher for the closed cavity case as there is no flow through the bottom in this case.

Thus the present investigations were able to identify the fluid mechanical mechanisms responsible for the surprising mean-flow characteristics of this kind of actuator design. Since the difference of the present setup to the one investigated experimentally by Lachowicz et al. is small, we may already claim at this stage that simulations of the Lachowicz et al. actuator can be performed at a high level of confidence and that these simulations will help to understand the different flow regimes of this kind of actuator. The latter consist of wall jets, as observed here, of vertical or oblique jets, or a large vortex above the plate, depending on the actuation parameters (frequency and amplitude). We will discuss these in the next chapter.

4. Comparative study of different actuator parameters

In the previous chapter we studied a test case of vortex mode with open and closed cavity. Our main focus was on the validation of the simulation tools. It had helped us to get a first idea of the underlying fluid dynamical principles of the JaVA. As, at present there is a complete lack of understanding of its function principle and absolutely no physical comprehension of how and why it works as observed. Thus, without understanding we are completely blind with respect to optimization or possible improvements which might be necessary to make such devices useful for applications in aerodynamics. Therefore, in the current chapter we will continue to study different parameters to see their effects on the flow field first by varying the geometrical parameters like cavity depth with closed bottom and also by moving the plate inside the cavity to see the effect of the plate position with respect to the cavity top wall then by changing the material properties from constant density to ideal gas law. These features are not documented nor mentioned in earlier work by Lachowicz et al. [18]. In the present chapter we will also discuss the effects of changing the flow parameters like frequency and scaled amplitude. We will compare the results with experimental results of Lachowicz et al. [18] where possible. The different parameters studied in this chapter are given in *Table 4.1*. The term “middle” is used for the case where the plate middle position is level with the upper surface in this case and case-4 is labeled “inside” because the plate moves completely inside the cavity at all time instances. The cavity depth “h” in each case is indicated with respect to the plate width “b”

Table 4.1 Different cases studied

Case	Frequency (f)	Scaled amplitude $Sa=2\pi a/b$	Cavity depth (h)	plate Position
<i>Cavity depth</i>				
2.1	128	0.1829	20.725b	Middle
2.2	128	0.1829	2.38b	Middle
2.3	128	0.1829	0.31b	Middle
<i>Plate position</i>				
2.4	128	0.1829	2.38b	Inside
<i>Compressible</i>				
2.5	128	0.1829	2.38b	Middle
<i>Flow parameters</i>				
2.6	70	0.13	2.38b	Middle
2.7	70	0.188	2.38b	Middle
2.8	210	0.11	2.38b	Middle

In the following sections we will discuss all these one by one.

4.1 Geometric parameters study

In this section we will discuss the effects of changing the different geometrical parameters like cavity depth and plate position with respect to the cavity top wall, upon the flow field outside the cavity. Remember these parameters are neither studied experimentally by Lachowicz et al. [18] nor numerically by Joslin et al. [14]. First, we will discuss the effects of cavity depth and then plate position.

4.1.1 Cavity depth study

Different simulations were performed by changing the cavity depth and keeping the rest of the parameters (gap widths, plate width “b”, plate position, frequency “f” and scaled amplitude “Sa”) fixed. Three different depths were used for comparison. *Figure 4.1* shows the contours of mean velocity magnitude for these different cases. Case 2.1 (subfigure a) is the same as the one from the previous chapter, here it is reproduced for comparison. In case 2.2 (subfigure b) the cavity is cut just below the secondary vortex inside the cavity. In case 2.3 the cavity depth is further reduced and it is cut just below the primary vortex inside the cavity. We can see that as we decrease the cavity depth the size of the vortex also decreases. Furthermore, velocities in the vortex increase as the size of the vortex decreases due to stronger blowing by reducing the cavity depth. For case 2.1 and case 2.2 we get a vortex but the case 2.3 where the cavity depth is very small we get a relatively small vortex followed by a wall jet towards the narrow gap ending in a weak start-up vortex in the opposite direction. If we continue our simulation beyond this point this secondary vortex will disappear and we will get a wall jet. This secondary vortex can also be seen in case 2.2 where it is closer to the primary vortex and stronger than in case 2.3. The reason is that by decreasing the cavity depth the reaction time inside the cavity during the blowing phase, when the plate is moving downward, also decreases and we get more intensive flow through the gaps especially in the narrow gap is more active. Also in the wide gap there is stronger reverse flow near the plate and the cavity wall for smaller cavity depths.

Figure 4.2 gives a comparison of gap velocity profiles. In the narrow gap (subfigure b) we can see that the velocity increases as cavity depth decreases. This phenomenon is more significant in the suction phase. The reason of these higher velocities in the narrow gap is that when we reduce the size of the cavity there is not

enough space for the fluid to move freely relative to the long cavity where the wide gap is more active. In the wide gap there is reverse flow near the plate being strongest for case 2.3, cf. blue line in subfigure (a). This reverse flow is stronger in the blowing phase compared to the suction phase. At the cavity walls the flow is more attached for the case with smaller cavity compared to the case with larger cavity. This difference is more significant during the suction phase. Velocity maxima in the profile are shifted towards the left for the suction phase but for the blowing phase they are shifted towards the right, which is the reason for a smaller vortex with decreasing cavity depth. One more observation is that the relative difference between the first and the second case is less significant than the difference between the second and the third case although the difference of cavity depth is more in the former than in the latter. Here we can conclude that due to this shift of velocity maxima towards the right (blowing phase) and also due to strong suction and blowing in the narrow gap with decreasing cavity depth, the flow turns earlier towards the narrow gap and due to this the vortex size reduces.

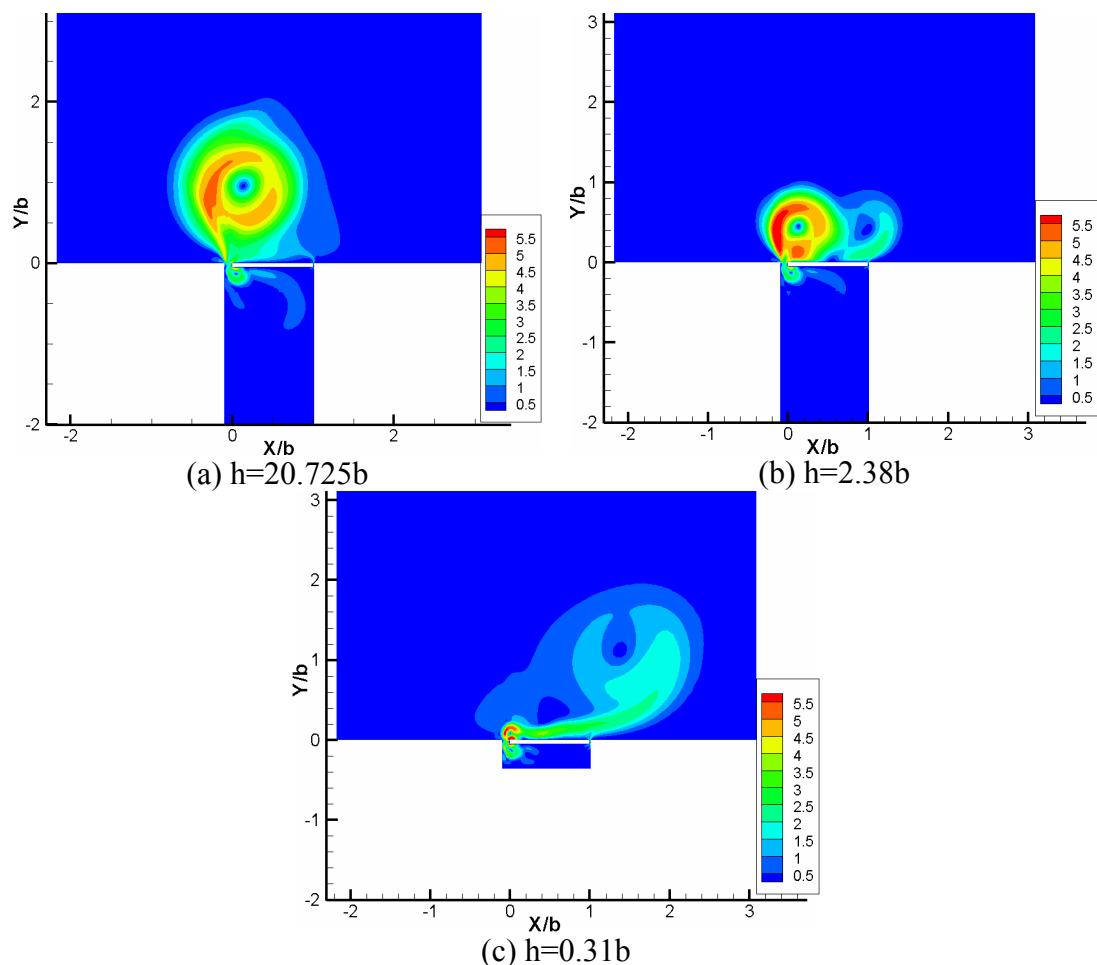
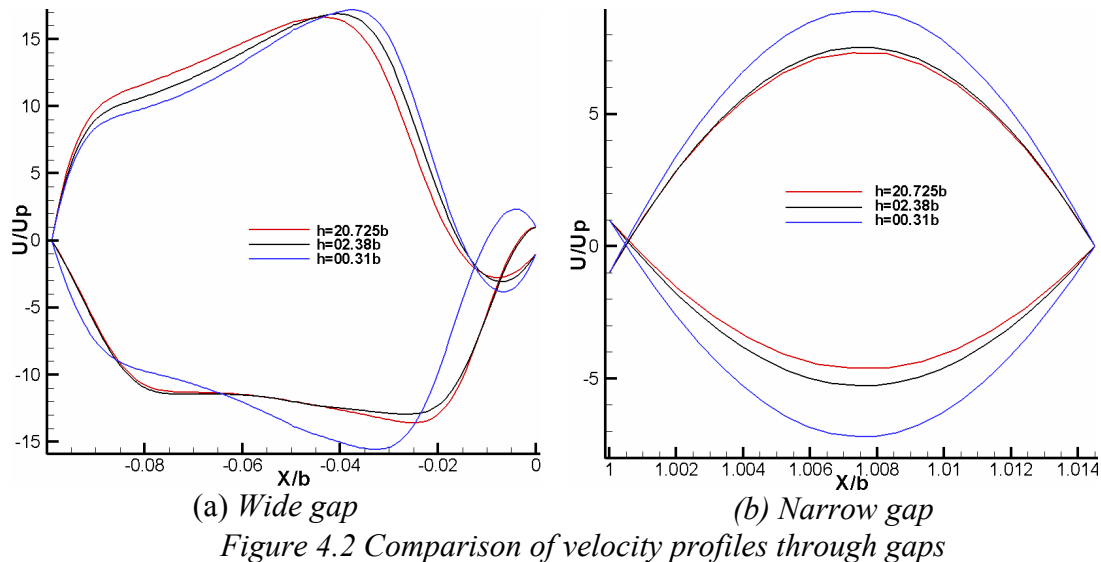


Figure 4.1 Contours of mean velocity magnitude for three cavity depths



In *Table 4.2* the total flow rate through the gaps is compared with the flow pushed by the plate at two instances during the oscillation when the plate is at its maximum velocity. The flow rate in the narrow gap slightly increases as the size of the vortex decreases. As the gap width is constant the velocities in the narrow gap increase. This is also observed above in *Figure 4.2b*. Accordingly, the flow rate in the wide gap slightly decreases with decreasing cavity depth, in order to conserve mass. We observe that for all cases the net flow is the same and only a difference of less than 1 percent exists. Even if the velocity in the gaps varies for different cases the flow rates remain the same. This also shows that the two gaps interplay (i.e. if the flow rate increases in one gap, then at the same time instance it decreases in the other gap and vice versa).

Table 4.2 Flow rate through the gaps

Cavity Depth	Phase	Plate $m^3/s(10^{-3})$	Narrow Gap $m^3/s(10^{-3})$	Wide Gap $m^3/s(10^{-3})$	Total $m^3/s(10^{-3})$
20.725b	180	2.1808	0.146038	2.037766	2.183804
	360	2.1808	-0.09608139	-2.084672	-2.180754
2.38b	180	2.1808	0.1529918	2.024412	2.177404
	360	2.1808	-.1047478	-2.075795	-2.180543
0.31b	180	2.1808	0.1808748	1.997389	2.178264
	360	2.1808	-0.1448068	-2.037657	-2.182464

An overview of the maximal vertical velocities in the center of the narrow and the wide gaps is given in *Table 4.3* together with the respective time phases when these maxima occur. Here we observe that in the narrow gap the velocity magnitudes of the maximal suction and blowing slightly increases with decreasing cavity depth.

The phase of the maximum is not affected by changing the cavity dept. It occurs around 130° and 310° , almost 40° after the maximal velocity of the actuator plate. This large phase shift is due to the unsteady viscous nature of the narrow-gap flow. Overall, there is higher peak suction and a lower peak blowing velocity in the narrow gap. The flow at the wide gap is completely different; the flow here is more of a suction-pumping type that is merely pressure driven. This is demonstrated in the clearest way by the according phases given in *Table 4.3*, all velocity maxima occur at slightly different phases for both phases.

Table 4.3 Comparison of maximum vertical velocities at the centers of the gaps

Case	Phase	Narrow gap		Wide gap	
		Velocity	Phase ($^\circ$)	Velocity	Phase ($^\circ$)
2.1	Suction	-7.35	312	-12.2	10
2.2		-8.1	310	-13.78	38
2.3		11.04	313	-14.69	22.5
2.1	Blowing	10.044	130	17.0	190
2.2		10.96	132	17.554	240
2.3		12.788	133	18.987	211

Table 4.4 compares the maximum velocities in the narrow gap from the simulation computed from *Figure 4.2b* with theory for mixed plane *Poiseuille-Couette* flow in which the pressure difference between the upper and lower side of the plate is used from the simulation to calculate the velocity by using the formula given by White 1974 [3] at two phases with plate peak velocity, i.e. for the suction phase at $\theta = 360^\circ$ and the blowing phase at $\theta = 180^\circ$. It is observed that the suction phase is in excellent agreement with theory for case 2.1 and case 2.2, but this does not happen for the blowing phase because of differences of *19 and 14%* for case 2.1 and case 2.2 respectively. For case 2.3 the observation is completely opposite to the first two cases. In this case, the difference during the suction phase is higher than the blowing phase. A closer look shows that during the suction phase the difference between analytical and simulation velocity increases as the cavity depth decreases, but during the blowing phase this difference decreases with decreasing cavity depth. The reason for this difference is that during blowing, the narrow gap becomes more efficient for smaller cavity depths as space inside the cavity is very small and there is not enough space for the flow to go towards the wide gap. But this is not the case for suction phase.

Table 4.4 Comparison of instantaneous peak velocities in the narrow gap at mean plate position

Case	Motion of the plate	Δp (N/m ³)	Analytical max. vel.	Simulation max. vel.	% difference
2.1	upward	8792	-4.646	-4.823	3
	downward	15762	7.301	9.049	19
2.2	upward	8278	-5.488	-5.752	4.3
	downward	16893	9.734	8.495	14
2.3	upward	11060	-6.202	-7.213	14
	downward	16120	9.268	8.85	4.7

In Figure 4.3 velocity profiles through the center of the vortex are compared. The size of the vortex in case 2.2 is very close to the experiment of Lachowicz et al. [18]. But in case 2.1 the vortex is very big and in the third case the vortex is very small compared to the one by Lachowicz et al. [18]. Blowing velocities in all cases is almost the same but the suction velocity in case 2.3 is slightly on the higher side. Different cavity depths yield different vortex size outside the cavity and as we are very close to the experimental results in case 2.2 with $h=2.38b$, we will take this cavity depth as a standard for our further investigations.

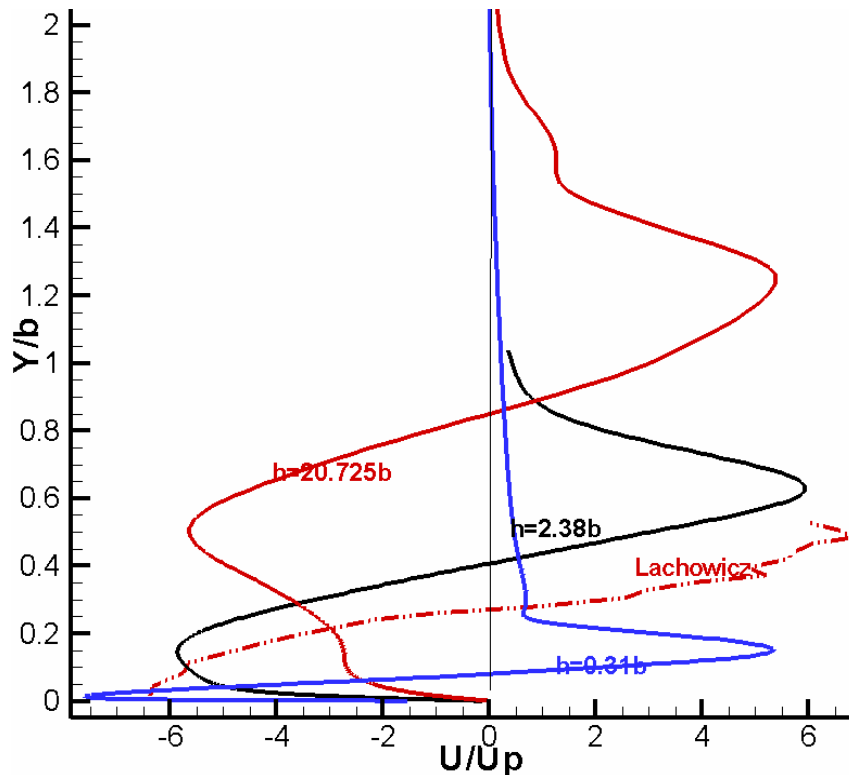


Figure 4.3 Comparison of velocity profiles through the center of the vortex

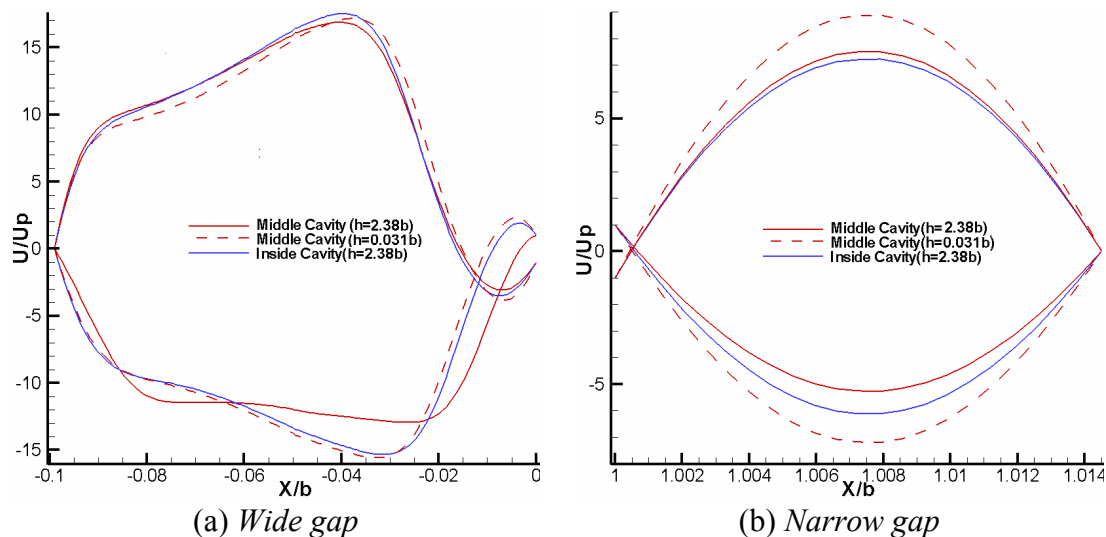
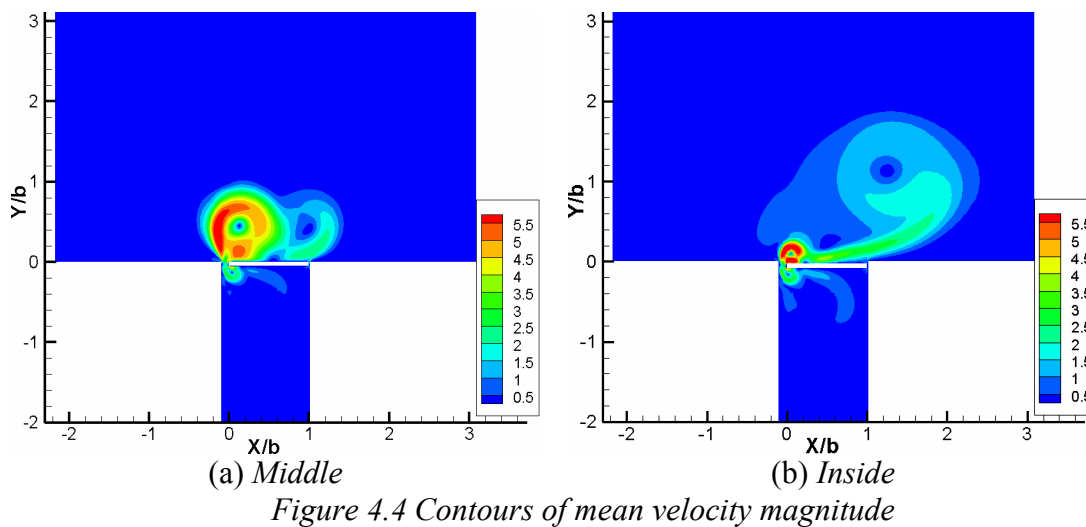
4.1.2 Plate position study

In the previous section we finalized the cavity depth at 2.38b following case 2.2 as this was safe to cut below the secondary vortex and also because the according results are very close to the experimental results. Now we will use the same cavity depth to investigate the influence of plate position relative to the cavity top wall. We moved the plate mean position inside the cavity by scaled amplitude (Sa) so that when it moves back to its top most position it is flush with the cavity top wall in such a way that at its upper turning point it would not exceed $y=0$. Thus in this case the plate always moves inside the cavity. An additional grid block of 350*50 points is introduced above the plate. Accordingly, the number of grid cells in blocks no 4, 5, 6 and 7 in the y-direction is also increased by 50.

Figure 4.4 shows the contours of mean velocity magnitude. Subfigure (a) is from the above case 1.2 reproduced here for comparison. We already have seen in the previous section that we get a vortex with this geometry and flow parameters but now when we move the plate inside the cavity we get a small but strong vortex followed by a wall jet. This vortex is almost half as large as the one produced by Lachowicz et al. [18]. The jet turns in counter clockwise direction at its end (start-up vortex). Remember that in the previous section in case 2.3 (see *Figure 4.1c*) the same kind of flow was observed in which the cavity depth was reduced to 0.31b. So either reducing the cavity depth or moving the plate inside the cavity has almost the same effect on the flow outside the cavity. Please note that neither Lachowicz et al. [18] nor Joslin et al. [14] have ever discussed any influence of the actuator plate's mean position. Thus, it is not fully clear which case has been investigated in their previous work. However, it is still not unreasonable to assume that case 2.2 with minor changes has been treated in the literature (as assumed before).

Figure 4.5 shows the comparison of instantaneous velocity profiles in the narrow and wide gap. For comparison we have also included the profiles of case 2.3 from the previous section because in this case we also get a wall jet, like in case 2.3. Again, there is not too much difference in the profiles despite the obviously large differences in the averaged vortex flow outside the cavity. In the wide gap during blowing the peak velocity is the same with a slightly higher value for case 2.4 while for case 2.3 the velocity maxima are slightly closer to the plate. During the suction phase a completely different behavior can be seen. In case 2.2 the suction profile is flat with a

very low velocity peak compared to the blowing profile but in the other two cases the profiles are more like the blowing profiles with velocity peaks closer to the plate and with lower values. Also flow is more attached to the cavity walls. Near the plate the reverse flow phenomenon is also more significant in these two cases compared to case 2.2. Now we turn to the narrow gap (subfigure b) where, as usual, blowing is stronger compared to the suction. Interestingly in case 2.4 blowing is weaker but suction is stronger than for case 2.2. Both the blowing and suction is very strong in case 2.3.



In *Figure 4.6* velocity profiles through the center of the vortex are compared. As we have observed in *Figure 4.3* that the size of the vortex in case 2.2 is very close to the experiment of Lachowicz et al. [18], but in case 2.3 and case 2.4 the vortex is very small. i.e. almost half in size compared Lachowicz et al. [18]. Interestingly, by

reducing the cavity depth in case 2.3 had almost the same impact as moving the plate mean position inside the cavity. The size of the vortex in case 2.4 is slightly bigger than in case 2.3. Blowing velocities in all cases are almost the same but the suction velocity in case 2.3 and case 2.4 is higher compared to the blowing velocity in case 2.2.

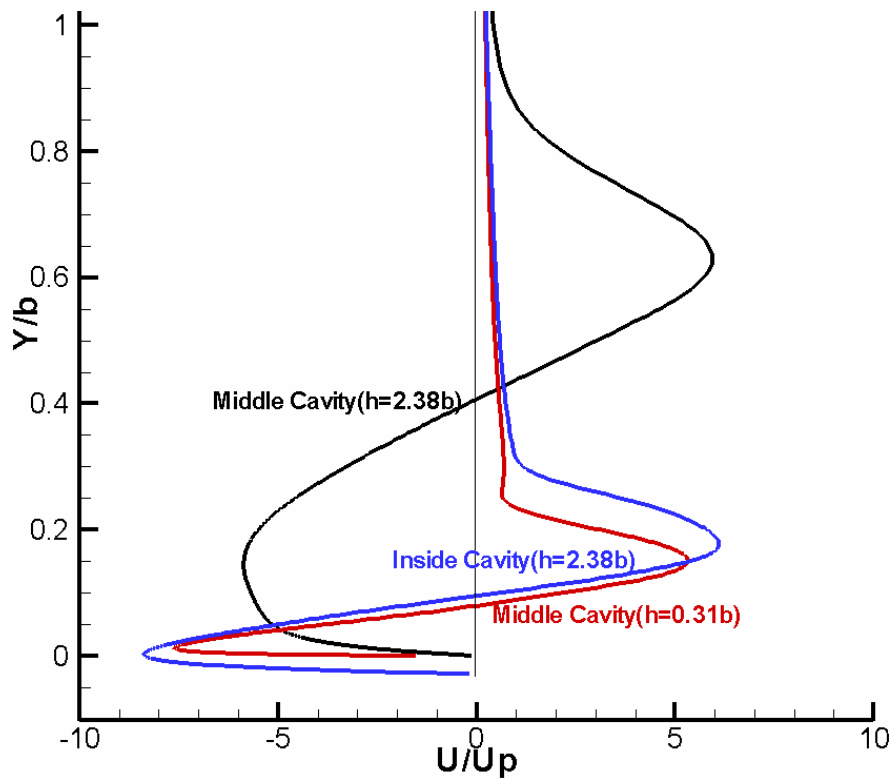


Figure 4.6 Comparison of velocity profiles through the center of the vortex

In Table 4.5 the net flow rate through the gaps is compared with the flow pushed by the plate at two time instances during the oscillation when the plate is at its maximum speed. The net flow rate through the gaps is perfectly similar to the flow pushed by the plate. Only a difference of less than 0.2% exists.

Table 4.5 Comparison of flow rates through the gaps

Cavity Depth	Phase	Plate $m^3/s(10^{-3})$	Narrow Gap $m^3/s(10^{-3})$	Wide Gap $m^3/s(10^{-3})$	Total $m^3/s(10^{-3})$
2.38b	180	-2.1808	0.1529918	2.024412	2.177404
	360	2.1808	-0.1047478	-2.075795	-2.180543
2.38b(inside)	180	-2.1808	0.1477406	2.029861	2.177601
	360	2.1808	-0.122695	-2.060006	-2.182701
0.31b	180	-2.1808	0.1808748	1.997389	2.178264
	360	2.1808	-0.1448068	-2.037657	-2.182464

An overview of the maximal vertical velocities in the center of the narrow and the wide gaps is given in Table 4.6 together with the respective time phases when

these maxima occur. Here, we observe that the velocity magnitudes of the maximal suction in the narrow gap slightly increase with moving the plate inside the cavity (case 2.2 and case 2.4). The phase of the maximum is not affected by moving the plate mean position, it occurs $130 - 135^\circ$ after the maximal downward velocity of the actuator plate. The same phase shift occurs for the blowing cycle's maximum in the narrow gap. This large phase shift is due to the unsteady viscous nature of the narrow-gap flow. The maximal blowing velocity is always greater than the suction velocity. As already shown in *Figure 4.5b* that the suction velocity in the narrow gap is higher for the case 2.4 but the blowing velocity is lower for this case. The flow at the wide gap is completely different, as already shown in the previous section. The flow here is more of a suction-pumping type that is merely pressure driven. This is demonstrated in the clearest way by the according phases given in *Table 4.6*. Changing the plate position has influence on these velocities as well. Both suction and blowing velocities increase with moving the plate inside the cavity. The phase at which velocity maxima exist is also affected with moving the plate inside the cavity and it is more significant for case 2.2 than for case 2.4.

Table 4.6 Comparison of maximum vertical velocities at the centers of the gaps

Case	Phase	Narrow gap		Wide gap	
		Velocity	Phase ($^\circ$)	Velocity	Phase ($^\circ$)
2.2	Suction	-8.1	310	-13.78	38
2.4		-9.248	315	-13.982	20
2.2	Blowing	10.96	132	17.554	240
2.4		8.407	136	18.672	202

Table 4.7 compares the maximum velocities in the narrow gap from the simulation computed from *Figure 4.5b* with theory for mixed plane *Poiseuille-Couette* flow in which the pressure difference between the upper and lower side of the plate is used from the simulation to calculate the velocity by using the formula given by White 1974 [14] at two phases with plate peak velocity, i.e. for the suction phase at $\theta = 360^\circ$ and the blowing phase at $\theta = 180^\circ$. It is observed that the suction phase is in excellent agreement with theory for both cases, which does not happen for the blowing phase because of the differences between 14 and 28% for case 2.2 and case 2.4, respectively. The reason for this difference is due to the asymmetry of the flow field with respect to the actuator plate. Minor differences of the flow through the wide gap may also contribute to this. Furthermore, in case 2.4 where the plate

moves completely inside the cavity, the difference is twice compared to case 2.2 where the plate moves in and out of the cavity.

Table 4.7 Comparison of instantaneous peak velocities in the narrow gap at mean plate position

Case	Motion of the plate	Δp (N/m ³)	Analytical max. vel. (m/s)	Simulation max. vel.(m/s)	% difference
2.2	upward	8278	-5.488	-5.752	4.3
	downward	16893	9.734	8.495	14
2.4	upward	10165	-6.637	-6.106	8.6
	downward	16479	9.487	7.389	28

With different cavity depths we have different vortex size outside the cavity and also with different plate positions the size of the vortex varies. As we are very close to the experimental results in case 2.2 ($h=2.38b$) therefore we can say that most probably Lachowicz et al. [18] in their experiments had investigated the setup of our case 2.2. Therefore for our further investigations we will take this cavity depth and plate position i.e. case 2.2 as a standard.

4.1.3 Summary

Results in the vortex mode of the JaVA were compared with the data available through Lachowicz et al. [18]. As we reduce the cavity depth the vortex size also reduces and ultimately for a very small cavity, this vortex converts to a very small one followed by a wall jet. Downward motion of the actuator leads to blowing and vice versa. The largest blowing velocity is obtained in case 2.3 for the shallowest cavity because the blowing rate increases with decreasing cavity depth. This is in contrast to the suction velocity where the velocity magnitude for case 2.2 is smaller than for the other two cases. When we move the plate inside the cavity the effect on the outer field is the same as reducing the cavity depth: we get a small vortex followed by a wall jet. The effect of the mean actuator position on the gap velocities is to slightly increase the blowing velocities with respect to the same case where the actuator is placed further above, which is again in large contrast to the observations in the suction phase, where the suction magnitude is considerably increased by placing the actuator inside the cavity.

4.2 Material properties study

In the previous sections we have finalized the cavity depth and plate position of case 2.2. Now in this case we perform simulations by changing the material properties in order to see the compressibility effects.

For this case the air density is changed from constant to an ideal gas and the same grid and the boundary conditions were used for this case as in the previous case. Contours of mean velocity magnitude are compared in *Figure 4.7*. As in the incompressible case, we get a big vortex from the wide gap along with a small vortex inside the cavity. The size of the “compressible” vortex is almost twice with slightly lower velocities. Another difference is that in this case the vortex is slightly further away from the actuator plate relative to the one obtained with the incompressible gas. There is no secondary vortex for this case like in case 2.2. Interestingly, this case is more like case 2.1 where we get a very big vortex with very long cavity.

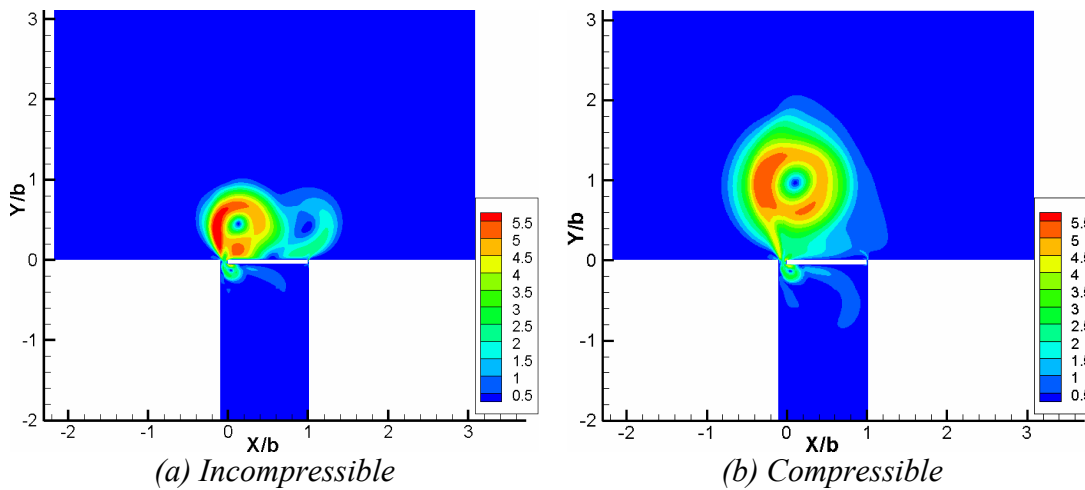


Figure 4.7 Contours of mean velocity magnitude

Similarly, *Figure 4.8* shows the contours of instantaneous velocity magnitude at four different time instances (two mean and two extreme plate positions). We can clearly see a very big vortex above the plate and a small vortex under the plate at the wide gap side. This vortex is present in all four time instances being strongest at $t=24.5T$ which corresponds to the blowing phase, i.e., the time instance of maximum plate velocity moving into the cavity. During each actuator cycle a pulse of high speed fluid ejects from the wide gap. This can be seen in subfigures (b) and (c). Each of these velocity pulses is a sign of a counter-rotating vortex pair that gets ejected from the wide gap at each cycle. With increasing distance from the orifice these pulses merge with the average flow field thus strengthening the outside vortex. This

can be seen in subfigure (d). The maximum velocity in the wide gap is more than $13U_p$ but in the vortex maximum the velocity is only $10U_p$ in the subfigure (a).

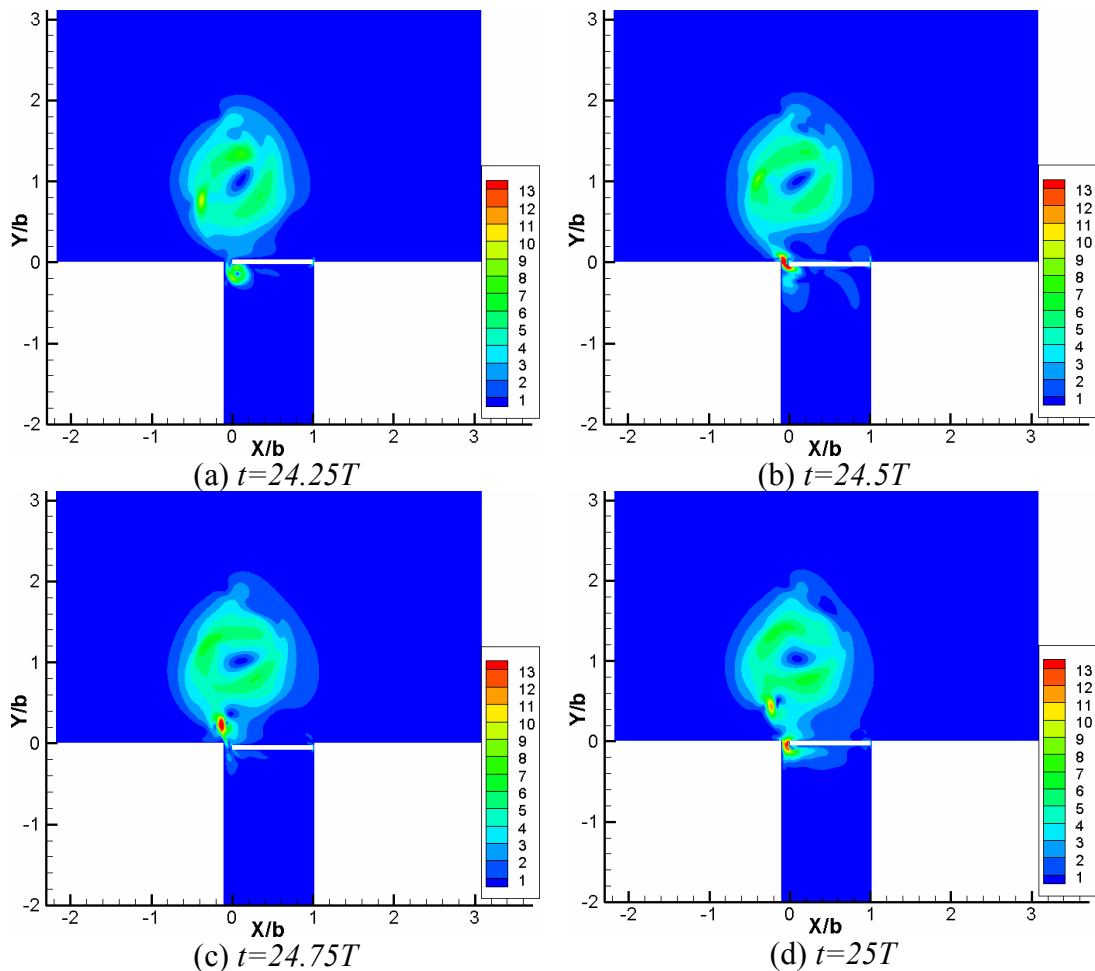


Figure 4.8 Contours of instantaneous velocity magnitude at four different time instances

Figure 4.9 (a) and (b) shows the comparison of instantaneous velocity profiles in the wide and narrow gaps respectively. There is no significant difference in the gap profiles for compressible and incompressible flow. In the wide gap velocity peaks are the same for both suction and blowing. The only difference is that in the blowing phase the velocity maxima slightly shift towards the left i.e. towards the cavity wall. While in the narrow gap the peak velocity during the blowing phase is slightly higher for the compressible case but for the suction phase the peak velocity is slightly lower than in the incompressible case.

Figure 4.10 shows a comparison of mean velocity profiles through the center of the vortex for the compressible and incompressible cases. In the compressible case we get a vortex that is almost 2.5 times bigger in size than the one we observed in the incompressible case. The vortex center in the present compressible case is at $0.97b$

above the plate while in the incompressible case it is at $0.41b$ above the plate. Maximum positive and negative velocities in the compressible case are smaller than in the incompressible case.

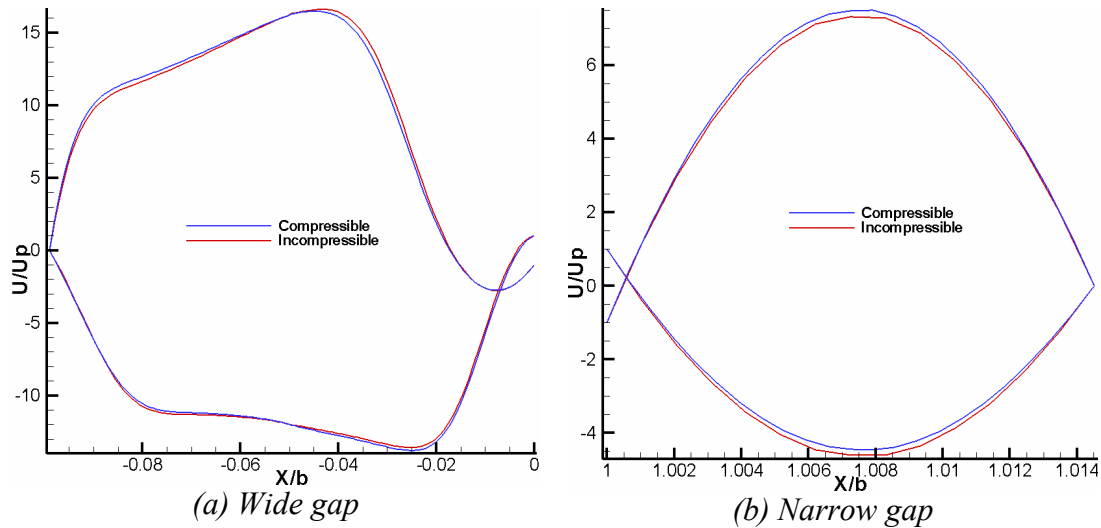


Figure 4.9 Comparison of gap profiles

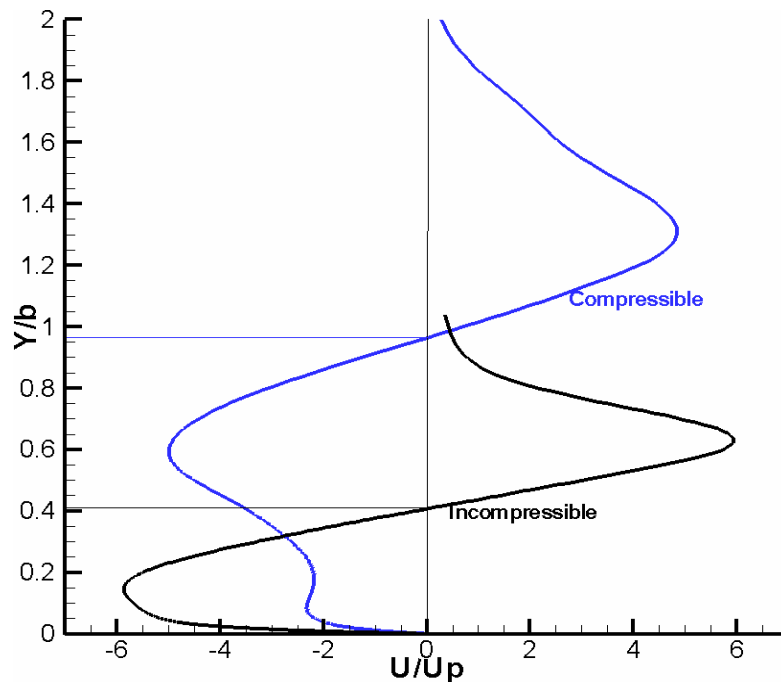


Figure 4.10 Comparison of velocity profiles through the vortex center

In Table 4.8 the net flow rate through the gaps is compared with the flow pushed by the plate at two time instances during the oscillation when the plate is at its maximum velocity. Again the net flow rate through the gaps is perfectly similar to the flow pushed by the plate. Only a difference of less than 0.2% exists. The change in density in the compressible case is only 0.000301 kg/m^3 , which is too small to be neglected.

Table 4.8 Comparison of flow rates through the gaps

Case	Phase	Plate $m^3/s(10^{-3})$	Narrow Gap $m^3/s(10^{-3})$	Wide Gap $m^3/s(10^{-3})$	Total $m^3/s(10^{-3})$
Incompressible	180	2.1809	0.1529918	2.024412	2.177404
	360	2.1809	-0.1047478	-2.075795	-2.180543
Compressible	180	2.1809	0.1534627	2.022304	2.175767
	360	2.1809	-0.08.8357	-2.101906	-2.190264

4.2.1 Summary

Results in the vortex mode of the JaVA for the compressible and incompressible cases were compared. Similar grid was used for both these cases and it was found that in the compressible case we get a vortex that is almost 2.5 times bigger in size than the one we observed in the incompressible case. The change in density in the compressible case is only 0.000301 kg/m^3 . In the wide gap during the blowing phase the velocity maxima slightly shift towards the cavity wall. In the narrow gap the peak velocity during the blowing phase is slightly higher but for the blowing phase it is slightly lower in the compressible case compared to the incompressible case. Although, in the compressible case density change is very small but the size of the vortex is very big in this case relative to the one obtained in incompressible case. The reason is that the compressible case is more grid sensitive compared to the incompressible case and we used same grid for both cases.

4.3 Flow parameters study

In the first section of this chapter we have studied effects of different geometry parameters like cavity depth and plate position with respect to the cavity wall by keeping one fixed and changing the other parameters and we concluded that our case 2.2 is the case studied by Lachowicz et al. [18]. We also studied the effects of compressible and incompressible flow in section 4.2. Now we will study the effects of changing the frequency and scaled amplitude again for the incompressible flow model.

4.3.1 Angled jet

In this case the simulation is performed at a lower frequency and scaled amplitude of 70Hz and 0.13 respectively. Results are compared with the same case of

Lachowicz et al. [18]. Note that there is no quantitative data available for this mode to compare the results with literature. For visualization of the *numerical* data in a way that is qualitatively comparable to the experimental flow visualizations we use *line-integral convolution* (LIC), invented by Cabral & Leedom, [1]. *Figure 4.11* shows contours of mean velocity magnitude after 25 oscillation periods of the plate. Results are averaged over the last four periods of oscillation. At relatively low Reynolds number ($Re = 58$) we get a superposition of a jet pointing away from the cavity and a clock-wise rotating vortex placed above the wide gap (see subfigure b) instead of an angled jet towards the plate in the experiments of Lachowicz et al. [18] (see subfigure a). The velocity magnitude contours (subfigure c) make clear that the oblique jet dominates over the vortex motion, which was not so clear in the previous figure. Thus, we basically now get an oblique jet pointing towards the left in this case. Moving the actuator plate somewhat into the cavity should hinder the jet from turning to the left, such that either a vertical jet or one that is inclined to the right will then occur. This would be in better agreement with the visualization in *Figure 4.11a*. It is not implausible to assume that a small mismatch of the actuator plate's mean position might have been present in the experiments (note, that according effects are not documented in the previous literature). *Figure 4.11d* shows the evolution of velocity traces versus time steps at the centers of the narrow and wide gaps for the last four complete periods for which time averaged results have been computed. The data shows an excellent periodicity of the results. The peak velocities both in the wide and in the narrow gap are much higher than the maximum velocity of the actuator plate (0.087 m/s). Multiplying the maximal plate velocity with the ratio of plate width "b" to sum of gap widths ($b/(W_w+W_n)$) yields a peak velocity of $8.81U_p$ which comes very close to the peak velocity of the narrow gap. Interestingly, the peak velocity in the wide gap turns out to be almost 1.5 times larger than the peak velocity in the narrow gap. Due to the closed cavity bottom all velocities have a positive mean and the positive peaks (blowing) are much stronger than the negative (suction) ones. Note that these velocities are at the centre of the gaps and *Figure 4.11d* does not cover the complete gaps width.

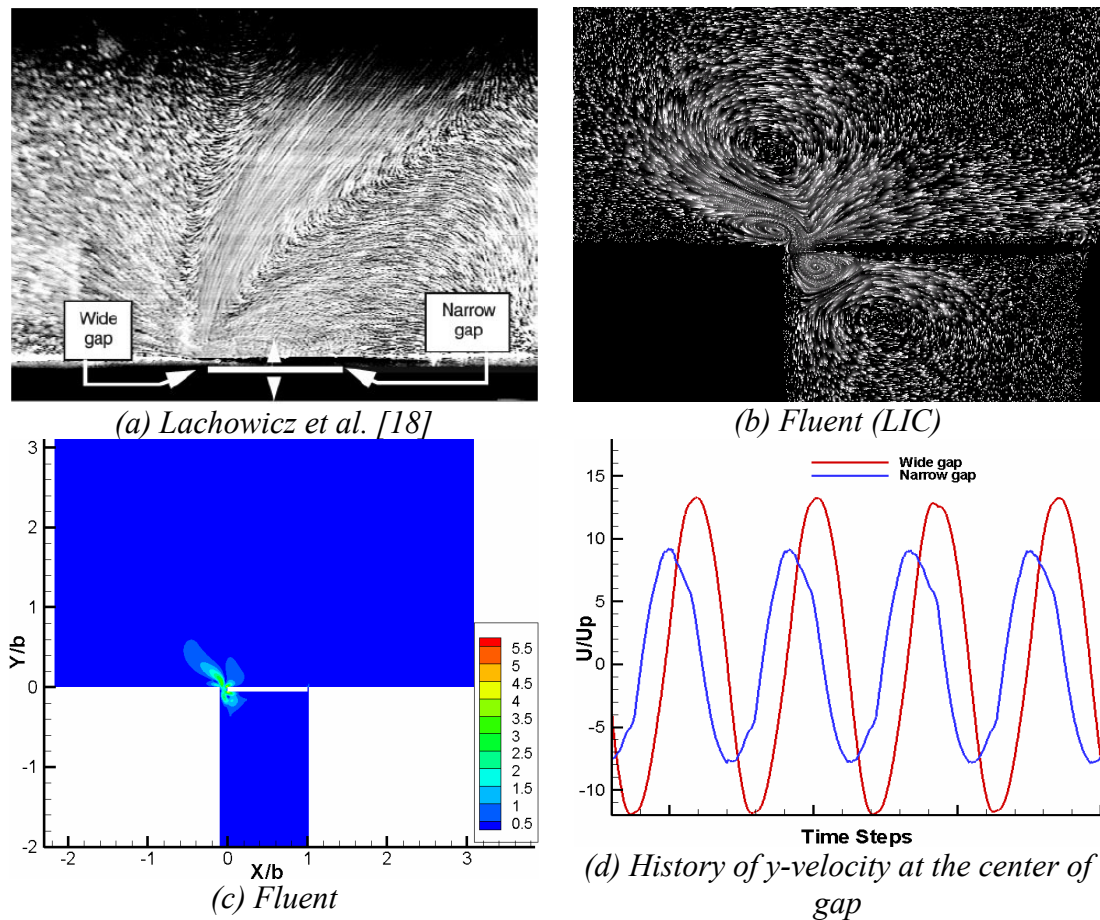


Figure 4.11 Contours of mean velocity magnitude and history at the center of the gaps

4.3.2 Free jet

This case is characterized by the same low frequency as in the previous case and by an increased scaled amplitude of 0.19. According to Lachowicz et al. [18], as the scaled amplitude increases at fixed frequency (i.e., increasing Re to 84), we get a free jet at the wide gap. In this case we get the same flow regime, i.e., a free jet from the wide gap as Lachowicz et al. [18]. So in this case we are extremely close to Lachowicz et al. [18] and this is shown in *Figure 4.12* which compares our results with the one published from the experiments. This may also be compared to the other experimental flow visualization depicted already in *Figure 4.11a* further above. All features which are observable there also appear in our numerical visualization. In addition, we also observe a small and a large vortex inside the cavity. Here, frequency and scaled amplitude are the same as those given in Lachowicz et al. [18] for their experiments. Thus, there is a very good agreement between the two results. Unfortunately, there is again no quantitative data available for this mode of actuator to compare the results in a more qualitative manner. Our quantitative information is

presented in *Figure 4.12c* using contours of instantaneous velocity magnitude. The results are averaged over the last four time periods. The velocity field confirms that we get a free jet from the wide gap which begins in vertical direction before it bends somewhat to the right. Continuing the simulation to later times, straightens the jet further, such that an inclined jet becomes clearer. *Figure 4.12d* shows the evolution of velocity traces versus time steps at the centers of the narrow and wide gaps for the last four complete periods for which time averaged results have been computed. The data shows an excellent periodicity of the results. The peak velocities both in the wide and in the narrow gap are much higher than the maximum velocity of the actuator plate (0.127 m/s). The peak velocity in the wide gap turns out to be almost 1.5 times larger. Due to the closed cavity bottom all velocities have a positive mean and the positive peaks are much stronger than the negative ones.

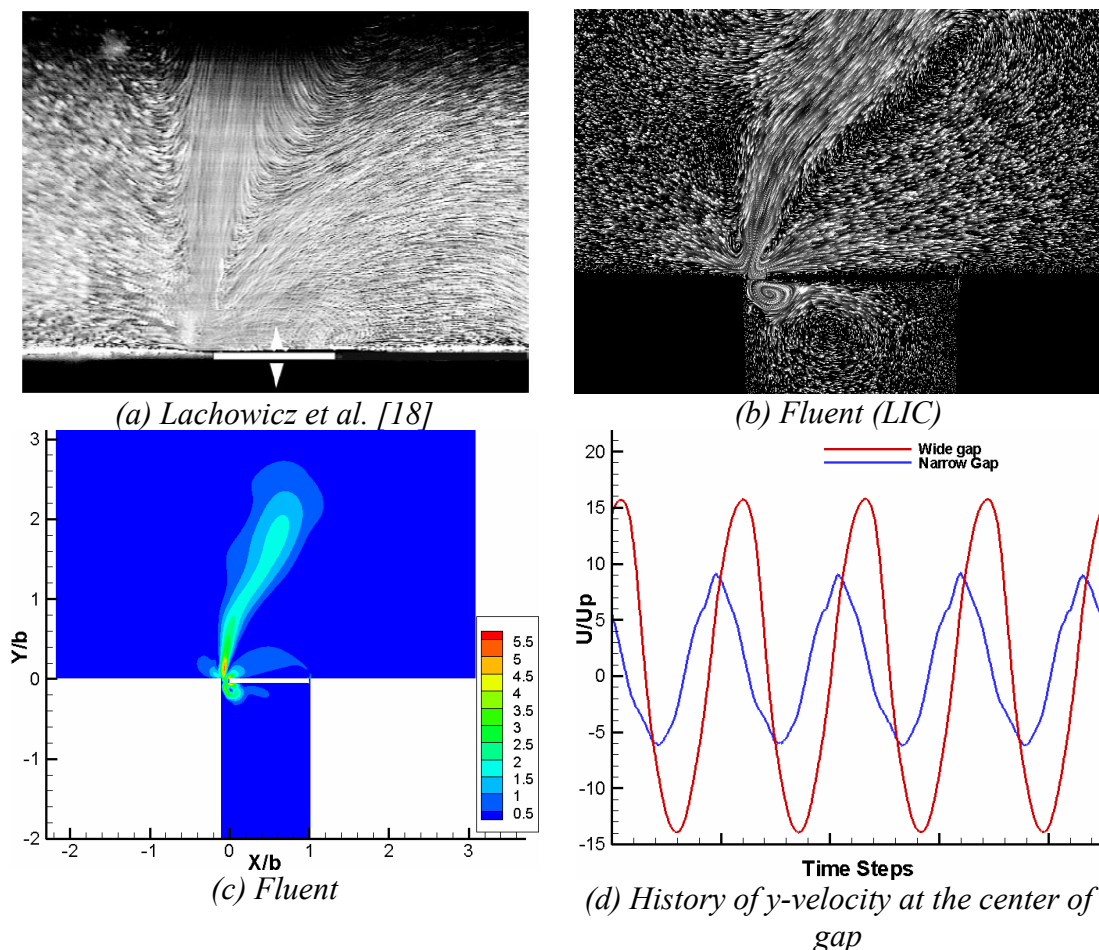


Figure 4.12 Contours of mean velocity magnitude and history at the center of the gaps

4.3.3 Wall jet

According to Lachowicz et al. [18] at low scaled amplitude and high frequency we should expect a wall jet pumping fluid from the wide gap to the narrow gap. Therefore, we increased the Reynolds number to 147 and the frequency to 210 Hz. With a scaled amplitude of $S_a=0.11$ we obtain $U_{max} = 0.224$ m/s for the maximal plate speed. In this case we get a wall jet from the wide to the narrow gap. So in this case again we get the same qualitative feature as observed by Lachowicz et al. [18] and this is shown in *Figure 4.13* where we compare the two averaged flow fields using LIC. A counter-clockwise rotating vortex sits above the narrow gap in both visualizations. In the experiment the flow towards the actuator on the left of the vortex appears clearer than in the numerical simulation but this is merely an effect of different integration times of the streamline segments. The next difference is that the wall jet in the experiment leaves the actuator region to the right while it leaves the wall in the simulation. Here, a continuation of the simulation could extend the jet further to the right.

Figure 4.13d shows the evolution of velocity traces versus time steps at the centers of the narrow and wide gaps for the last four complete periods for which time averaged results have been computed. The data shows an excellent periodicity of the results. The peak velocities both in the wide and in the narrow gap are much higher than the maximum velocity of the actuator plate (0.224m/s). Due to the closed cavity bottom all velocities have a positive mean and the positive peaks are much stronger than the negative ones. In this case narrow gap is more active compared to the previous cases and the difference of maximum velocities of the narrow and the wide gap is very small. The peak velocity in the wide gap turns out to be only 1.2 times larger.

Now we look at the flow in the gaps in more detail for all cases. In *Table 4.9* the total flow rate through the gaps is compared with the flow pushed by the plate at two time instances during the oscillation when the plate is at its maximum velocity. The flow rate through the gaps increases with increasing plate velocity as expected. However, in all cases the net flow rate is almost the same as the mass pushed by the plate.

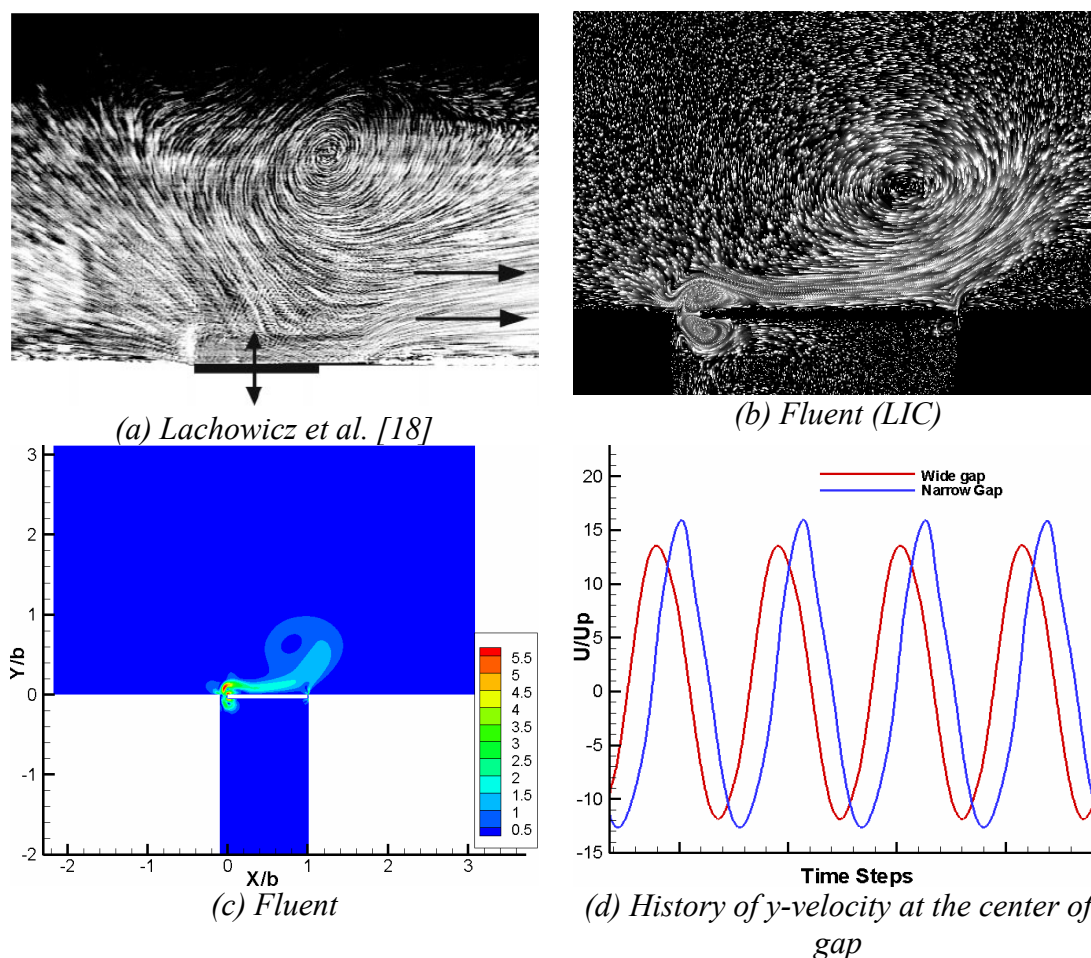


Figure 4.13 Contours of mean velocity magnitude and history at the center of the gaps

Table 4.9 Comparison of flow rates through the gaps

Case	Phase ($^{\circ}$)	Plate $m^3/s(10^{-3})$	Narrow Gap $m^3/s(10^{-3})$	Wide Gap $m^3/s(10^{-3})$	Total $m^3/s(10^{-3})$
Angled jet	180	-0.8488	0.04010971	0.8081999	0.8483097
	360	0.8488	-0.03411192	-0.814891	-0.8490029
Free Jet	180	-1.2308	0.06077965	1.170086	1.230865
	360	1.2308	-0.04540864	-1.185767	-1.231176
Wall Jet	180	-2.164	0.182783	1.98162	2.164403
	360	2.164	-0.1600584	-2.004879	-2.164938
Vortex	180	-2.18	0.1529918	2.024412	2.177404
	360	2.18	-0.1047478	-2.075795	-2.180543

As such, the flow fields in the narrow gap at the suction and blowing phases, i.e. when the actuator plate moves upward or downward through its mean position, respectively, are analyzed for the present cases in the same way as before for the vortex mode of operation in *Table 4.10*. The pressure difference over the narrow channel is extracted from the instantaneous pressure fields and inserted into the equation for plane *Poiseuille-Couette* flow in order to compute the maximal

instantaneous velocities. These analytical velocities are compared with those obtained in the simulation. As before in cases 2.6 and 2.7 there is an excellent agreement between the analytical and simulation velocities during the suction phase but for blowing, as usual, this difference is higher. As the Reynolds number increases, this difference also increases. In case 2.8 this difference is very high about 19 % but in this case the difference is the same for both suction and blowing phases. The wall jet must have an influence on the narrow gap because it moves over the gap.

Table 4.10 Comparison of instantaneous peak velocities in the narrow gap at mean plate position

Case	Motion of the plate	Δp (N/m ³)	Analytical max. vel. (m/s)	Simulation max. vel.(m/s)	% difference
2.6	upward	1923	-0.307	-0.31	1
	downward	2906	0.353	0.365	3.28
2.7	upward	3264	-0.51	-0.52	2
	downward	4652	0.57	0.65	12
2.8	upward	9999	-1.48	-1.8	17
	downward	12655	1.62	2	19

An overview of the maximal vertical velocities in the middle of the narrow and wide gaps is collected in *Table 4.11* together with the respective time phases when these maxima occur. Here we observe how the velocity magnitudes of the maximal suction in the narrow gap increase (case 2.6 through 2.8). However, the phase of the maximum is not affected in any of the above cases, despite the more than three-fold increase in velocity. It occurs $130 - 135^\circ$ after the maximal downward velocity of the actuator plate. The same phase shift occurs for the blowing cycle's maximum in the narrow gap. This large phase shift is due to the unsteady viscous nature of the narrow gap flow. The maximum blowing velocity is always greater than the suction velocity. The flow at the wide gap is completely different, as already shown in the previous velocity profiles. It is more of a suction-pumping type that is merely pressure driven. This is demonstrated in the clearest way by the according phases also included in *Table 4.11*. All velocity maxima occur only about 10° after occurrence of the according maximum actuator plate velocity ($\theta = 180^\circ$ for blowing, and $\theta = 0^\circ$ or 360° for suction). Changing the frequency and amplitude has almost no influence on these phases. As in the narrow gap, velocities increase with increasing frequency and amplitude.

Table 4.11 Comparison of maximal vertical velocities at the centre of the gaps

Case		Narrow gap		Wide gap	
		velocity (m/s)	phase (°)	velocity (m/s)	phase (°)
2.6	suction	-7.78	310	-11.7	11.25
2.7		-6.34	310	-13.93	11.25
2.8		-11.83	310	-12.66	11.25
2.6	blowing	9.09	130	12.82	190
2.7		12.83	130	15.83	190
2.8		13.55	135	15.89	187

4.4 Summary and conclusions

The purpose of the studies in the previous subsections was to perform a comparison with Lachowicz *et al.* for operation modes documented there and also see the effect of different parameters which were not documented in the literature. In the first and second sections of this chapter we took a case of vortex mode and checked the influence of cavity depth, plate position and density of fluid on the vortex size. We observed that by reducing the cavity depth the vortex size also reduces. Similarly by moving the plate inside the cavity the vortex size is reduced. But when we changed the fluid model from incompressible to compressible the vortex size is more than two times larger than for the same case with incompressible flow. Further, it is observed that in the wide gap the flow is more attached to the cavity wall and intensive reverse flow near the plate along with the velocity peak shifts towards the plate for the cases where we get a smaller vortex. In the narrow gap the general trend is that the blowing and suction velocities increase for the cases with smaller vortex but an exception is case 2.4 where the suction velocity is slightly lower than the same case with different plate position. For compressible and incompressible flows there is no significant difference in the gap profiles. In the third section we varied the flow parameters frequency and scaled amplitude and saw the influence upon the flow field. Here we took the same three cases (angled jet, free jet and wall jet) as by Lachowicz *et al.* [18] in their experiments. As already explained, that for these cases only some long-time-exposure flow visualizations that show mean-flow stream lines of the experiments, are available so we compared our flow field with these experimental flow fields. We get the same flow fields in these cases as Lachowicz *et al.* [18] in their experiments with the exception of angled jet case where our jet is in the opposite direction compared to Lachowicz *et al.* [18].

In Table 4.12 the maximum velocities in both gaps are compared to the maximal plate velocity $U_{max} = 2 \cdot \pi a \cdot f$ which is used for normalization of the gap velocities. Here the cases are arranged with respect to increasing U_{max} . The last column relates the velocities in the wide gap to those in the narrow one. Thus, it becomes clear how the gap flows are related to the plate speed. The general trend is that the wide gap has always more activity, as the ratio is always larger than 1. All the cases that produce a jet (i.e. case 2.6, 2.7 and 2.8) show increasing relative velocities in both gaps with increasing plate velocity. Despite a slightly larger U_{max} in the vortex mode, case 2.2, the gap velocities are considerably smaller there. However, the ratio between maximal wide-gap and maximal narrow-gap velocity is again higher in this case. There is no proportionality between this latter parameter and U_{max} . The relative speeds are more related to flow regimes than actuator speeds. The relative jet speeds at the exit of both gaps are eighteen times larger than the plate speed in some cases. This indicates that the present actuator works like a “fluid dynamical gear box” that significantly amplifies the motion of its mechanical parts. This is a general trend and also a welcome requirement for such devices, because this feature allows using micro electro-mechanical systems (MEMS) as mechanical actuator elements. Note that their amplitudes are usually small, such that a fluidic amplification is highly welcome to increase their impact. Further note that in case 2.2 and 2.8 the plate velocity is the same but due to different ratios of gap velocities and length of Stokes the flow regime is different.

Table 4.12 Comparison of maximum velocities in the gaps

Case	Plate velocity U_{max} (m/s)	Wide gap U_p	Narrow gap U_p	ratio (-)
2.6	-0.088	15.1	7.8	1.94
2.7	-0.127	15.4	6.3	2.42
2.8	-0.224	15.1	11.8	1.28
2.2	-0.226	13.0	7.1	1.83
2.6	0.088	13.6	9.1	1.50
2.7	0.127	15.2	12.8	1.18
2.8	0.224	17.8	13.5	1.31
2.2	0.226	16.8	10.2	1.65

In Figure 4.14, observed flow regimes are plotted with respect to Reynolds number and scaled amplitude $S_a = 2\pi a/b$ and compared with the results of Lachowicz et al. [18]. This comparison is a complete success! Note that no such detailed comparison is available in the open literature so far. However, the present unsteady

data offers much more insight and possibilities for an understanding of the reasons for these qualitative flow changes.

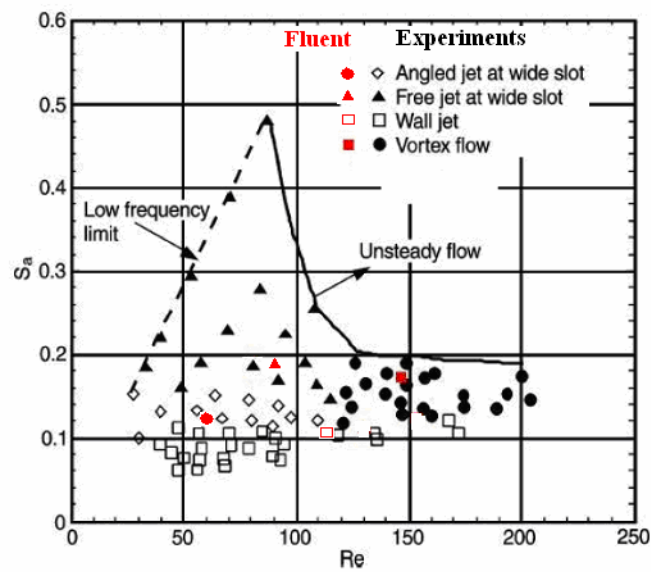


Figure 4.14 Comparison of experimentally observed flow regimes for non-dimensional wide gap width $g_w = 0.099$ according to Lachowicz et al. [18] with the present cases (Fluent)

5. Modified design

In the previous chapters our focus was on the validation of the simulation tool (Fluent) with experimental results of the original JaVA by Lachowicz et al. [18]. First an unsteady test case of the vortex mode of the JaVA with open cavity bottom and then with closed cavity bottom were studied. Variations of the actuator geometry and grid density have helped us to get an idea of the different fluid dynamical principles of the JaVA. Different modes of the actuator were studied and results were compared with experimental results by Lachowicz et al. [18].

In the present chapter we will suggest a modified design of the JaVA and will discuss in detail the flow fields for this design. The basic motivation to study the variation of the JaVA is to better understand its working principles. We will also discuss effect of different flow parameters, like frequency and scaled amplitude. In order to completely understand the mechanism of this modified JaVA system we will also discuss the relationship between different dimensionless parameters like Reynolds number, Stokes number and Strouhal number.

5.1 Geometry and grid distribution

The geometry and grid distribution for the modified design are shown in *Figure 5.1*. For this modified design two plates are used instead of one as in the original design. A horizontal but stationary one which closes the cavity at its top (flush with the surrounding wall such that it becomes part of the horizontal wall of cavity) and just leaves the wide and narrow gap open, as before. And a second one which is placed vertically inside the now closed cavity and oscillating towards the left and right which works like an oscillating piston pumping and sucking fluid periodically out and in through the gaps. Here, the motion in each gap is always in anti-phase to that in the other gap.

Since the cavity is now split into two parts with opposite flow rates (opposite signs but same magnitude) the flow through the narrow gap will become the more energetic one, and we can expect the narrow gap to take over a more decisive role compared to the original design. Also, the simultaneous suction at the wide gap that occurs while the narrow gap blows can be expected to ‘attract’ the fluid towards the actuator such that a counter-clockwise-rotating vortex might be formed. The horizontal plate has the same dimensions as in the original design while the vertical

actuator plate has a length of ‘ $1h$ ’ as this length is used to normalize all the lengths for this modified design. The wide and narrow gap widths are also kept the same as before. For this new actuator configuration once again we get different flow regimes (free jet, angled jet and vortex flow) but from the narrow gap. One advantage of this actuator is that it is more robust with respect to wear or contamination with dirt because it has no moving parts at the surface.

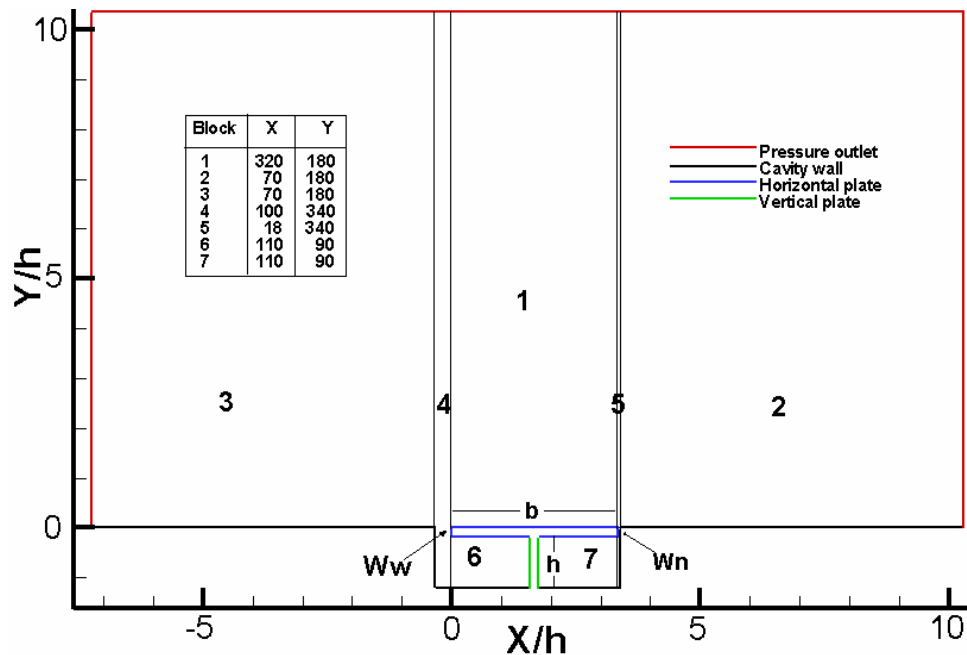


Figure 5.1 Geometry and grid distribution

5.2 Cases studied

In the following chapter we will discuss four different cases (3.1 -3. 4) with different flow regimes out of a large number of cases studied, see Table 5.1. In these four cases the narrow and wide gap widths are fixed to $0.04667h$ and $0.3183h$, respectively. The length of the horizontal plate is $b=3.21667h$ and the height of the oscillating vertical plate is ‘ h ’ which is the most important parameter in this design as it determines the flow rate through the gaps and thus the Reynolds number and the Stokes number upon which the flow field outside of the cavity depends. The scaled amplitude is now computed with the horizontal displacement ‘ a ’ and height ‘ h ’ of the vertical plate, see Table 5.1

Table 5.1 Different cases studied

Case	Frequency f (Hz)	Scaled amplitude $S_a = 2\pi a/h$	Reynolds no. $Re_{plate} = Up_{max} h/\nu$	Stokes no. $St = (2\pi f w_n^2/\nu)^{1/2}$	Flow Mode
3.1	128	0.589	46	1.04	vortex
3.2	128	0.441	35	1.04	angled (free) jet
3.3	128	0.294	23	1.04	vertical jet
3.4	128	1.1846	96	1.04	unsteady

In all four cases the oscillator frequency is fixed to $f = 128$ Hz and the scaled amplitude is varied from 0.294 to 1.18. Case 3.1 as before is for vortex flow as it is important in this case too because for fixed frequency if we increase the scaled amplitude in case 3.4 we don't get a fixed flow pattern but an unsteady vortex-shedding flow. But in contrast, if the scaled amplitude in case 3.2 decreases we get an angled jet and by further decreasing the scaled amplitude in case 3.3 we get a nice vertical jet. Now we will discuss all these cases in detail.

5.2.1 Case-3.1 Vortex flow

In this section we fixed the frequency and scaled amplitude to vortex mode and performed simulation with both compressible and incompressible material properties in order to see the effects of compressibility on the outer flow. Now we will discuss these one by one.

a. Incompressible vortex flow

In this section results are presented for simulations carried out at a scaled amplitude $S_a=0.589$ by keeping the density constant (incompressible). The maximum plate velocity is used to normalize all the velocities. The simulation was carried out for 25 periods of plate oscillation and results are averaged over the last four periods. *Figure 5.2* shows contours of mean velocity magnitude. As in this modified design one plate forces the flow through both gaps, the flow rate through both gaps must be the same. Due to this the narrow gap is more active compared to the wide gap. At this frequency and amplitude a very nice and big vortex is obtained from the narrow gap. A small vortex occurs inside the cavity because of the suction of flow into the right

part of the cavity. No significant activity can be observed at the wide gap side of the cavity. The maximum velocity in the vortex is $4.5U_p$.

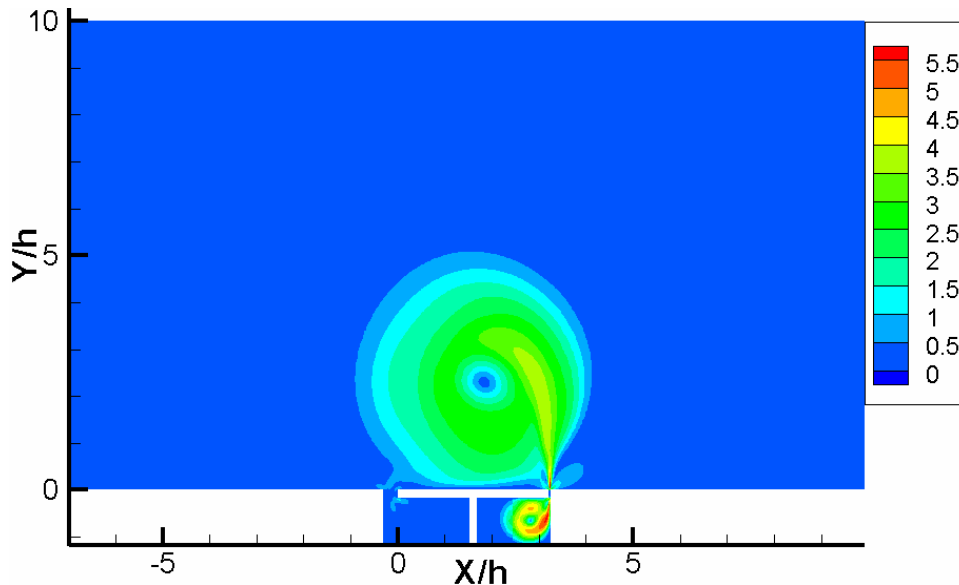


Figure 5.2 Contours of mean velocity magnitude

Figure 5.3 shows contours of instantaneous velocity at four different time instances during the 25th period of oscillation. Strong inner and outer vortices appear near the narrow gap. A big vortex is present in all four time instances being strongest at $t=24.75T$ and $t=25T$ which corresponds to the blowing phase. The maximum instantaneous velocity at the narrow gap in Figure 5.3d is more than $15U_p$ but the maximum velocity in the vortex is $5.0U_p$. Each actuator cycle ejects a pulse of high-speed fluid. These can be followed in the subfigures (a) through (d). Each velocity ‘pulse’ is a sign of a counter-rotating vortex pair that gets ejected from the narrow gap at each cycle. With increasing distance from the orifice these pulses merge with the average flow field thus strengthening the outside vortex, so this vortex becomes stronger and stronger with each period until $t=15T$ after which it stabilizes.

Figure 5.4 shows contours of instantaneous pressure at the same four time instances. There is no significant pressure disturbance in the outer field except at $t = 25T$. The pressure develops only inside the cavity or in the narrow gap. High pressure inside the cavity at different time shows the direction of the plate motion. When the plate is at its extreme left or right position there is no high pressure inside the cavity because the plate is almost at rest at this time instance and there is no significant flow at this time. Inside the cavities more pressure develops on the right side due to the small gap width.

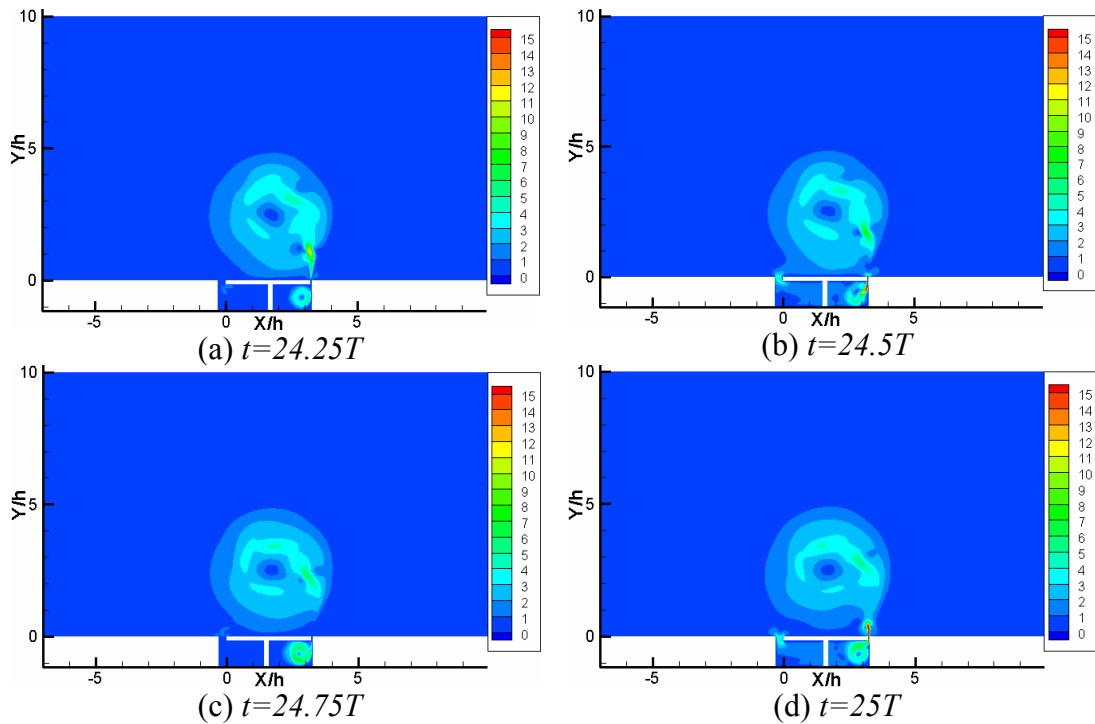


Figure 5.3 Contours of instantaneous velocity magnitude

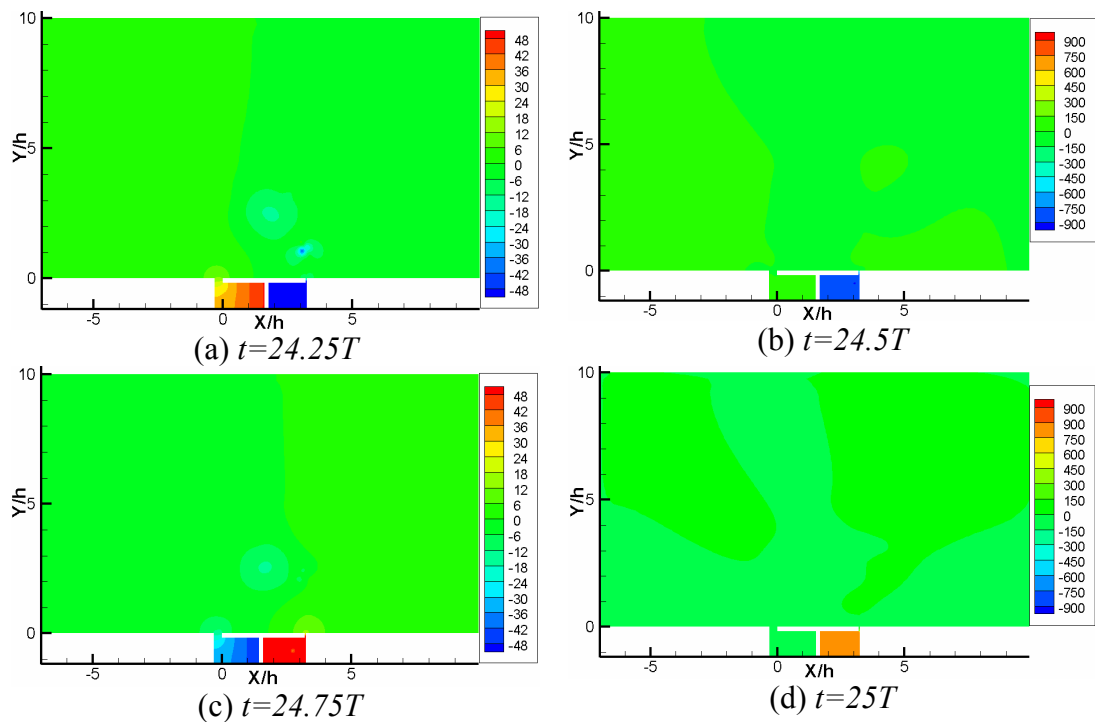


Figure 5.4 Contours of instantaneous pressure

Figure 5.5 shows contours of vorticity at eight different time instances. The large outer vortex is made up of consecutive vortex pairs which periodically detach from the jet orifice (narrow gap), one vortex pair per cycle. This is nicely illustrated by the opposite signs of vorticity belonging to each such pair. The left of these

vortices (red) merges with the main vortex above the plate (also red). In the velocity contours in Figure 5.3 each vortex pair generates a velocity maximum by induction, which is clearly visible in the instantaneous velocity contours. The small vortices follow each other in a circular motion around a common center.

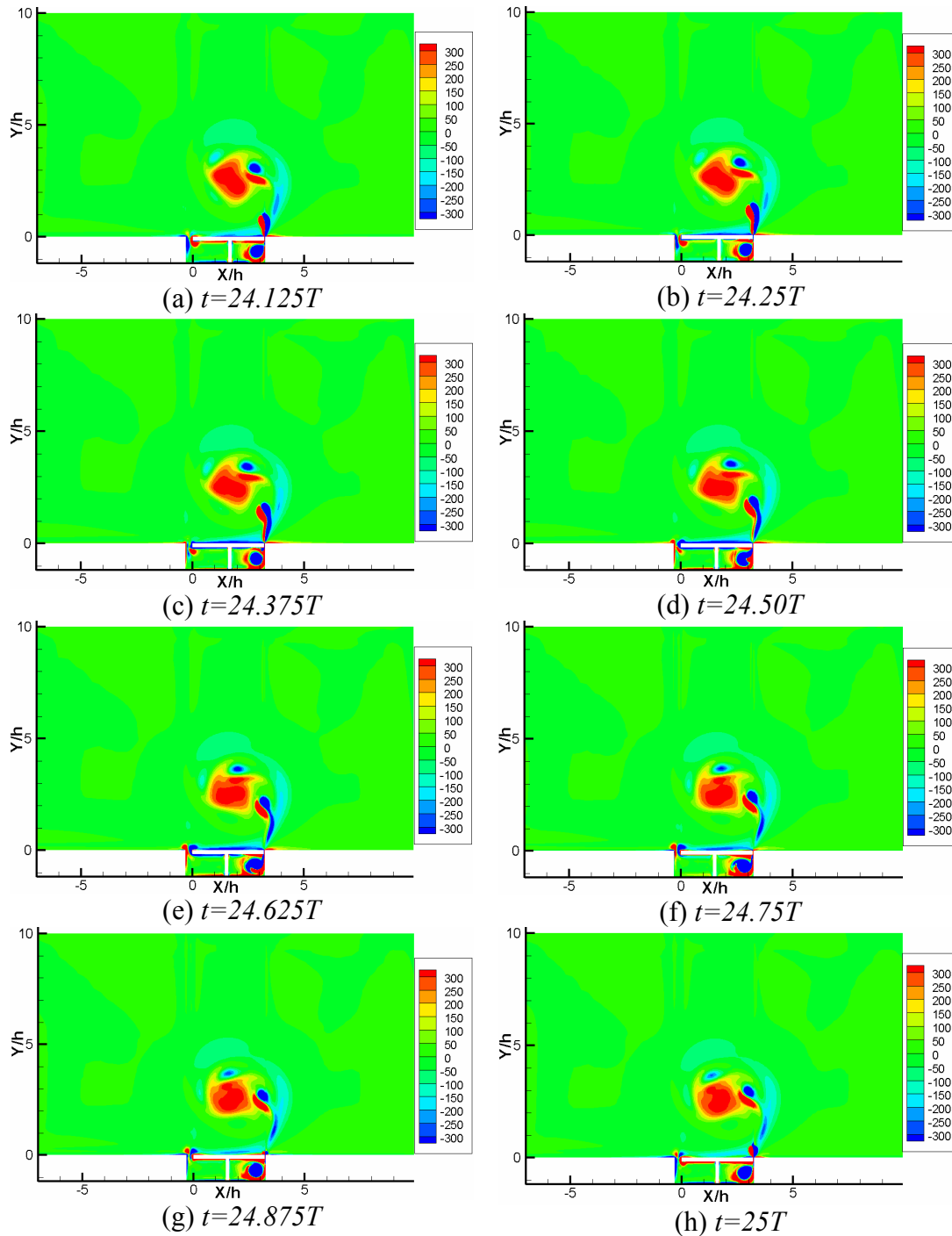


Figure 5.5 Contours of instantaneous vorticity magnitude

Figure 5.6 shows a zoom-in-view on the narrow gap with instantaneous velocity overlaid by velocity vectors and pressure contours at maximum plate velocities. In this figure we also include plots of instantaneous velocity in the center of the narrow gap for eight different time instances, for better comparison. From this figure we can see that a perfect oscillating Poiseuille flow develops in the narrow gap. This is expected, since the gap flow is now purely pressure driven (no relative motion of the side walls). Accordingly, there is no phase shift across the channel or with respect to the actuator motion, as can be observed in sub figure (b). We get maximum velocities at the same time instances when the plate is at its maximum velocity and at its mean position (i.e. at $\theta = 180^\circ$ and $\theta = 360^\circ$). Another contrast to the previous configurations is that the gap flow is now symmetric with respect to time.

The plots at phases $\theta = 90^\circ$ and $\theta = 270^\circ$ as well as those at $\theta = 45^\circ$ and $\theta = 315^\circ$ or and $\theta = 225^\circ$ are almost equal to each other. This indicates an almost perfect harmonic oscillation of the flow in the gap. This is a quite important observation. It means that there is no interaction of the outer fluid with the cavity, i.e., the narrow gap isolates the two from each other. Thus, in a numerical simulation of the outer flow region the action of a jet through a narrow gap can be safely specified as a velocity wall-boundary condition. This avoids the need to resolve the inner details of the actuator in such a situation. The according jets are nicely captured in Figure 5.6. Regardless of their direction the jets either extend far into the external field or far into the cavity. A counter rotating vortex pair is generated at the upper edge of the expelled jet.

In order to provide more insight into the narrow gap, plots are made at different heights in the narrow gap at two peak plate velocities in Figure 5.7. It can be observed that blowing and suction profiles are slightly different. It is because entrance and exit conditions are different for suction and blowing. The pink line during blowing and the red line during suction shows the entrance profiles which are different from each other due to different conditions. In case of suction, at all positions the profiles are symmetric and the same but in case of blowing as we move downward the velocity maximum slightly moves towards the cavity wall.

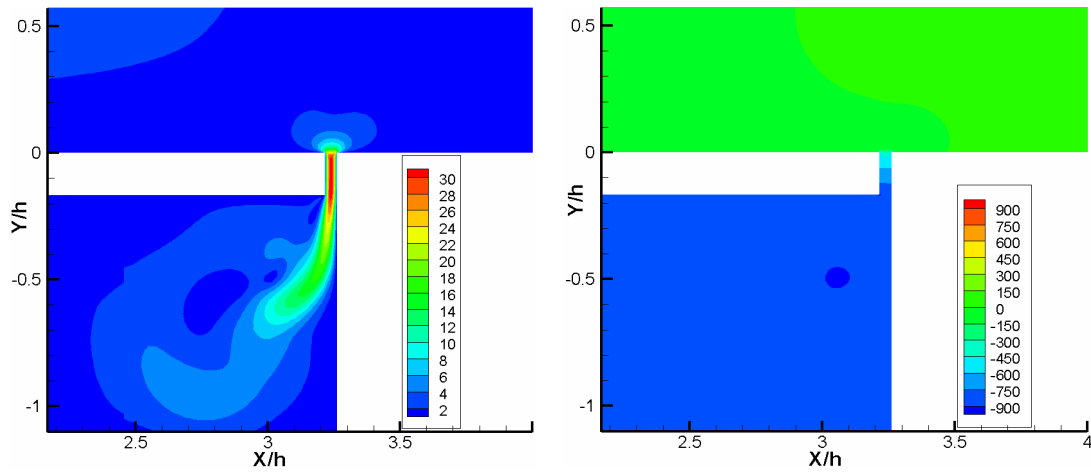
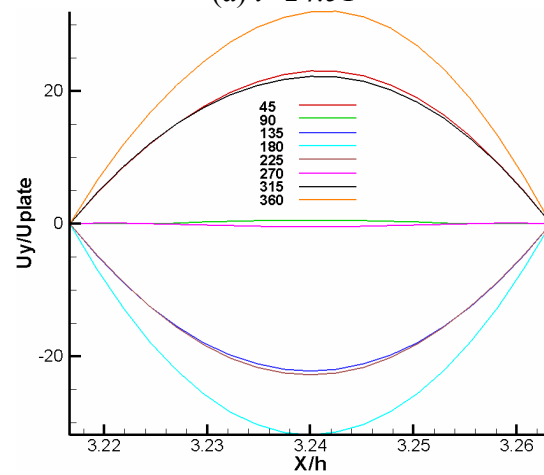
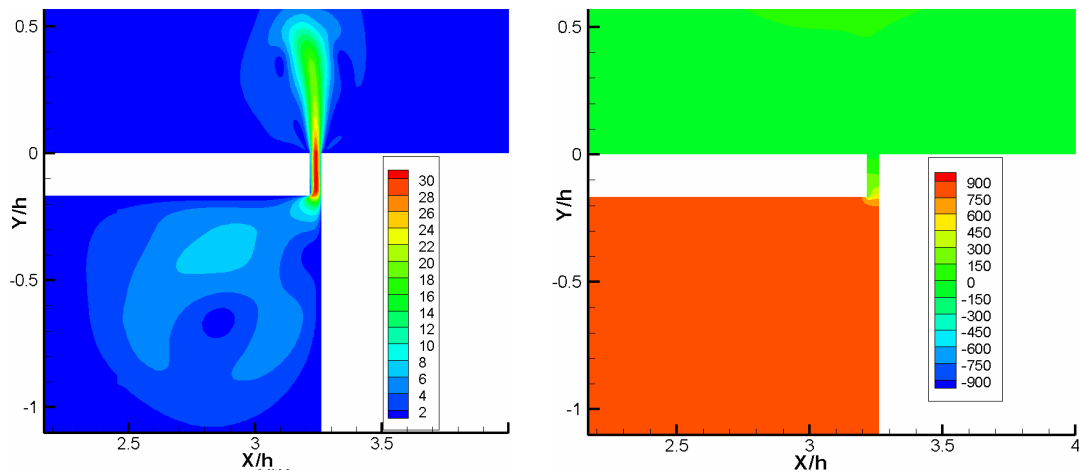
(a) $t=24.5T$ (b) Plot of y -velocity (m/s) in the narrow gap for various phases(c) $t=25T$

Figure 5.6 Contours of instantaneous velocity and pressure in the narrow gap

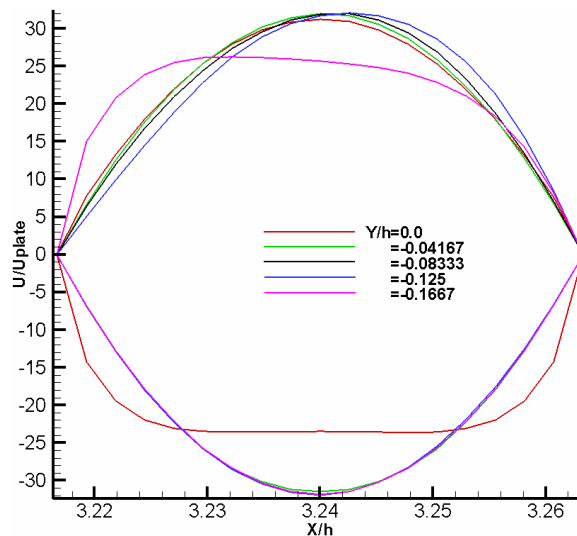
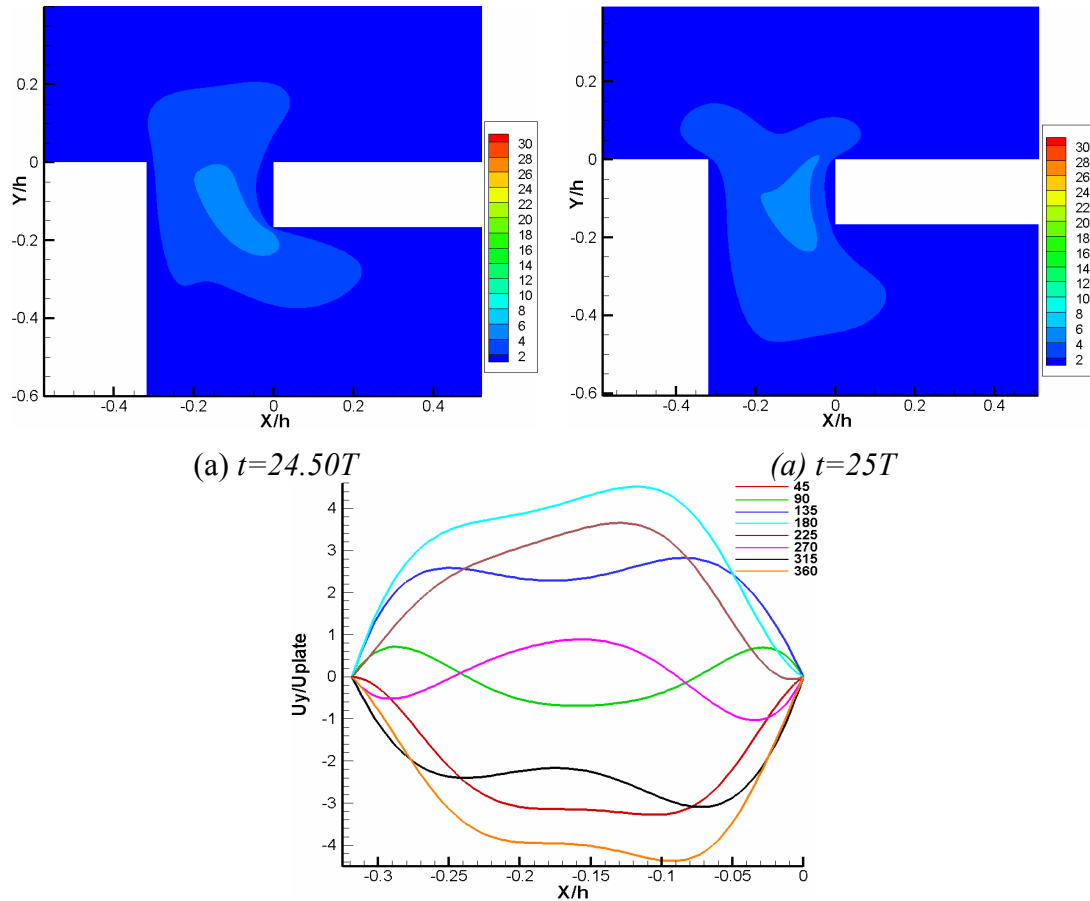


Figure 5.7 Instantaneous velocities in the narrow gap at different y -positions

The zoom into the wide gap in Figure 5.8 reveals that the velocity magnitudes are much smaller than in the narrow gap (4.5 vs. 32 i.e. 14%), the velocity profiles are no more symmetric with respect to time (max. suction and blowing velocities are -4.5 and 4.4, respectively), and the gap is so wide that a rather complicated flow develops. The gap flow is not symmetric with respect to its center line and at the phases where the actuator plate is at rest ($\theta = 90^\circ$ and $\theta = 270^\circ$) there is simultaneous in and outflow over the gap. This occurs in such a way that the higher momentum fluid in the center continues to follow the previous actuator motion, i.e. inwards for $\theta = 90^\circ$ while the low momentum fluid at the walls goes in opposite direction in order to fulfill continuity.

In the Table 5.2 we tried to compare flow rates through the gap with those pushed by the plate at eight different phases of 25th period. We see that the flow through the gaps is absolutely the same which is pushed by the plate at all time instances. The small difference would be numerical error. Therefore, we can say here that there is no leakage from the gaps; the same amount of fluid pushed or sucked alternatively from the gaps equals the one which is pushed by the plate.



(b) Plot of y-velocity (m/s) in the wide gap for various phases
 Figure 5.8 Contours of instantaneous velocity and pressure in the narrow gap

Table 5.2 Comparison of flow rate through the gaps

Phase	Plate	Wide gap	Narrow gap	Net
0	0.0587	-0.0587	0.0587	$1.551e^{-8}$
45	0.0415	-0.04187	0.0419	$9.240e^{-7}$
90	0	$-4.886e^{-4}$	$4.876e^{-4}$	$-9.763e^{-7}$
135	-0.0415	0.0412	-0.0411	$1.009e^{-4}$
180	-0.0587	-0.0587	-0.0587	$2.739e^{-6}$
225	-0.0415	0.0419	-0.0417	$2.086e^{-4}$
270	0	$5.333e^{-4}$	$-5.328e^{-4}$	$-5.603e^{-7}$
315	0.0415	0.0411	0.0410	$-1.68e^{-4}$
360	0.0587	0.0587	0.0587	$4.175e^{-7}$

b. Compressible vortex flow

This simulation is performed by changing the material properties in order to see the compressibility effects. All the parameters are kept the same, only the air density is changed from constant to ideal gas. In this case as in incompressible case we get a big vortex from the narrow gap along with a small vortex inside the cavity. The size of the vortex is almost the same with slightly lower velocities. Contours of mean

velocity magnitude are shown in Figure 5.9. Another difference is that in this case the vortex is slightly away from the actuator plate relative to the one obtained with the incompressible case.

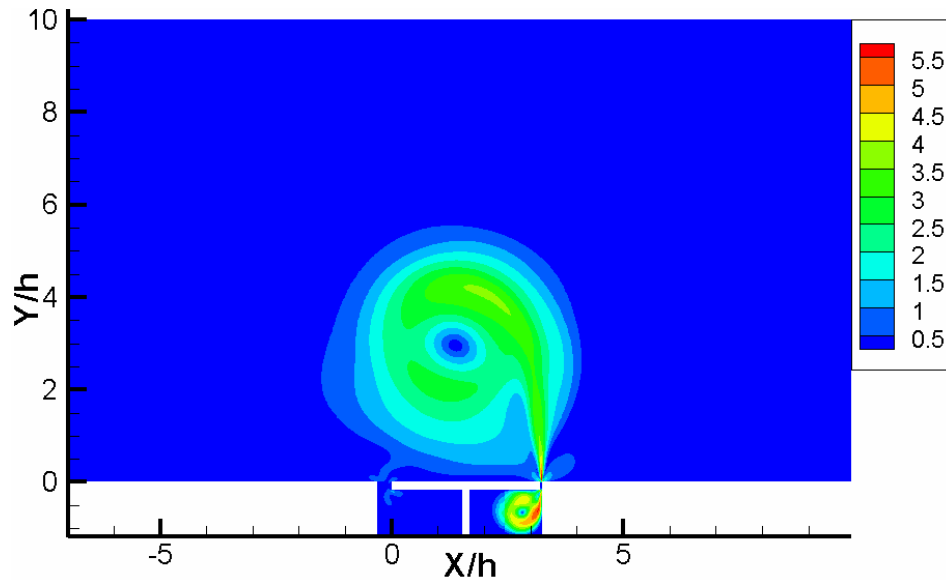


Figure 5.9 Contours of mean velocity magnitude

Similarly, Figure 5.10 shows the contours of velocity magnitude at four different time instances (two mean and two extreme plate positions). We can clearly see a very big vortex above the plate and a small vortex under the plate at the narrow-gap side. This vortex is present in all four time instances being strongest at $t=25T$ which corresponds to the blowing phase, i.e., the time instance of maximum plate velocity moving towards the narrow gap. During each actuator cycle a pulse of high speed fluid ejects from the narrow gap. This can be seen in subfigures (a) and (d). Each of these velocity pulses is a sign of a counter-rotating vortex pair that gets ejected from the wide gap at each cycle. With increasing distance from the orifice these pulses merge with the average flow field thus strengthen the outside vortex. This can be seen in subfigure (d). The maximum velocity in the narrow gap is more than $15U_p$ and the average velocity in the jet emerges from the narrow gap is $15U_p$. The maximum velocity in the vortex is only $3.2U_p$ in subfigure (a) and this is slightly lower than in the incompressible case where the maximum velocity was $4U_p$.

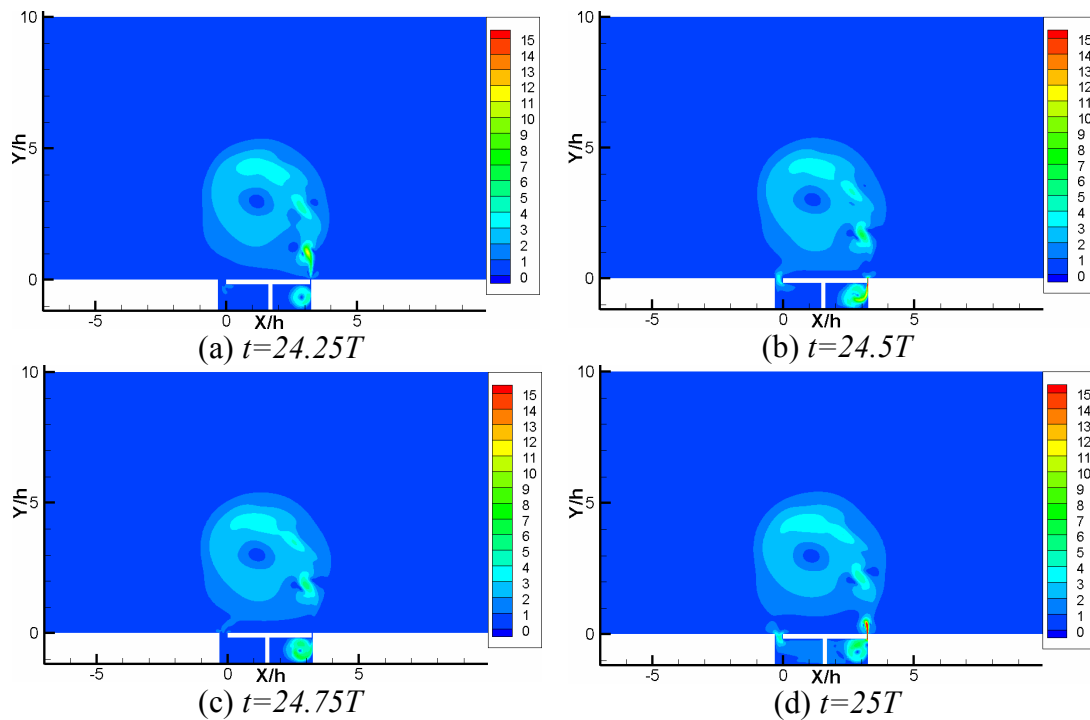


Figure 5.10 Contours of instantaneous velocity magnitude at four different time instances during last oscillation period

Figure 5.11a shows contours of Mach number at two time instances when the plate is at maximum speed. The Mach number is very small showing that there is no significant compressibility. This is further confirmed from subfigure (b) which shows contours of density at the same two time instances. Slight changes in density show that there is only a very small effect on the flow by changing from incompressible to compressible conditions. Due to this small effect the vortex size in this case is slightly bigger but this is so negligible that we can easily consider this case as incompressible.

Figure 5.12 (a) and (b) shows the comparison of instantaneous velocity profiles in the wide and narrow gaps, respectively. There is no significant difference in the narrow gap profiles while in the wide gap the velocity peak during the suction is slightly higher and it is also shifted toward the plate compared to the incompressible case.

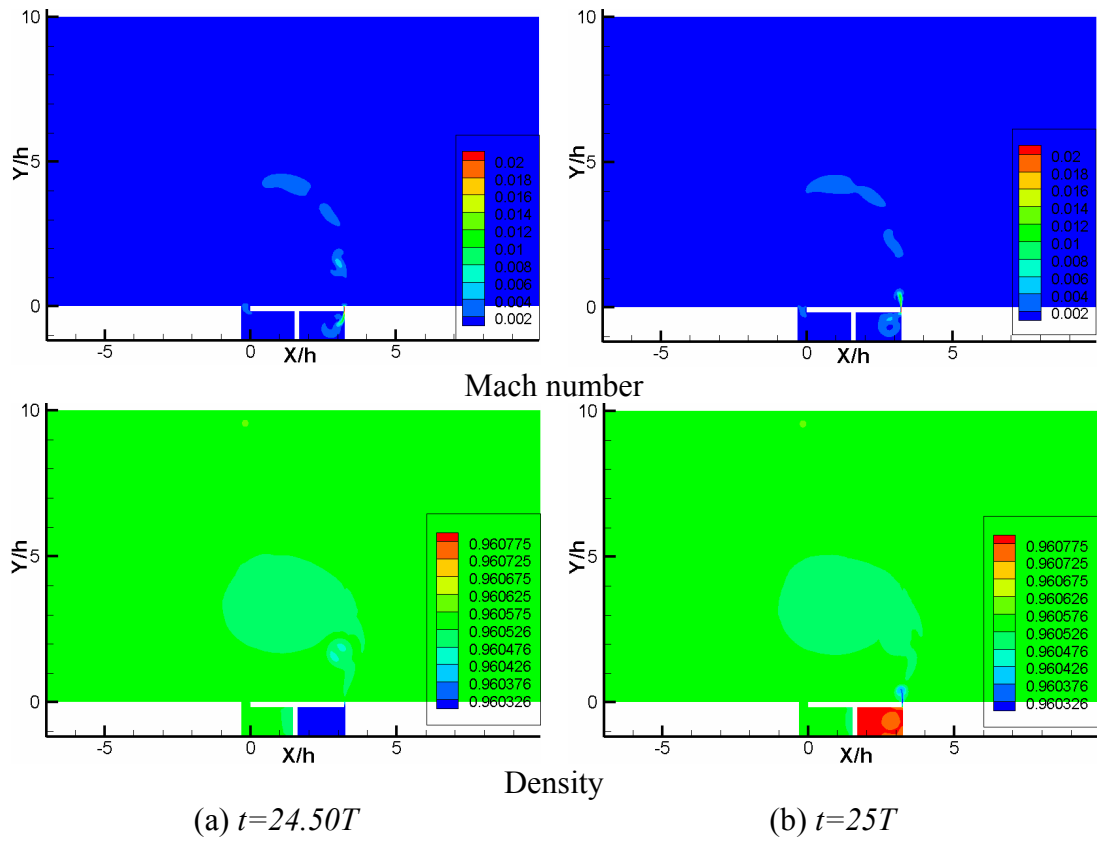


Figure 5.11 Contours of Mach number and Density

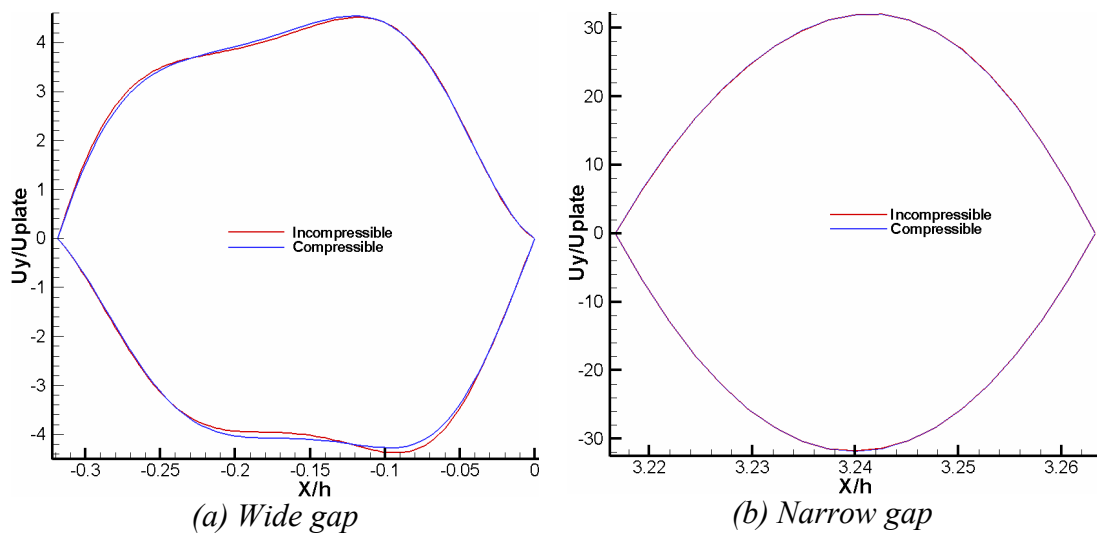
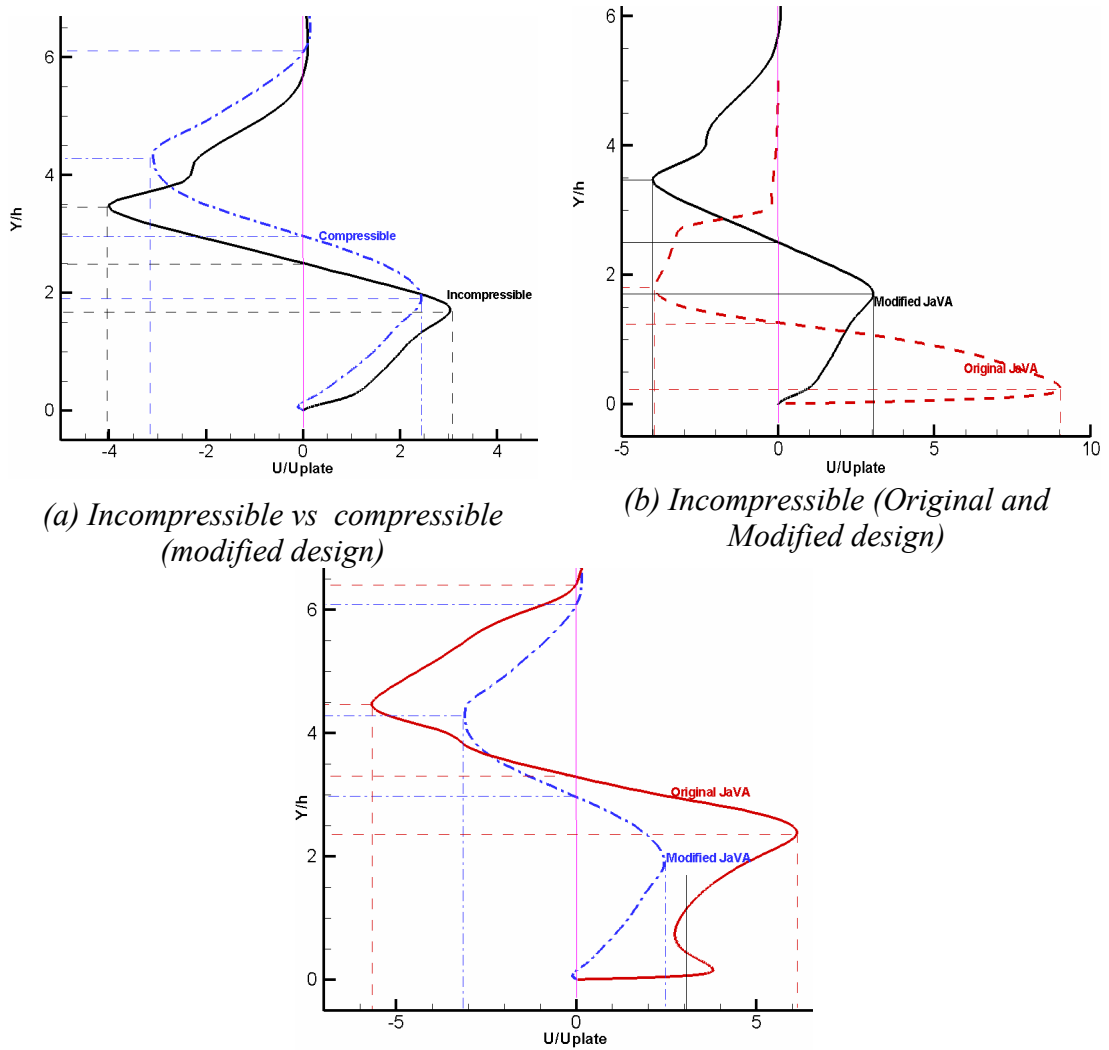


Figure 5.12 Comparison of gap profiles

c. Comparison of compressible and incompressible flow

In order to provide a quantitative assessment of the vortex strength and a comparison with the one produced in the vortex mode of the original JaVA *Figure 5.13* shows a plot of the velocity profile through the center of the vortex and perpendicular to the upper plate. Note that for comparison we have non-dimensionalize all profiles with the same parameter (i.e. plate height h) furthermore we have multiplied the velocities of the original design by -1 , so that we have negative (suction) and positive (blowing) velocities on the same direction, which means close to the axes we have positive velocities and away from the axes we have negative velocities.

In *Figure 5.13a* compressible and incompressible profiles for the modified design are compared. The size of the vortex is almost the same but for the incompressible case the vortex is closer to the actuator plate. The center of the vortex is at a height of $2.5h$ where as for the compressible case the vortex center is at $2.95h$. Maximum and minimum velocities for the incompressible vortex are also higher. The maximum suction and blowing velocities are $2.9U_p$ and $4.0U_p$ for the incompressible vortex in comparison to $2.4U_o$ and $3.2U_p$ for the compressible vortex respectively. The incompressible vortex is stronger and closer to the actuator plate. In *Figure 5.13b* profiles for the original and modified design are compared for the incompressible cases. The vortex in the modified design is bigger and weaker compared to the one obtained in the original design. For the incompressible case, see *Figure 5.13b* the size of the vortex is almost twice compared to the original design. Comparing velocities, the maximum suction velocity is $3U_p$ and the blowing velocity is $4U_p$ whereas in the original design the positive velocity is $9U_p$ and the negative velocity is $4U_p$. This is an interesting finding that in the original design the suction velocity is higher than the blowing velocity in contrast to the modified design where the blowing velocity is higher than the suction velocity. The possible reason would be the size of the cavity as in the modified case the cavity is divided into two parts, therefore the suction capacity decreases compared to the original design. Blowing velocities in both cases are the same. The center of the vortex for the present case is at $1.7h$ but for the original design where the vortex is small its center is closer to the actuator plate at $0.2h$. In *Figure 5.13c* profiles for original and modified design are compared for the compressible cases. The vortex is almost same for both the cases. The vortex suction and blowing velocities are lower in the modified design.



(a) Incompressible vs compressible (modified design)

(b) Incompressible (Original and Modified design)

(c) Compressible (Original and Modified design)

Figure 5.13 Velocity profile comparison through the vortex center

d. Summary

Results in the vortex mode of the modified JaVA for the compressible and incompressible cases were compared. Similar grid was used for both these cases and it was found that in the compressible case the size of the vortex is slightly bigger with velocities on the lower side. The change in density in the compressible case is only 0.000517 kg/m^3 . Because the difference in the vortex size and velocities for both the compressible and incompressible cases in the modified JaVA is very small, we can consider this case as an incompressible case.

5.2.2 Case 3.2 Angled (free) jet

In this case the scaled amplitude is decreased to $Sa = 0.441$ and the maximum plate velocity is 0.169 m/s which is again used to normalize velocities in this case. The relative importance of jet and vortex in the outer flow becomes again more apparent in the mean-velocity contours in Figure 5.14. In subfigure (a) at this relatively low actuator amplitude we get an angled jet from the narrow gap with a maximum mean velocity of $5U_p$ together with a weaker vortex but if we continue our simulation to some longer time this angled jet slowly converts into a vertical jet see subfigure (b). The fact that we initially get a vortex indicates that by slightly increasing amplitude we might be able to drive the actuator into the vortex mode but due to lower amplitude instead it convert into a vertical jet.

Figure 5.15 shows contours of instantaneous velocity at four different time instances during the 25th period of oscillation. In all time instances the jet is present. The strongest expulsion through the narrow gap occurs at $t=52T$ when the actuator plate is at its maximum positive velocity. Each actuator cycle ejects a pulse of high-speed fluid. Three such vortex pairs are present. One is just about to be formed above the orifice, and two others from the previous cycles. Their intensity rapidly decays as they travel their way. With increasing distance from the jet orifice these pulses merge with the average flow field. The high velocity fluid above the wide gap exists due to the fact that first it was an angled jet and afterward it straightens up and converts into a free jet.

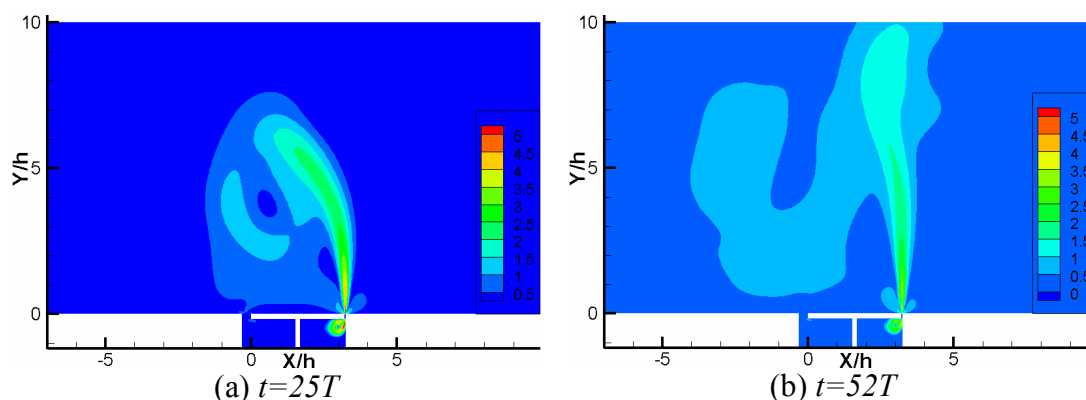


Figure 5.14 Contours of mean velocity magnitude

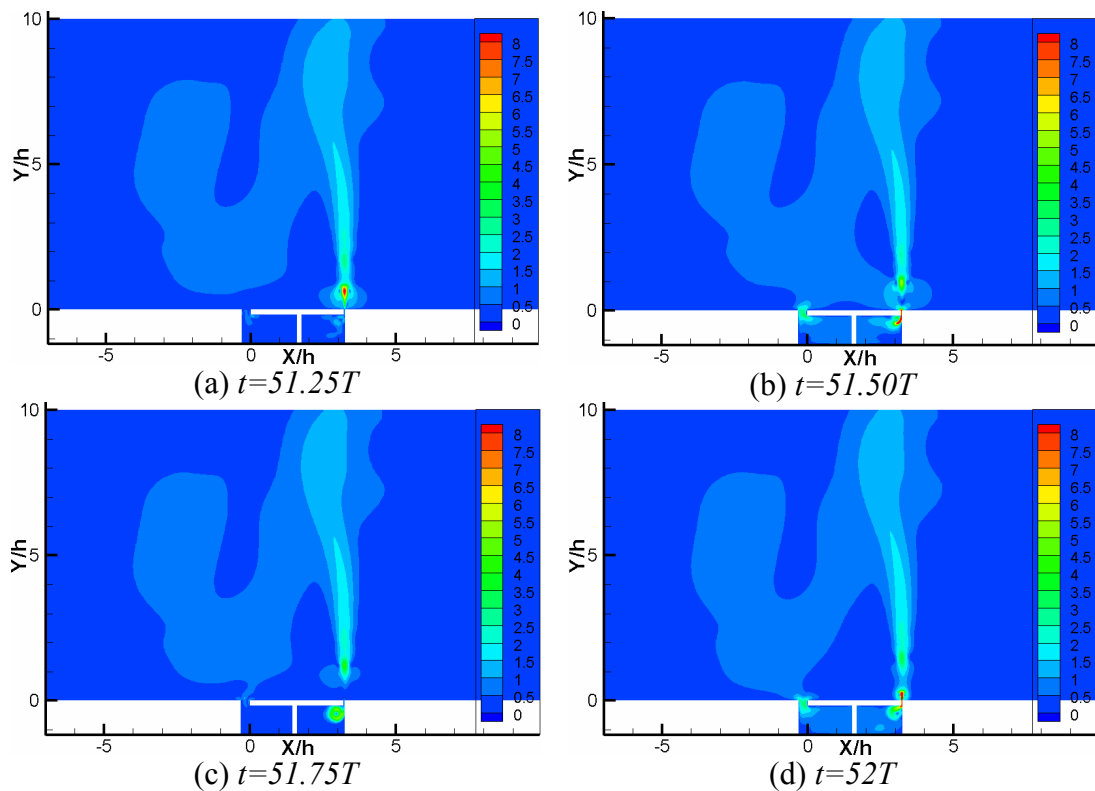


Figure 5.15 Contours of instantaneous velocity magnitude

5.2.3 Case 3.3 Vertical jet

This case is characterized by a frequency of 128Hz and scaled amplitude of $Sa = 0.294$ with a maximum plate velocity of 0.113 m/s again used to normalize all velocities. The simulations were run over 52 periods of oscillation such that time averaged results could be computed over the last 2 periods and instantaneous data became available for various phases of the actuator motion.

Figure 5.16 shows the contours of mean velocity magnitude. At this low amplitude we get a nice vertical jet at the narrow gap that is almost symmetric with a recirculation on each side that brings the fluid back towards the wall. A small vortex occurs inside the cavity because of the suction of flow into the right part of the cavity. Note that the jet would reach farther out when the simulation were continued beyond the 52nd oscillation cycle. No significant activity can be observed at the wide gap side of the cavity. Figure 5.17 shows contours of instantaneous velocity at four different time instances during the 52nd period of oscillation. The jet is present in all four time instances being strongest at $t=52T$ which corresponds to the blowing phase, i.e., the time instant of maximum plate velocity. Outside the cavity the jet velocity is rather constant, i.e. independent from the cavity flow. The latter shows alternating activity in the suction and blowing phases at $t=51.5T$ and $t=52T$. Two subsequent

velocity maxima are generated by blowing through the narrow gap. The inclination of the jet as well as its extent into the outer fluid is only very weak for the present set of parameters.

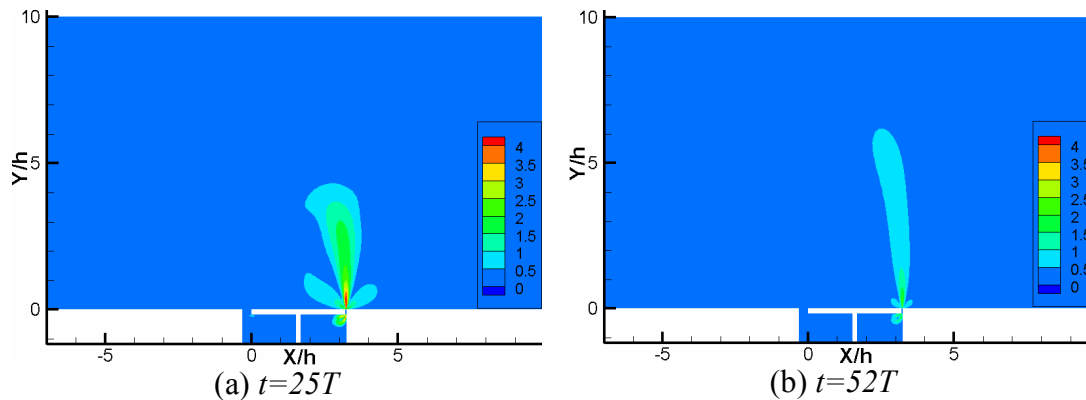


Figure 5.16 Contours of mean velocity magnitude

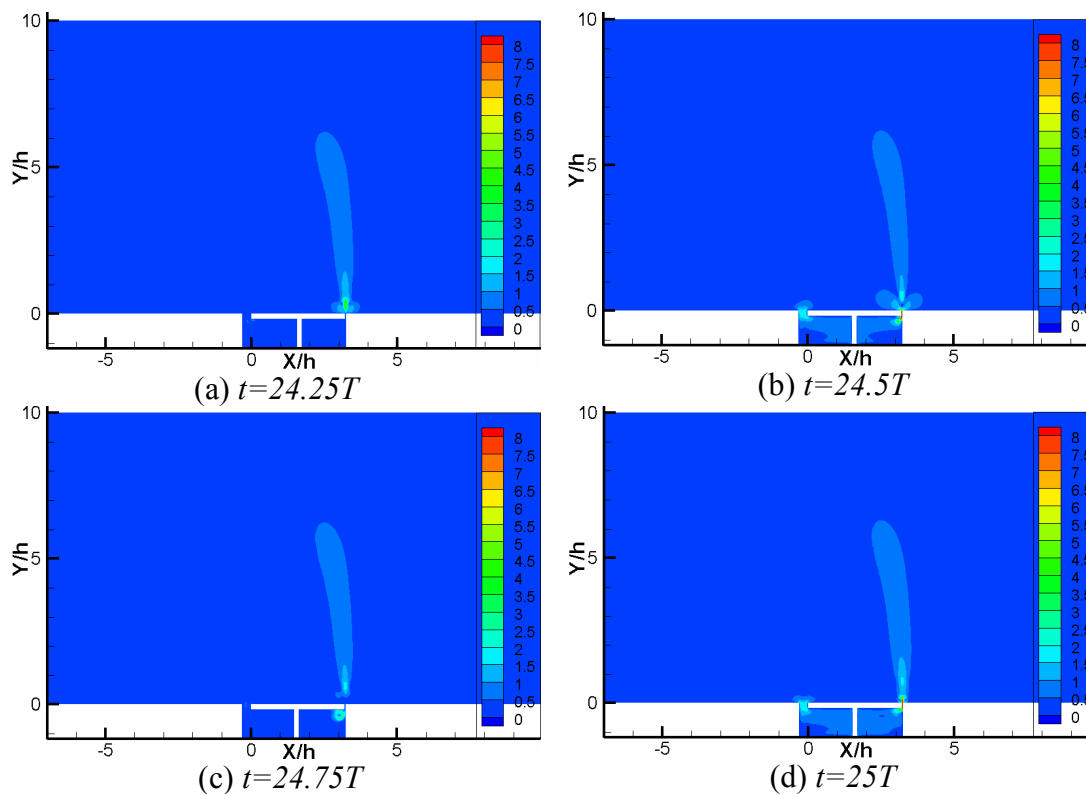


Figure 5.17 Contours of instantaneous velocity magnitude

5.2.4 Case 3.4 Unsteady vortex flow

In this case, the scaled amplitude is increased to $Sa = 1.177$ such that a maximum plate velocity of 0.451 m/s occurs. At this amplitude we observe that the flow becomes unsteady and we don't get a meaningful average pattern. The maximum mean velocity at the narrow gap is now $8U_p$. Nevertheless, we illustrate the flow

obtained by averaging over 4 periods. The according time-averaged velocity contours are shown in *Figure 5.18*. The changes to case 3.1 are quite dramatic. Apparently, the actuator produces an alternating sequence of vortices as in a Karman vortex street. The increased activity at the wide gap might be responsible for this qualitative change because the jet produced there is now also much stronger than before.

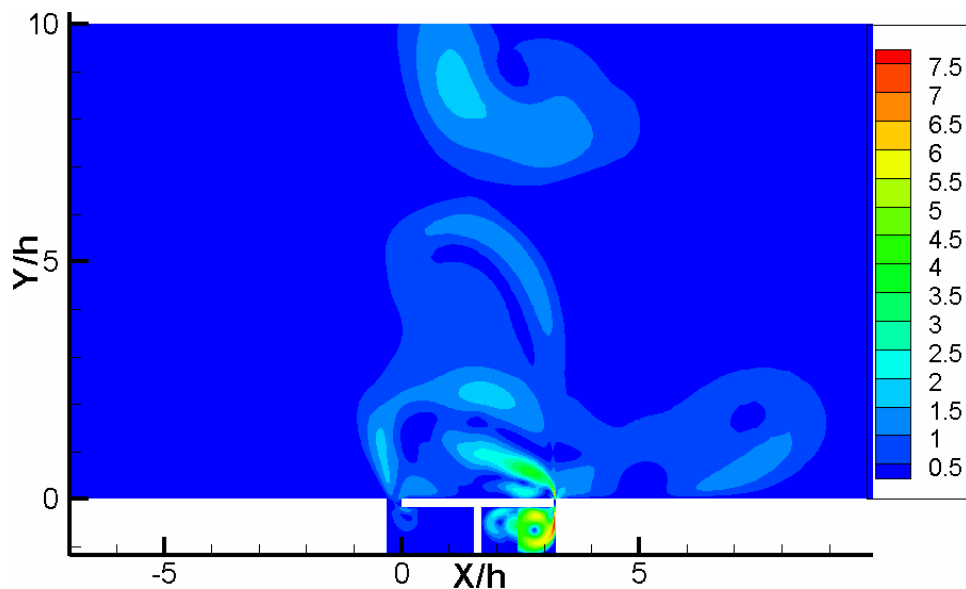


Figure 5.18 Contours of mean velocity magnitude

A more realistic view is provided through the contours of instantaneous velocity at four different time instances during the 25th period of oscillation in *Figure 5.19*. A Karman-vortex-street-like arrangement of the vortices becomes apparent. The highest activity is above the narrow gap and the smaller vortices seem to emerge from there periodically driven by the intensive jet that occurs at $t=25T$. We see that the most dominant vortex is generated at the left of the narrow gap by intensive blowing from the narrow gap at phase $\theta = 0^\circ$ (360°) that it then travels to the left while drifting away from the wall. The jet at the wide gap at $t=24.5T$ appears "at the wrong time" because it blows against the vortex motion there. If the actuation frequency were lower, one could imagine that the wide gap would blow at a time where the right, upward turning part of the traveling vortex would be above the gap and that the gap would then further accelerate the vortex.

Because of the "out-of-phase" blowing at the wide gap the vortex is blown away from the wall. A feature that is obtained via the instantaneous vorticity is shown in *Figure 5.20*. The counter-clockwise intensive vortex that emanates from the narrow gap appears as a red spot. It travels to the left and then lifts off from the wall due to

the jet from the wide gap. The main difference to case 3.1 is that the vortices from the narrow gap which periodically follow each other do no longer merge into a larger one. In the outer field the flow is no longer periodic despite the strict periodical forcing at the wall.

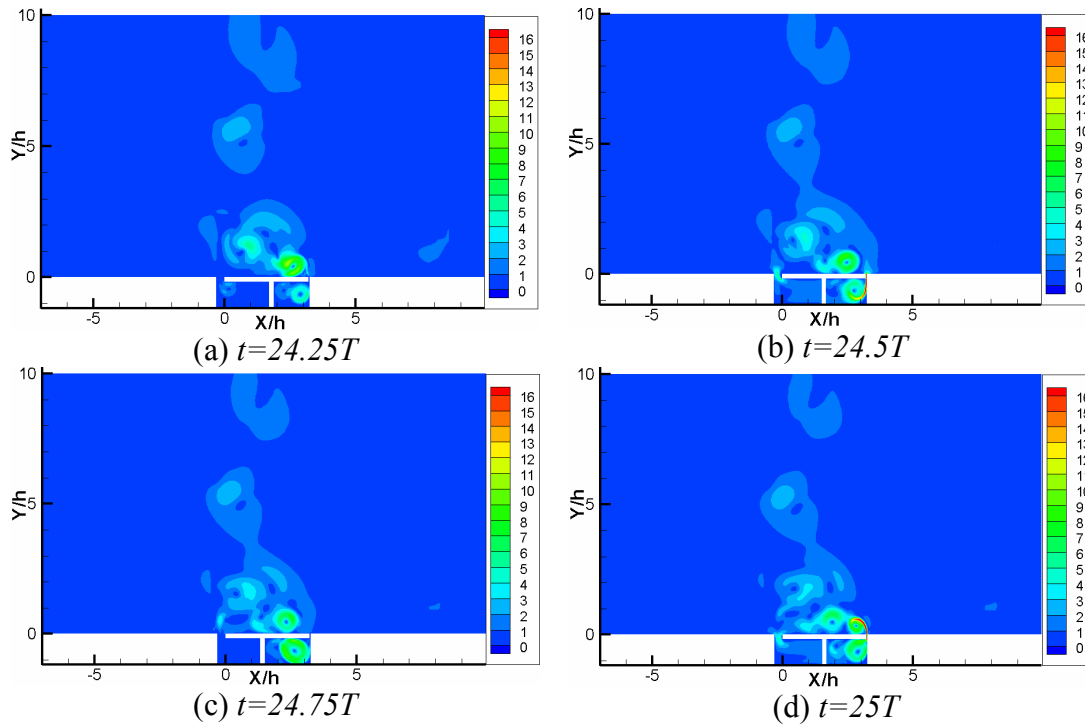


Figure 5.19 Contours of instantaneous velocity magnitude

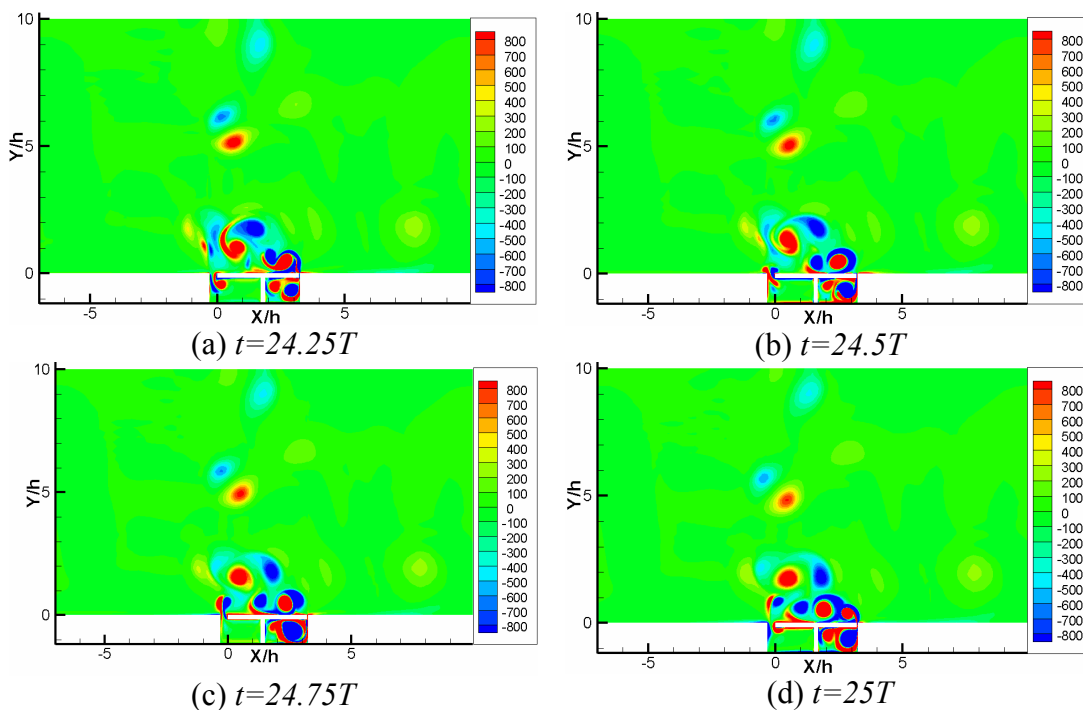


Figure 5.20 Contours of instantaneous vorticity

5.3 Comparison of all cases

In this section we will discuss different non-dimensional parameters which govern this actuator system. *Table 5.3* gives an overview of the different cases investigated. These are defined by geometrical parameters like gap widths and cavity depth. Note that the cavity depth “h” equals the actuator plate width in this design, i.e. a fluid volume proportional to the area “2ah” is moved by the actuator plate, where ‘a’ is the mean-to-peak amplitude of the motion. The oscillation is characterized by its frequency ‘f’ and the maximal plate speed $U_p = 2\pi a f$. From these, several non-dimensional parameters, like scaled amplitude, Reynolds number, Stokes number and Strouhal number have been derived.

Two Reynolds numbers can be used, one based on the dimensions and speed of the actuator plate $Re_{plate} = U_{p \max} h/\nu = 2\pi a f h/\nu$ and one based on the maximum speed and width of the narrow gap $Re_{gap} = U_{n \max} W_n / 2 \nu$, where $U_{n \max}$ is the maximum speed inside the narrow gap obtained from the numerical simulation. We concentrate our attention on the narrow gap instead of the wide gap because the flow speed there is always higher and therefore more important compared to the wide gap. The data collected in *Table 5.3* demonstrate that the Reynolds number is the decisive parameter to distinguish the different cases. The smallest Reynolds numbers lead to a vertical jet. Increasing Reynolds number inclines the jet or produces a vortex, while the highest Reynolds number leads to unsteady vortex shedding. Note that the definition of an “angled jet” isn't very precise here. Usually, the angled jets roll up into a vortex, as shown further above. Therefore, the discrimination between these two flow regimes is not as clear as between the others. In the previous chapter it was shown that the Stokes number is not an independent parameter for the original JaVA design, because it can be related to the scaled amplitude, the Reynolds number and the gap width. This is still the same for the current design.

We nevertheless included the Stokes number of the narrow gap in the table for comparison with other work. Even if the highest Stokes numbers occur in the unsteady cases 3.4.x no clear distinction is possible based on the Stokes number. We therefore considered the Strouhal number as well. As with the Reynolds number, two Strouhal numbers can be used, a global one and a local one. The global one is already present in the table via the so-called “scaled amplitude “Sa” because the Strouhal number is just the inverse of the scaled amplitude:

$$Str = fh/Up_{max} = fh / 2 \pi a f = h / 2 \pi a = 1/S_a$$

The local Strouhal number for the narrow gap is $Str_{gap} = f w_n / U_{n,max}$. However, for a better comparison and consistency with the scaled amplitude S_a we present the inverse of Str number in the table. *Table 5.3* demonstrates that the Reynolds number, Stokes number and Strouhal number are the main non-dimensional parameters which affect the flow field. For instance, if we keep the Stokes number fixed and vary the Reynolds number we can have different flow fields: For Stokes number 1.04 a vertical jet in cases 3.3.1 and 3.3.3, an angled jet in case 3.2.1, a vortex flow in cases 3.1.1, 3.1.2, and 3.1.7-3.1.9, until an unsteady flow in cases 3.4.1-3.4.3 and 3.4.9. This sequence repeats for other Stokes numbers because of the clear dependence of the flow fields on the Reynolds number.

Table 5.3 Parameters for all cases of the modified design

Case	Narrow gap (W_n)	Wide gap width (W_w)	Cavity Depth (h)	Frequency f (Hz)	Scaled amplitude $S_a = 2\pi a f/h$	Plate Reynolds no. $Re_{plate} = Up_{max} h/\nu$	Gap Reynolds no. $Re_{gap} = Un_{max} W_n/2 \nu$	Stokes no. $St = (2\pi W_n^2/\nu)^{1/2}$	Strouhal no: $1/Str = U_{max} / f W_n$
3.1.1	0.0466	0.3183	1	128	0.589	46	70	1.04	405
3.1.2	0.0466	0.3183	1	128	0.883	69	104	1.04	603
3.1.3	0.0466	0.3183	1	64	1.77	46	70	0.73	811
3.1.4	0.0466	0.3183	1	70	1.347	58	87	0.768	925
3.1.5	0.0466	0.3183	1	96	0.88	52	78	0.899	606
3.1.6	0.0466	0.3183	1	176	0.428	46	70	1.21	295
3.1.7	0.0933	0.3183	1	32	2.354	46	70	1.04	408
3.1.8	0.0466	0.6367	1	128	0.589	46	70	1.04	405
3.1.9	0.0466	0.3183	2	128	0.147	46	70	1.04	406
3.2.1	0.0466	0.3183	1	128	0.44	35	52	1.04	305
3.2.2	0.0466	0.3183	1	256	0.294	46	70	1.47	203
3.2.3	0.0466	0.3183	1	192	0.391	46	69	1.27	270
3.2.4	0.0933	0.3183	1	64	1.177	46	70	1.47	204
3.2.5	0.0933	0.3183	1	128	0.589	46	71	2.07	103
3.2.6	0.0933	0.6367	1	128	0.589	46	71	2.07	103
3.3.1	0.0466	0.3183	1	128	0.294	23	35	1.04	204
3.3.2	0.0466	0.3183	1	70	0.419	18	27	0.77	290
3.3.3	0.0933	0.3183	1	32	0.5885	23	35	1.04	204
3.4.1	0.0466	0.3183	1	128	1.18	93	138	1.04	804
3.4.2	0.0466	0.3183	1	128	1.026	81	121	1.04	703
3.4.3	0.0466	0.3183	1	128	1.91	150	220	1.04	1283
3.4.4	0.0933	0.3183	1	128	2.354	186	268	2.08	391
3.4.5	0.0933	0.3183	1	128	4.7	371	580	2.08	845
3.4.6	0.0933	0.3183	1	128	1.177	93	136	2.08	199
3.4.7	0.0466	0.6367	1	128	1.177	93	138	2.08	804
3.4.8	0.0933	0.6367	1	128	1.177	93	137	2.08	199
3.4.9	0.0466	0.3183	2	128	0.294	93	137	1.04	798

According to the non-dimensional parameters, cases 3.2.3 and 3.1.6 are almost identical. This agrees with the according flow-field pictures in Figure 5.21c and f. This coincidence also reflects that there is a smooth transition from the oblique jet modes to the vortex mode at $Re_{\text{gap}} \approx 70$. Even if the Stokes numbers are generally higher in the unsteady cases 3.4.x this parameter cannot be related to the features observed in the flow fields. It is therefore eliminated from our following discussion. Ordering the different flow cases with respect to the scaled amplitude or the Strouhal number of the gap flow is more promising. This is done for the jet and vortex flows separately in Figure 5.21 and Figure 5.22, respectively. From subfigure (a) to (f) the inverse of the Strouhal number increases, i.e. the Strouhal number decreases. In cases with the same Strouhal number the case with the smallest scaled amplitude is shown first. This rearrangement gives the clearest ordering found so far, i.e. for high Strouhal number the jet leaves the gap and a vortex is formed only further away from the actuator. While for decreasing Strouhal number the vortex develops closer above the actuator surface. The range of Strouhal numbers that is covered continues with the pure vortex flows in Figure 5.22. According to the flow field and the Strouhal number ($1/\text{Str} < 300$) case 3.1.6 could have also been placed in the series 3.2.x as already noted above.

Table 5.4 is intended to illustrate the actuator's efficiency in a more quantitative way using maximal velocities and relating them to the maximal plate speeds, i.e. to the mechanical input. Our present configuration differs from the original JaVA in such a way that the relative velocities through both gaps now only depend on geometrical parameters such that they are easy to predict. That is why the relative velocities (i.e. those related to the maximum plate speed) are practically constant in each respective column of *Table 5.4*. Only the case 3.4.1 somewhat deviates from this rule in the wide gap, due to the much more complicated flow field there. Still, the ratio between the maximal velocity at the narrow gap and the wide gap is higher than the ratio of the two gap widths, $32 / 4.3 = 7.44$ for the first and $0.955 / 0.14 = 6.82$ for the second. Thus, the narrow gap takes a somewhat bigger share of the relative activity. This can be explained by the observed counter-motion and 'flutter' velocity profiles in the wide gap. There is an almost linear relation between the two Reynolds numbers introduced. This is illustrated graphically in Figure 5.23. Using this result the Reynolds numbers can be converted. In the following the structuring of the

different flow features with respect to the parameter space will be shown based on the dimensionless parameters.

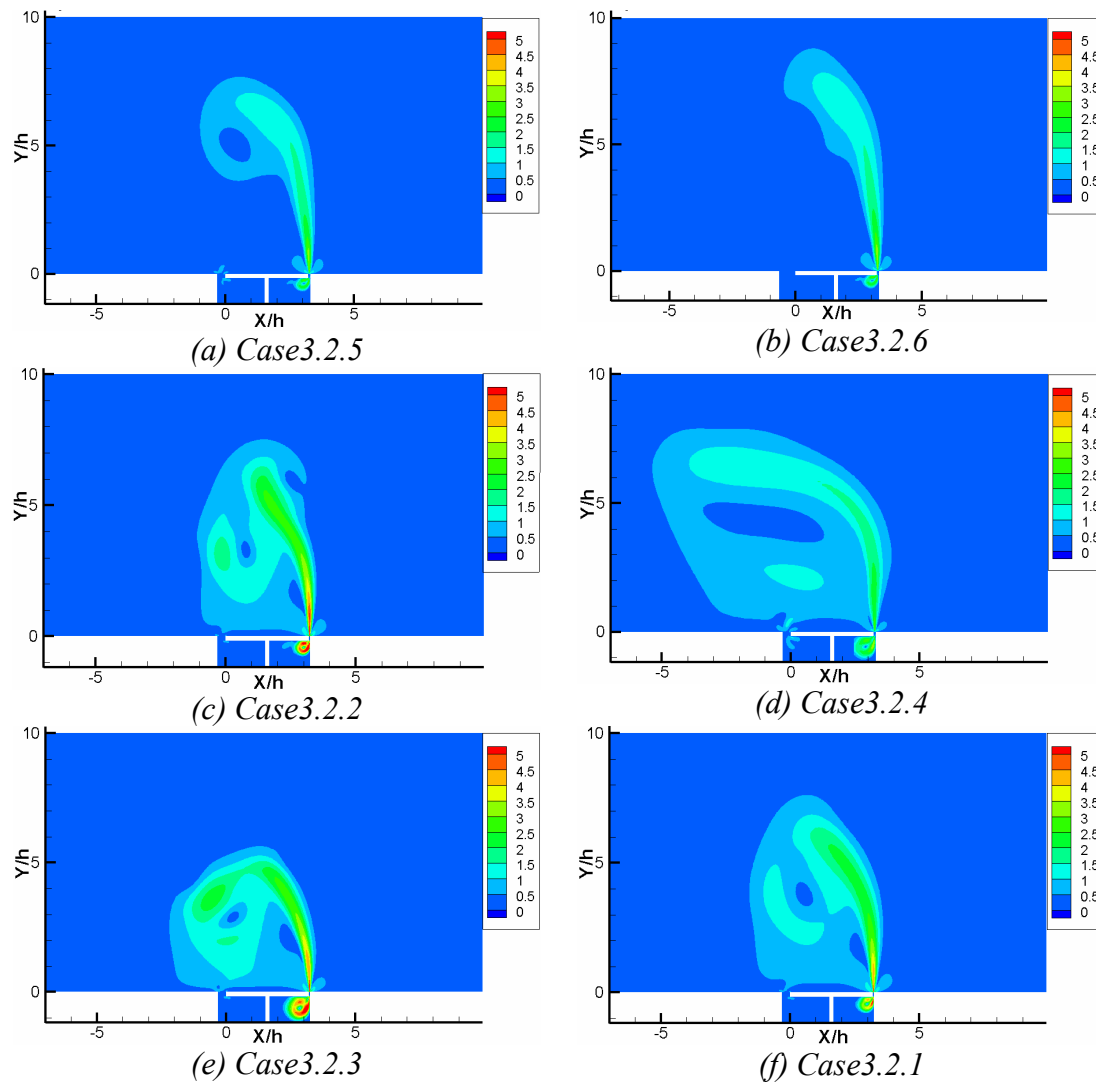


Figure 5.21 Contours of mean velocity magnitude re-arranged with respect to increasing $l = Sr$

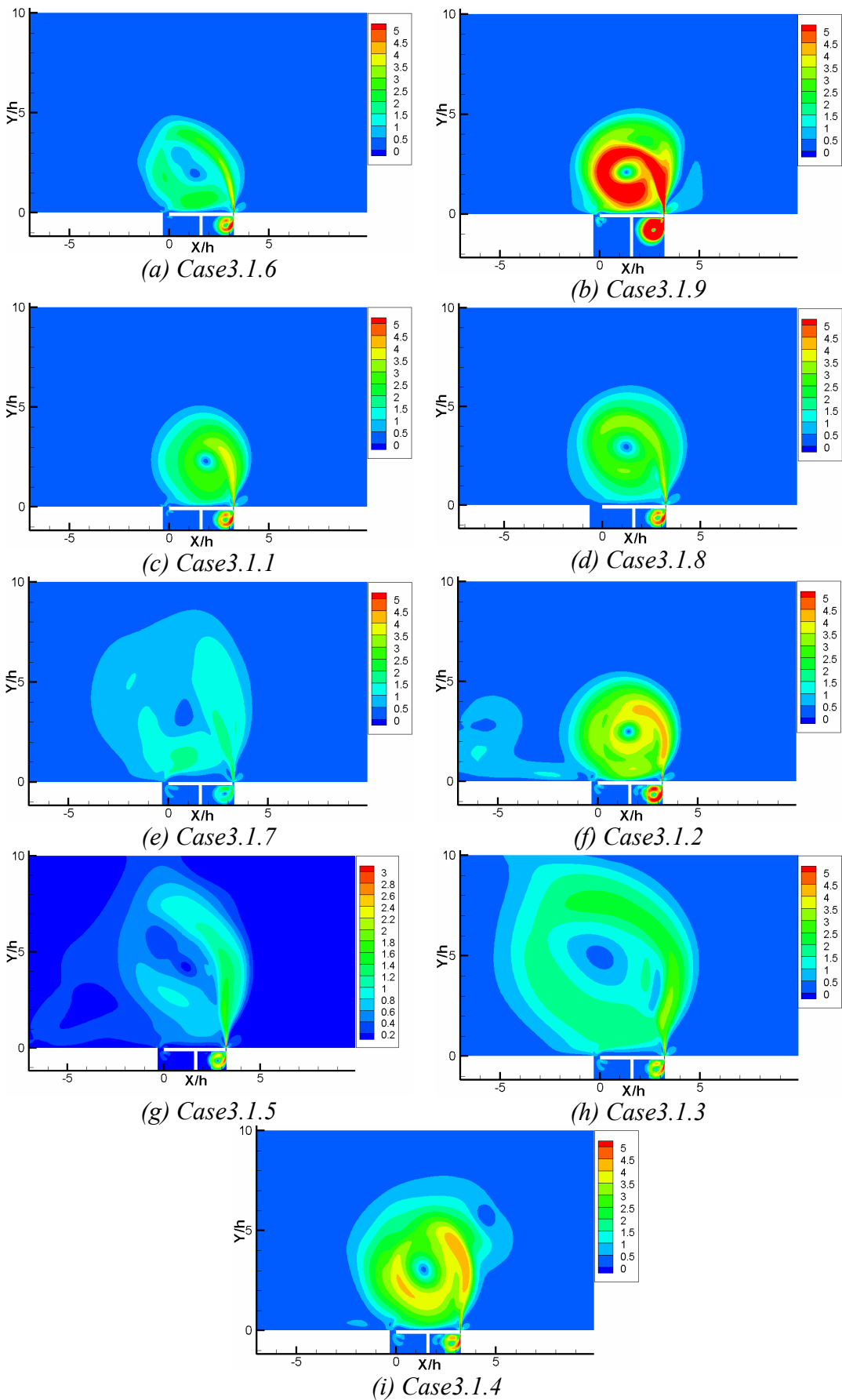


Figure 5.22 Contours of mean velocity magnitude re-arranged with respect to increasing $I=Sr$

Table 5.4 Maximal velocities observed in the gaps

Case	Motion of the plate	Max. plate speed (m/s)	Wide gap max. vel. $U_{w_{max}}/U_{p_{max}}$	Relative velocity (-)	Narrow gap max. vel. $U_{w_{max}}/U_{p_{max}}$	Relative velocity (-)
3.1	Left	-0.226	4.451	-4.451	-31.95	31.95
	Right	0.226	-4.38	-4.38	31.95	31.95
3.2	Left	-0.169	4.23	-4.23	-31.95	31.95
	Right	0.169	-4.32	-4.32	31.95	31.95
3.3	Left	-0.113	4.03	-4.03	-31.86	31.86
	Right	0.113	-4.20	-4.20	31.86	31.86
3.4	Left	-0.451	5.23	-5.23	-31.11	31.11
	Right	0.451	-4.39	-4.39	31.71	31.71

Figure 5.24a shows the plot of plate Reynolds number versus Stokes number and the different flow regimes present at these parameters. The flow regimes appear quite structured with some uncertainty with respect to the discrimination of "angled jet" and "vortex" modes near $St \approx 1$. Generally, at low Reynolds number and low Stokes number there is a vertical jet but for constant Stokes number around '1' if the Reynolds number is increased we move to the vortex mode and on to an unsteady flow. Similarly for constant Reynolds number around 50 if we increase Stokes number, first at low Stokes number we get a vortex and at high Stokes number we get an angled jet. If we increase the Stokes number beyond this range flow becomes unsteady. At very low Reynolds and Stokes number we get a weak vertical jet but at very high Reynolds and Stokes number the flow is always unsteady. In Figure 5.24b the Strouhal number is used instead of the Stokes number. Now the data points lie closer to the axes and slightly more clustered compared to the presentation before. As already noted before, using the gap Strouhal number has a certain advantage compared to use of the Stokes number.

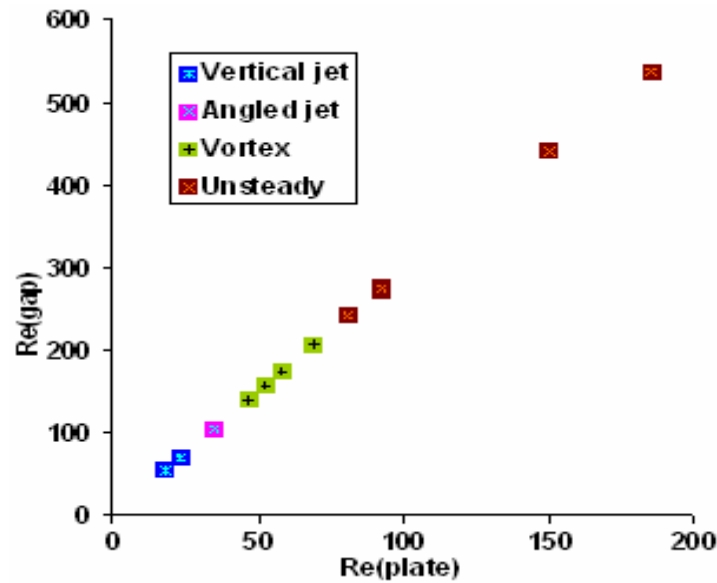


Figure 5.23 Plot of narrow gap Reynolds number versus plate Reynolds number

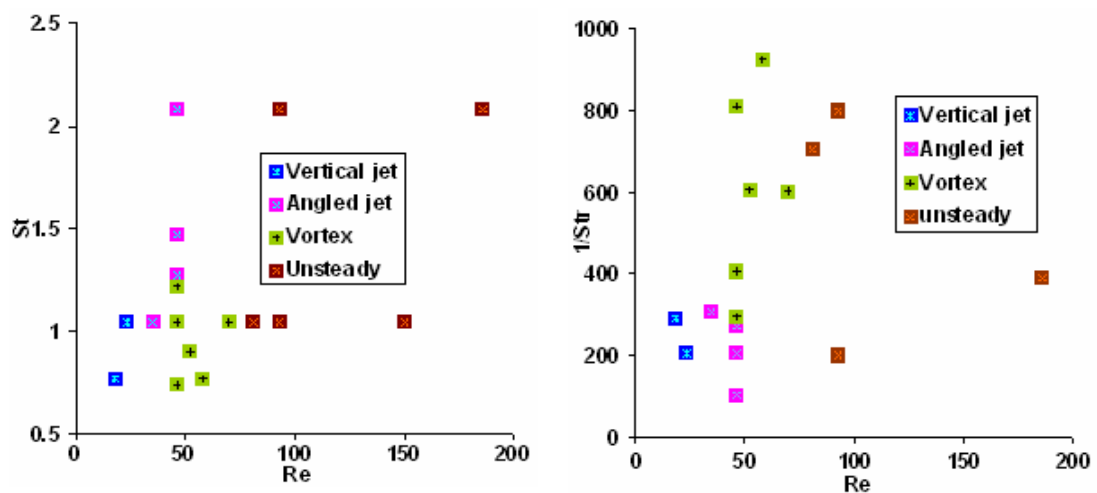


Figure 5.24 (a) Plot of Stokes number vs. Reynolds number
(b) Plot of Strouhal number vs. Reynolds number

By definition scaled amplitude S_a and $1/Str$ are equivalent. The difference is that “global” parameters are used for the first and “local” for the second. However, in contrast to the Reynolds number their relation is not linear as shown in Figure 5.25a. There is no clear correlation between the two, “vortex” and unsteady cases are completely interspersed with each other. In Figure 5.25b the Stokes number is used instead of the Strouhal number, the data is more intensively interspersed and we cannot even separate any zone.

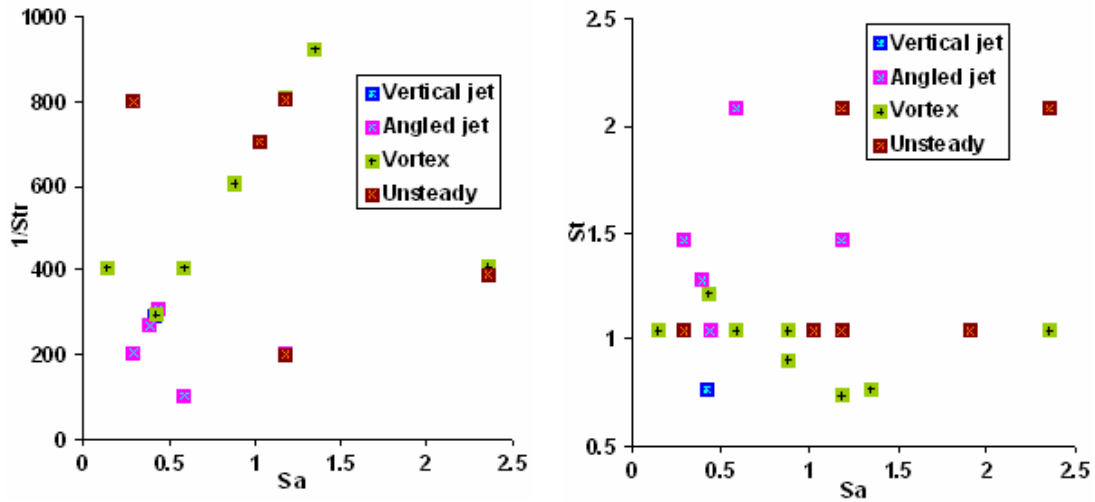


Figure 5.25 (a) Plot of Strouhal number vs. scaled amplitude
(b) Plot of Stokes number vs. scaled amplitude

When the flow regimes are plotted with respect to Reynolds number and scaled amplitude as in Figure 5.26a the data is restructured along the bisector of the domain instead of the axes. The angled jet now appears as a clear interim between vertical jet and vortex. Using the product of Stokes number and scaled amplitude in Figure 5.26b clusters the data even denser. The only outliers are the vortex mode in case 3.1.7.

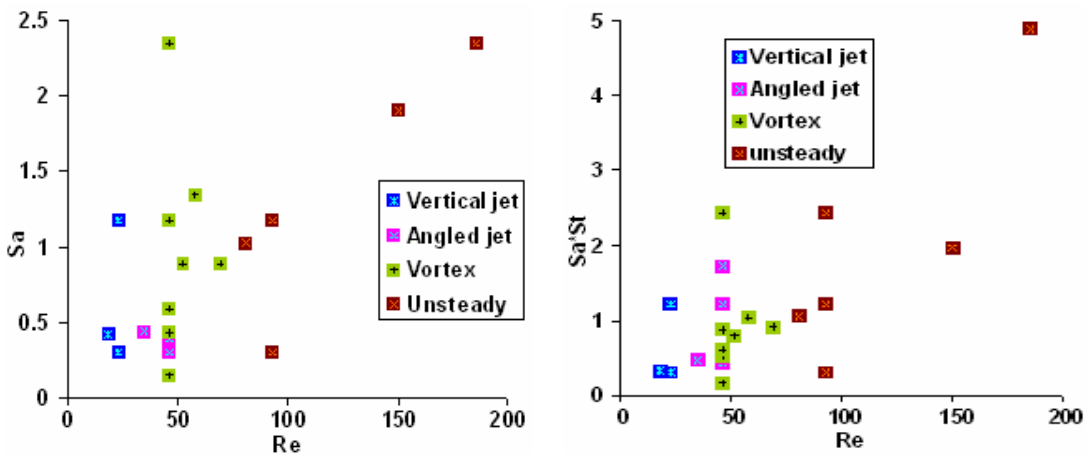


Figure 5.26 (a) Plot of scaled amplitude vs. Reynolds number
(b) Plot of product of scaled amplitude and Strouhal number vs. Reynolds number

A correlation of the data with respect to Stokes number and the ratio of Reynolds and Strouhal number is tried in Figure 5.27a. This kind of plot compresses the data along the abscissa. High Re/Str leads to vortex flow or unsteady flow. Low values to vertical or angled jets. In Figure 5.27b the product of scaled amplitude and

Strouhal number is plotted. In this case a very clear distinction between the flow zones with respect to Reynolds number can be seen.

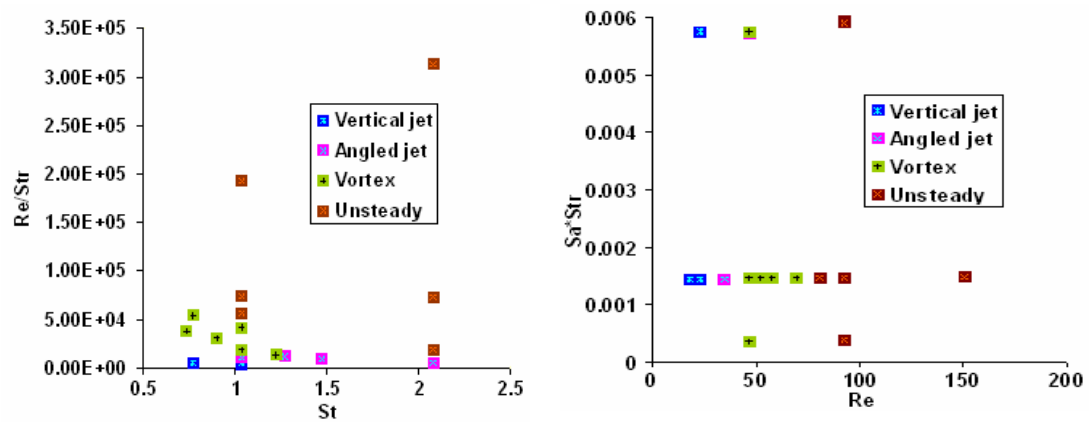


Figure 5.27 (a) Plot of product of Reynolds and Strouhal number vs. Stokes Number
(b) Plot of product of scaled amplitude and Strouhal number vs. Reynolds number

5.4 Summary

A modified design of the Lachowicz et al. [18] “Jet and Vortex Actuator (JaVA)” has been investigated here. The moving plate element was no longer placed at the surface but retracted into the cavity such that it produces an alternating periodic suction and blowing through the wide and the narrow gap i.e., the two motions are in anti-phase with respect to each other. Since the same flow volume must pass through the wide and the narrow gap at the same time, the flow through the latter is much more intensive and thus dictates the external flow field. Because of its small width to length ratio a harmonic suction and blowing velocity develops, while the wide gap has a large width-to-length ratio such that inertial effects can be observed in the gap's center. There is again a small phase lag with respect to the piston motion in the center of the wide gap which is caused by the inertia of the fluid. Thus, the flow in the center continues to follow the previous main direction while the lower-momentum fluid closer to the gap walls moves in opposite direction in order to compensate for the excessive in- or out-flowing volume. This explains why different flow regions in the wide gap move in opposite directions at the phases when the actuator plate itself is at rest.

As for the original JaVA design, it is possible to change the actuator mode from jet to vortex mode in this alternative configuration just by a simple change of

actuation frequency and amplitude, despite a completely opposite asymmetry of the flow through the gaps (and according opposite sense of rotation of the main vortex as well as different relative speeds through the gaps). This is another extremely important finding because it allows us to optimize the original JaVA by changing significant geometrical parameters without losing its flexibility and it shows that the effect first observed by Lachowicz et al. is much more general than originally assumed.

The Reynolds number, Stokes number and Strouhal number along with scaled amplitude are the important parameters in defining the flow regimes in the modified JaVA. If we plot the Reynolds number versus any of the Stokes number or Strouhal number or the product of both we get vertical jet at low Re and as we increase Re number first we get angled jet which rolls up into a vortex as the Re is further increased.. At a very high Re we get unsteady flow. If the plot does not contain Re there is no distinction between the flow regimes which suggests that Re is the most important parameters.

6. JaVA in cross flow

In the previous chapters our focus was on the validation of the simulation tools (Fluent) and experimental results the original JaVA by Lachowicz et al. [18]. Different modes of the actuator were studied and results were compared with experimental results by Lachowicz et al. [18] and simulations by Joslin et al. [14]. Variations of the actuator geometry and grid density have helped us to get an idea of the different fluid dynamical principles of the JaVA. We also studied a modified design of the JaVA and characterized it in detail. We discussed non-dimensional parameters which govern the different flow modes of this modified JaVA. It was found that, as for the original JaVA, it was possible to change the actuator mode from jet to vortex mode in our modified JaVA as well. Flow regimes which were observed in the original design of JaVA by Lachowicz et al. [18] are also present in the modified design of JaVA.

Until now there is a complete lack of knowledge about how this actuator will behave in a cross-flow condition. In order to see this we performed simulations with a cross flow boundary layer. In the present chapter therefore we will present results with cross flow both for the original design (2D) and the modified design (2D). We will also present 3D results with and without cross flow in order to get some understanding of three-dimensional effects and how this modified JaVA behaves in an actual environment.

6.1 Geometry and grid distribution

In the present chapter we will present results for the original and the modified design with a cross flow boundary layer. The used geometry configurations and different gap orientations with respect to the cross flow are shown in Figure 6.1. Note that the cross flow is always in the positive x-direction while the gap orientation is changed with respect to the latter by rotating the geometry. In each case we extended the domain after the actuator with respect to the simulations without cross flow. The number of grid cells used in the original design are 564626. Numbers of grid cells used for 2D modified design are 170800 and for the modified 3D (configuration-1) the grid cells are 21476146 while in configuration-2 the grid cells are 23758464.

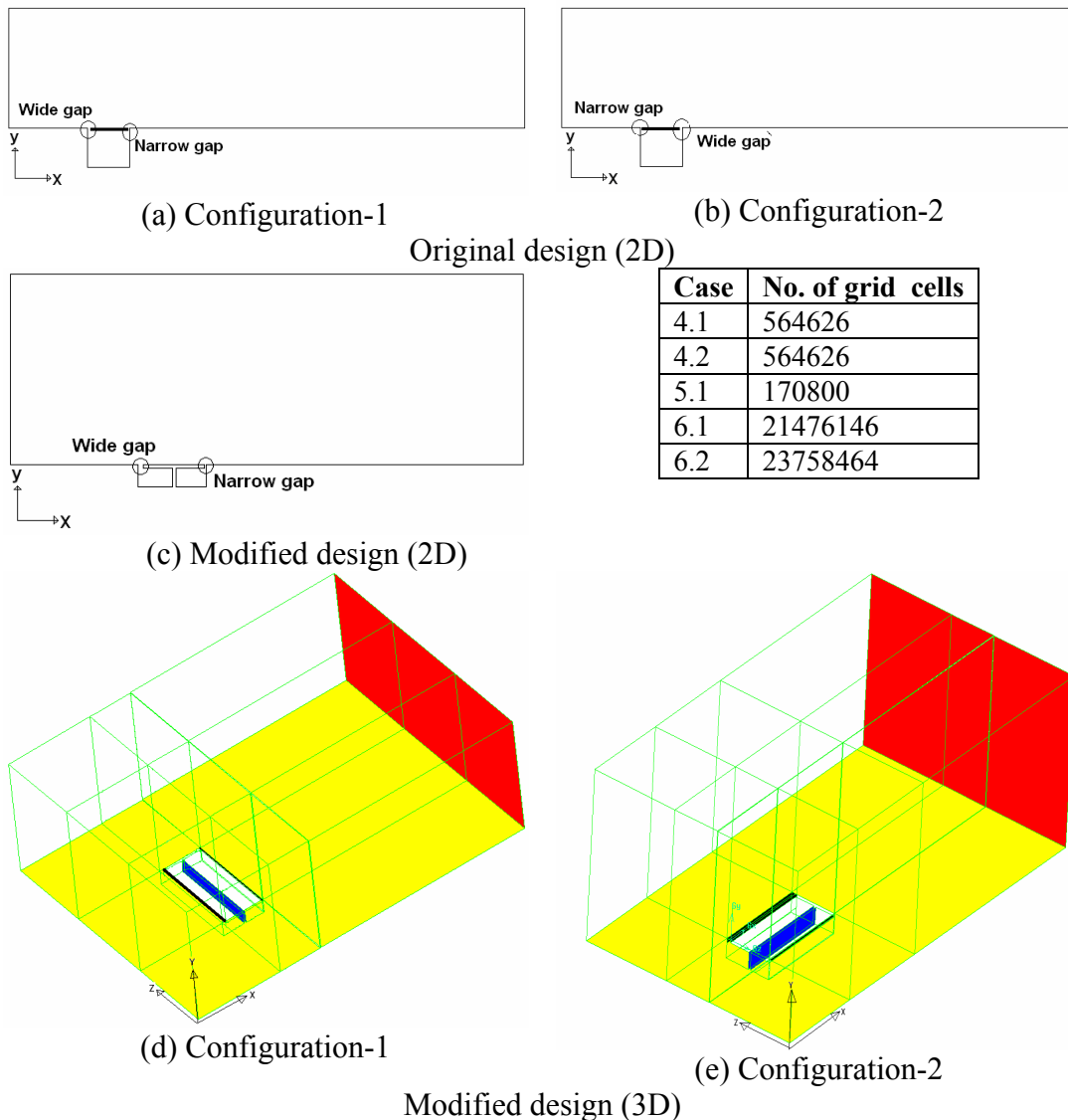


Figure 6.1 Grid geometry, boundary conditions, and number of grid points used in each case

6.2 Cases studied

Table 6.1 gives the details of the different cases studied. For this study we take a vortex-mode case in which the frequency is fixed to 128Hz. The cross-flow velocity is also fixed to $U/U_p=4.425$ and its boundary layer thickness is set to $\delta=1.0363b$. Narrow and wide gap widths are fixed to $W_n=0.0145b$ and $W_w=0.099b$, respectively. For the original design the scaled amplitude is $S_a=2\pi a/b=0.1829$ and for the modified design it is $S_a=2\pi a/h=0.589$. The length of the horizontal plate “b” is 9.65mm and the length of the vertical plate in the modified design “h” is $0.3109b$. For the 3D cases the spanwise length of the gap is set to $2.225b$ which is twice the streamwise length of the cavity.

Table 6.1 Parameters for different cases

Case	Scaled amplitude $S_a = 2\pi a/b$ (original) $S_a = 2\pi a/h$ (modified)	Cavity Depth h (mm)	Configuration	Domain	Flow direction
Original design(2D)					
4.1	0.1829	9.5	Configuration-1	standard	With cross flow
4.2	0.18296	9.5	Configuration-2	reversed	With cross flow
Modified design(2D)					
5.1	0.589	3	Configuration-1	standard	With cross flow
Modified design(3D)					
6.0	0.589	3	3Configuration-1	standard	Without cross flow
6.1	0.589	3	3Configuration-1	standard	With cross flow
6.2	0.589	3	3Configuration-2	Rotated about y-axis	With cross flow

6.3 Case-4.1 original design (2D)

This section will present detailed flow fields for the 2-D original design with a cross flow of $U/U_p = 4.425$. In this case two different geometry configurations are used. They differ by the arrangement of the wide and narrow gaps with respect to the cross flow, see Figure 6.1 (a) and (b). In configuration-1 the wide gap is on the left side (i.e. the upstream side of the cavity) while the narrow gap is on the other (downstream) side. In configuration-2 we reversed the gap orientation (i.e. narrow gap towards left and wide gap towards right, respectively) while the flow direction is still the same (positive x-direction). The domain after the actuator in each case is increased to 10D in order to see the flow behavior in greater details.

6.3.1 Configuration-1

The simulation is performed at a frequency of 128 Hz and scaled amplitude of 0.18296 as in case 2.2 in the fourth chapter with a cross flow velocity of $U/U_p = 4.425$. The simulation is performed for thirty oscillation periods and averaged over the last ten periods. Results presented here are for the last oscillation period.

In Figure 6.2 contours of velocity magnitude at two time instances where the plate velocity is maximum, are shown. At both time instants a separation bubble exists which extends almost one actuator width after the actuator. Further above the actuator, outside of the cross-flow boundary layer, a velocity maximum exists. There are two reasons for these two features. The first is the high suction and blowing

velocity through the gaps, especially at the wide gap. The second is because the actuator plate moves outside the cavity such that it produces resistance to the cross flow which is then deflected upwards and accelerated. Now with the cross flow the narrow gap is more active relative to the case when there was no cross flow. A zoom-in-view of the previous figures overlaid by velocity streamlines are shown in subfigures (c) and (d). At $\theta=180^\circ$ during the blowing phase a big vortex is formed which covers the whole plate and further $0.5b$ to the right of narrow gap. The height of the vortex is almost half the boundary layer thickness " δ ". At $\theta=360^\circ$ during the suction phase a relatively small vortex is present above the narrow gap. The effect of the vortex above the plate at both time instances goes into the boundary layer more than one " δ ". Inside the cavity there exists a vortex at both time instances, i.e. the cavity fluid rotates in counter-clockwise direction.

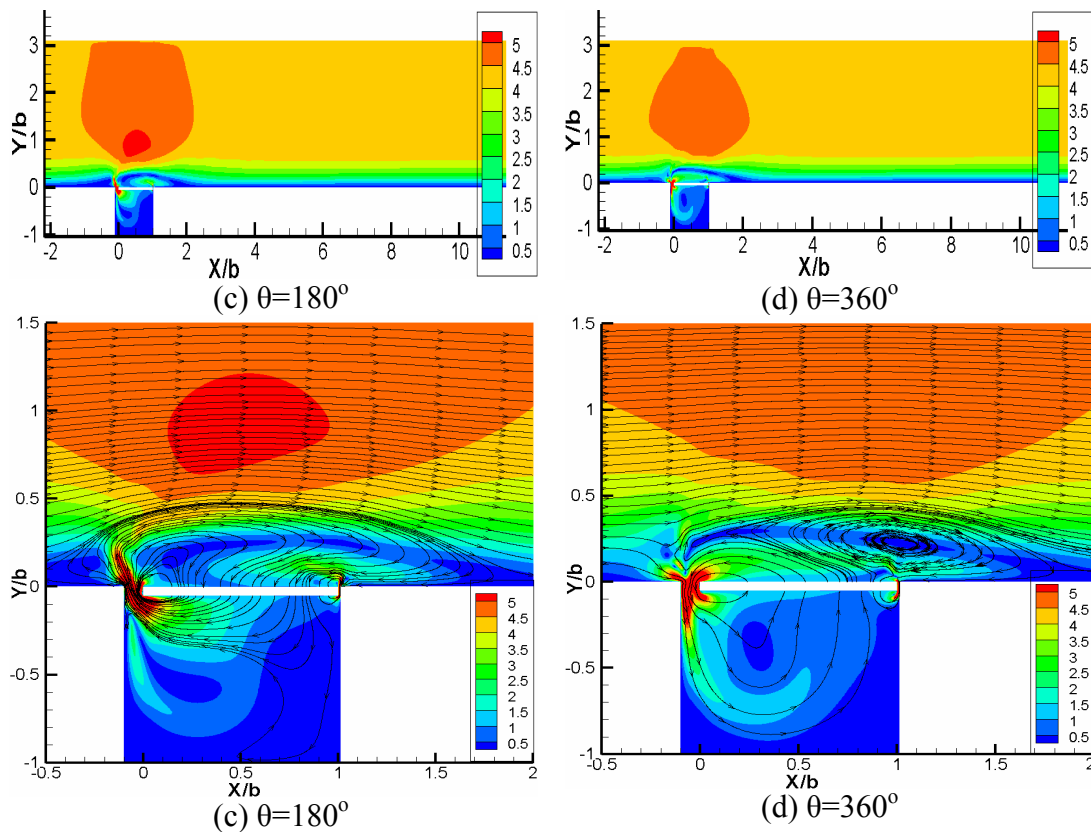


Figure 6.2: Contours of velocity magnitude, 2D configuration-1

Figure 6.3 shows contours of velocity magnitude in the narrow and the wide gap. Suction and blowing is very strong from both gaps. In the narrow gap during blowing a jet emerged surrounded by a pair of small vortices. While in the wide gap during suction a small vortex is on the other side of the actuator plate. The jet through the wide gap splits into two and it is more prominent in the suction phase.

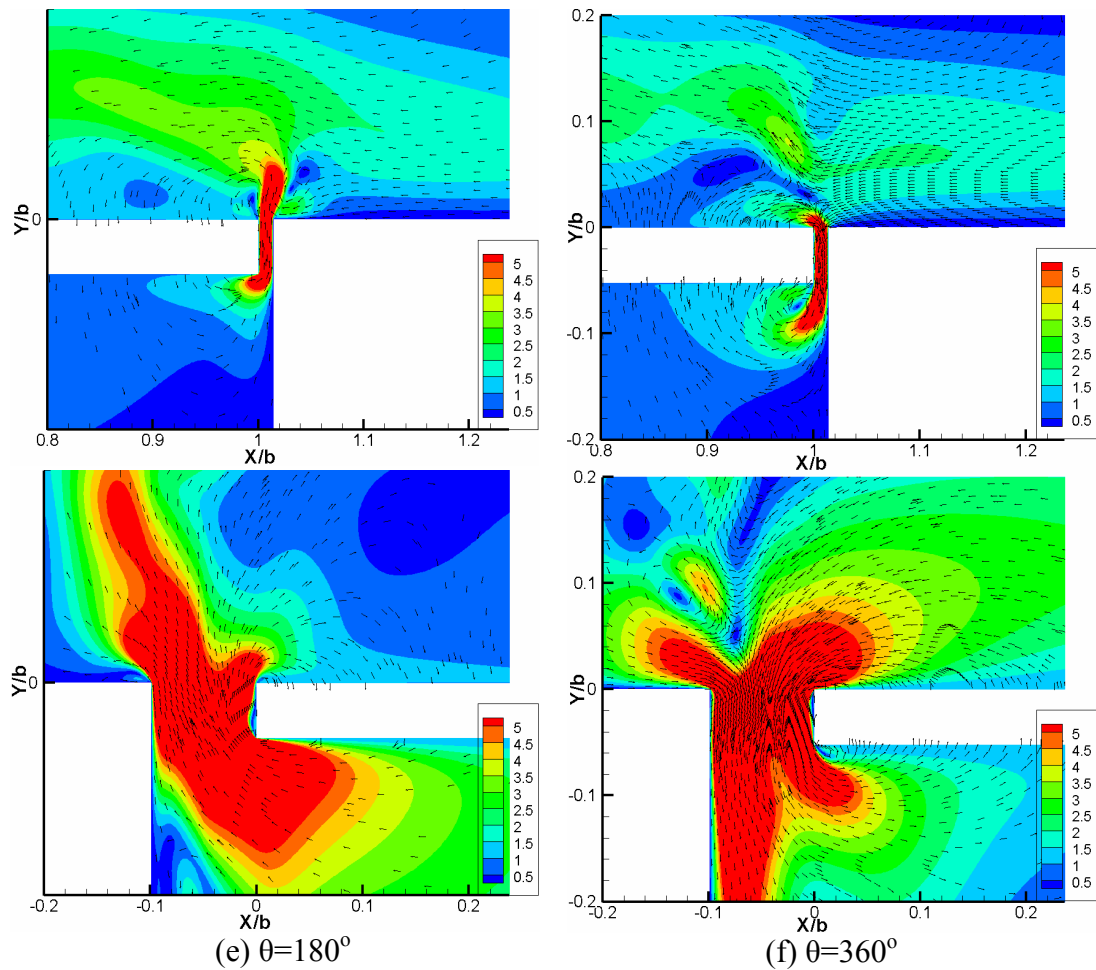


Figure 6.3: Contours of velocity magnitude (zoom-in-view on narrow and wide gap), 2D configuration-1

In Figure 6.4 contours of mean velocity magnitude are shown. There is no significant difference to the instantaneous contours until we zoom in on subfigure (b) where we see that a big vortex is present above the plate. This vortex is formed covers the whole plate and further $0.5b$ to the right of narrow gap. The height of the vortex is almost half the boundary layer thickness “ δ ”. The effect of the vortex above the plate at both time instances goes into the boundary layer more than one “ δ ”.

Now we have a closer look at the flow through the gaps. Figure 6.5 (a) and (b) shows the velocity profiles in the wide and narrow gap, respectively at eight different time instances during the 30th oscillation period. As in case 2.2 in the fourth chapter there is a phase shift in the narrow gap here as well. As already mentioned above, it is also evident in subfigure (d) that the narrow gap in this case is more active compared to the case without flow. In this case the velocities in the narrow gap are about twice as high. During blowing the velocity peaks are slightly shifted towards the cavity wall but this is not the case during suction. In the wide gap in subfigure (a) the flow becomes more complex compared to case 2.2. In the present case reverse

flow near the plate occurs only at the phases 45° and 225° at which there is also a high velocity peak. Note that these are the same phases at which there is minimum flow through the narrow gap. At phases 90° and 270° when the plate is at rest and changing its direction of motion a strong reverse flow exists at the center of the gap. In wide gap in subfigure (c) during suction velocity peak is slightly lower. In subfigure (e) different velocity profiles are extracted from the narrow gap at three different gap heights for the phases with maximum plate velocity during suction and blowing. Interestingly, the suction profile at $y=0$ and the blowing profile at $y=-0.0518b$ are almost the same. Remind that these are the profiles at the entrance of the channel at their respective times. Velocity peaks during blowing are shifted toward the cavity wall and towards the plate. One observation is that in the center of the gap there is a small velocity jump in the profile as well as in the contours. This jump is at the location of the interface boundary. So we can say that this small discrepancy is due to the interpolation of these two interface boundaries but this effect is very small and it does not affect the overall flow field.

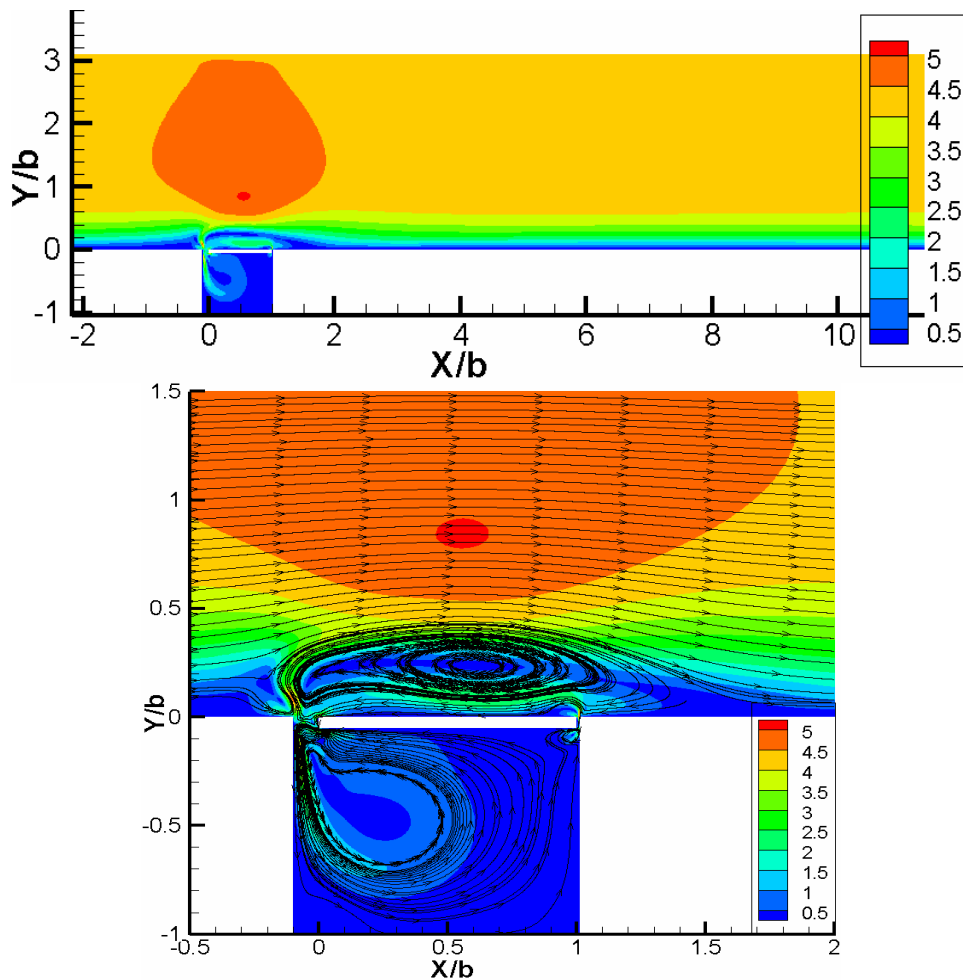


Figure 6.4: Contours of mean velocity magnitude, 2D configuration-1

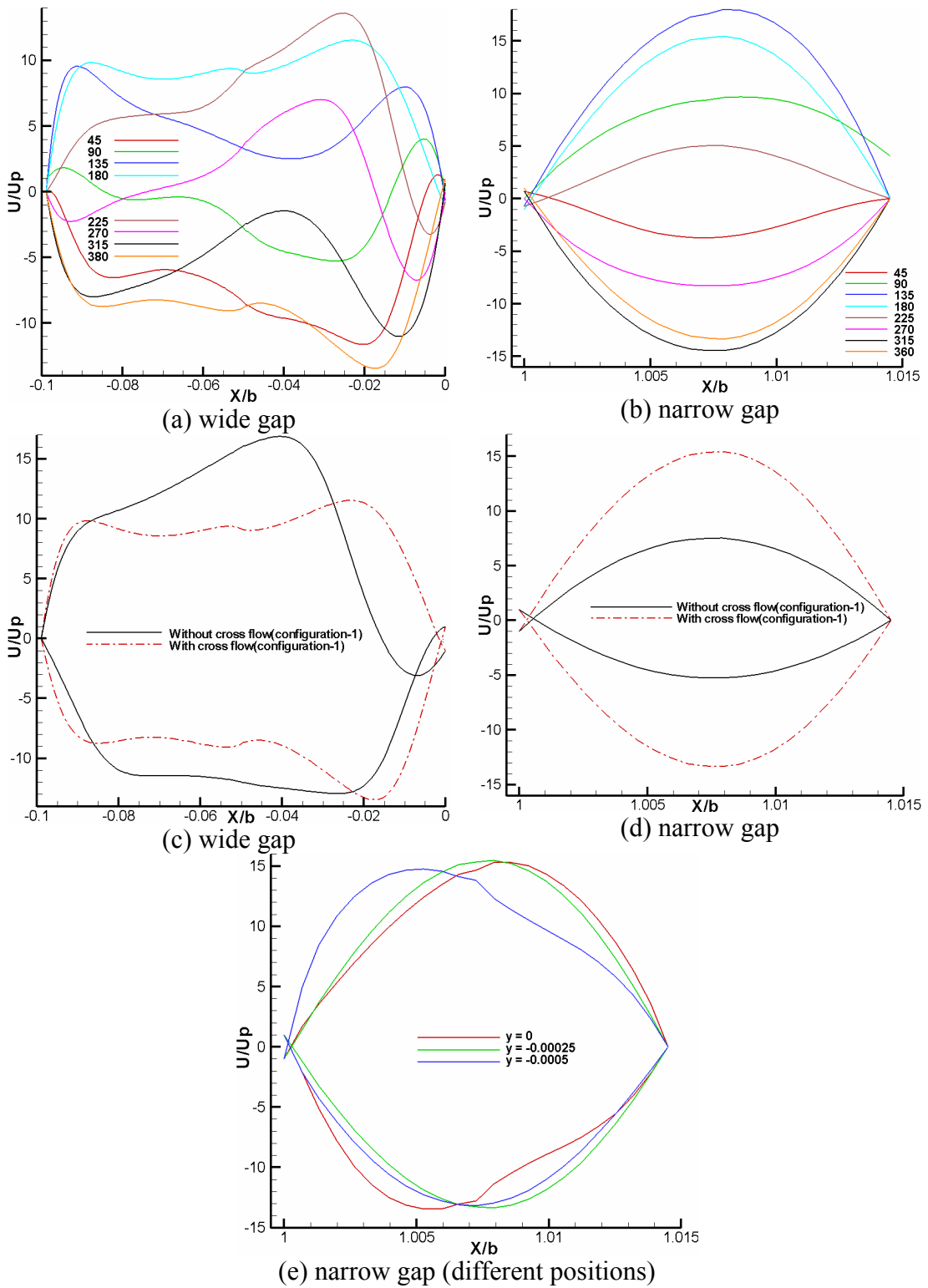


Figure 6.5: Velocity profiles through the narrow and wide gap, 2D configuration-1

Now we shall look at the effect of this actuator on the cross-flow boundary layer. *Figure 6.6* shows the velocity profiles at different distances from the actuator for comparison with the cross-flow reference profile (left part of the figure). For a better perception of the differences to the reference profile the difference “ $(U-U_{ref})/U_p$ ” is plotted in the right part of the figure. Here “reference profile” stands for the profile at the same distance from the inflow but for the unactuated flow. The distance from the actuator is given with respect to the length scale $D=1.1135b$, which is the actuator width, i.e. the sum of plate width and narrow and wide gap widths. The inflow boundary layer thickness used for the simulations is $1.063b$. Thus, actuator width D and boundary layer thickness δ are almost the same in the present work.

At a distance of $1-D$ after the actuator we see that the profile close to the wall (red line) is almost on top of the reference profile (black line) until a vertical distance of $0.28b$, after which it decreases faster. At the edge of the boundary layer there is a small overshoot, as already mentioned in the contour plots above. The close-up in subfigure (b) confirms that the red profile merely oscillates around the reference. Further downstream, at a distance of $2-D$, $4-D$, and $7-D$ all profiles are all almost the same. Compared to the reference they show the opposite effect compared to the first profile, i.e., that the velocity inside the boundary layer is higher now while it is smaller outside the boundary layer. Such an increase of speed close to the wall is what we wanted to achieve with the actuator. It helps to delay flow separation from the wall.

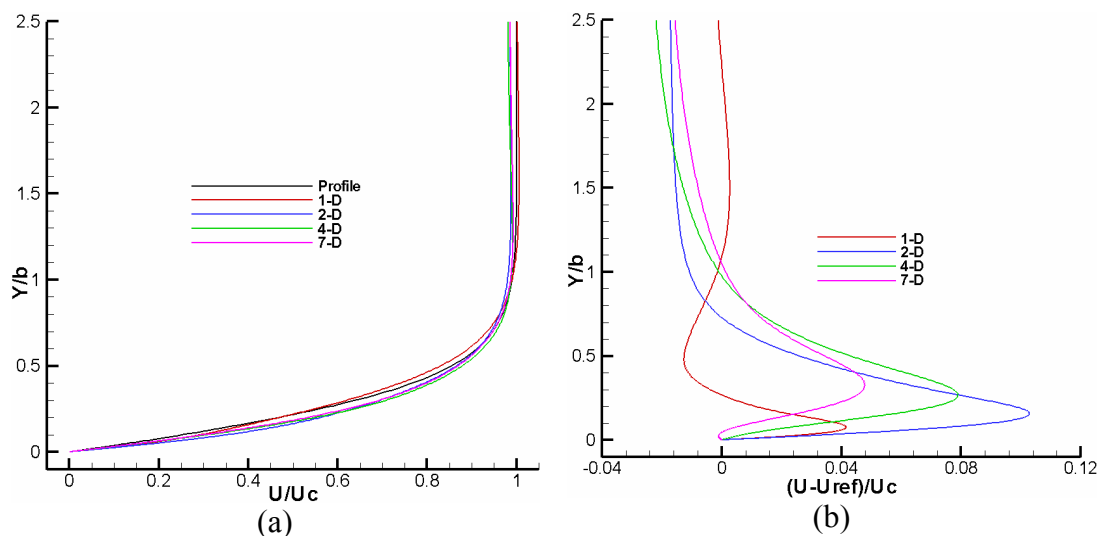


Figure 6.6: Mean velocity profiles at different x -distances from the actuator, 2D configuration-1

6.3.2 Configuration-2

In this case the simulation is again performed at a frequency of 128 Hz and scaled amplitude of 0.18296 and with a cross flow velocity of $4.425U_p$, as in the previous case, but the gap orientation with respect to the cross flow is inverted now, see Figure 6.1 *b*. The simulation is performed for thirty oscillation periods and averaged over the last ten periods as before and results of the last oscillation period are presented here.

In Figure 6.7 contours of velocity magnitude at two time instances (where the plate is at its maximum velocity) are shown. At $\theta=360^\circ$ (i.e. the suction phase) a low-velocity zone sits above the narrow gap but at $\theta=180^\circ$ this low velocity zone moves above the wide gap. Strong suction and blowing above the wide gap can be seen as well. There exists a vortex inside the cavity on the wide gap side at both time instances. Once again, with cross flow the narrow gap is more active relative to the case when there was no cross flow. A zoom-in-view of the same figures along with overlaid velocity streamlines is shown in subfigures (c) and (d). At $\theta=180^\circ$ during the blowing phase a jet emerges from both gaps being stronger from the wide gap as expected. In the wide gap this jet splits into two.

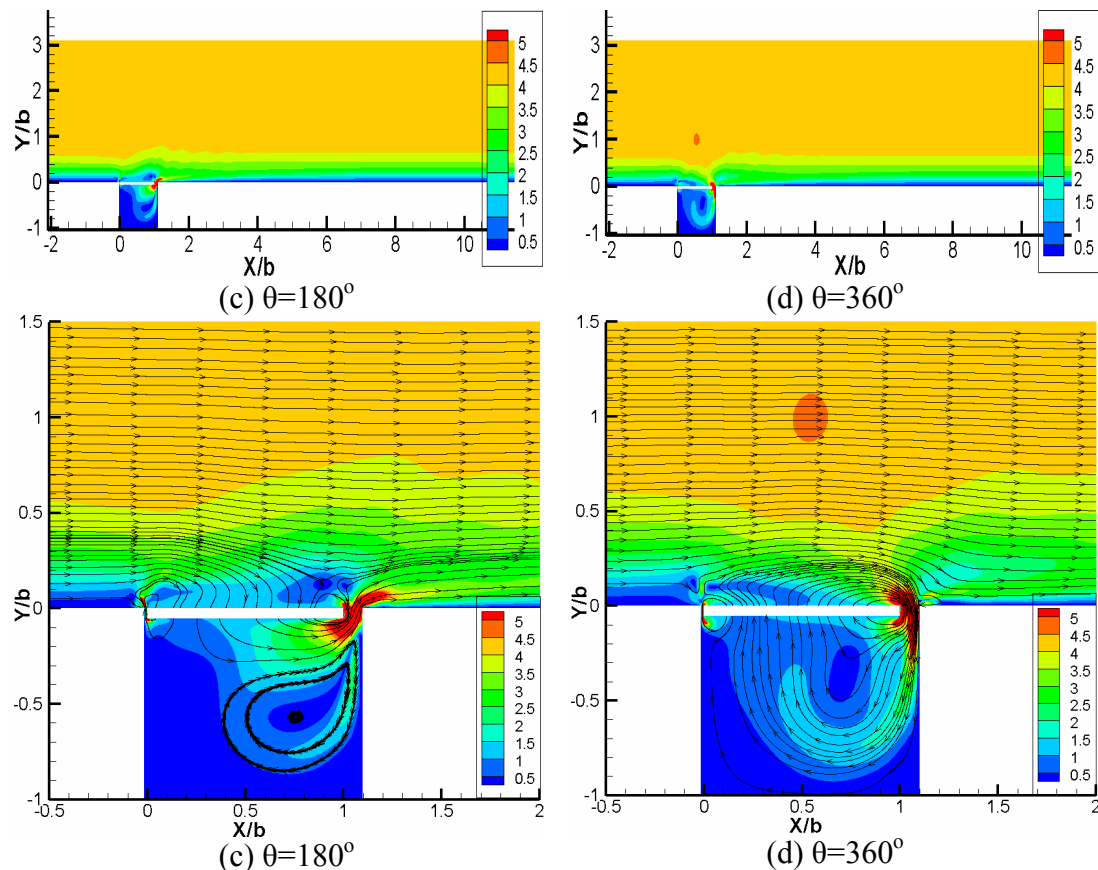


Figure 6.7: Contours of velocity magnitude, 2D configuration-2

Figure 6.8 shows contours of velocity magnitude in the narrow and wide gap. Suction and blowing are very strong from both gaps. During blowing ($\theta=180^\circ$) a jet emerges from the narrow gap along with two counter rotating vortices. This jet is directed slightly away from the actuator. During suction ($\theta=360^\circ$) there is mainly a sink flow. In the wide gap during suction and blowing a jet is produced which splits into two in the blowing phase, one being very small and the other one long enough to disturb the boundary layer. During suction there is a vortex at the right of the actuator.

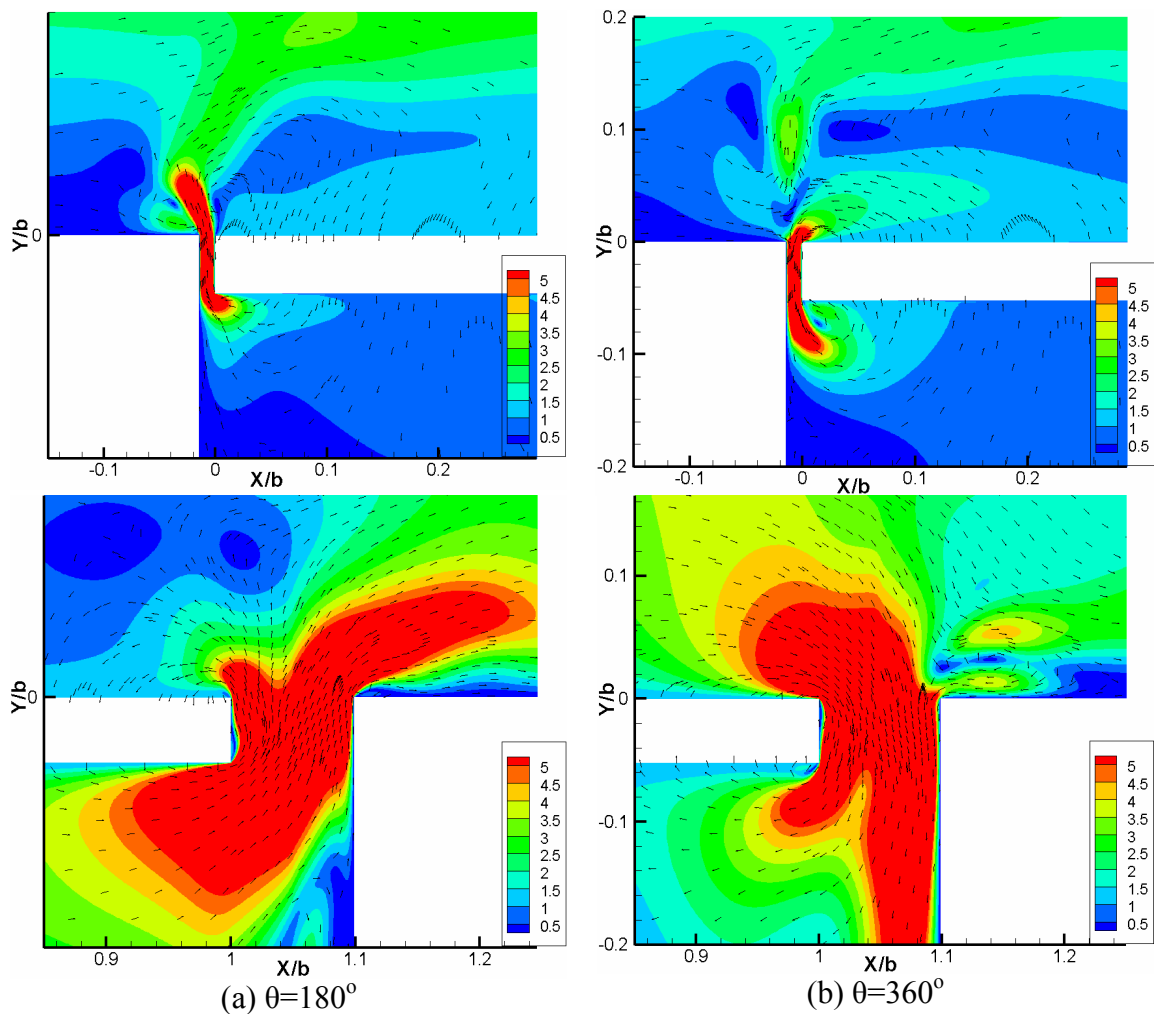


Figure 6.8: Contours of velocity magnitude (zoom-in-view of narrow and wide gap), 2D configuration-2

In Figure 6.9 contours of mean velocity magnitude are shown. From both gaps there is a strong jet with vortex on the downstream side of the narrow gaps in the mean flow. Above the narrow gap and above the plate the boundary layer thickness reduces while it increases above the wide gap and to some distance after the wide gap.

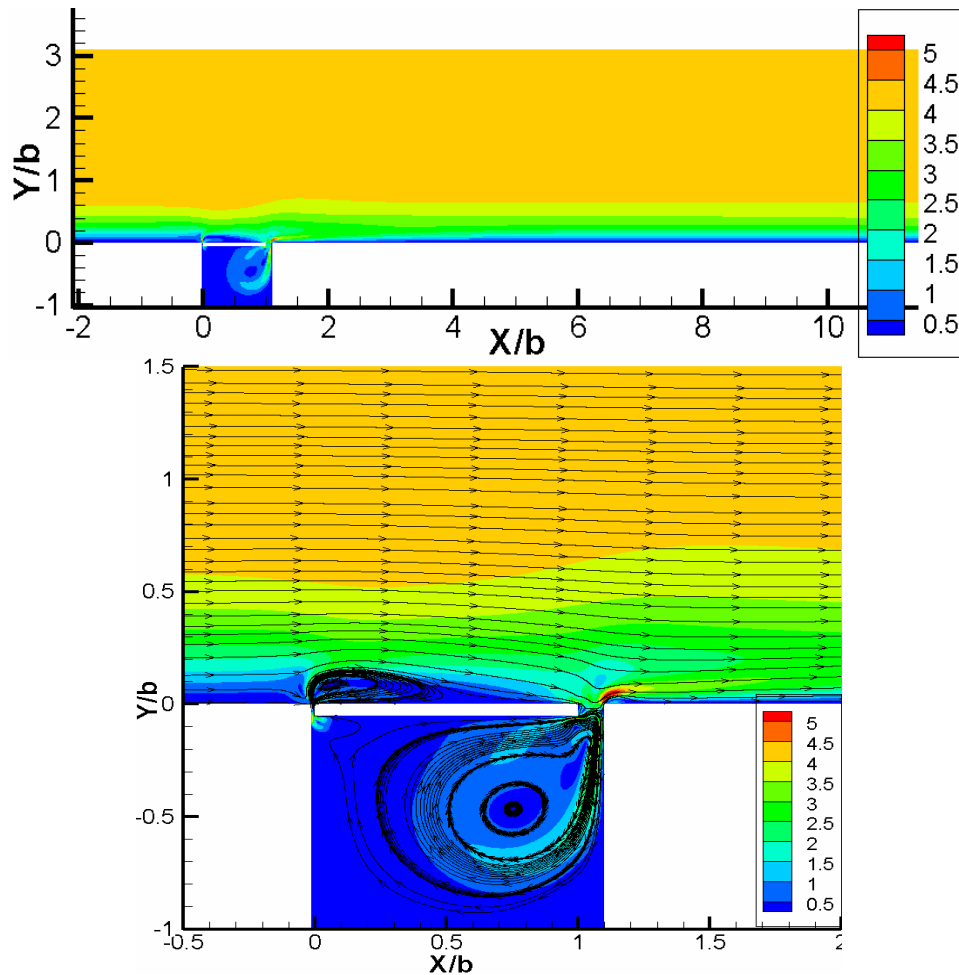


Figure 6.9: Contours of mean velocity magnitude, 2D configuration-2

Again we shall have a look at more details in the gaps in Figure 6.10 (a) and (b) which shows the velocity profiles in the narrow and wide gap respectively at eight different time instances during the 30th oscillation period. As in the previous case, there is a phase shift with respect to the plate velocity in the narrow gap. Again the narrow gap is more active in this case, as already mentioned above, such that the velocities in the gap are higher. During blowing the velocity peaks are slightly shifted towards the left, i.e. away from the cavity wall, which is different from the previous case. Relative to the cross flow in both cases the velocity peak is towards the oncoming cross flow side. In the wide gap in subfigure (b) the flow is as

complex as in the previous case but the velocity peaks are on the opposite side. In this case the reverse flow near the plate is only at the phases 45° and 225° at which there are also high velocity peaks. Note that these are the same phases at which there is minimum flow through the narrow gap. At phases 90° and 270° when the plate is at rest and changing its direction a strong reverse flow exists at the center of the gap. In subfigure (e) different velocity profiles are extracted from the narrow gap at three different gap heights for phases with maximum plate velocity during suction and blowing. Interestingly, the suction profile at $y=0$ and the blowing profile at $y=-0.0518b$ are almost the same. These are the profiles at the entrance of the channel during the respective phases. Velocity peaks during blowing are shifted towards the left and away from the plate.

Now we shall look at the effect of this actuator on the cross-flow boundary layer. Figure 6.11 shows the velocity profile at different distances from the actuator in comparison with the profile used for the cross flow. Again, D is the sum of plate width and gap widths, i.e. the cavity diameter. Looking at the first profile (red line) at a distance of $1D$ after the actuator, the boundary layer is now immediately much more attached to the wall compared to the original profile (black line). The velocity is higher inside the boundary layer until a vertical distance of about $0.4b$ afterwards; it jumps back to the value of the reference profile. From then on the velocity stays below the reference. Now, the maximal overshoot close to the wall is about 20% of the free-stream velocity compared to only 2% in the previous case (compare Figure 6.6 (b) to Figure 6.11 (b)) at a distance $2-D$. The first profile looks as if a small vortex were imposed on the boundary layer. A similar behavior can be observed with the next profile at $2-D$ distance (blue line) but with smaller effects. The other profiles at a distance of $4-D$ and $7D$ are largely undisturbed but inside the boundary layer a slightly higher velocity and outside the boundary layer a slightly lower velocity still occur. Their difference to the reference flow is still of the order of 10%, i.e. much larger as in the previous case discussed further above.

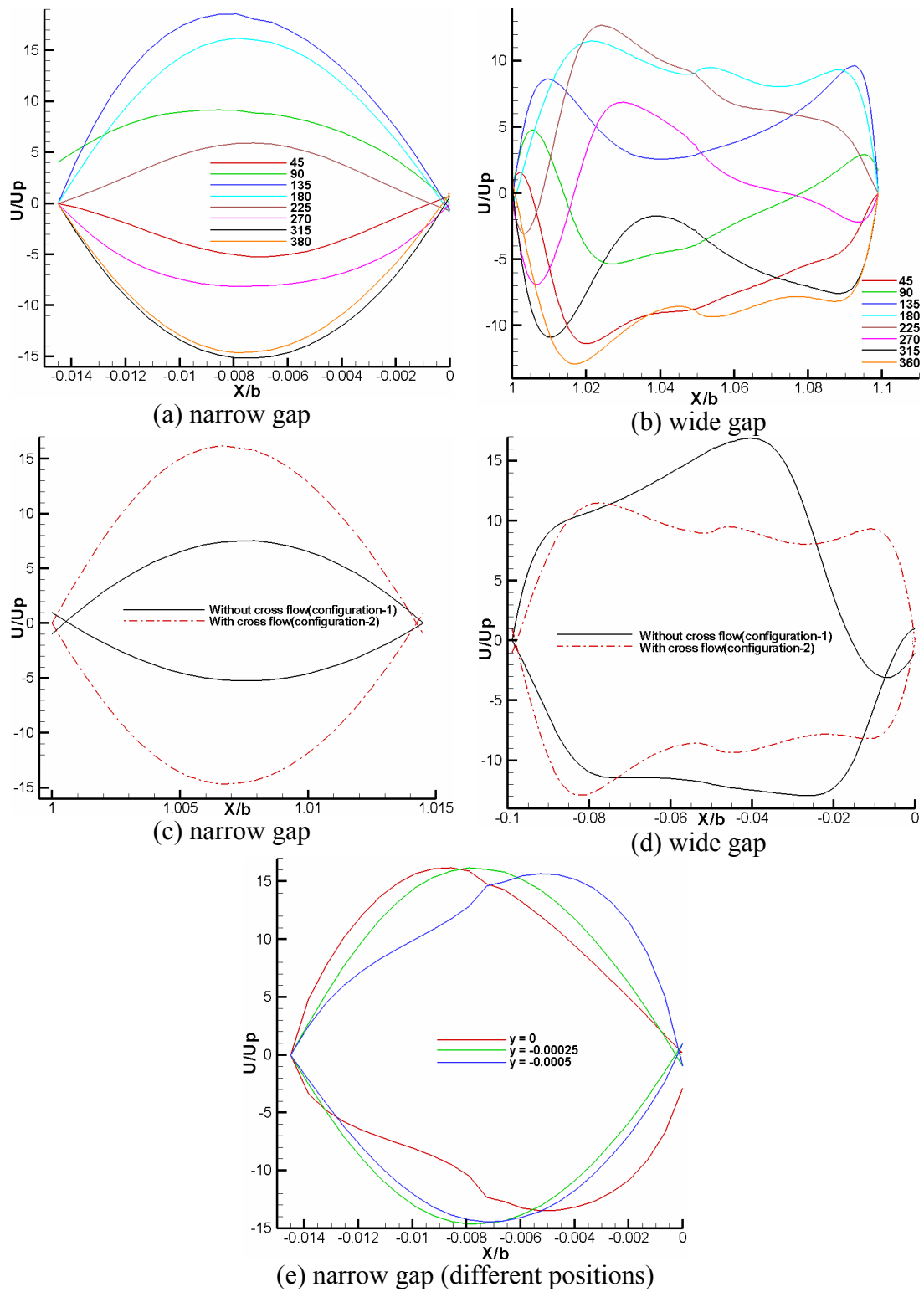


Figure 6.10: Velocity profiles through the narrow and wide gap, 2D configuration-2

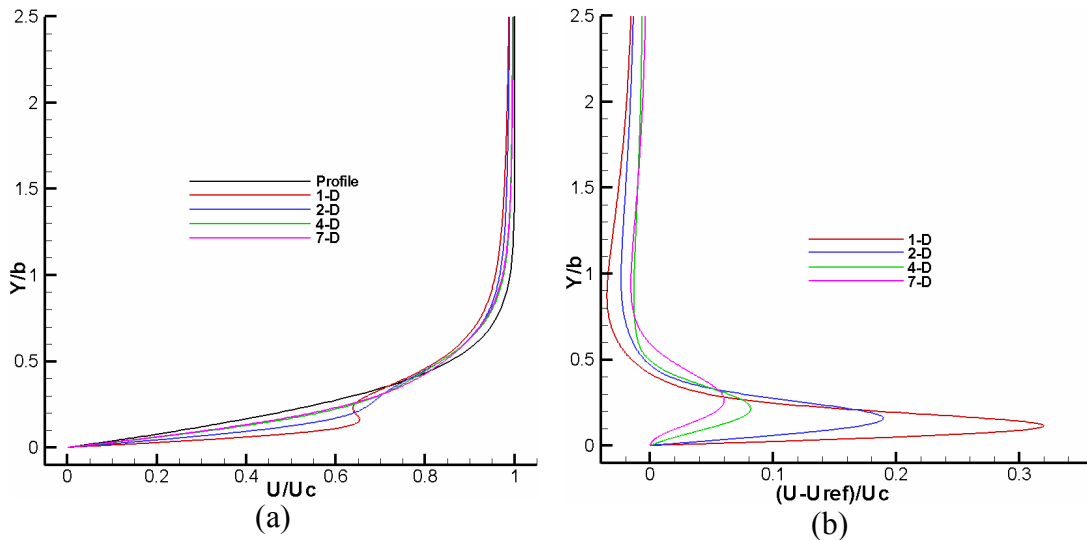


Figure 6.11: Mean velocity profiles at different x - distances, 2-D configuration-2

6.3.3 Direct comparison of the 2D cases

In this section we will compare the results obtained in the previous sections. In Figure 6.12 (a) and (b) velocity profiles in the narrow and wide gap respectively are compared with case 2.2 at phases with maximum plate speed. In the narrow gap both suction and blowing velocities for the cases with cross flow are very high compared to the case without cross flow. Peak velocities are almost twice as large. When we compare the profiles in the wide gap there are two velocity peaks in cases with cross flow while in the case without it there is only one peak during blowing and the profile is flat during suction. Note that in the present cases, there is no reverse flow near the plate in contrast to case 2.2 where there is strong reverse flow near the plate. These comparisons show that the flow through the gaps ‘communicates’ with the cross flow.

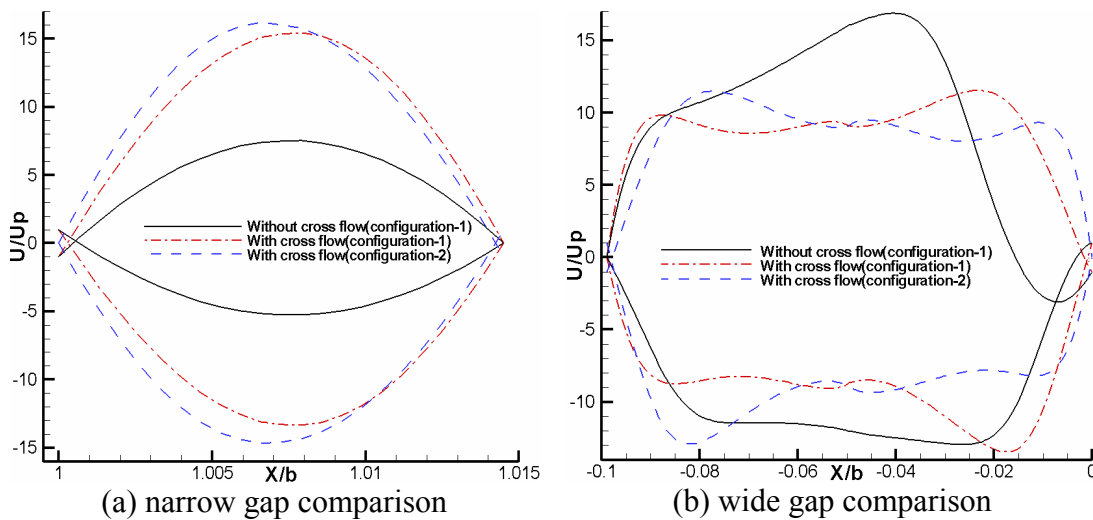


Figure 6.12: Comparison of velocity profiles in narrow and wide gap.

Figure 6.13 shows the comparison of boundary layer velocity profiles at different positions after the actuator for both configurations. We can see that in configuration-1 (red lines) there is no significant difference from the original profile in obvious contrast to configuration-2 where a strong effect of actuation can be seen until the distance $x = 2-D$. The boundary layer profiles of configuration-2 are more attached to the wall compared to the original profile until a vertical distance of $0.5b$, and the velocity is very high until this distance. Afterwards there is a jump and the velocity decreases relative to the original profile. The effect at a distance of $2-D$ is the same but to a lesser extent. Now we can say that the actuator arrangement of configuration-2 can control the boundary layer more efficiently, for the current plate position however Gunes et al. [13] that configuration-1 is better when the JaVA is operating inside the cavity while configuration-2 is better when a considerable part of the JaVA operates “outside” the cavity which is also in agreement of our findings.

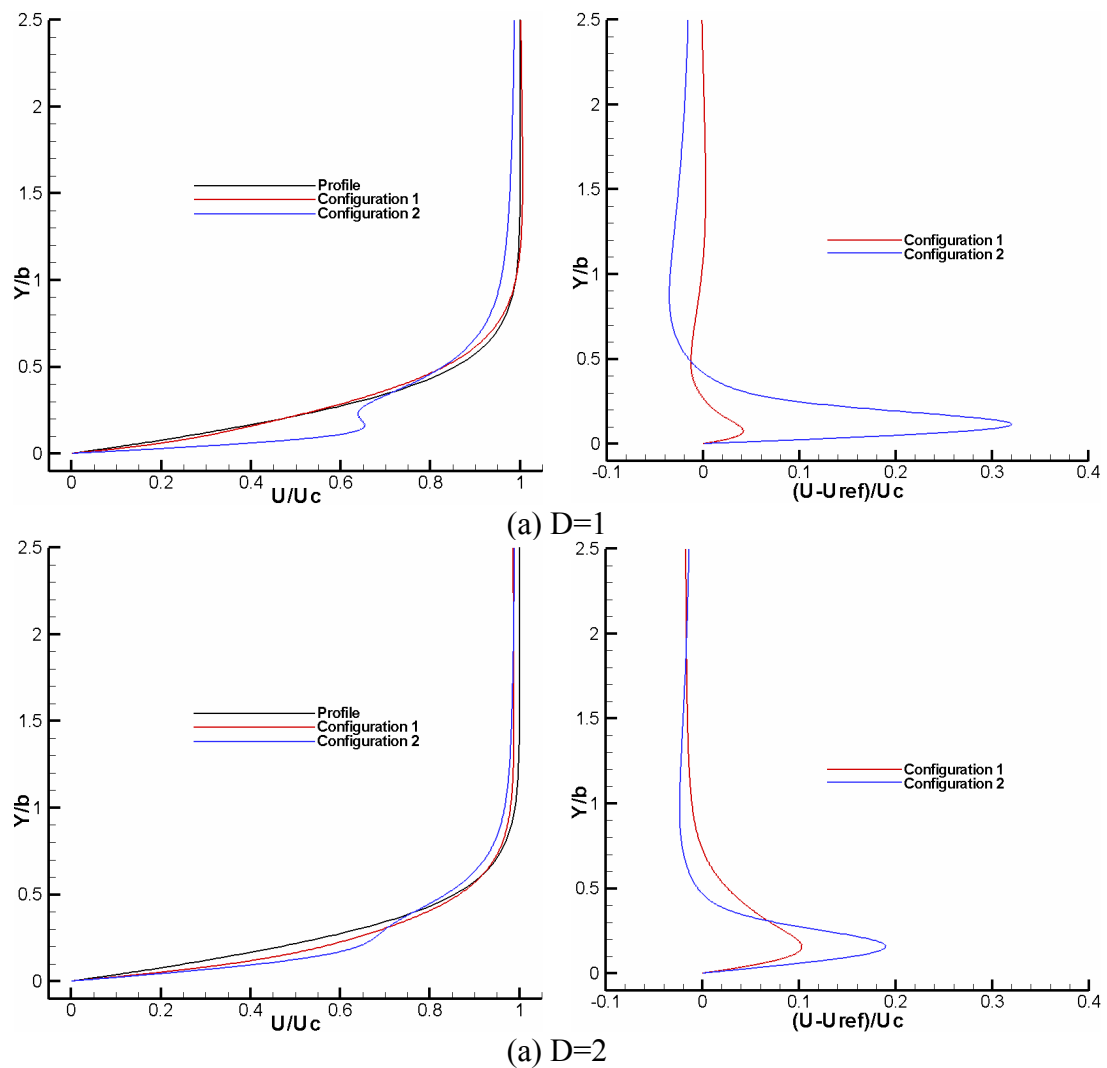


Figure 6.13: Comparison of velocity profiles at different x -positions

6.4 Modified design (2D)

This section will present detailed flow fields for the 2-D modified design. The simulation is performed at a frequency of 128 Hz and scaled amplitude of 0.589 as in case 3.3 with a cross flow velocity of $4.425U_p$. In the present configuration the flow is along the positive x-axis and the same domain size after the actuator is increased to $4.6535D$ in order to cover the downstream boundary layer development to a certain extent. The wide gap is on the left (i.e. upstream) side and the narrow gap is on the right side. At first sight this seems to be a contradiction to the findings of the previous 2-D configuration, where the narrow gap was on the left. Since the narrow gap is the more active in the modified design by definition (because the same mass has to pass through each gap at the same time) this configuration actually mimics the previous one and is thus consistent to that one. Simulation is performed thirty oscillation periods and averaged over the last ten periods. Results presented here are for the last oscillation period.

In Figure 6.14 contours of velocity magnitude at two time instances where the plate velocity is maximum, are shown. At $\theta=180^\circ$, i.e. the suction phase, the boundary layer above the plate is thin and at $\theta=360^\circ$, i.e. the blowing phase, the boundary layer is thick compared to the entrance boundary layer. Zoom-in-views of the same figures along with overlaid velocity vectors are shown in subfigures (c) and (d). At both phases a vortex is present to the right of the narrow gap which is stronger at $\theta=360^\circ$, i.e. in the blowing phase. At the wide gap there is no significant activity, because there is less activity as expected above.

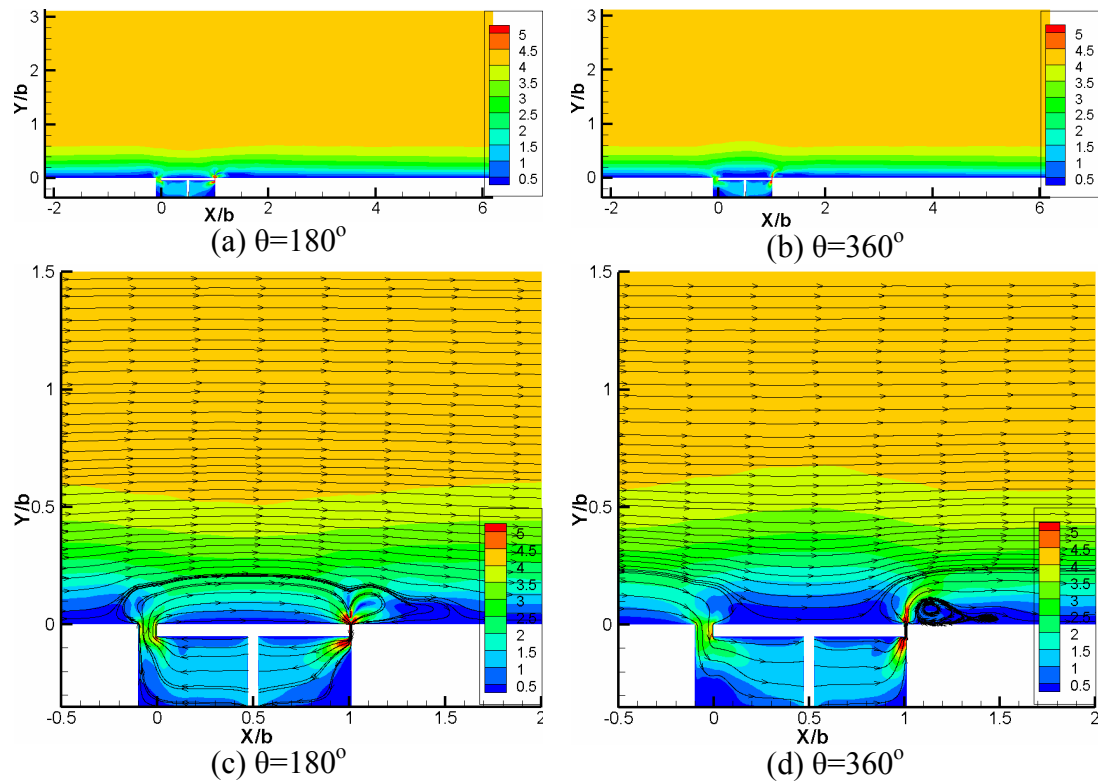


Figure 6.14: Contours of velocity magnitude, modified design, configuration-1

Figure 6.15 shows the contours of mean velocity magnitude. Velocities in the wide gap are very small compared to the narrow gap. Inside the wide gap there is a very weak vortex. A jet emerges from the narrow gap and there is a vortex to the right of the narrow gap.

Next we discuss the details in the gaps. Figure 6.16 (a) and (b) therefore shows the velocity profiles in the wide and narrow gap, respectively at eight different time instances during the 30th oscillation period. As in the case without cross flow, there is no phase shift in the narrow gap. These profiles are symmetric with respect to the gap width. Velocities during the blowing phase are slightly higher compared to the velocities during the suction phase. In the wide gap in subfigure (a) the profiles peaks are relatively flat with relatively small side peaks near the plate and cavity wall. In this case reverse flow occurs only at the phases 90° and 180° which are those phases where the plate is at rest because it changes its direction. In subfigure (c) velocity profiles in the wide gap are compared with the case without cross flow at phases of maximum plate velocity. In the present case the flow is more attached to the walls and the velocity profiles are relatively flat. In subfigure (d) the velocity profiles in the narrow gap are compared with the case without cross flow at the phases of maximum plate velocity. There is no significant difference in the narrow gap except that the

velocity peak in this case is slightly lower. This is in contrast to the original design where the velocity in the narrow gap with cross- flow is very high.

Now we look at the effect of this actuator on the cross-flow boundary layer. *Figure 6.17* shows velocity profiles at different distances after the actuator and compares them with the profile used for the cross flow. $D=1.1135b$ is the actuator width and the boundary layer thickness is $\delta=1.0363b$. Looking at the profiles we can observe that there is no significant change in the profiles after actuation. The difference to the reference flow increases with downstream distance (from 5 to 20%). It is in contrast to the original design. The possible reason is that in this case the domain after the actuator is small (only $5-D$) compared to the original design ($10-D$) due to which effects of outflow boundary are present. If we increase the domain after the actuator, this effect will reduce.

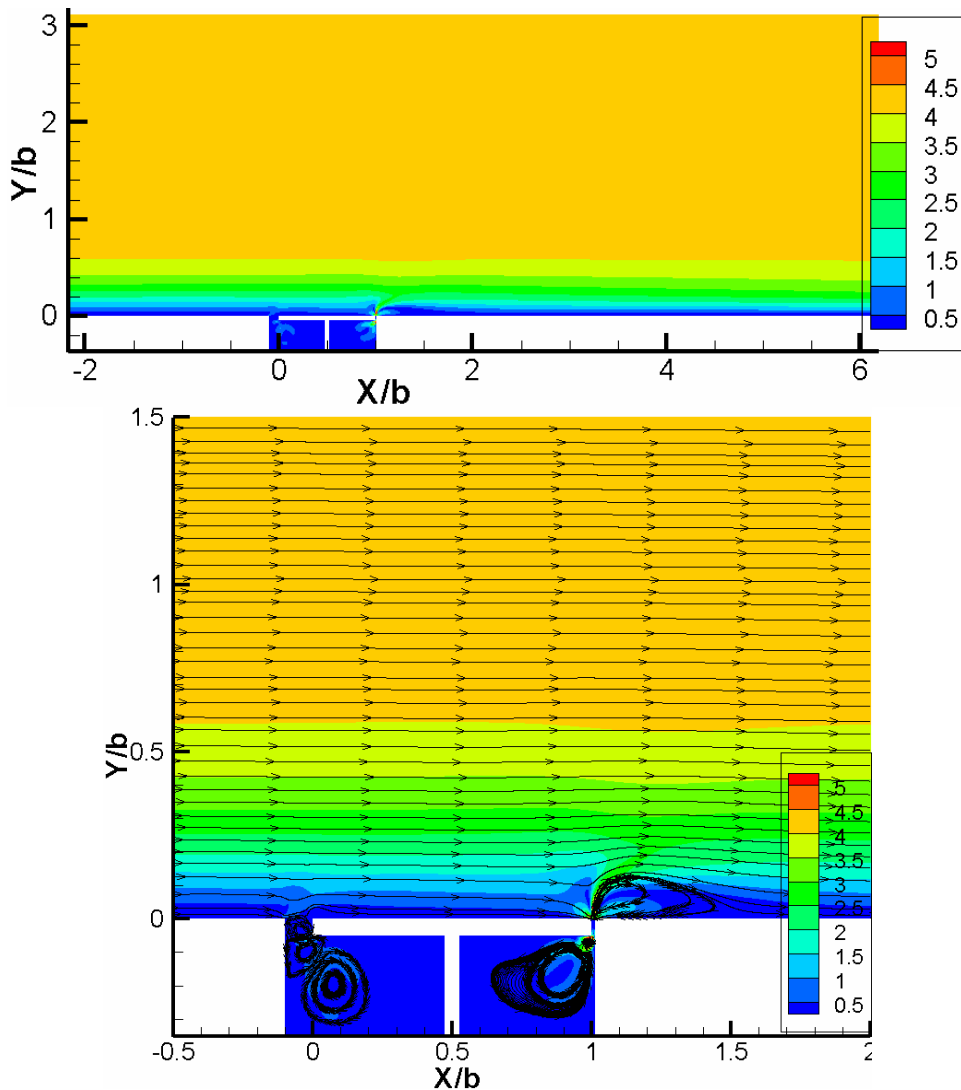


Figure 6.15: Mean velocity magnitude, modified design, configuration-1

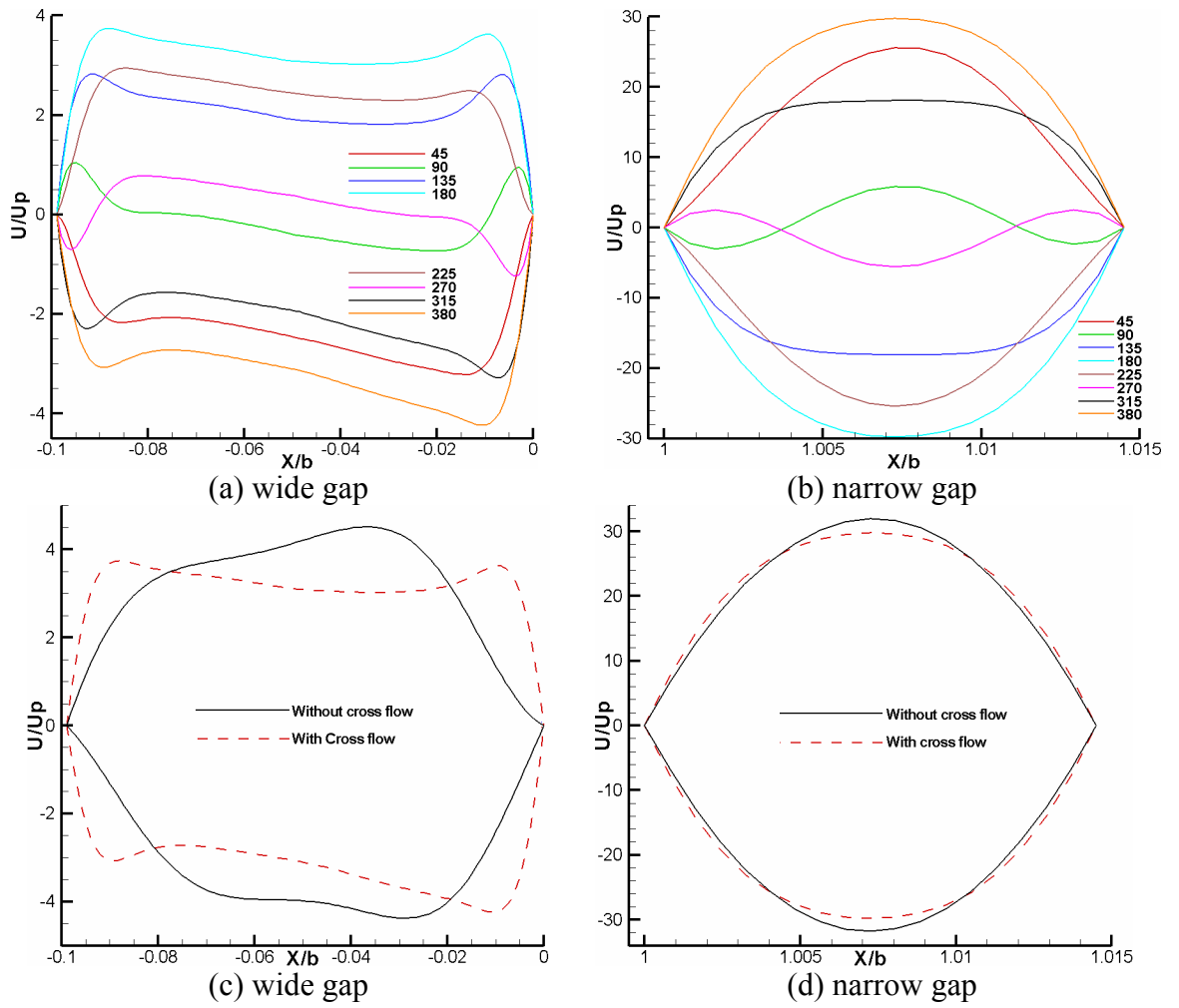


Figure 6.16: Velocity profiles in narrow and wide gap, modified design, configuration-1

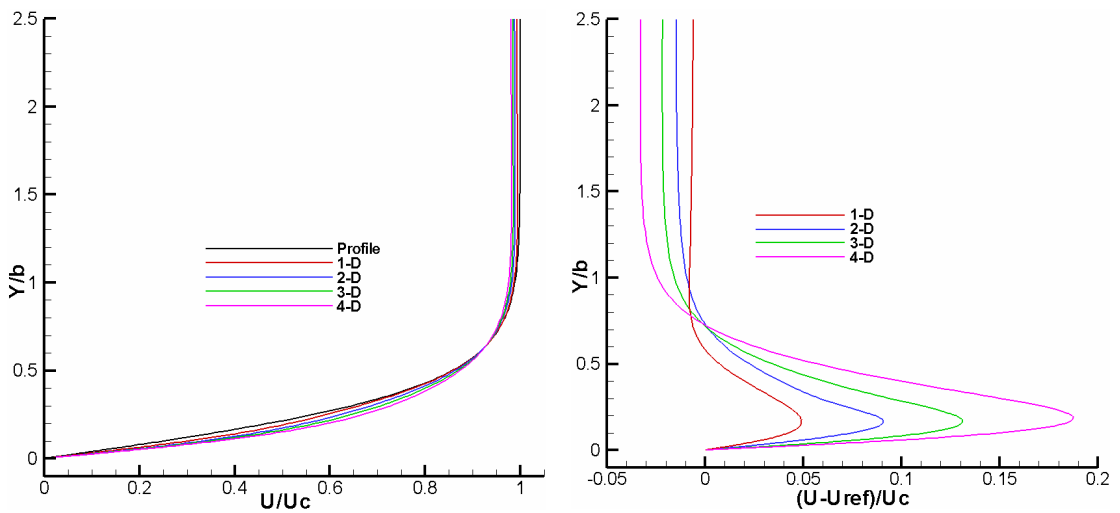


Figure 6.17: Comparison of velocity profiles at different x-positions, modified design, configuration-1

6.5 Modified design (3D)

This section presents detailed 3-D flow fields for the modified design with and without cross flow. A cross flow velocity of $4.425U_p$ is used. Two different actuator arrangements are used, see *Figure 6.1* (d) and (e). In configuration-1 the flow is along the positive x-axis and, as in the 2-D case, across the gaps. The wide gap is on the left side (i.e. it is towards the flow) and the narrow gap is on the downstream side. In configuration-2 (which is now completely different to the 2-D case!) the geometry is rotated about the y-axis in such a way that the cross flow is along both gaps. The domain after the actuator in each case is increased to $4.6535D$ as in the 2-D case in order to capture the flow behavior after the actuator. The length of the gaps is chosen to be twice the extent of the cavity in the other direction.

6.5.1 Without cross flow

In this case the simulation is performed at a frequency of 128 Hz and scaled amplitude of 0.589 as in the 2D case above. The simulation is run for 22 oscillation periods and averaged over the last 4 periods. Results presented here are for the last oscillation period.

In *Figure 6.18* contours of velocity magnitude are shown in cutting planes parallel to the front view (x-y). In subfigure (a) at $z=0$ (i.e. at the edge of the gap) there is no significant activity. At the center plane in subfigure (b) we can see a free jet from the narrow gap. It is different from the 2-D case where we get a vortex with this set of actuation parameters. This difference suggests the presence of strong 3-D effects.

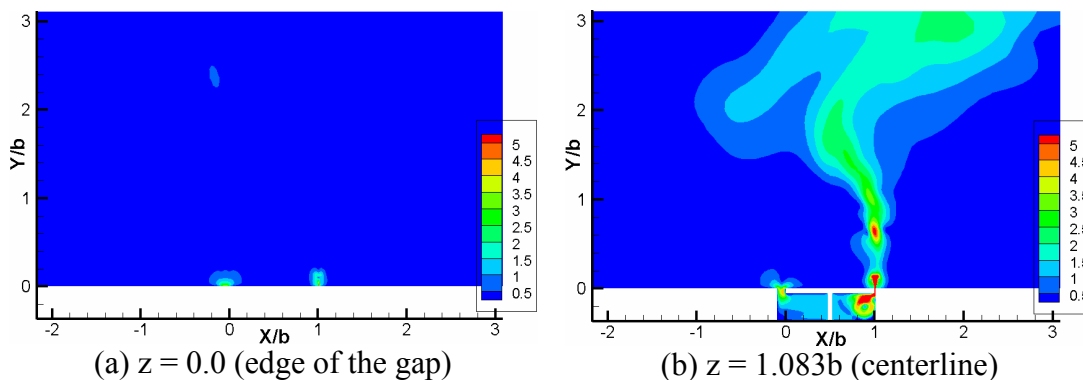


Figure 6.18: Contours of velocity magnitude at different z-positions (front view)

In Figure 6.19 velocity magnitude contours are shown at the center plane at different time instances in order to illustrate how this jet develops. We can see that the jet emerges from the narrow gap and at $t=6T$ and $t=9T$ it try to form a vortex but with the time it converts into a vertical jet. Still, this jet is not constant as it moves towards the right and left after a vertical height of $1.04b$. This jet is almost the same for the last two periods. In *Figure 6.20* contours of mean velocity magnitude at the center plane (front view) are shown. We mainly observe a jet until a height of $y = 1.04b$ after which it spreads. This is due to the fact that the jet oscillates to the left and right with time after this height, as shown in Figure 6.19.

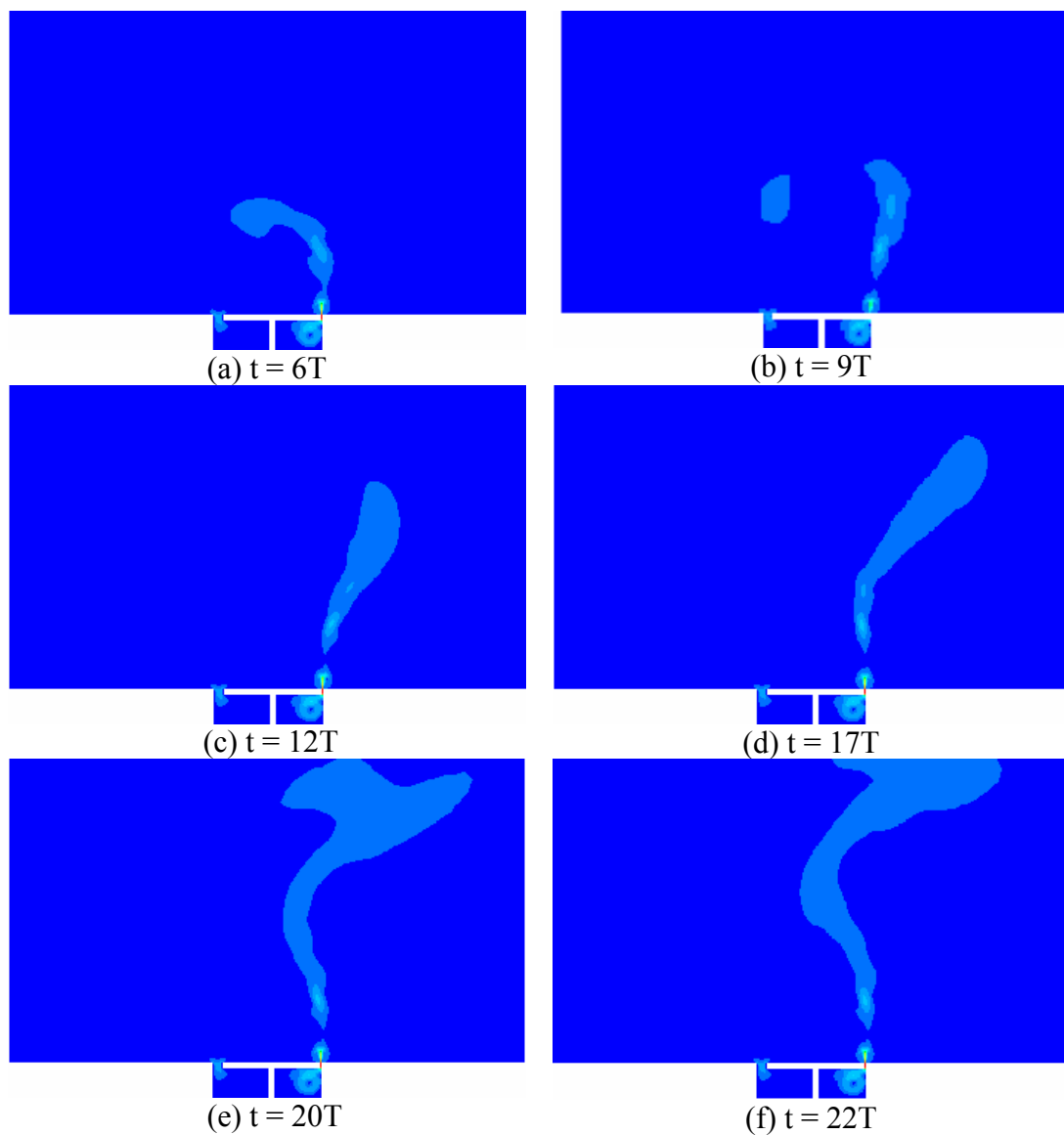


Figure 6.19: Contours of velocity magnitude at different times (front view)

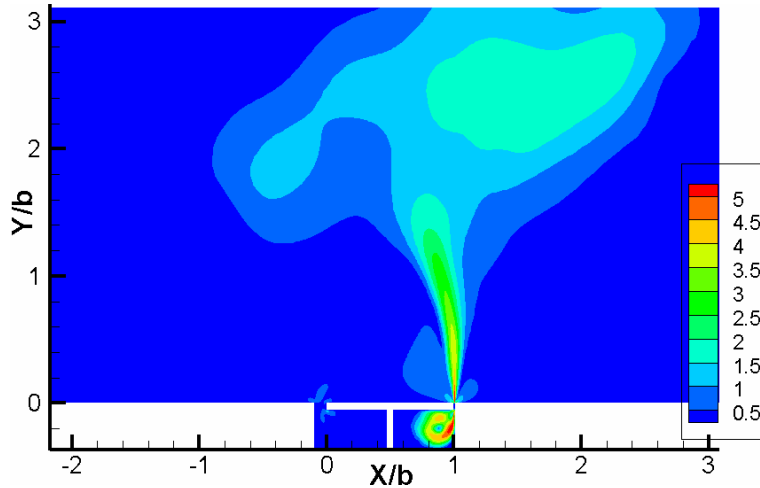


Figure 6.20: Contours of mean velocity front view at $z=1.083b$

In Figure 6.21 contours of mean velocity magnitude at different x -positions (side view) along with contours of x -vorticity are shown. There is no activity in the wide gap. The flow at the top of the wide gap is due to the bending of the jet from the narrow gap. In the narrow gap we can see a sharp jet which converges as it moves away from the actuator. This is the effect of the edges which make the jet converge and rotate inwards at its sides, see subfigure (d).

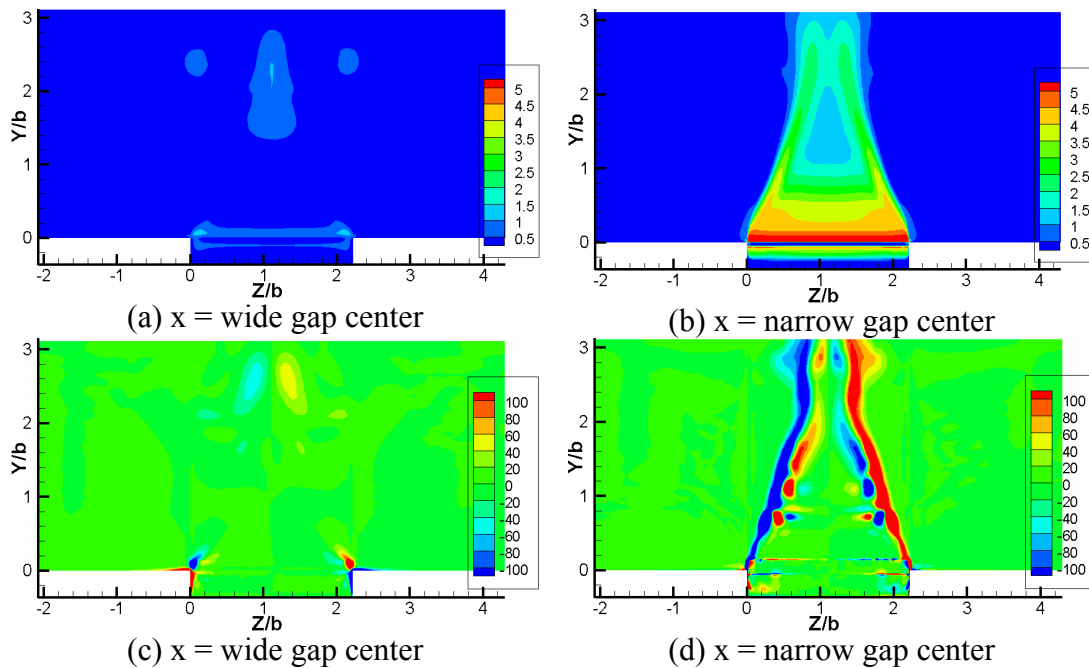


Figure 6.21: Contours of mean velocity magnitude and vorticity about y -axis at different x -positions (side view)

In Figure 6.22 contours of mean velocity magnitude at different y -positions (top view) along with contours of x -vorticity are shown. There is no activity in the wide gap. In the narrow gap we can see a sharp jet which spreads as we move away from the actuator. We can also observe the effect of the edges which causes this jet to rotate inward at the edges.

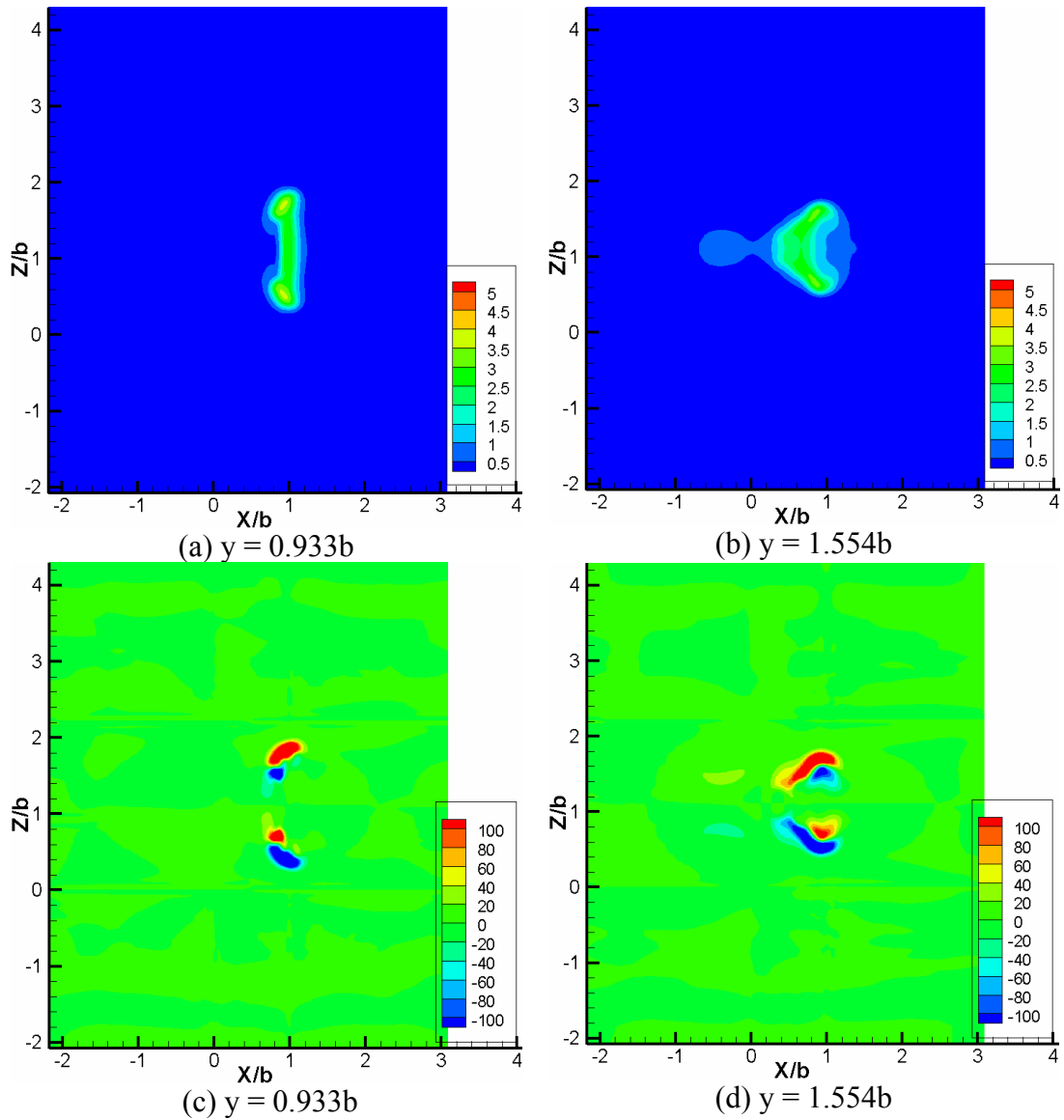


Figure 6.22: Contours of mean velocity magnitude and Vorticity about y -axis at different y -positions (top view)

In Figure 6.23 contours of mean velocity magnitude at different x-positions (side view) are compared with the experimental results by Nies [24], which contains the only available experimental data for the 3D flow structure of this kind of actuator! If one compares subfigures (b) and (d) one can see the same kind of flow, i.e. a very nice qualitative agreement of our simulations with experimental flow visualizations.

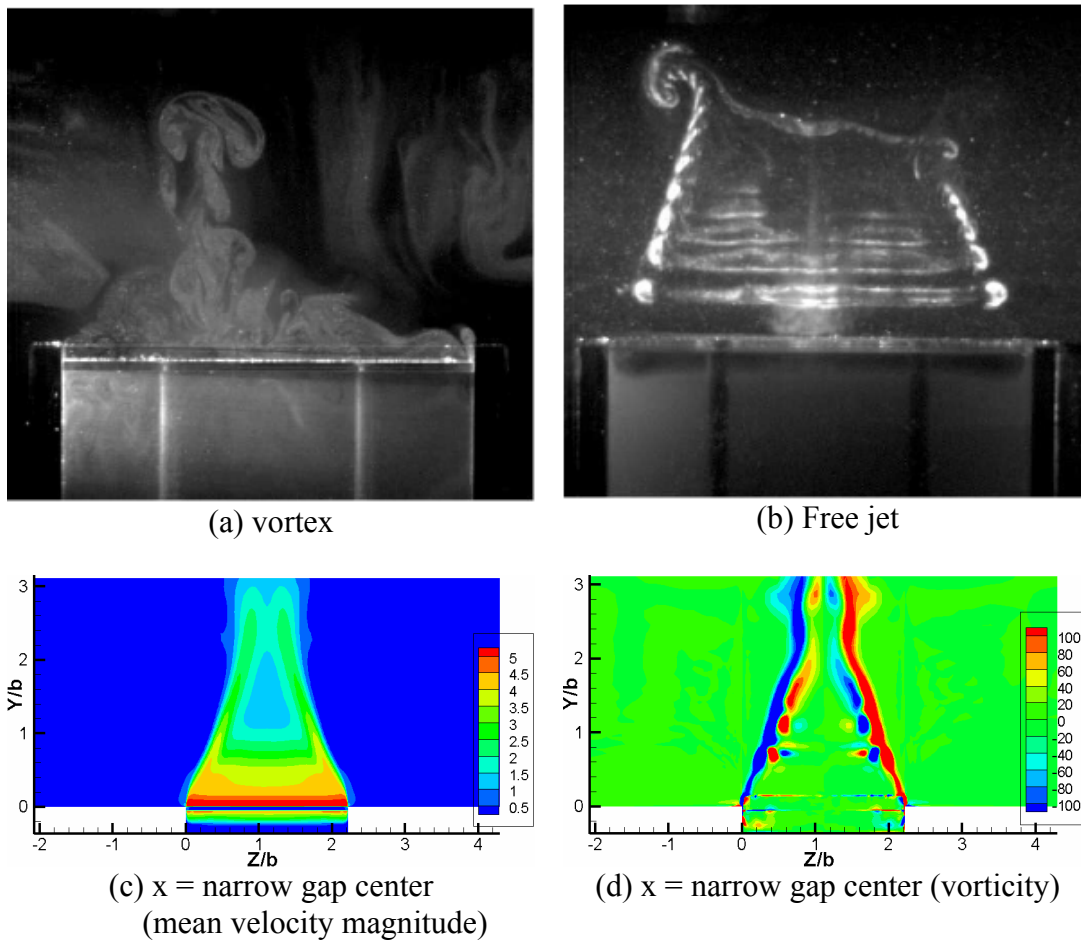


Figure 6.23: Comparison with experiments by Nies [24]

Iso-surfaces of mean velocity magnitude overlaid by contours of velocity and vorticity magnitude are shown in Figure 6.24. The mean-velocity iso-surface of $2.21U_p$ in subfigure (a) splits into two sides further away from the actuator. The high-velocity region of the jet remains very short and extends only for about $0.2b$ from the narrow gap, as illustrated with the iso contour of $4.425U_p$ in subfigure (b). The iso-surface of vorticity magnitude in subfigure (c) is similar to subfigure (a), i.e. it splits into two jets as it goes further away from the actuator.

Next we discuss the details in the gaps. Figure 6.25 (a) and (b) therefore shows the velocity profiles in the wide and narrow gap in stream wise direction, respectively at eight different time instances during the 22nd oscillation period. As in

the case of 2D, there is no phase shift in the narrow gap. These profiles are symmetric with respect to the gap width. Velocities during the blowing phase are slightly higher compared to the velocities during the suction phase. In the wide gap in subfigure (a) the profiles peaks are slightly low. Figure 6.25 (c) and (d) therefore shows the velocity profiles in the wide and narrow gap in span wise direction, respectively at eight different time instances during the 22nd oscillation period. Due to large span wise length of the gaps velocity profiles are flat in both the gaps. Only in the wide gap there is a slight jump of velocity near the edges.

Velocity profiles in the wide and narrow gap for the 2D and 3D simulations are compared in *Figure 6.26*. There is almost complete agreement between the two. This means that 3D effects are not too strong there despite the fact that the edges of the gaps divert the vortex into a jet.

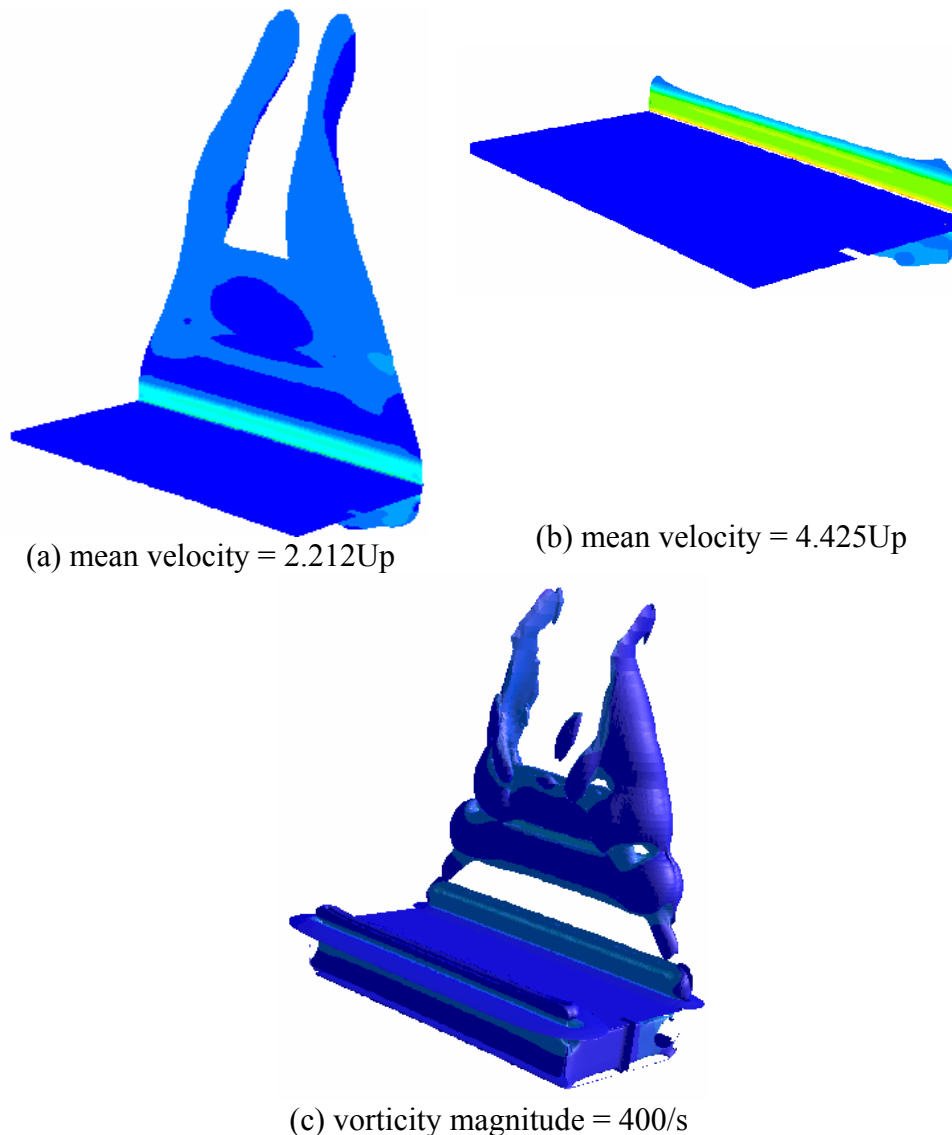
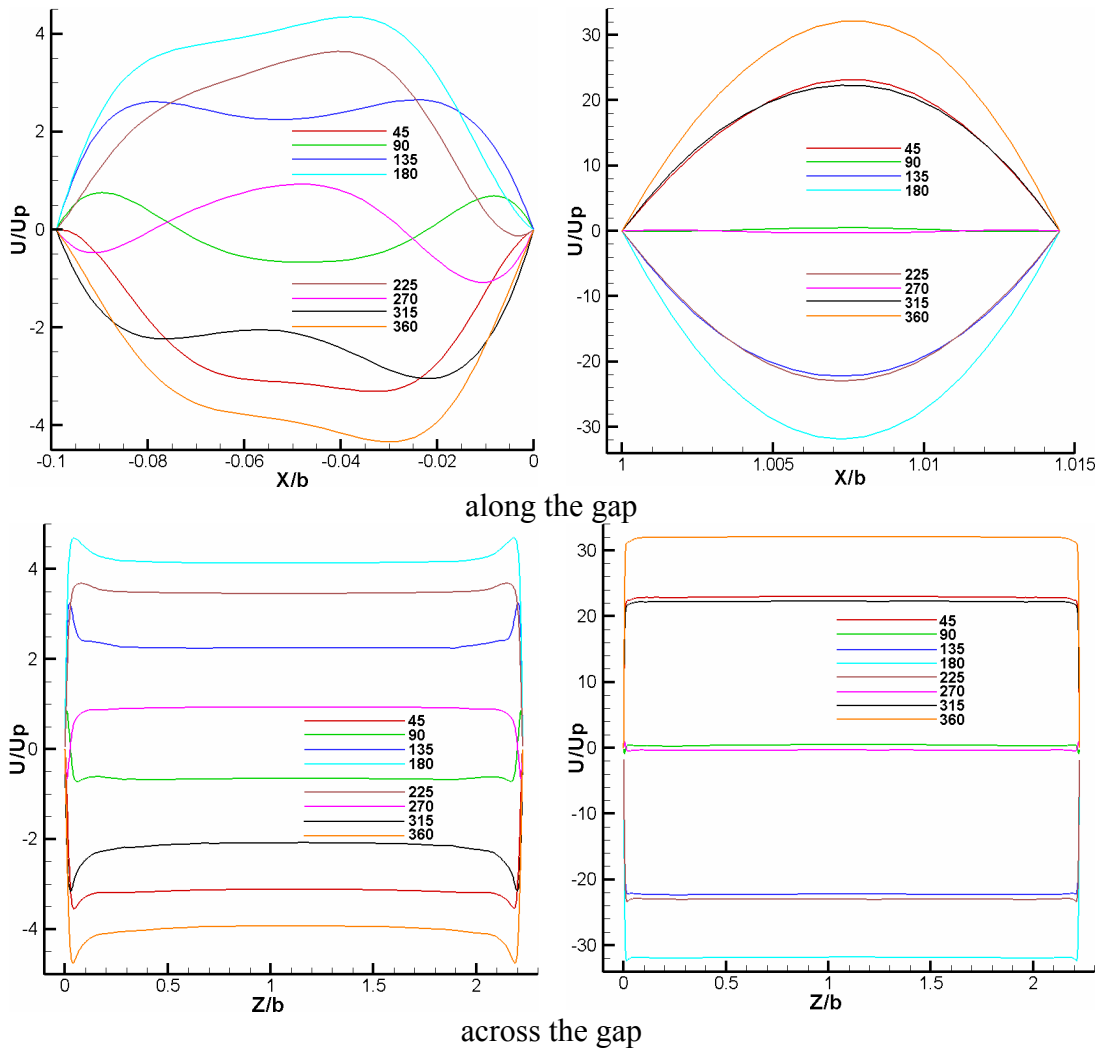
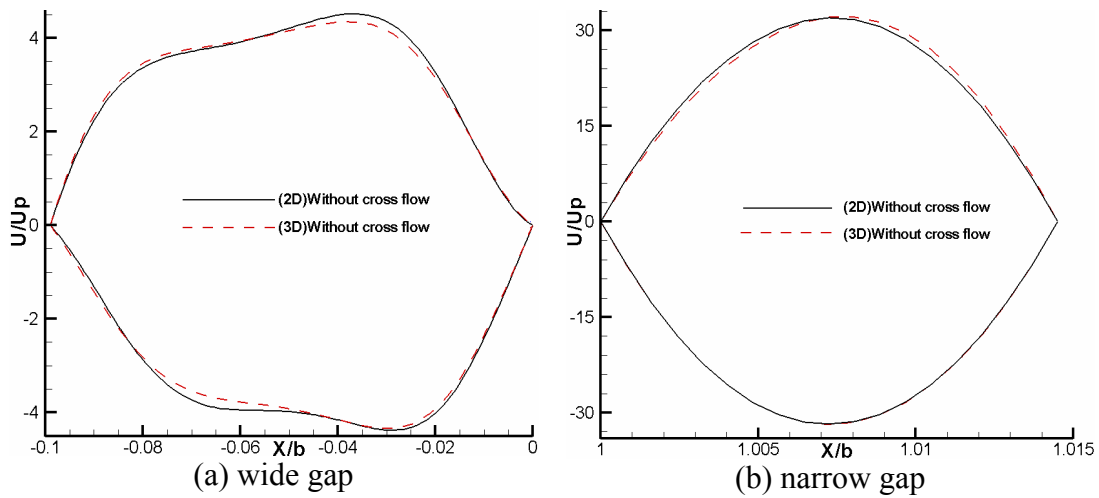


Figure 6.24: Contours of mean velocity magnitude and vorticity magnitude



(c) widegap (d) x = narrow gap
 Figure 6.25 velocity profiles in the narrow and wide gap



(a) wide gap (b) narrow gap
 Figure 6.26: Comparison of velocity profiles in the narrow and wide gap

6.5.2 Configuration-1 (with cross flow)

This section presents detailed flow fields for 3D simulations of the modified design with a cross flow of $4.425U_p$. In this case “configuration 1” means the same arrangement as “configuration 2” in the 2D case further above, see Figure 6.1(d). The flow is along the positive x-axis and as in the 2D case it is across the gaps. The wide gap is on the left side (i.e. towards the flow) and the narrow gap is on the right side, i.e. further downstream. The domain after the actuator is increased to $4.653D$ as in the 2D case in order to capture the flow behavior downstream of the actuator. The gap length in the spanwise direction is twice the diameter of the cavity in the other direction. The simulation is performed at a frequency of 128 Hz and scaled amplitude of 0.589 as in the previous case. It is carried out for 30 oscillation periods and averaged over the last ten periods as in the 2D case. Results presented here are again for the last oscillation period.

Figure 6.27 shows contours of mean velocity magnitude at two cutting planes viewed from the top. From these figures we can see that there is no significant activity at the centerline (i.e. at $z = 1.113b$) but at the edges of the gaps (i.e. at $z = 0$ and $z = 2.226b$), where a weak high-speed streak is produced. This is in agreement with the case without cross flow where we observe the flow at the edges to be stronger compared to the center of the gap. Now here it is confirmed that the spanwise ends of the gaps play an important role in 3D. This can also be seen in Figure 6.28 where contours of mean velocity magnitude are plotted at different z-positions (front view). At $z=0\text{mm}$ (i.e. at the edge of the gap) a strong effect after the actuator can be seen. Moving further away from the actuator we observe that this effect goes more and more into the free stream flow. There is no significant change in the flow behavior after the actuator at the center plane in subfigure (b).

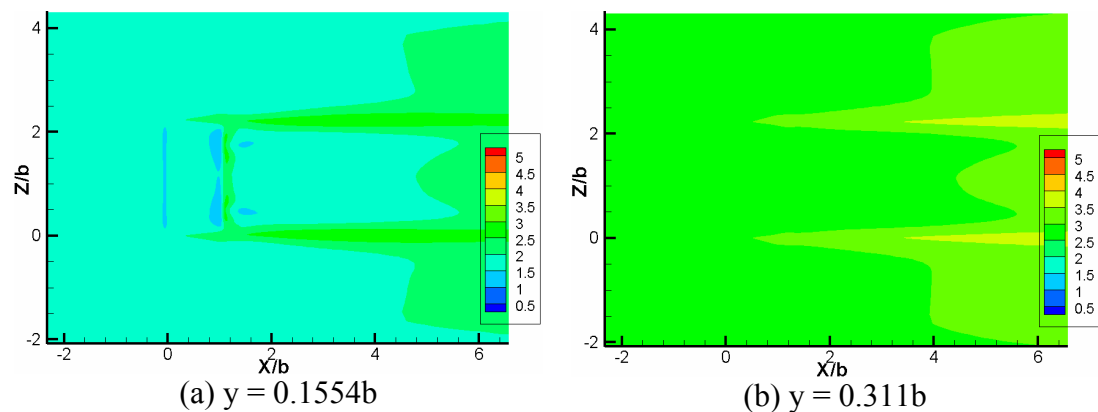


Figure 6.27: Contours of mean velocity magnitude at different y-positions (top view)

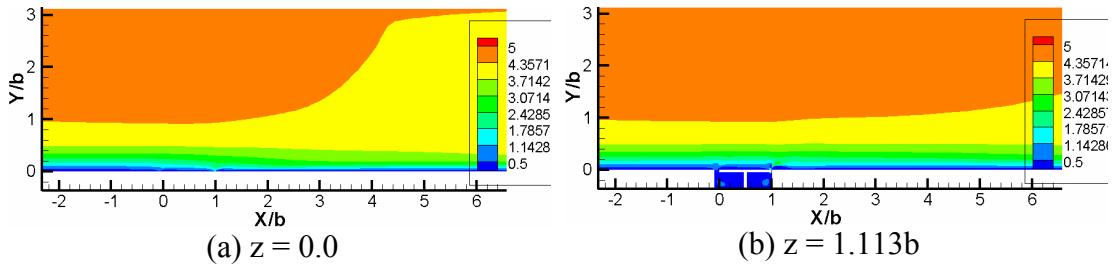


Figure 6.28: Contours of mean velocity magnitude at different z -positions (front view)

The influence of the jet on the boundary layer can be further observed in Figure 6.29 which shows contours of mean velocity magnitude at different x -planes (upstream view). At the narrow gap there is no significant change in the flow behavior but as we move from subfigure (a) to subfigure (d) through subfigure (b) and (c) the effects of the edges become more and more significant. This can be further confirmed in the perspective views in Figure 6.30 which show iso-surfaces of mean velocity magnitude and vorticity magnitude. In subfigure (a) the iso-surface of mean velocity magnitude overlaid by instantaneous velocity magnitude is shown and we can see that the flow at the edges reaches further out compared to the center line of the actuator. In subfigure (b) it is even more evident that the vortex streaks coming out from the edges of the gaps extend far into downstream direction. This is a very important observation and is in agreement with the previous case where there was no cross flow.

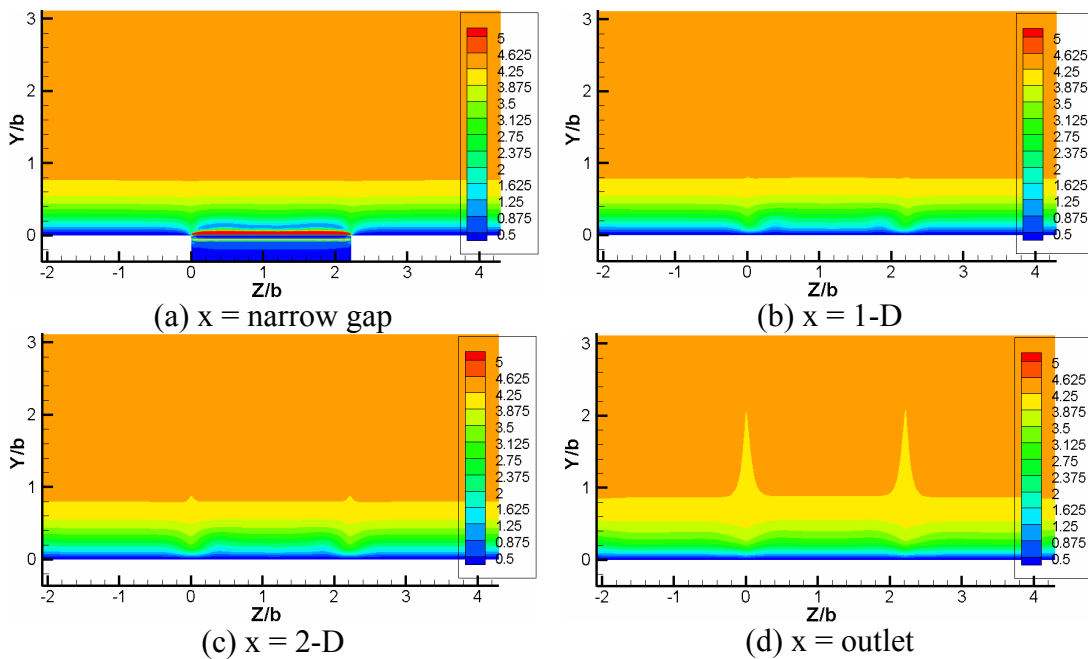


Figure 6.29: Contours of mean velocity magnitude at different x -positions (upstream view)

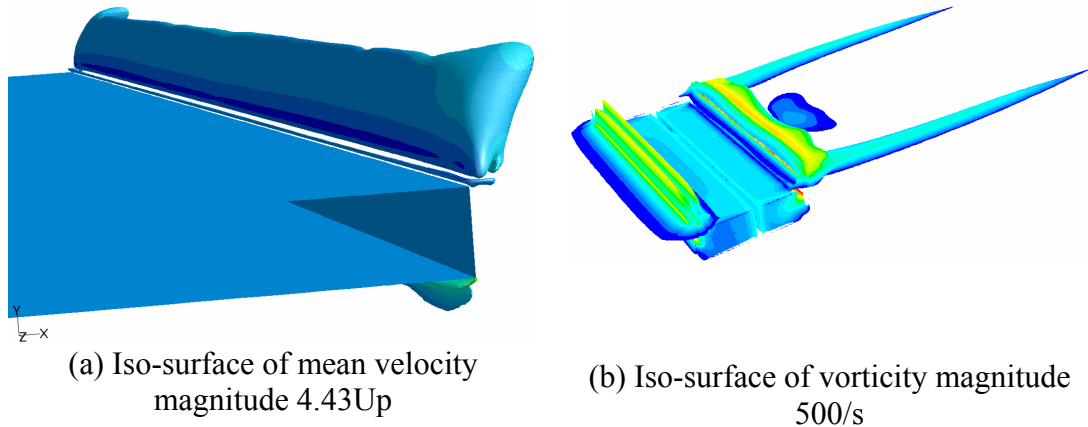


Figure 6.30: Iso-surface of mean velocity and vorticity magnitude (500/s)

Next we show the instantaneous flow but we will not discuss it in details as there is no significant difference to the mean flow. Figure 6.31 gives contours of instantaneous x-velocity at different planes (top and front view). The time instant is when the plate is at its maximum velocity towards the right as it moves through the mean position. Compared to Figure 6.27 there is no significant difference in the contours. We get the same behavior as in the mean flow except in subfigure (a) where there is also some activity at the center of the actuator.

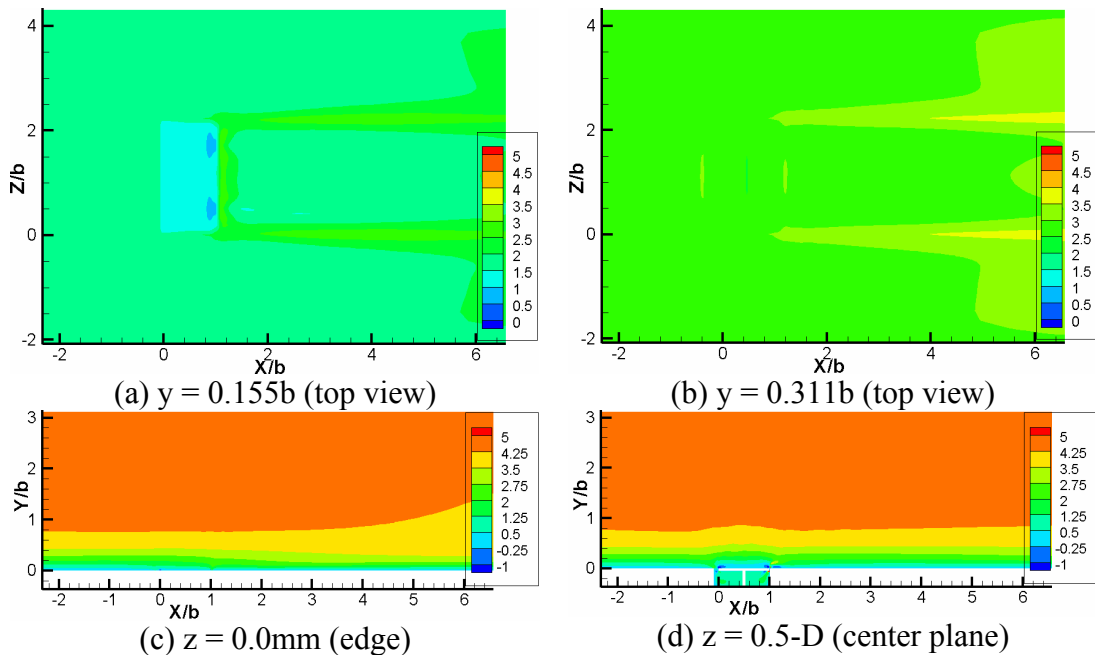
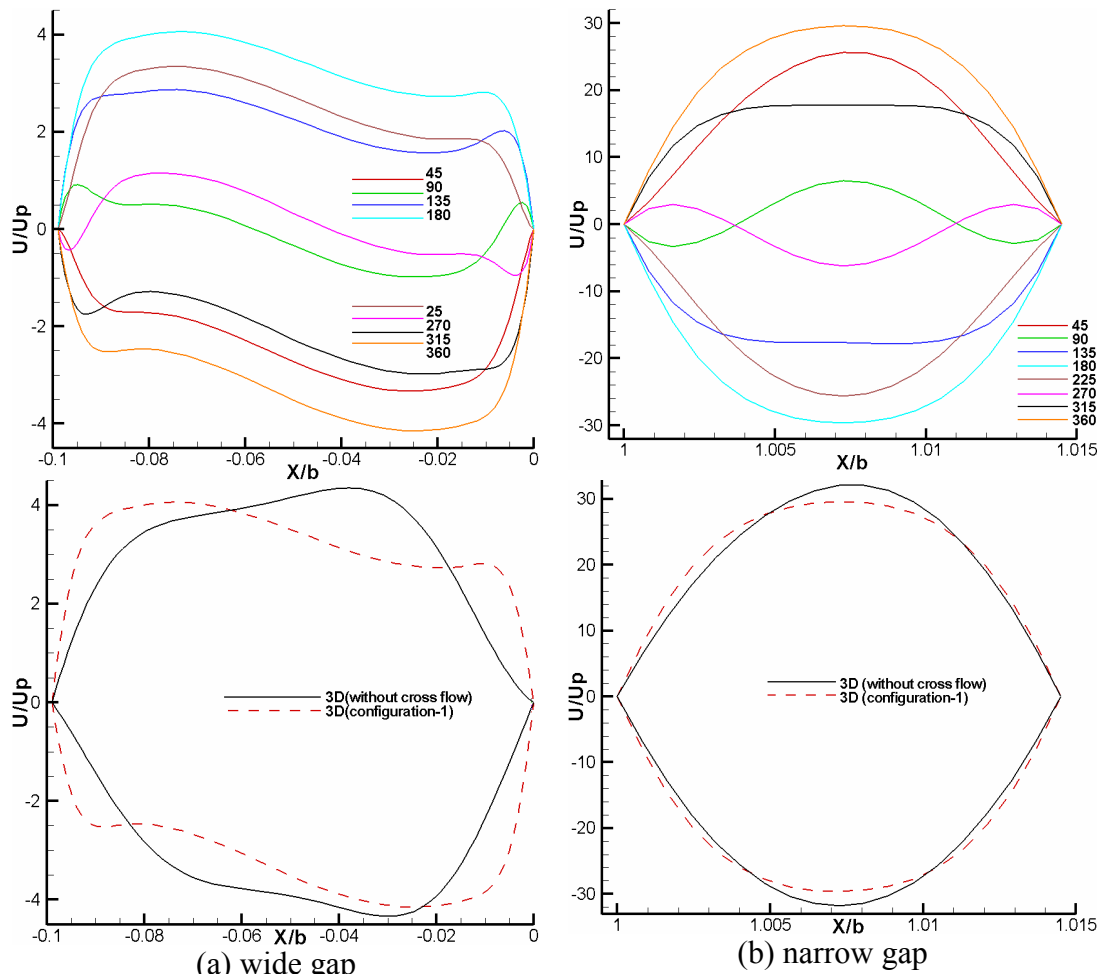


Figure 6.31: Contours of instantaneous x-velocity at different planes

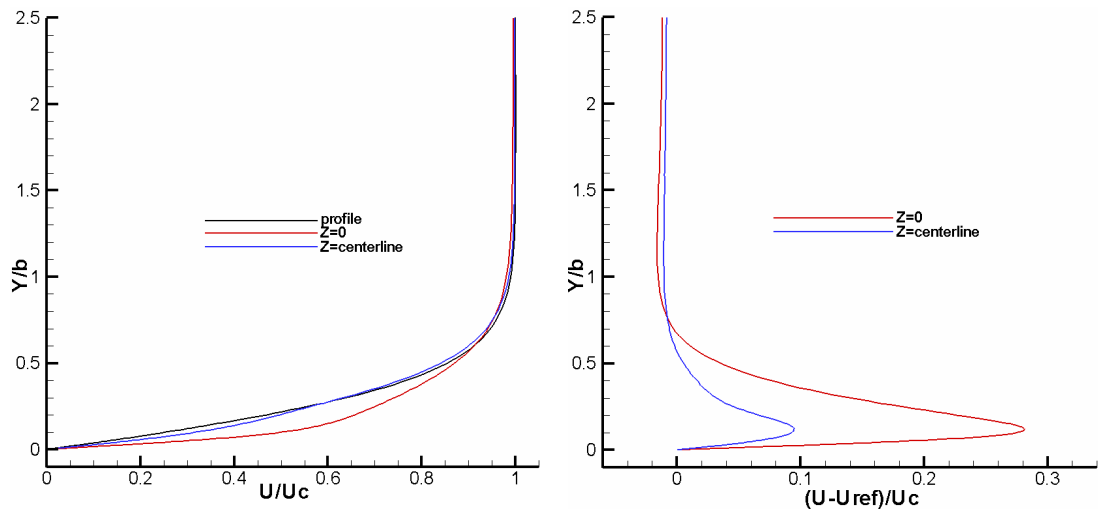
Now we look at more details in the gaps. Figure 6.32 (a) and (b) show the velocity profiles in the narrow and wide gap, respectively at eight different time instants during the 30th oscillation period. In the narrow gap in subfigure (a) there is almost perfect symmetry with respect to space and also with respect to time. In the wide gap in subfigure (b) the profiles are flat. Profiles in the narrow and the wide

gap are compared with the profiles of the previous case without cross flow in subfigures (c) and (d). In the narrow gap there is no significant difference as in the 2D case. Only the velocity peak is slightly lowered by the cross flow. In the wide gap there is a significant difference because the flow velocity peak is almost at the center of the gap in the case without cross flow while it is near the plate during suction and near the cavity wall during the blowing phase in the case with cross flow.

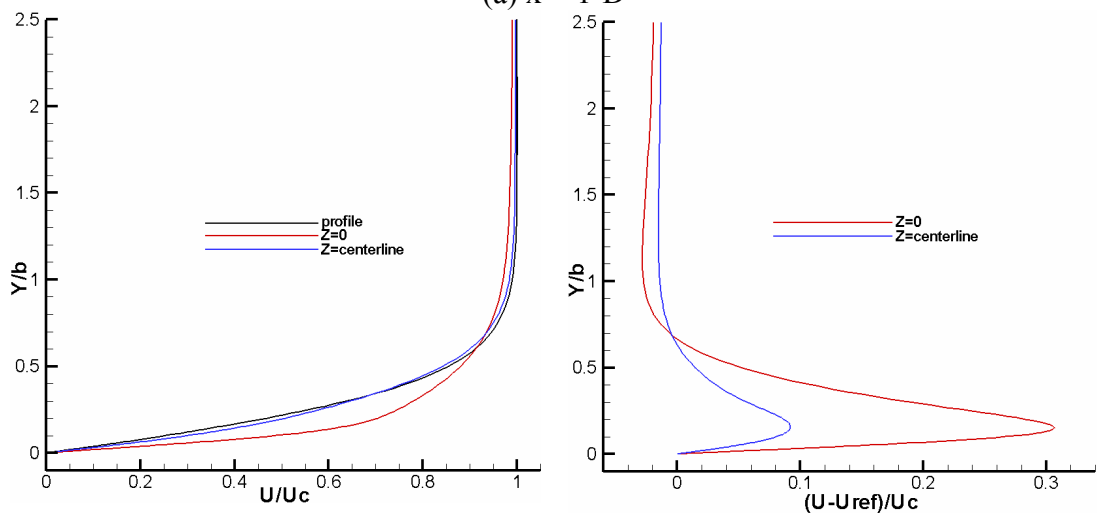
Figure 6.33 shows detailed comparisons of boundary layer velocity profiles at different positions after the actuator. We can see in subfigures (a), (b) and (c) that the centerline boundary layer is not much disturbed by the actuator flow (less than about 5%) while at $z=0\text{mm}$ i.e. at the edge of the actuator (red lines) the boundary layer is fuller compared to the original profile. The difference to the undisturbed profile may reach 25%. This can be further seen in subfigure (d) which compares the velocity profiles at different distances from the actuator directly. This illustrates that the boundary layer becomes fuller as we move further away from the actuator which means that this can be used to delay flow separation.



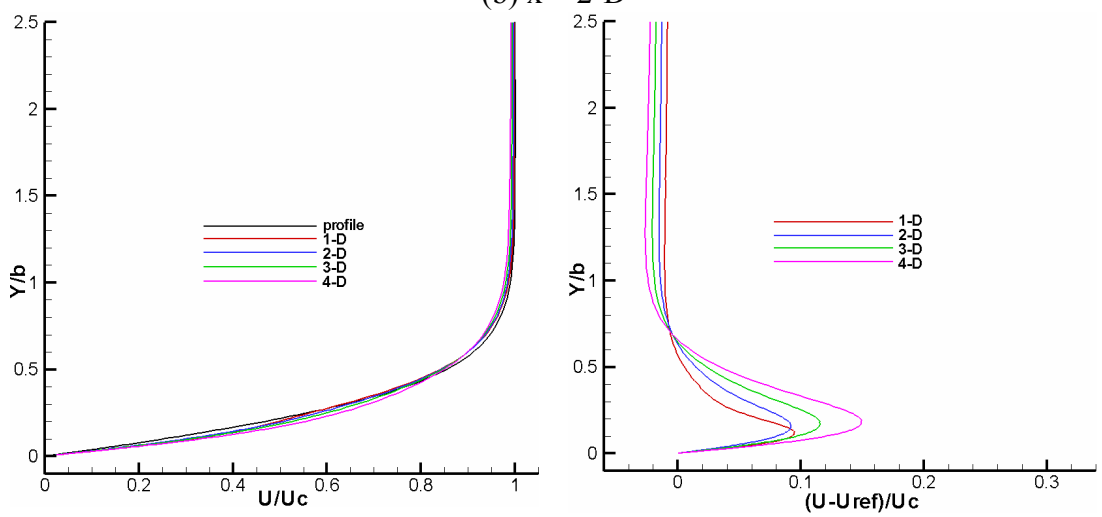
(a) wide gap
(b) narrow gap
Figure 6.32: Velocity profiles in the narrow and wide gap



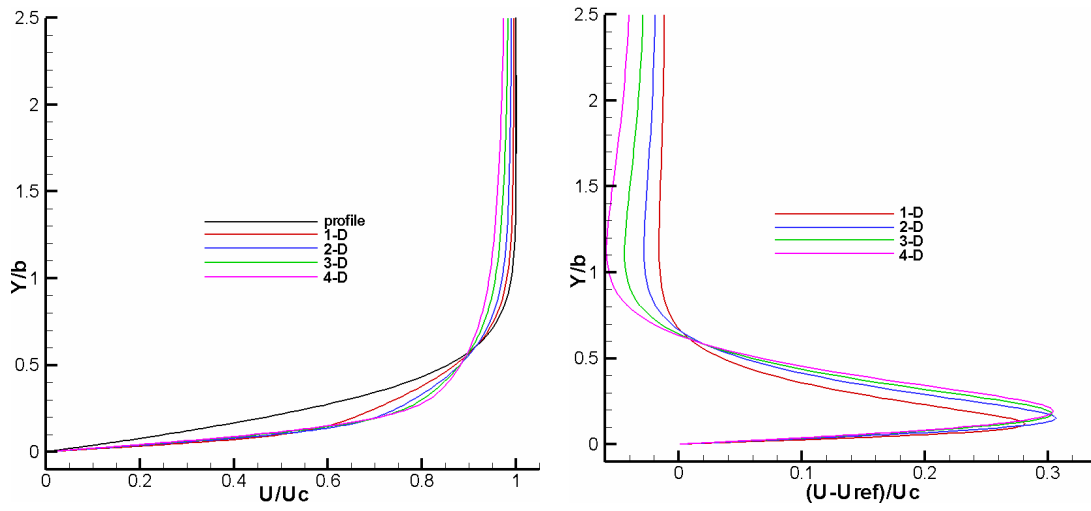
(a) $x = 1-D$



(b) $x = 2-D$



(c) $z = \text{centerline}$



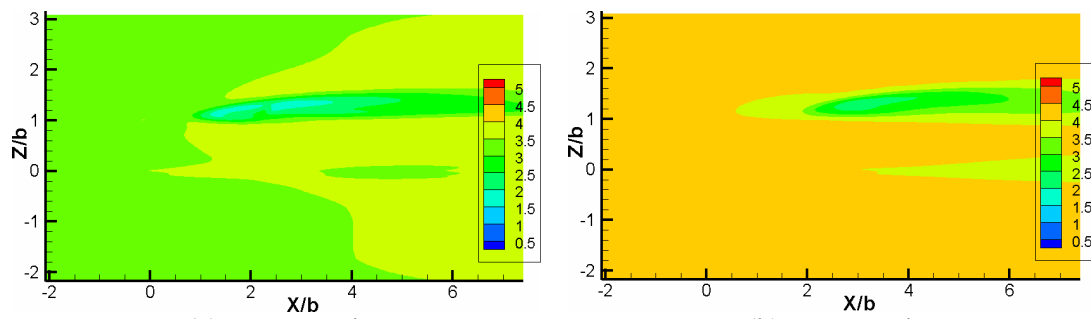
(d) $z = 0.0$

Figure 6.33: Comparison of boundary layer velocity profiles at different stream- and spanwise positions

6.5.3 Configuration 2 (with cross flow)

In this case the simulation is performed for the same conditions as the previous one with only one exception that the gap orientation with respect to the cross flow is changed by 90° , see Figure 6.1e, such that the gaps are oriented along the cross flow direction now! The simulation is performed for thirty oscillation periods and averaged over the last ten periods as before and results of the last oscillation period are presented here.

Figure 6.34 shows contours of mean velocity magnitude at two cutting planes in top view. From these figures we can see that there is no large activity at the centerline (i.e. at $z = 0.5b$) but at the gaps (i.e. at $z = -0.0495b$ and $Z = 1.007b$) a streak is produced which is weaker at the wide gap compared to the narrow gap.



(a) $y = 0.414b$

(b) $y = 0.622b$

Figure 6.34: Contours of mean velocity (m/s) at different y -positions (top view)

Figure 6.35 shows contours of the mean velocity magnitude plotted at different z -positions (in front view, i.e. with the cross flow going from left to right). At $z=0.0495b$ (wide gap center) the effect goes exponentially into the free stream flow after the actuator. Inside the boundary layer a weak vortex streak can be seen until a distance $x=6.2b$. At $z=1.007b$ (center of the narrow gap) the situation is similar to the wide gap: a velocity reduction that extends far into the free stream and vortex streak inside the boundary layer. This vortex turns out to be very strong compared to the one after the wide gap. These effects can be further observed in Figure 6.36 which shows contours of mean velocity magnitude at different x -planes (upstream view). The vortices developing at each gap and the low-speed streaks which extend in vertical direction are clearly observable. It can also be seen that the vortex at the narrow gap is stronger than the one at the wide gap. A closer inspection revealed that these vortices rotate clock wise and the right one moves towards the right as the cutting plane moves downstream. This can be further seen in Figure 6.37 which shows iso-surfaces of mean velocity magnitude and vorticity magnitude. In subfigure (a) the iso-surface of mean velocity magnitude overlaid by instantaneous velocity magnitude is displayed and we can see that the strongest ejection is from the narrow gap. At the same time this is rather constant over the entire length of the gap. Iso-surfaces of vorticity magnitude overlaid by velocity magnitude in subfigures (b) and (c) make the vortical motions more evident (as well as the vortex inside the actuator cavity). The vortex at the narrow gap is strong and goes all the way to the outlet boundary in contrast to the one at the wide gap which is weaker and diminishes before reaching the outlet boundary. This is a very important observation.

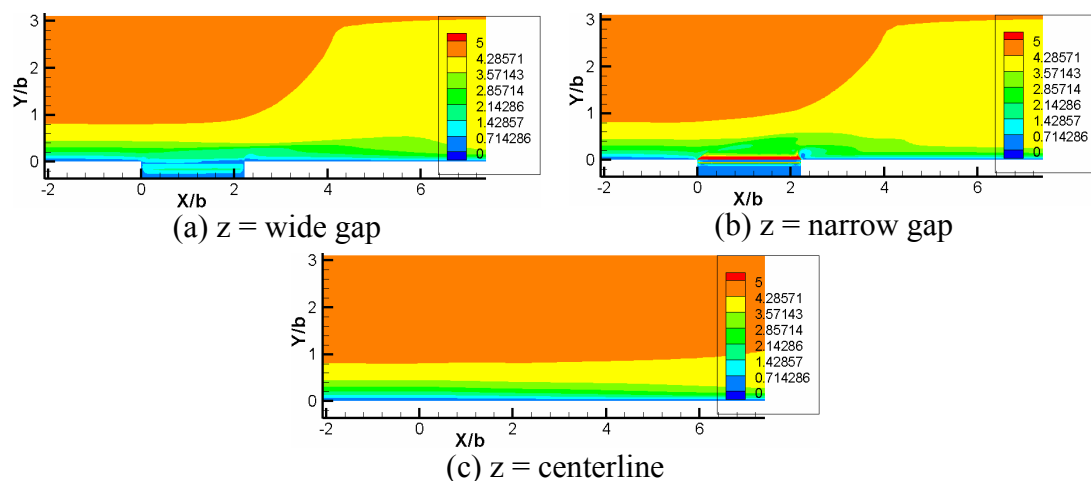


Figure 6.35: Contours of mean velocity (m/s) at different z -positions (front view)

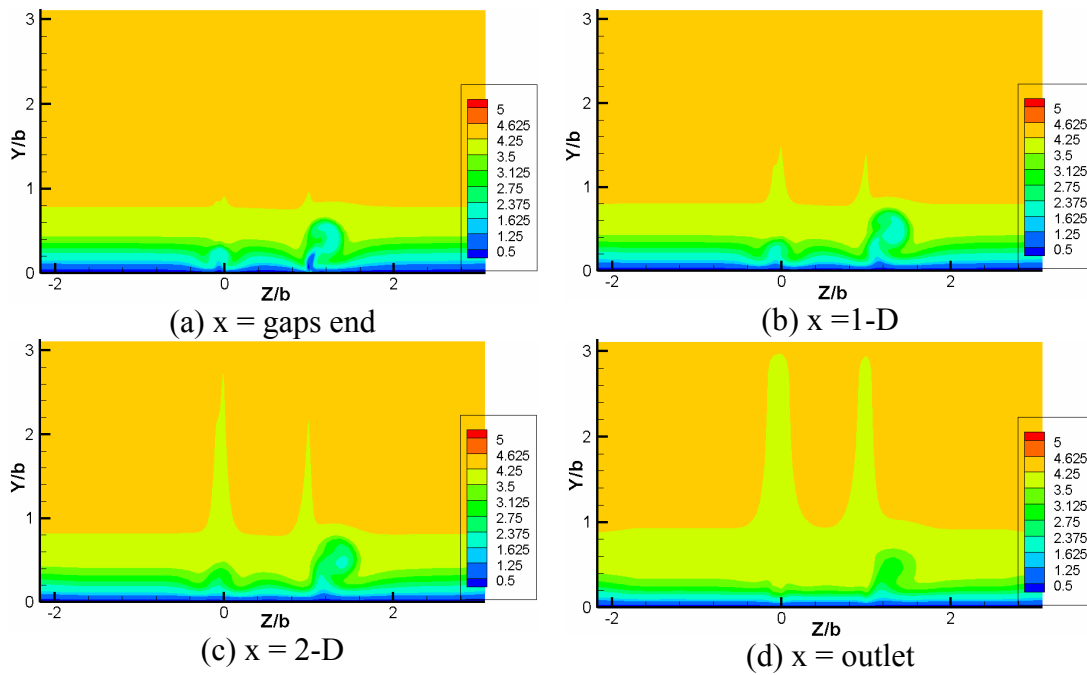


Figure 6.36: Contours of mean velocity (m/s) at different x -positions (upstream view)

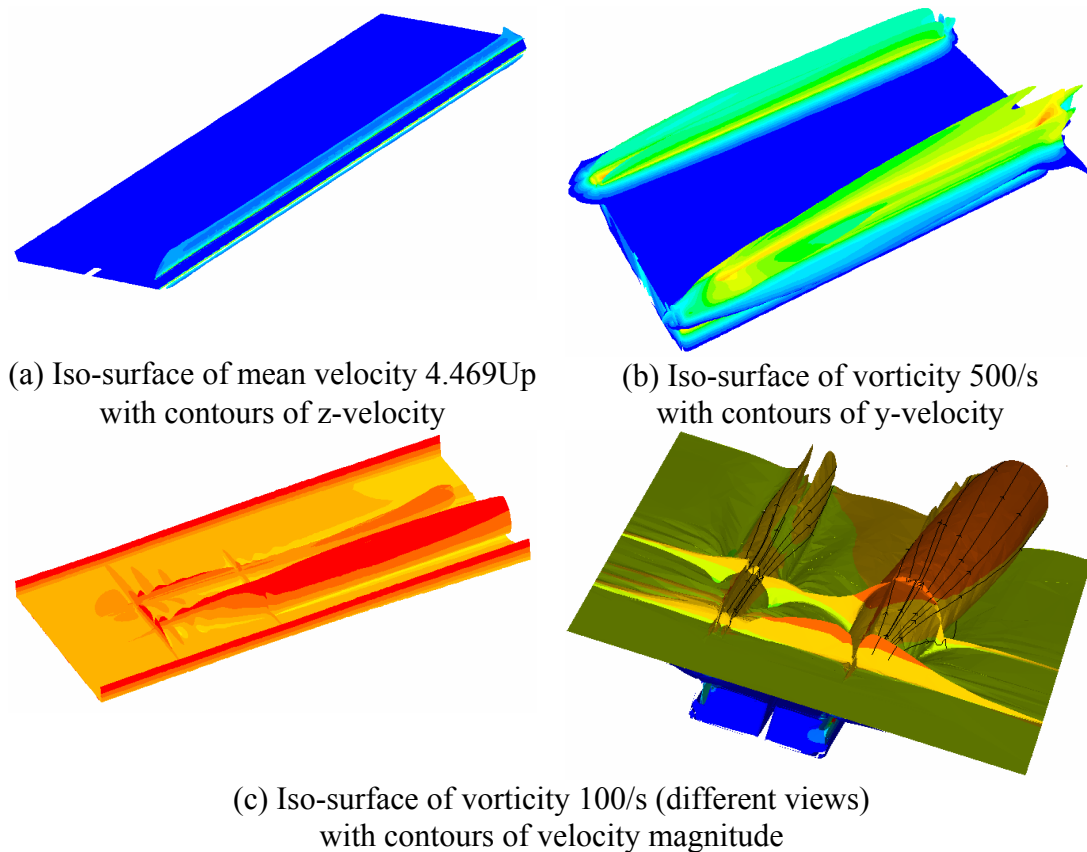


Figure 6.37: Iso-surfaces of mean velocity magnitude and vorticity magnitude

Now we look at the instantaneous flow field in more detail. *Figure 6.38* and *Figure 6.39* show contours of instantaneous z -velocity and streamwise vorticity, respectively at different planes viewed in upstream direction. Here we see the vortex

emerging from the narrow gap quite clearly: the according structures are larger and more intense than at the wide gap (on the left). The contours of spanwise velocity in *Figure 6.38* (a) through (d) indicate a positive spanwise motion (red) with according negative velocity (blue) around it. This is typical for a ring-like vortex. The corresponding stream wise vorticity maxima are shown in *Figure 6.39*. At the wide gap (at negative z coordinates in the figures) the secondary flow induced by the actuator always stays local, i.e., there is no strong vortex that detaches from the actuator outlet, only shear near the left and right of the outlet.

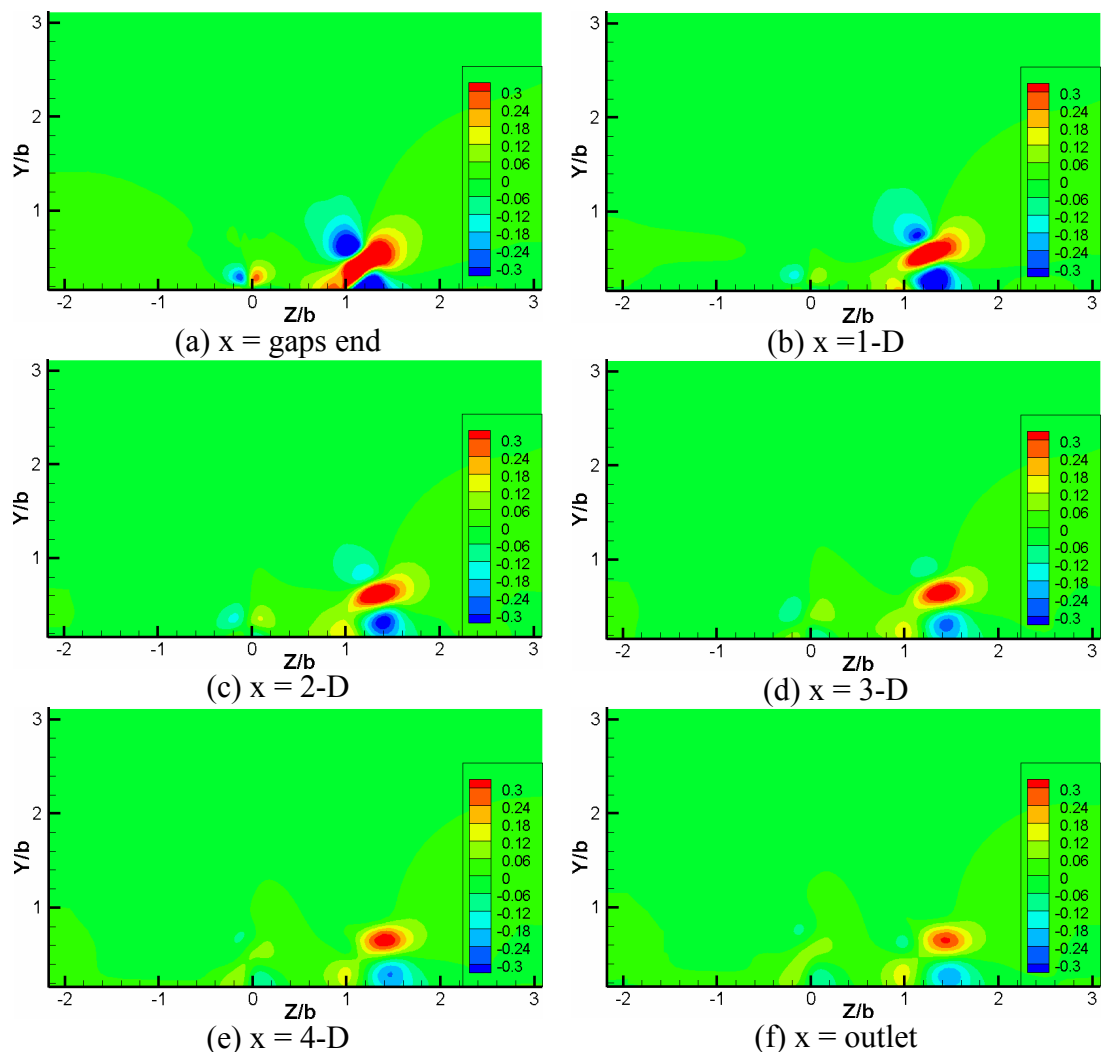


Figure 6.38: Contours of z -velocity (m/s) at different x -positions (upstream view)

The effect on the spanwise shear (i.e. the boundary layer) is illustrated in *Figure 6.40* for two cuts downstream of the actuator viewed in upstream direction. This shows two things: The local deformations of the boundary layer by the flow from the gaps and the deformation of the boundary layer downstream of the actuator position (i.e. between the gap positions at $z \approx 0$ and $z \approx 1.04b$). Actually, the latter effect

extends beyond the mere actuator position to $-0.4b < z < 1.85b$. This visualization confirms the presence of a longitudinal vortex at $z > 1.04b$ which induces additional spanwise shear at the boundary layer edge.

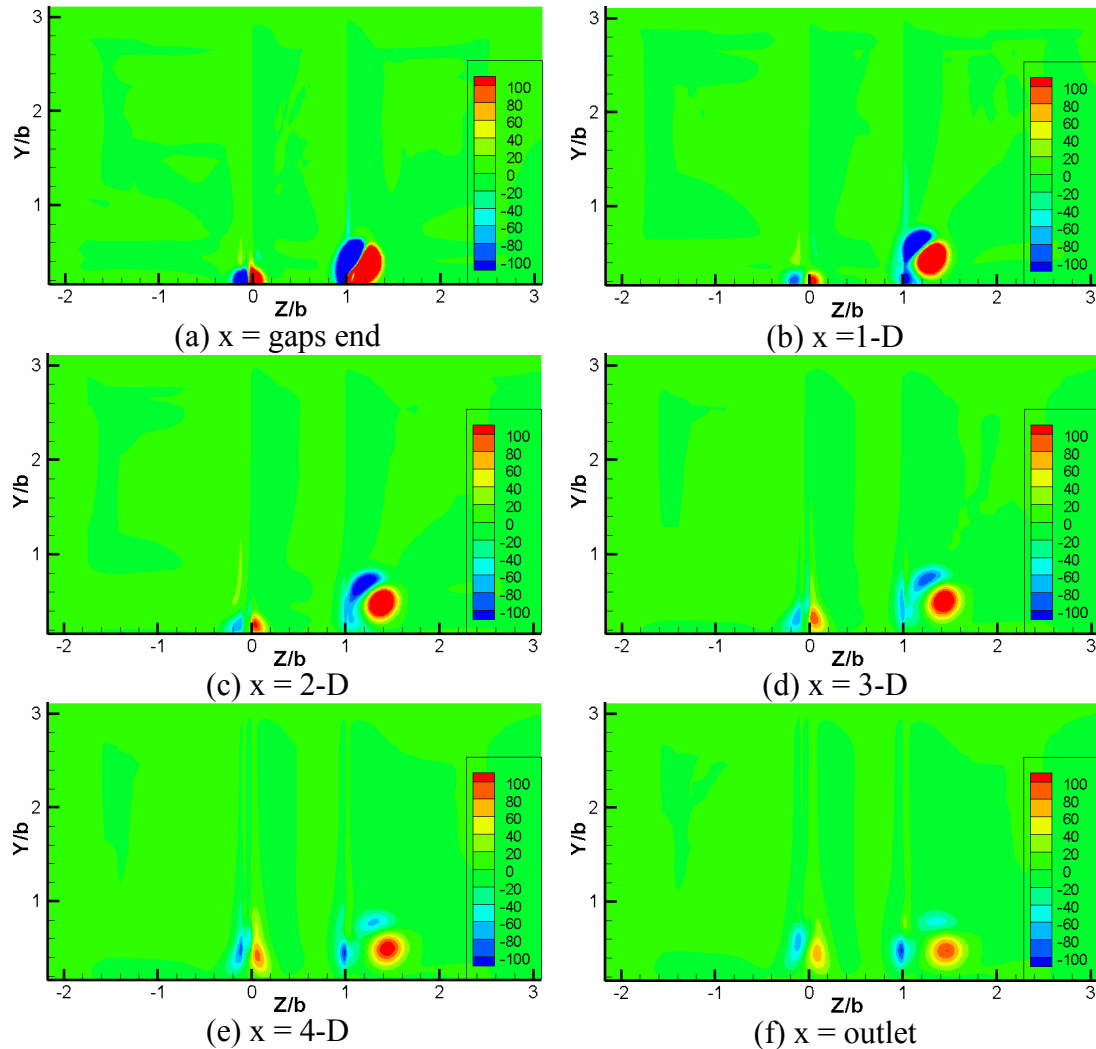


Figure 6.39: Contours of x -vorticity at different x -positions (side view)

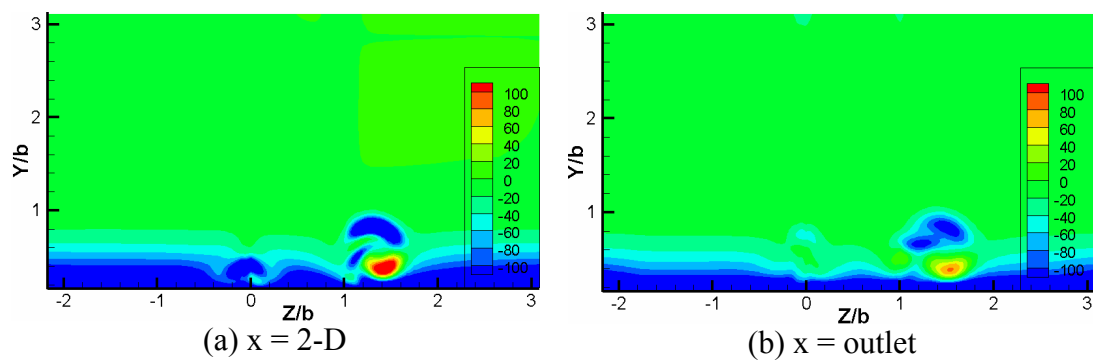


Figure 6.40: Contours of z -vorticity at different x -positions (upstream view)

The next series of figures presents the flow in the gaps, first for the velocity profiles in the narrow and wide gap in Figure 6.41 (a) and (b) respectively at eight different time instances during the 30th oscillation period. In the narrow gap in subfigure (a) there is almost perfect symmetry with respect to space and also with respect to time as in the previous case. In the wide gap in subfigure (b) the profiles are flat and antisymmetric. Profiles in the narrow and wide gap are compared with the profiles of configuration-1 in subfigures (c) and (d). It is surprising that changing the orientation of the gaps with respect to the cross flow has no influence on the gap profiles despite the largely different effects upon the boundary layer flow of these two orientations.

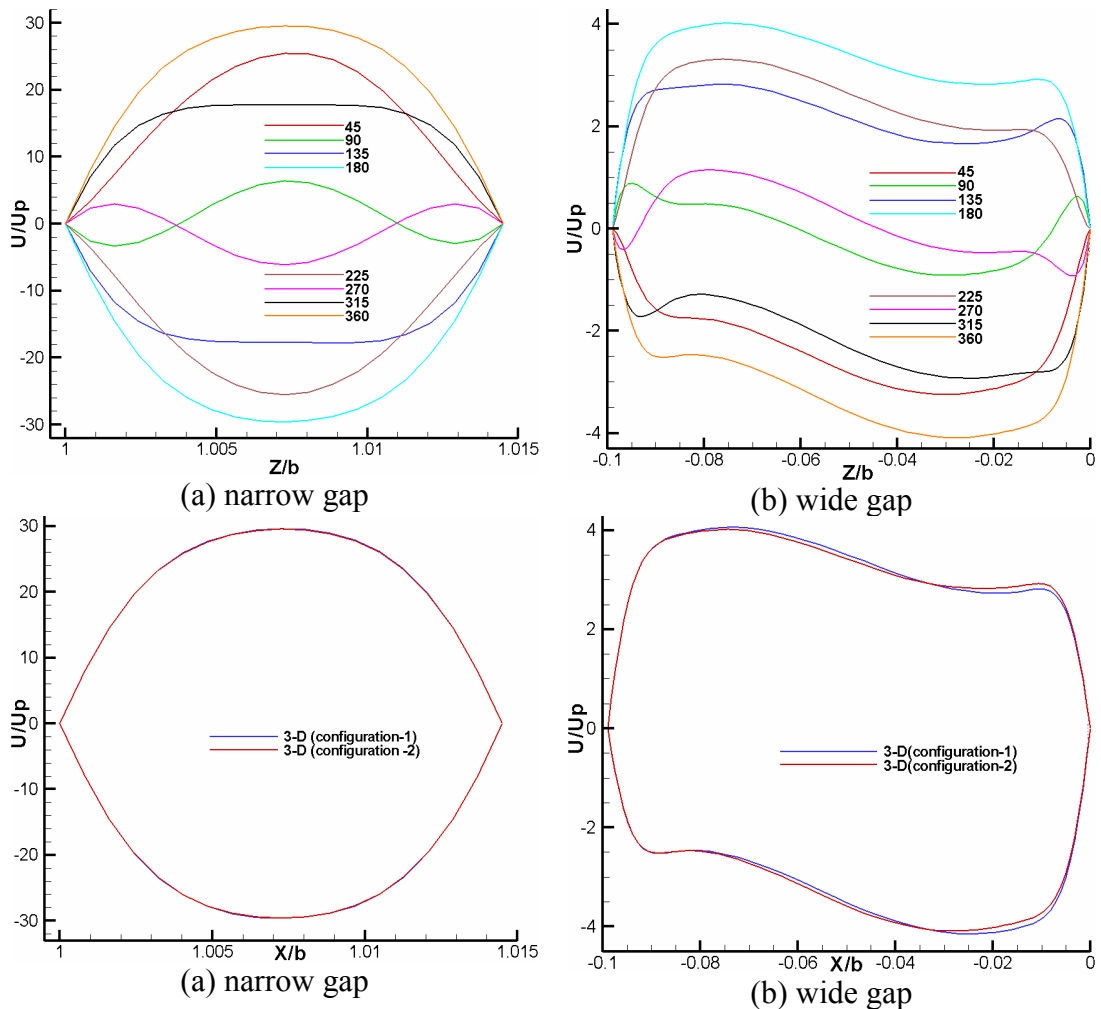
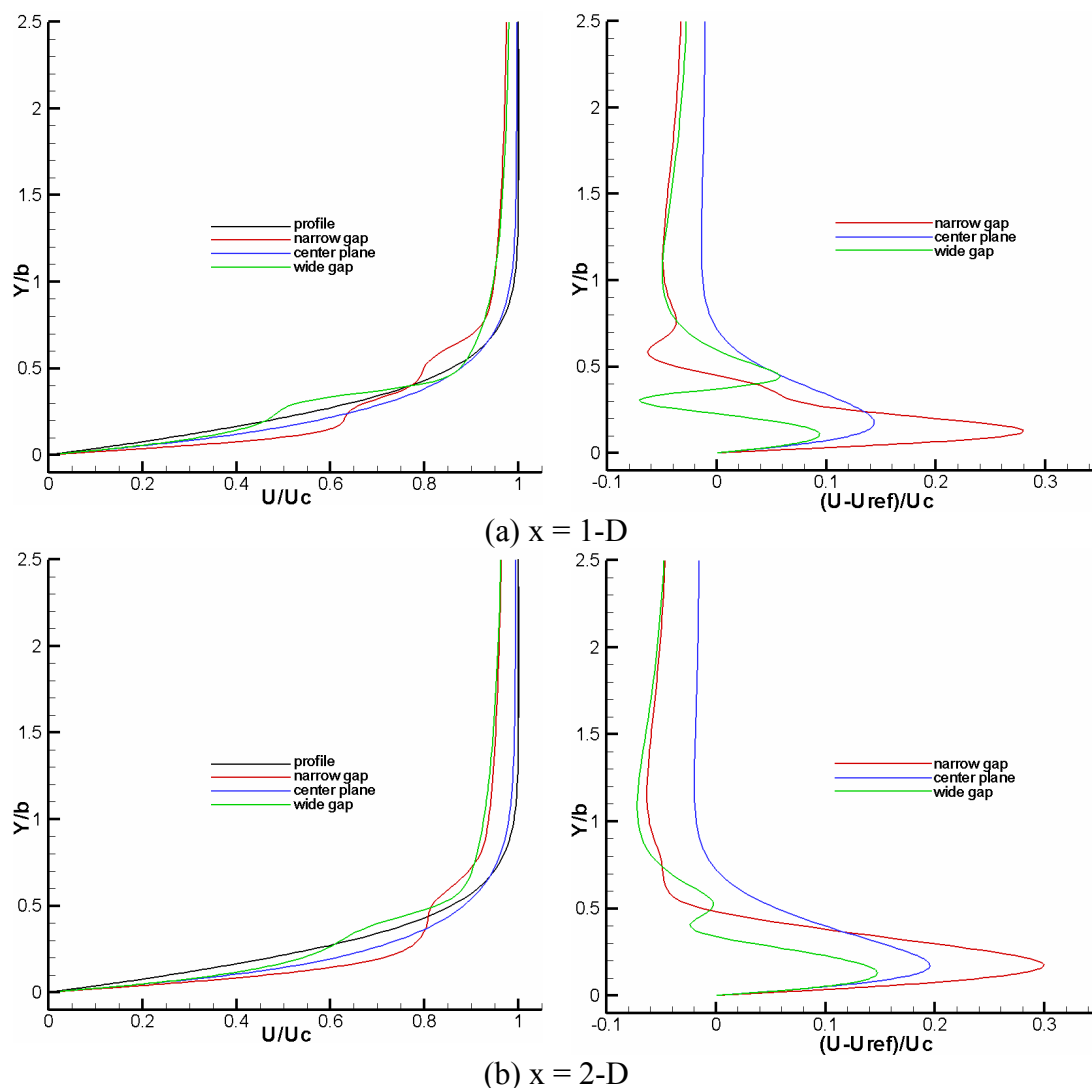


Figure 6.41 Velocity profiles in narrow and wide gap

Figure 6.42 shows a series of comparisons of boundary layer velocity profiles at different positions after the actuator. We can see in subfigures (a) and (b) that the centerline boundary layer is fuller at the wall and that the difference to the reference flow even increases with downstream distance (from 15 to 20%). Behind the gaps there are two velocity jumps in each profile due to the presence of the vortex. The flow behind both gaps accelerates close to the wall up to 30% behind the narrow gap and until 15% behind the wide one. Outside the boundary layer there is a low-speed streak at both positions. The comparison is repeated in subfigures (c) through (e), but now for constant z coordinates.



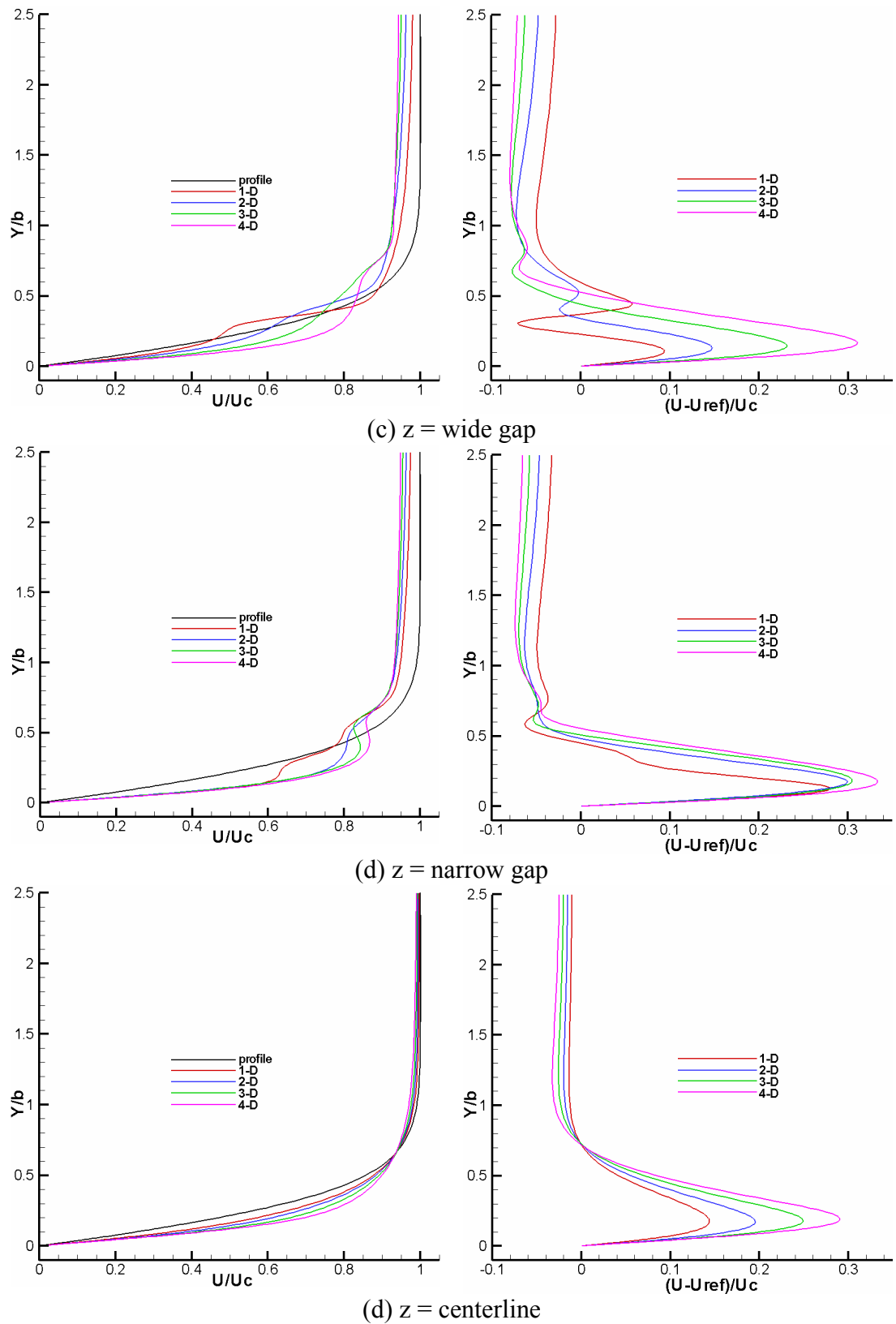


Figure 6.42: Comparison of boundary layer velocity profiles at different stream- and spanwise positions

6.5.4 Comparison of all cases

In this section we will compare the different results presented above. Figure 6.43 (a) and (b) show the comparison of velocity profiles extracted from the narrow and the wide gaps respectively for all cases of the modified design at two time instances when the plate has maximum velocity. In the narrow gap the profiles for the cases without cross flow and the profiles for both 2D and 3D are perfectly the same but different from the profiles with cross flow which are again the same for 2D and 3D, no matter which geometry configuration is used. In the wide gap the profiles for the cases without cross flow are the same, as are the profiles for the 3D cases with cross flow. Only the profile for the 2D simulation with cross flow is different.

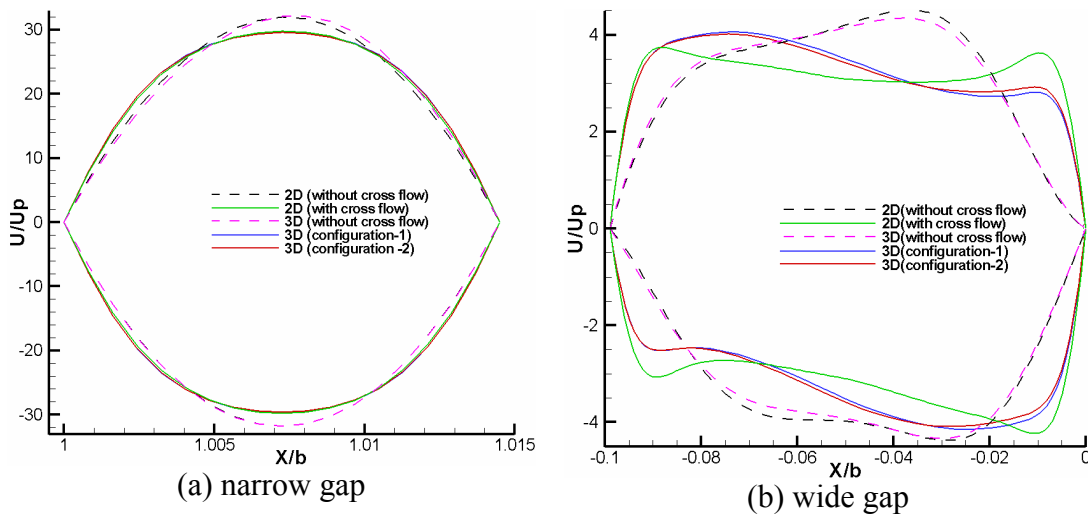
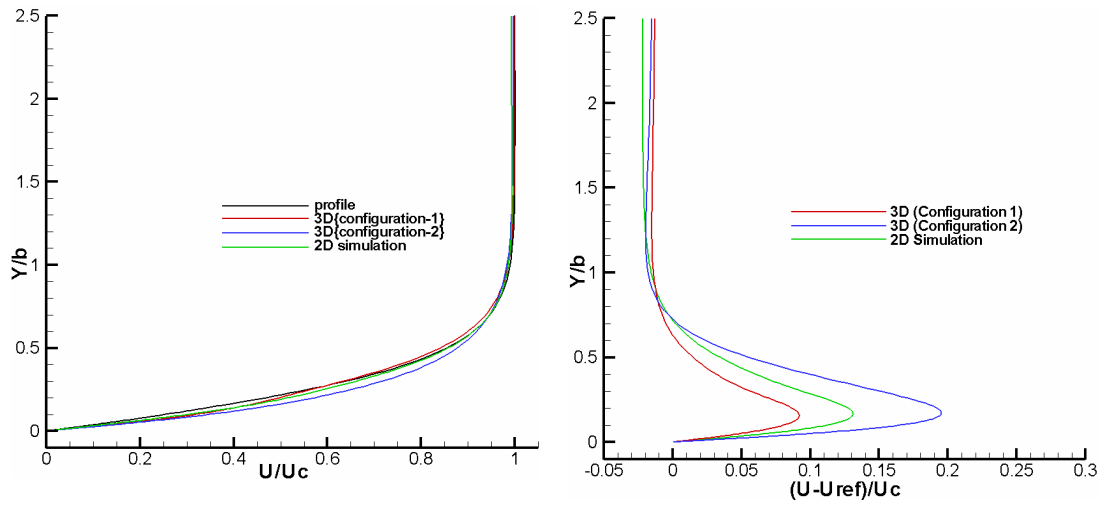
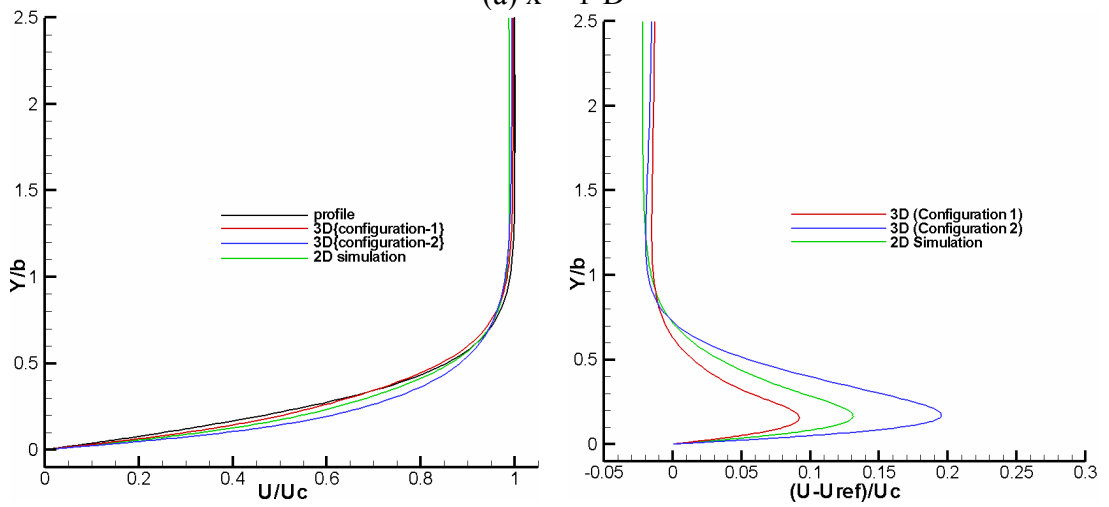


Figure 6.43: Comparison of velocity profiles in narrow and wide gap

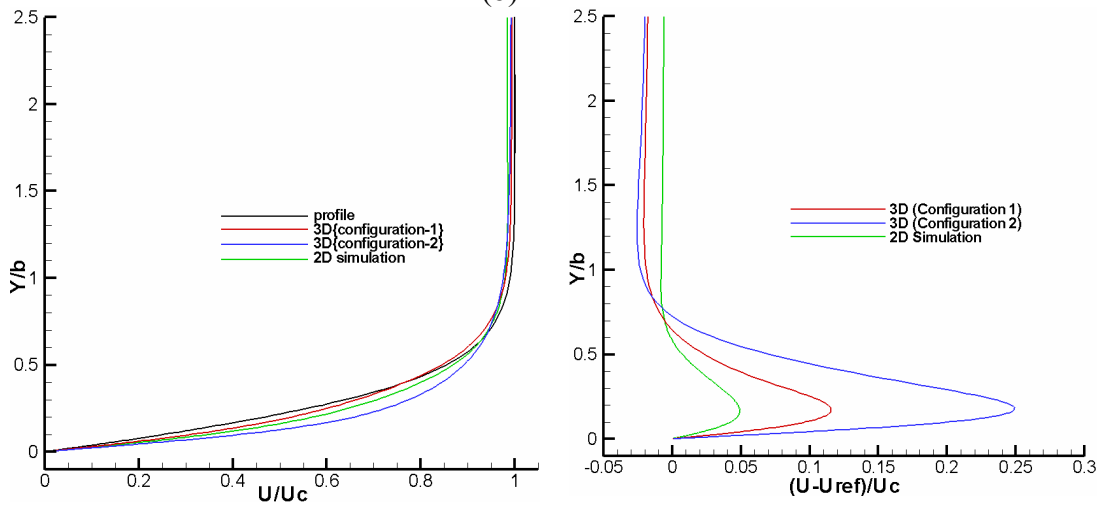
Figure 6.44 compares the velocity profiles across the boundary layer as well as their quantitative difference to the reference flow for the different cases behind the centerline of the actuator. This figure summarizes the results of the present research. We observe that our three-dimensional configuration 2 is by far the most efficient, i.e., the one where the gaps (slots in the surface) are oriented in streamwise direction. At all x stations its effect is twice as large as in the 3D configuration 1 or its two-dimensional counterpart. The difference to the reference profile increases with x and we can say that the effect of the actuators lasts at least more than five boundary layer thicknesses. Due to the large grids that are necessary for a three-dimensional simulation it was not feasible to extend the domain further in streamwise direction in order to check at which distance from the actuator the effect finally vanishes.



(a) $x = 1-D$



(b) $x = 2-D$



(c) $x = 3-D$

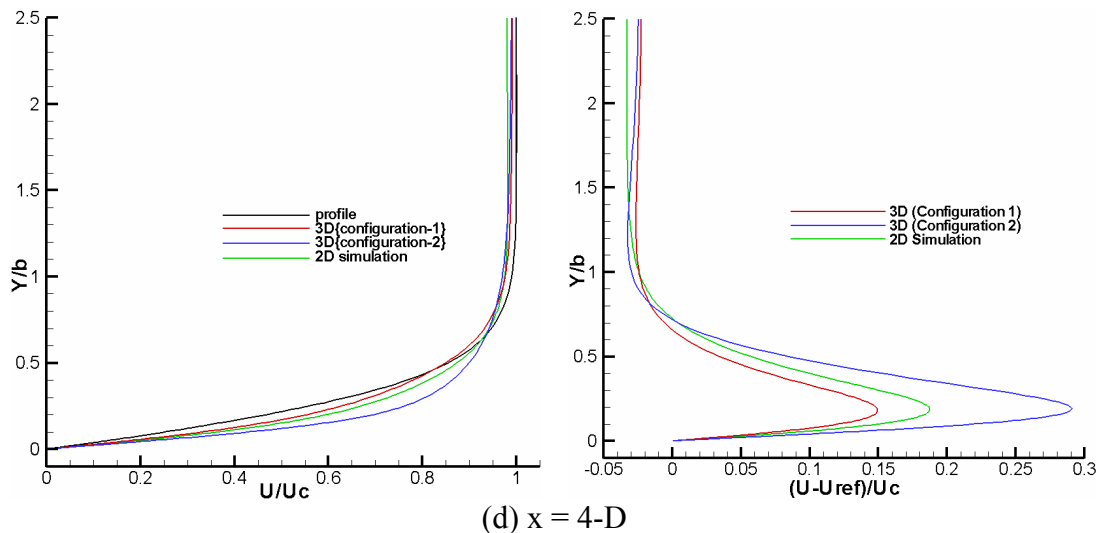


Figure 6.44: Comparison of boundary layer velocity profiles at the center line of the actuator

6.6 Summary and conclusions

In the first part of this chapter we performed 2D simulations for the original JaVA design with cross flow (two different gaps arrangements with respect to the cross flow). We found that when the wide gap is upstream and narrow gap is downstream with respect to the cross flow there was no significant change in the flow inside the boundary layer but when the narrow gap is upstream and wide gap is downstream with respect to the cross flow there was a significant change in the boundary layer even at a distance of 2-D after the actuator: the boundary layer is fuller compared to the original profile. In the second part we performed a 2D simulation of the modified JaVA design with cross flow and in this case too there was no large effect upon the boundary layer. In the third part of this chapter full 3D simulations were carried out for the geometry of the modified design without cross flow and with cross flow with two different orientations of the gaps with respect to the cross flow. When gaps arrangement is across the cross flow in configuration-1 we found that only the edges of the gaps have a significant effect upon the boundary layer. The latter is fuller there. When the gaps are arranged along the cross flow in configuration-2 a vortex emerges from the narrow gap and goes until the end of the domain, as the narrow gap is more active than the wide gap in the modified design. The effect of the longitudinal vortex on the mean flow in the central part of the actuator is to increase the velocity close to the wall. Thus, this last actuator configuration turns out to be the most effective with respect to increasing the flow momentum close to the wall, such that this kind of actuator can be used for boundary layer (separation) control.

7. Summary and conclusions

The Jet and vortex actuator (JaVA) was characterized for its original and a modified design in still air and also with cross flow using flow visualization and mean velocity measurements. In still air these actuators produce several different flows (vertical jet, wall jet and vortex flow) that may be used for active flow control. With cross-flow different orientations of the gaps with respect to the cross flow were studied.

At first a vortex mode test case related to the actuator design proposed and investigated by Lachowicz et al. (1999-2001) has been studied using the commercial CFD software Fluent® available at the Universität Stuttgart. The aim of this was to perform quantitative validations of the CFD results with respect to analytical solutions and experimental results and understanding the contributions of the basic building blocks of the actuator. By using this setup we were able to verify the computational results in a quantitative manner.

Simulations were performed by increasing the cavity length, first using a pressure outlet boundary condition at the bottom and then by closing the cavity. We also compared the results where possible with theory and also with Lachowicz et al. [18]. In case of an open cavity we got a wall jet from the wide gap but with closed cavity we got a very big vortex like Lachowicz et al. [18]. The size of the vortex in our case is bigger than the experimental results. The reason is that many parameters (like effects of cavity depth, plate position with respect to cavity wall) were missing in the literature. Therefore, we investigated these parameters further and found that they are very important and after adjusting them we get a very good agreement with Lachowicz et al. [18]. Other interesting observations are that, at the bottom of the cavity (case-1) and in the narrow gap a phase shift of the velocity with respect to the plate velocity exists. Further, velocities in the narrow and wide gap are higher for the closed cavity case as there is no flow through the bottom in this case.

After the validation of the simulation tools and our simulation methodology (since the difference of the present setup to the one investigated experimentally by Lachowicz et al. [18] is small), we had a high level of confidence, that these simulations will help to understand the different flow regimes of this kind of actuator. Unfortunately, in the literature of Lachowicz (1999-2001) there is no information available about the effect of different parameters (like cavity depth, plate position with respect to the cavity top wall and compressibility effects) upon the flow

field. Therefore, we investigated these parameters for the vortex mode. It has been shown that these parameters have decisive influence on the size of the vortex in the vortex mode of operation of the JaVA. It has been found that, as we reduce the cavity depth the vortex size also reduces and ultimately for a very small cavity, this vortex converts to a very small one followed by a wall jet. Downward motion of the actuator leads to blowing and vice versa. The largest blowing velocity is obtained in case of the shallowest cavity because the blowing rate increases with decreasing cavity depth. When we move the plate inside the cavity the effect on the out field is the same as reducing the cavity depth, we get a small vortex followed by a wall jet. The effect of the mean actuator position in the gap velocities is to slightly increase the blowing velocities with respect to the same case where the actuator is placed further above, which is in large contrast to the observations in the suction phase, where the suction magnitude is considerably increased by placing the actuator inside the cavity.

After the above investigations, we fixed the plate position and cavity depth and performed incompressible simulation to further investigate different flow modes of this actuator. We changed flow parameters (frequency and scaled amplitude) and obtained their influence upon the flow field. Here we have selected the same three cases (angled jet, free jet and wall jet) as by Lachowicz as in their experiments. For these cases, only some long-time-exposure flow visualizations that show mean-flow stream lines and scatter plots which document the observed flow structures with respect to the scaling parameters of the experiments are available for comparison with our flow fields. We get the same flow fields in these cases as Lachowicz in their experiments with the exception of an angled jet case where our jet is in the opposite side compared to Lachowicz.

For the original JaVA the significant conclusions are summarized as follows:

1. It is possible to reproduce all flow regimes (free jet, wall jet and vortex flow) which were observed by Lachowicz et al. [18] experimentally in the computer simulations by using commercial CFD software Fluent®.
2. According to the observation of Lachowicz et al. [18] the general flow-field regimes depend on scaled amplitude, actuator Reynolds number, and slot spacing, but in contrast our observation is that along with these parameters the plate position with respect to the cavity top wall and the cavity depth are also important parameters and they influence the flow significantly.

3. By reducing the cavity depth or by moving the plate inside the cavity the vortex size also reduces.
4. By changing the medium (air) density from incompressible to compressible the vortex size is almost twice.

After investigating and validating the original JaVA we also suggested a modified JaVA design and discussed it in detail in chapter 5. The basic concept to study the variation of JaVA was to better understand its working principles. In this design the moving plate element was no longer placed at the surface but is retracted into the cavity such that it produces an alternating periodic suction and blowing through the wide and the narrow gap i.e., the two motions are in anti-phase with respect to each other. In this design the narrow gap is more active since the same flow volume must pass through the wide and the narrow gap and thus it dictates the external flow field.

Different flow parameters like frequency and scaled amplitude were studied. It was found that as for the original JaVA design, it was possible to change the actuator mode from jet to vortex mode in this alternative configuration also just by a simple change of actuation frequency and amplitude, despite a completely opposite asymmetry of the flow through the gaps (and according opposite sense of rotation of the main vortex as well as different relative speeds through the gaps). This is another extremely important finding because it allows us to optimize the original JaVA by changing significant geometrical parameters without losing its flexibility and it shows that the effect first observed by Lachowicz et al. is much more general. Reynolds number, Stokes number, Strouhal number and scaled amplitude along with the plate position are very important parameters in this modified design, too. At very low Reynolds and Stokes number we get a weak vertical jet but at very high Reynolds and Stokes number the flow is always unsteady. In between we get angled jet and vortex for different sets of Reynolds and Stokes numbers. We can have different flow modes at the same frequency but different scaled amplitudes. At low scaled amplitude we get a vertical jet and as we increase the scaled amplitude we move to unsteady flow through angled jet and vortex mode.

For the modified JaVA the most significant conclusions are summarized as follows:

1. As for the original JaVA it is possible to change the actuator mode from jet to vortex mode.

2. The flow field depends upon Reynolds number (plate or gap), scaled amplitude, Stokes number and Strouhal number.
3. According to Knoll [16] by moving the horizontal plate into the cavity, it is possible to change the vortex mode to the wall jet mode and by moving the horizontal plate outside the cavity a vortex can be obtained right out of the cavity instead of above the plate.
4. Another interesting finding by Knoll [16] is that by moving the plate inside the cavity the unsteady flow becomes steady. Furthermore for this modified JaVA a vortex flow can also be achieved by removing the wide gap and moving the plate inside the cavity for the same set of flow parameters, which means that we either need a wide gap or a step between the plate and cavity top wall.
5. As for the original JaVA by changing the medium (air) density from incompressible to compressible the vortex size is increased with smaller velocities but in the modified design this increase in size is very small.

Until this point there was a complete lack of knowledge about how this actuator will behave in a cross-flow condition. In order to see this we performed simulations with a cross-flow boundary layer. 2D simulations were performed with cross flow both for the original design and the modified design. We also performed 3D simulations with and without cross-flow for the modified design in order to get some understanding of 3-dimensional effects and how this modified JaVA behaves in the actual environment.

For the original JaVA two different arrangements were used. They differ by the order of the wide and narrow gaps with respect to the cross flow. In configuration-1 the wide gap is on the upstream side of the cavity while the narrow gap is on the downstream side. In configuration-2 we reversed the gap orientation while the flow direction is still the same (positive x-direction). We found that in configuration-1 there was no significant change in the flow inside the boundary layer. The maximum difference to the reference profile is only 10%, but in configuration-2 there is a significant change in the boundary layer even after a distance of $2D$ after the actuator: the boundary layer is fuller compared to the original profile. The maximal overshoot close to the wall is about 30% of the free-stream velocity.

In the 2D simulation of the modified JaVA design with cross flow there was no large effect upon the boundary layer after the actuation. The difference to the

reference profile doesn't exceed 9%, i.e. it is much weaker than in the previous configurations.

In the last part of the sixth chapter full 3-D simulations were carried out for the geometry of the modified design without cross flow and with cross flow with two different orientations of the gaps with respect to the cross flow. In configuration-1 the flow is along the positive x-axis and, as in the 2-D case, *across* the gaps. The wide gap is on the upstream side (i.e. it is towards the flow) and the narrow gap is on the downstream side. In configuration 2 (which is now completely different to the 2-D case!) the geometry is rotated about the y-axis in such a way that the cross flow is *along* both gaps. In configuration-1 we found that only the edges of the gaps have a significant effect upon the boundary layer. The latter is fuller there. In configuration-2 a vortex emerges from the narrow gap and goes until the end of the domain, as the narrow gap is more active than the wide gap in the modified design. The effect of the longitudinal vortex on the mean flow in the central part of the actuator is to increase the velocity close to the wall. Thus, this last actuator configuration turns out to be the most effective with respect to increasing the flow momentum close to the wall, such that this kind of actuator can be used for boundary layer.

References

- [1]. Cabral, B., Leedom, L.C.: "Imaging vector fields using line integral convolution", in: SIGGRAPH 1993 Conference Proceedings, pp. 263–270, 1993
- [2]. Compton, DA., Johnston, JP.: "Streamwise vortex production by pitched and skewed jets in a turbulent boundary layer", AIAA J 30: 640-647, 1992
- [3]. F.M. White.: "Viscous Fluid Flow", McGraw-Hill, 1974
- [4]. Fluent Inc.: FLUENT 6.3 User's Guide. Documentation, 2008.
- [5]. Gad-el-Hak M.: "Flow Control- Passive, Active and Reactive Flow Management", Cambridge University Press, 2006.
- [6]. Gad-el-Hak, M., and Bushnell, D.M.: "Separation Control: Review", Journal of Fluids Engineering 113, pp. 5-30, 1991.
- [7]. Gunes, H., Cadirci, S., and Rist, U.: "Numerical Investigation of Jet and Vortex (JaVA) Actuator for Active Flow Control", AIAA 2008-3761, 4th Flow Control Conference and Exhibit 23-26 June 2008, Seattle, WA.
- [8]. Gunes, H., Cadirci, S., and Rist, U.: "An Experimental Investigation of Jet and Vortex Actuator for Active Flow Control", AIAA 2010-4410, 5th Flow Control Conference 28 June-01 July 2010,
- [9]. Hasegawa, H., Matsuuchi, K.: "Effect of Jet Pitch Angle of Vortex Generator Jets on Separation Control." Third International Conference on Fluid Mechanics, pp.526-531, 1998.
- [10]. Ingard U; Labate S.: "Acoustic circulation effects and the nonlinear impedance of orifices." J Acoust Soc America 22: 211-218, 1950.
- [11]. Jacobson SA, Reynolds WC.: "An experimental investigation towards the active control of turbulent boundary layers." Stanford Univ. Rep. TF-64, 1995. Palo Alto, Calif.
- [12]. Jacobson, S.C., Reynolds, W.C.: "Active control of stream wise vortices and streaks in boundary layers," Journal of Fluid Mechanics 360 (1998): 179-994
- [13]. Johnston J; Nishi M.: "Vortex generator jets-a means for passive and active control of boundary layer separation." AIAA J 28: 989-994, 1990.
- [14]. Joslin, R.D., Lachowicz, J. T., and Yao, C.: "DNS of Flow Induced by a Multi-Flow," ASME paper Number FEDSM98-5302, ASME Fluid Engineering Meeting, 1998.

-
- [15]. K. McManus, J. Magill.: "Airfoil performance enhancement using pulsed jet separation control." AIAA paper 97-1971, 1997.
- [16]. Knoll, A., "Numerische Untersuchung eines Jet-and-Vortex-Actuators mit fester Oberfläche." Studienarbeit, Institut für Aerodynamik und Gasdynamik, Universität Stuttgart 2008.
- [17]. Koumoutsakos, P.: "Simulations of Vortex Generators," Center for Turbulence Research, Annual Research Briefs, 1995, pp. 233-240.
- [18]. Lachowicz, J. T., Yao, C., and Wlezien, R. W.: "Flow Field Characterization of a Jet and Vortex Actuator," Experiments in Fluids, Vol. 27, 1999, PP. 12-20
- [19]. Lachowicz, J.T., C.-S. Yao, R.D. Joslin (1999a): Physical analysis and scaling of a jet and vortex actuator, FEDSM99-6921, 3rd ASME/JSME Joint Fluids Engineering Conference, July 18-22, 1999, San Francisco, Ca
- [20]. Lachowicz, J.T., C.-S. Yao, R.W. Wlezien.: "Scaling of an Oscillatory Flow-Control Device." AIAA Paper 98-0330, 1998.
- [21]. Lachowicz. J.T., C.-S. Yao ; R.D. Joslin (2001), Physical analysis and scaling of a jet and vortex actuator, J. Aircraft, Vol. 38 (3), May-Jun 2001, 573 – 575
- [22]. Magill, J. C. and McManus, K.R.: "Control of Dynamic Stall Using Pulsed Vortex Generator Jets." AIAA Paper 98-0675, 1998.
- [23]. Mc Manus K. and Magill J.: "Separation Control in Incompressible and Compressible Flows Using Pulsed Jets", AIAA Paper No. 97, Washington D.C., 1971.
- [24]. Nies, J.: "Experimentelle Untersuchung dreidimensionaler Effekte eines Jet-and-Vortex-Actuators." Studienarbeit, Institut für Aerodynamik und Gasdynamik, Universität Stuttgart 2008.
- [25]. O.A. Kandil, R.D., Lachowicz, J. T., and Z. Yang.: "Computational and physical analysis of active vortex generators," Aerospace conference proceedings, IEEE, Vol 2, 121-127, 2000.
- [26]. Rist, U., Rashad, M.A., Baysal, K.: Dritter Zwischenbericht zum Vorhaben „Numerische Untersuchungen Massenneutraler Mikro-Jet-Aktuatoren“, Institut für Aerodynamik und Gasdynamik Universität Stuttgart, Mai 2007
- [27]. Rist, U., Rashad, M.A., Baysal, K.: Funfte Zwischenbericht zum Vorhaben „Numerische Untersuchungen Massenneutraler Mikro-Jet-Aktuatoren“, Institut für Aerodynamik und Gasdynamik Universität Stuttgart, April 2010

-
- [28]. Rist, U., Rashad, M.A., Baysal, K.: Viertel Zwischenbericht zum Vorhaben „Numerische Untersuchungen Massenneutraler Mikro-Jet-Aktuatoren“, Institut für Aerodynamik und Gasdynamik Universität Stuttgart, Mai 2007
- [29]. Rist, U., Rashad, M.A.: Zweiter Zwischenbericht zum Vorhaben „Numerische Untersuchungen Massenneutraler Mikro-Jet-Aktuatoren“, Institut für Aerodynamik und Gasdynamik Universität Stuttgart, Mai 2007
- [30]. Rist, U., Söhner, V., Sielemann, M., Rashad, M.A.: Erster Zwischenbericht zum Vorhaben „Numerische Untersuchungen Massenneutraler Mikro-Jet-Aktuatoren“, Institut für Aerodynamik und Gasdynamik Universität Stuttgart, Mai 2007
- [31]. Saddoughi, S.G., Koumoutsakos, P., Bradshaw, P., Mansour, N.N.: “Investigation of on demand vortex generators,” Center for Turbulence Research Manuscript No. 171, Stanford University, 1998
- [32]. Tang, H., Zhong, S.: “2D numerical study of circular synthetic jets in quiescent flow”, *Aeronautical Journal* 109, 89-97, 2005
- [33]. Wallis R. A., and Stuart C. M.: “On the Control of Shock Induced Boundary Layer Separation with Discrete Jets”, *Aeronautical Research Council Current Paper No. 494*, London, Great Britain, 1958.
- [34]. Wallis, R.A.: “A Preliminary Note on a Modified Type of Air Jet for Boundary Layer Control.” *Current paper No.513*, *Aeronautical Research council*, Australia, 1956.
- [35]. Wallis, R.A., and Stuart, C.M.: “On the control of Shock-Induced Boundary-Layer Separation with Discrete Jets.” *Current Paper No. 595*, *Aeronautical Research Council*, Australia, 1958.
- [36]. Wiltse, J. M. and Glezer, A.: “Active control of a free jet using a synthetic jet” *International Journal of Heat and Fluid Flow* Volume 29, Issue 4, August 2008, pages 967-984, 1993.
- [37]. Wiltse, J. M. and Glezer, A.: “Manipulation of free shear flows using piezoelectric actuators.” *J. Fluid Mech*, 249, 261–285, 1993.

Appendix

```

/*****
UDF for specifying unsteady velocity to the plate
*****/

#include <udf.h>
#define PI 3.141592654
DEFINE_CG_MOTION(mixer, dt, cg_vel, cg_omega, time, dtime)
{
    real f = 128;
    real a = 0.281;
    real omega= 2.0*PI*f;
    real vel = a*omega*cos(omega*time);
    cg_vel[0] = 0.0; /* x-velocity*/
    cg_vel[1] = vel; /* y-velocity*/
    cg_vel[2] = 0.0; /*z-velocity*/
    NV_S (cg_omega, =, 0.0); /* no angular motion */
}

```

```

/*****
UDF for specifying unsteady velocity profile boundary condition at the plate
*****/

#include "udf.h"
#define PI 3.141592654
DEFINE_PROFILE(unsteady_velocity, thread, position)
{
    face_t f;
    real t = CURRENT_TIME;
    begin_f_loop(f, thread)
    {
        F_PROFILE(f, thread, position) = 0.000281*256*PI*cos(256*PI*t);
    }
    end_f_loop(f, thread)
}

```

```

/*****
UDF for specifying the steady-state velocity profile for inlet boundary layer
*****/

#include "udf.h"
DEFINE_PROFILE(inlet_x_velocity, thread, position)
{
    real x[ND_ND]; /* this will hold the position vector */
    real y;
    face_t f;
    begin_f_loop(f, thread)
    {
        F_CENTROID(x,f,thread);
        y = x[1];
        F_PROFILE(f, thread, position) = 1.0*tanh(y/0.00377);
    }
    end_f_loop(f, thread)
}

```


Curriculum Vitae

Personal Data

Name	Muhammad Aqeel Rashad
Date of birth	November 20 th , 1974
Place of birth	Sheikhupura, Pakistan
Nationality	Pakistani
Marital status	married
Email address	rashad@iag.uni-stuttgart.de aqeel_rashad@yahoo.com

Qualifications

2003	Master of Mechanical Engineering, National University of Science and Technology (NUST), Rawalpindi, Pakistan
1998	Bachelor of Metallurgical Engineering University of Engineering and Technology (UET), Lahore, Pakistan

Experience

2000-2001	Research assistant National University of Science and Technology (NUST), Rawalpindi, Pakistan
2001-2005	Assistant manager (Tech) National Engineering and Scientific Commission (NESCOM) Islamabad, Pakistan
2006-2010	IAG (Institute of Aerodynamics and Gasdynamics), University of Stuttgart, Stuttgart, Germany